Structural, Dielectric and Magnetic Properties of Single-phase Room Temperature Multiferroic – (Ho, La)-LuFeO$_3$

A Thesis submitted in partial fulfillment of the award of the degree of

Doctor of Philosophy

By

Leelashree S

Reg.No: 15PHPH07

SCHOOL OF PHYSICS
UNIVERSITY OF HYDERABAD
HYDERABAD 500046, TELANGANA, INDIA

December, 2021

Dedicated …

To my mother

The woman who gave me two things,

Wings and Roots…..

And to my brother

For the unconditional love….

DECLARATION

I, **Leelashree S**, hereby declare that the matter embodied in the thesis- "**Structural, Dielectric and Magnetic Properties of Single-phase Room Temperature Multiferroic – (Ho, La)-LuFeO$_3$**", is the result of the investigations carried out by me in the School of Physics, University of Hyderabad, Hyderabad, India, under the supervision of **Prof. S. Srinath**. This thesis is free from plagiarism. I hereby declare that it has not been submitted previously in part or in full to this University or Institution for award of any degree or diploma.

S. Leelashree

(Leelashree S)

Reg. No: 15PHPH07

Date: 16-12-2021

Place: Hyderabad

CERTIFICATE

This is to certify that the thesis entitled **"Structural, Dielectric and Magnetic Propertie of Single-phase Room Temperature Multiferroic – (La,Ho)-$LuFeO_3$",** submitted by Ms. Leelashree S, bearing registration number 15PHPH07, in partial fulfilment of the requirements for award of Doctor of Philosophy in the School of Physics is a bonafide work carried out by her under my direct supervision.

This thesis is free from plagiarism and has not been submitted previously in part or in full to this or any other University or Institution for award of any degree or diploma.

The student has the following publications and conference proceedings before the thesis for adjudication.

1. Effect of progressive substitution of Lu by Ho on the structural and dielectric properties of nanocrystalline $LuFeO_3$ orthoferrite

   Leelashree S, S.N. Kaul and S. Srinath; Materials Research Bulletin **145**, 111570 (2020).
2. Investigation of Structural, Ferroelectric, and Magnetic Properties of La-Doped $LuFeO_3$ Nanoparticles

   S Leelashree, S Srinath; Journal of Superconductivity and Novel Magnetism **33** (6), 1587-1591 (2020).
3. Structural and Magnetic properties of Room Temperature Multiferroic $Lu_{0.9}Ho_{0.1}FeO_3$

   Leelashree S, P.D. Babu, S.N. Kaul and S. Srinath; International Journal of Innovative Research in Physics **1** (2), 37-41 (2020).

4. Effect of La doping on dielectric and magnetic properties of room temperature multiferroic $LuFeO_3$
S Leelashree, PD Babu, S Srinath; American Institute of Physics Conference Series **1953** (1), 120076 (2018).

Further, the student has passed the following courses towards the fulfilment of course required for PhD.

Course code	Name	Credits	Pass/Fail
PY801	Advanced Quantum Mechanics	4	Pass
PY803	Advanced Statistical Mechanics	4	Pass
PY804	Advanced Electromagnetic Theory	4	Pass
PY821	Research Methodology	4	Pass

16/12/2021
(Thesis Supervisor)

Dr. S. Srinath
Professor
School of Physics
UNIVERSITY OF HYDERABAD
Central University P.O.
Hyderabad-500 046.

Dean

School of Physics

University of Hyderabad.

DEAN
School of Physics
University of Hyderabad
Hyderabad-500 046, INDIA

Acknowledgements

I express my heartfelt respect and gratitude to my supervisor Prof. S. Srinath for his excellent mentorship, continuous support and for his kindness throughout the duration of my research period. It is my privilege to have learnt research from him. I have also learnt how to be kind and how to treat all people alike from him. I am rendered speechless at how Prof. Srinath has taught me to believe in me. Thank you, sir, for giving me the space to fail, to make mistakes and learn from them. I also extend my gratitude to Dr. Vijaya Laxmi for her caring nature and for the occasional treats towards all of us in the lab. I specially thank Prof. S. N. Kaul for shepherding me well through the work and for teaching me the importance of passion and patience in research. His constant patronage and valuable suggestions helped me overcome all the difficulties and make things happen. I am at a loss for words when I attempt to express how much I am obliged to him.

I want to express my gratitude to my Ph.D. review committee members Dr. Venkataiah Gorige and Prof. Ashok Chatterjee for their suggestions during doctoral review presentations. I would also like to thank the present dean Prof. K. C. James Raju and the former deans Prof. R. Singh, Prof. Bindu A Bambah, Prof. V. Seshubai, Prof. Ashok Chatterjee for providing the necessary facilities.

I thank Dr. P.D. Babu, UGC-DAE, CSR Mumbai for providing the experimental facilities for magnetic measurements. I would also like to extend my thanks to Dr. MSS Bharathi, Mr. Jagganath Rathod and Prof. Venugopal Rao Soma, who are also acknowledged for their help in carrying out Raman measurements.

I thank Dr. Mangesh Mahajan (Application specialist, Xpert Panalytical) for the continuous help during the XRD measurements and analysis. I also thank Mr. Scott P Chapman (Digital Engineer, Radiant Technologies) for his timely help during ferroelectric measurements.

I am thankful to the School of Physics office staff Mr. Narasimha Rao, Mr. Prasad, Ms. Deepika, Mr. Abraham, Mrs. Vijayalakshmi, Mr. Sudarshan, Ms. Shashikala for their help in administrative matters. I would also like to thank the operators, Mr. Suresh, Mr. Rajesh, Dr. Manjunath, Dr. Syed Maqbool Ahmed from CIL and Ms. Sunitha, Mr. Laxmi Narayan and Ms. Jyothi from School of Physics for helping me carry out the experiments.

I am grateful to UoH BBL fellowship for the financial support.

I thank all my seniors Dr. A. Sendhil Kumar, Dr. Suresh Pittala, Dr. Pavan Venu Prakash Madduri, Dr. B Ravi kumar, Dr. Binoy Krishna Hazra, Dr. Anshu Gaur for their encouragement and support. I also would like to thank my lab mates Lanuakum Longchar, Saarthak Dulgaj and Mainur Rahman for creating a lively lab atmosphere, and for their continuous co-operation and stimulating discussions. I couldn’t have asked for a better lab mates.

I am also thankful to Dr. Pradeep Reddy Vanga for inspiring me to pursue research and also for standing-up for me during difficult times. I am indebted to my dearest friends, C. Nivetha, Manasa Kalla, Giri Mani, Sebin Devasia, Avisek Das, Muhammed Rasi, Naresh Shyaga, Zahid Malik and Siva Raju for their love and care. I would also like to thank my batch mates Sujai Matta, Md Abu Taher, Bappaditya Sankhari, Karra Vinod Kumar, Nilanjan Basu, Rashmi Ranjan Suna, B. Praneetha for their support and for making my stay in the university enjoyable.

I am extremely grateful to Amma, Kanagaraj maama, Kamali athai, my brother, Dr. S. Gopinath and my cousin Sowmi Narendran for providing me with the nurturing environment and for always believing in me. If not for them, I wouldn’t have reached where I am today.

CONTENTS

1. Introduction: Single phase room temperature multiferroics

References

2. Experimental Techniques employed

2.2. Synthesis method

2.3. Sample Characterization

2.4. Physical property measurements

References

3. Synthesis and Structural Characterization of Lu$_{1-x}$Ho$_x$FeO3 ($0 \leq x \leq 1$)

4. Nature of magnetism in $Lu_{1-x}Ho_xFeO3$ ($0 \leq x \leq 1$)

5. Dielectric polarization and relaxation in $Lu_{1-x}Ho_xFeO_3$ ($0 \leq x \leq 1$)

6. Structural, Dielectric and Magnetic properties of $Lu_{1-x}La_xFeO_3$ ($0 \leq x \leq 0.25$)

7. Summary and Future Scope of the Present Thesis

CHAPTER 1

Introduction:
Single-phase room temperature multiferroics

In this chapter, a brief introduction to the multiferroic oxides is presented. Various types of magnetic order and interactions relevant to this field are outlined. A brief survey of the literature highlighting the interest in pure and RE doped $LuFeO_3$ *is made. This chapter ends with aim and scope of the thesis.*

1.1. Introduction

In this chapter, an outline of perovskites, orthoferrites, fundamental magnetic interactions, ferroelectricity, multiferroics, a detailed literature review on $LuFeO_3$, and the motivation of this thesis work is briefly explained.

1.2. Perovskites

Materials with the chemical formula ABX_3 are perovskites. Here. 'X' can be any anion; generally, it is oxygen. 'A' and 'B' are cations with different ionic radius. The first-ever found perovskite material is $CaTiO_3$ by the Russian mineralogist L.A. Perovski [1]. Generally, the 'A' cations are larger compared to the 'B' cation. Twelve oxygen ions surround the 'A' cations and six oxygens ions surround the 'B' cations forming an octahedral cage (FeO_6). The coordination number plays a major role in the ionic radius of the cations. The crystal structure and stability of the perovskite structure strongly depend on the ionic radius. The stability of the perovskite structure can be calculated using Goldshmidt's tolerance factor, t [2], given as

$$t = \frac{r_A + r_O}{\sqrt{2}\,(r_B + r_O)} \qquad eqn\ 1.1$$

Where r_A, r_B, r_O are the ionic radius of A, B cations and O anion, respectively. The cubic crystal structure with space group Pm3m is ideal with a tolerance factor '1' [3]. When the ionic radius of 'A' and 'B' cation radius are comparable, it can form a cubic structure (figure 1.1 (a)) [4]. As the difference between the size of the 'A' and 'B' cation increases, crystal structures such as orthorhombic and tetragonal forms [5]. In the cubic system, the B-O-B bond angle is 180°. Also, the FeO_6 octahedra cages lie parallel to the axis. When the 'A' cation size is much larger compared to the 'B' cation, to stabilize the structure, the B-O-B angle bends and in turn, tilts the FeO_6 octahedra cages (figure 1.1 (b)) [6–8]. The properties of the perovskite materials are decided by the electronic structure of 'A' and 'B' cations, B-O-B bond angles and distortion of FeO_6 octahedra cages. The physical properties can be tuned by doping appropriate atoms in the 'A' site. There are a lot of studies on the effect of the nature of the cations on the dielectric and magnetic studies [9–11]. Some common perovskites are $SrTiO_3$, $BaTiO_3$, $RFeO_3$s, $RMnO_3$s.

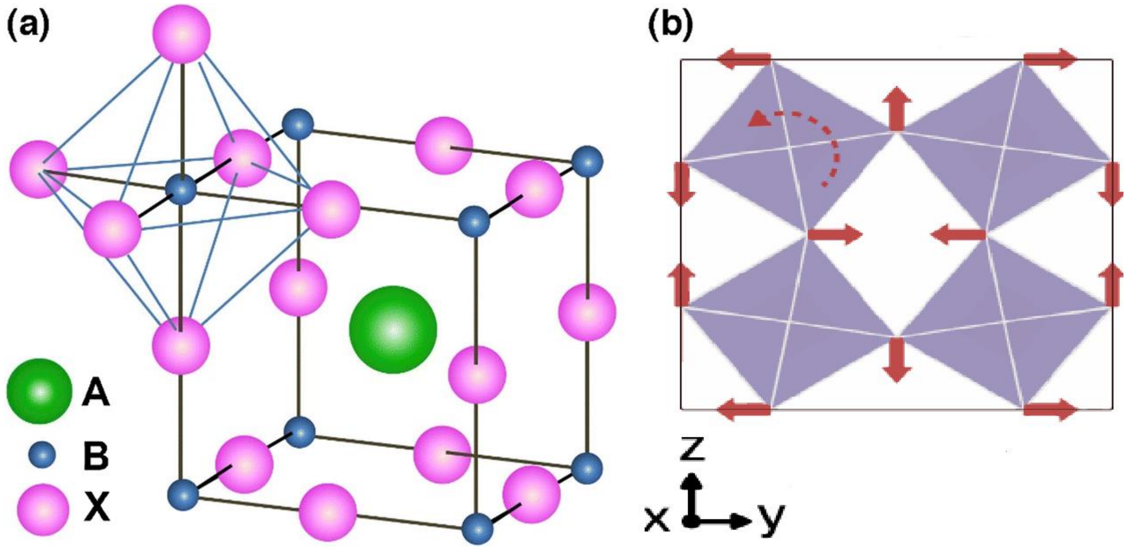

Figure 1.1. (a). ABX_3 perovskite structure showing BX_6 octahedral and larger A cation occupied in cubooctahedral site; **(b)** in-phase tilting of octahedra. [6]

1.3. Orthoferrites

Othoferrites ($RFeO_3$) are distorted perovskites with orthorhombic crystal structure. Here, 'R' can be any rare earth element (La-Lu). As the ionic radius decreases from La to Lu due to lanthanide contraction, the distortion in the system enhances [12]. These distortions play an essential role in the magnetic, dielectric, and optical properties. Orthoferrites have long been known for their exotic magnetic properties such as G-type antiferromagnetic ordering (arising from the super-exchange interaction operating between the Fe^{3+} spins via O^{2-}, i.e., Fe^{3+}- O^{2-} - Fe^{3+}), an antiferromagnetic to paramagnetic phase transition at a temperature T_{N1} as high as ~ 650 K [12], ordering of R magnetic moments at $T_{N2} < 10$ K and the reorientation of Fe^{3+} spins at T_{SR} [13,14]. The combined effect of the super-exchange and spin-orbit interactions leads to the interaction of the Dzyaloshinsky-Moriya (DM) form, which gives rise to canted Fe^{3+} spins and accounts for weak ferromagnetism prevalent in these systems at low temperatures [15,16]. Apart from the interest in their fundamental properties, $RFeO_3$s attract significant attention in applications like magnetic sensors, memory applications, optical switches [17], gas sensors [18], solid-state fuels cells, and multiferroics properties [19–21]. $LuFeO_3$, which is the last candidate in the orthoferrite family, is studied with and without rare-earth substitution (La and Ho) in the present thesis.

1.4. Fundamentals of magnetism

1.4.1. Crystal field effect

Generally, the magnetic interactions in the 3*d* metal ions are due to the partially filled electrons in the outermost orbital. In the case of 3*d* metal ions, the wave functions overlap compared to the 4*f* electrons due to their localized nature. The 3*d* electrons experience an electric field produced by the surrounding ions called as crystal field (figure 1.3 (a)) and the magnetic properties of the materials change based on the symmetry of the crystal field [22]. In general, the 3d electrons consist of five degenerate energies based on the shape of their orbitals [23]. They are d_{xy}, d_{yz}, d_{zx}, $d_{x^2-y^2}$, d_{z^2} and they are shown in figure 1.2. The energy levels can be categorized into e_g ($d_{x^2-y^2}$, d_{z^2}) and t_{2g} (d_{xy}, d_{yz}, d_{zx}) levels. Δ denotes the energy difference between the e_g and t_{2g} levels. Based on the symmetry of the neighboring ions, the degeneracy will be lifted. In the case of a spherical symmetry produced by the surrounding ions, all the energy levels will be raised without affecting the degeneracy.

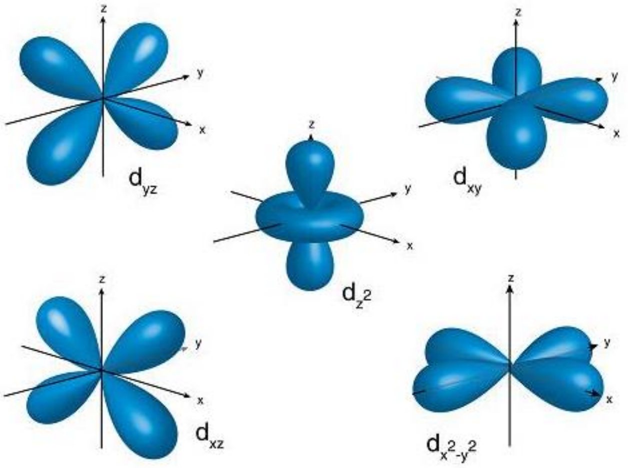

Figure 1.2. Representation of *d*- orbitals [23]

When the surrounding ions are arranged in an octahedral symmetry, the energy levels $d_{x^2-y^2}$, d_{z^2} experience higher repulsive energy because they lie along the *xyz* axes, resulting in increased energy compared to the t_{2g} levels. Since d_{xy}, d_{yz}, d_{zx} lie in between the axes, they experience lesser repulsive force. The different repulsive forces experienced by the energy levels lift the degeneracy. The e_g levels are raised by 2Δ/5 and the t_{2g} levels are decreased by 3Δ/5.

None of the surrounding ions will lie along the *xyz* axes in a tetrahedral environment, but the t_{2g} levels lie closer to the surrounding ions than the e_g levels. This increases the energy of t_{2g} levels by $3\Delta/5$ and decreases the e_g levels by $2\Delta/5$. The schematic representation for the crystal effect in octahedral and tetrahedral environments is given in figure 1.3 (b) & (c) [24].

In the transition metals, orbital angular momentum is quenched (L=0) and only the spin angular momentum (S) contributes to total angular momentum (J). Thus, the effective magnetic moment can be calculated from the equation, $\mu_{eff} = g\sqrt{S\,(S+1)}\,\mu_B$. In the case of 4*f* electrons, the electrons are screened by 6*s* orbital; thus, they are not affected by the crystal field as strong as the 3*d* electrons. Due to this, both the spin and orbital angular momentum contributes to the total angular momentum J. Then, the effective moment can be calculated as $\mu_{eff} = g\sqrt{J\,(J+1)}\,\mu_B$.

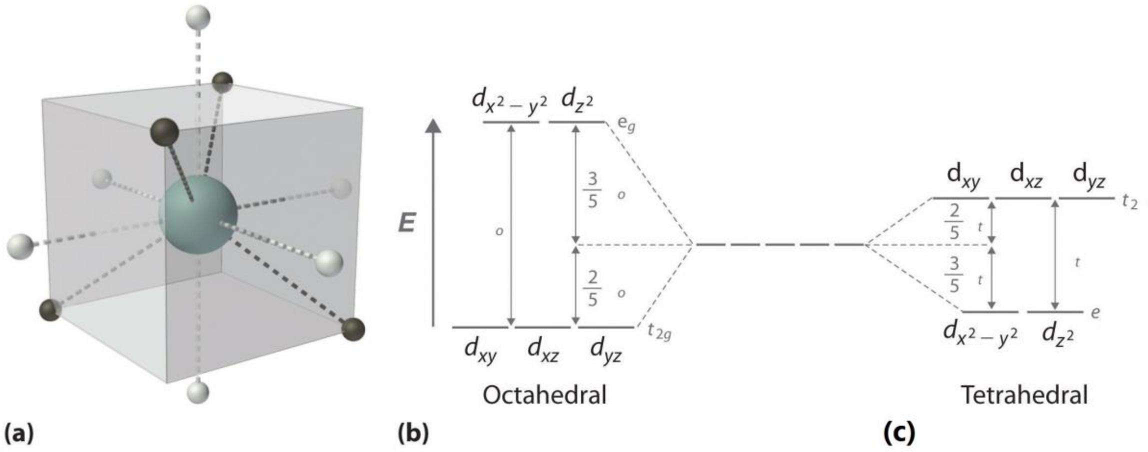

Figure 1.3. (a) Tetraheral field surrounding a central transition metal. **(b)** Splitting of the degenerate d-orbitals due to an octahedral field and **(c)** the tetrahedral field. [24]

1.4.2. Different magnetic orders

The magnetic materials can be classified based on the nature of the magnetic moments interact with each other. The different magnetic orders are briefly introduced here [25].

1.4.2.1. Diamagnetism

Materials with no unpaired electrons in the outermost shells (or filled shells) exhibit diamagnetism. Diamagnetism is an induced effect. When the diamagnetic materials are subjected to the magnetic field, the orbital motion of the electrons changes opposing the field, resulting in negative magnetization (figure 1.4 (a)). Diamagnetic materials have a minimal but negative susceptibility [26]. The diamagnetic susceptibility is independent of temperature (figure 1.4 (b)). Some examples of diamagnets are Cu, Bi, NaCl.

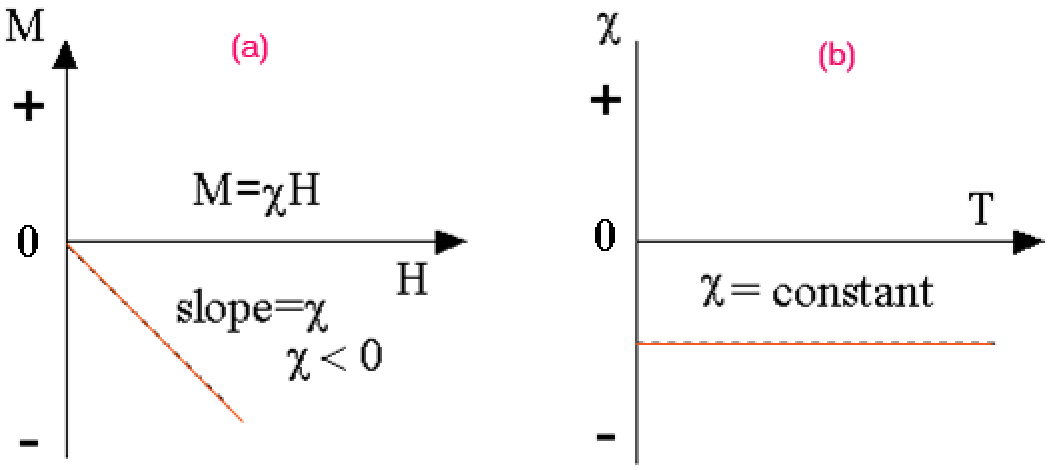

Figure 1.4. (a) Magnetisation as a response to an applied field of a diamagnetic material and **(b)** the variation of diamagnetic susceptibility with temperature [26].

1.4.2.2. Paramagnetism

When there are unpaired electrons available in the outermost shells, the material can exhibit paramagnetism. These unpaired electrons give rise to permanent dipole moments. All the dipole moments are oriented randomly in the paramagnetic state due to thermal energy resulting in zero net magnetization. The dipoles try to orient along the field direction in presence of the field competing against the thermal energy, thus giving rise to a small yet finite net magnetization. The temperature-dependent susceptibility based on Curie's law, for a paramagnetic material with N number of magnetic moments is given by

$$\chi = \frac{\mu_0 N \mu^2}{3K_B T} = \frac{C}{T} \qquad eqn\ (1.2)$$

Where K_B is Boltzmann constant and $\frac{\mu_0 N \mu^2}{3K_B}$ is Curie's constant. Curie's law holds good only when the magnetization is low ($\mu_B H \leq K_B T$) and the spins are non-interacting. When the spins are interacting, the general behavior is well depicted by Curie- Weiss law,

$$\chi = \frac{C}{T - \theta} \qquad eqn\ (1.3)$$

Where θ represents transition temperature below which there is an interaction between the dipole moments, the sign of θ indicates the nature of the ground state magnetic interaction.

1.4.2.3. Ferromagnetism

The magnetic dipoles spontaneously align parallel within the domain in ferromagnetic materials below the Curie transition temperature (T_C). Weiss postulated that this is due to the internal molecular field. The origin of the molecular field is exchange energy and Heisenberg gave the Hamiltonian as

$$H = -2J\, S_i . S_j \qquad eqn\ (1.4)$$

It can be understood from the eqn. (1.4) that the parallel spin orientation will lower the energy, thus giving rise to ferromagnetism. Below the transition, all the dipoles are oriented in the same direction due to the strong internal field dictated by magneto-crystalline anisotropy (easy axis). Increase in temperature disorients the dipoles and results in paramagnetic behavior. Ferromagnetic materials have very high and positive susceptibility. Fe, Co, Ni are some examples of transition metal ferromagnets.

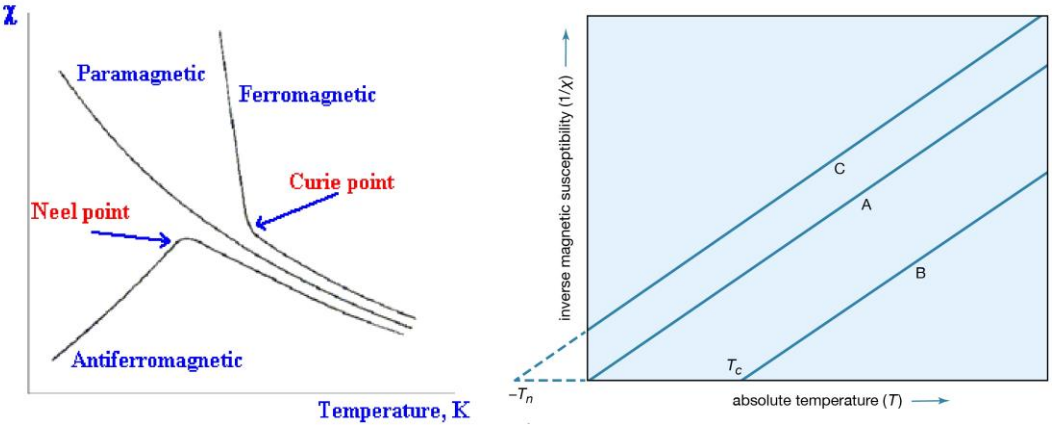

Figure 1.5. Curie-Weiss behaviour of paramagnetic (A), ferromagnetic (B) and antiferrromagntic (C) material. [27]

1.4.2.4. Antiferromagnetism

When the magnetic dipoles orient anti-parallel below the Neel temperature (T_N), the net magnetization goes to zero and the magnetic materials exhibiting this phenomenon are antiferromagnetic. Above T_N, they show paramagnetism. Antiferromagnetic materials have a small and positive susceptibility [27]. α- Fe_2O_3, MnO, FeMn, Cr_2O_3 are some examples of antiferromagnetic materials. Based on their interaction, antiferromagnetic materials can be classified as follows:

A type- The magnetic dipoles in the plane are ferromagnetically coupled and the planes are antiferromagnetically coupled.

C type- The magnetic dipoles in the plane are antiferromagnetically coupled and the planes are ferromagnetically coupled.

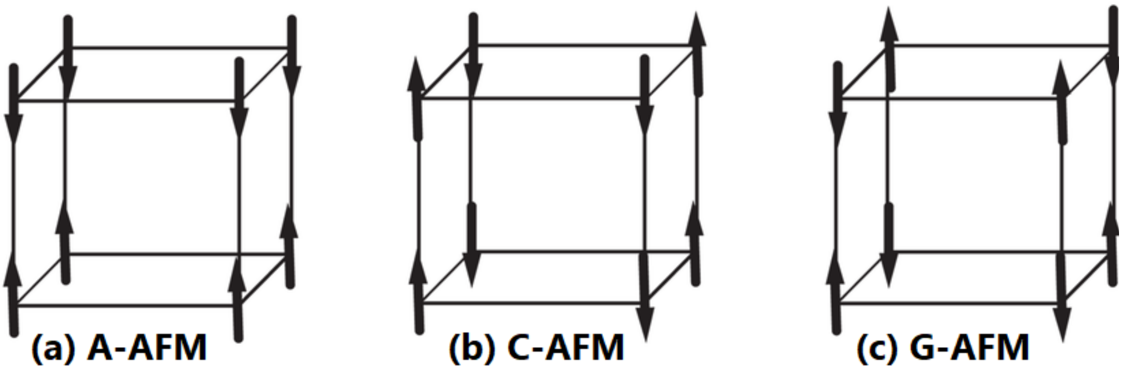

Figure 1.6. Three types of antiferromagnetic (AFM) structures. [28]

G type- The magnetic dipoles within the plane and between the planes are antiferromagnetically coupled.

The schematic representation of the various types of antiferromagnets [28] is shown in figure (1.6).

1.4.2.5. Ferrimagnetism

In ferrimagnetic materials, the ground state magnetic coupling is antiferromagnetic. Due to chemically different species and or different valance states (Fe^{2+} and Fe^{3+}), net magnetization is observed despite antiparallel arrangement. The different valence states possess different molecular field; thus, the temperature-dependent magnetization varies for the sublattices. $MnFe_2O_4$, $NiFe_2O_4$, $CoFe_2O_4$, Fe_3O_4 are some of the ferrimagnetic materials.

1.4.3. Various magnetic interactions

Based on the nature of the magnetic interaction between the magnetic ions, the magnetic properties of a material is determined. The interactions are direct interaction and indirect interactions such as double exchange, super-exchange, and antisymmetric Dzyaloshinsky-Moriya (DM) interactions.

1.4.3.1. Direct exchange interaction

The direct exchange interaction occurs when the wave functions of the neighboring ions' magnetic moment's overlap. Heisenberg described the interactomic Coulomb interaction by the Hamiltonian equation (1.4). The interaction strength depends on the distance between the wave functions. When the wave functions are closer (farther), due to the strong (weak) overlap, antiferromagnetic (ferromagnetic) ordering is favored, obeying Pauli's exclusion principle (figure 1.7 (a)).

1.4.3.2. Indirect exchange

Many solids like MnO exhibit magnetic properties even though the magnetic ions are too far for any direct exchange to occur (figure 1.7 (b)). The reasons for indirect exchange to occur are: 1. If magnetic ions are farther apart, like 4*f* electrons of rare-earth atoms, overlapping of the wave functions is weaker. 2. Magnetic ions are mediated through a non-magnetic ion such as oxygen. In both cases, the direct exchange is not possible. Based on the separation between the magnetic ions, the nature of the magnetic coupling is decided.

1.4.3.3. Super-exchange interaction

When the magnetic ions with the same oxidation states (Mn^{3+}) are separated farther and mediated through an oxygen atom, the interaction is called super-exchange interaction. The nature of the super-exchange interaction is decided by the symmetry between the magnetic ions and the results are summarized and given as Goodenough- Kanamori rules [29]. Figure 1.7 (c) shows that the two valence electrons of oxygen form a 180° covalent bonding with the Mn ion. The spin-down electron (e^-) of O^{2-} couples antiferromagnetically with the spin-up of the left side Mn^{3+} ions. The spin-up e^- of O^{2-} pairs antiferromagnetically with the spin-down of the right side Mn^{3+} ions. The exchange interaction is stronger when the magnetic ions are connected with a bond angle of 180°. Any deviation from 180° gives rise to a weak

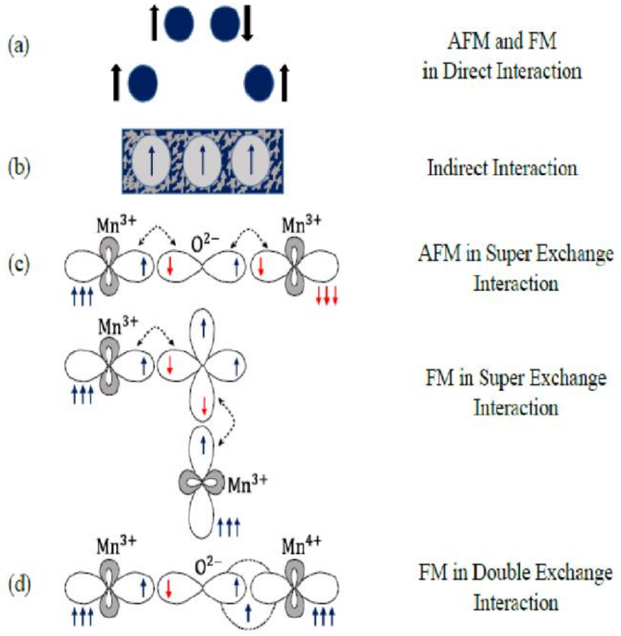

Figure 1.7. Schematic representations of various magnetic interactions [29]

ferromagnetic moment. The interaction becomes completely ferromagnetic when the overlap is weaker and the bond angle is 90°, as shown in figure 1.7 (c).

1.4.3.4. Double-exchange interaction

Double-exchange interaction, established by Zener [30,31], occurs only when mixed oxidation states of magnetic ions are present in the material, for example, Mn^{3+} and Mn^{4+}. The schematic representation of double-exchange for $LaMnO_3$ is shown in figure 1.7(d). In this material, the Mn ions are in an octahedral environment. The degeneracy of the *d*- orbital energy levels is lifted as a consequence of the crystal field effect. The Mn^{3+} state has one spin-up electron in the e_g level and Mn^{4+} has no electrons in the e_g level. When O^{2-} gives up one spin-up electron to Mn^{4+}, the electron from Mn^{3+} hops to oxygen ion retaining its spin. The hopping of electrons from Mn^{3+} to O^{2-} to Mn^{4+} occurs simultaneously within the same spin-state electrons, thus giving rise to ferromagnetic coupling. The hopping of electrons becomes difficult when the spins are antiparallel due to Hund's rule.

1.4.3.5. Dzyaloshinsky-Moriya (DM) interaction

Another significant interaction is DM interaction which occurs via spin-orbit coupling proposed by Igor Dzyaloshinsky [32] and Toru Moriya [33,34]. Instead of an oxygen atom, the spin-orbit coupling excites the ion and the interaction happens between the excited ion and the ground state ion. This interaction is also called as antisymmetric-exchange interaction. The Hamiltonian of the magnetic interaction through a non-magnetic ion that can be expressed as

$$H_{DM} = D_{ij} . (S_i \times S_j) \qquad eqn\ (1.5)$$

Where S_i and S_j are the spins involved in the interaction, D_{ij} is the DM vector. The D_{ij} vector vanishes when there is inversion symmetry. The D vector is directly proportional to the spin-orbit coupling. The DM interaction forces the spins to rotate (or cant) slightly and orient perpendicular to the direction of the D vector so that the energy will be negative. This spin canting occurs in antiferromagnetic materials and results in a weak ferromagnetic moment perpendicular to the spin-axis.

1.5. Dielectric properties

The materials that are of interest are insulators. Dielectric materials have lots of applications. The relative dielectric constant of a material can be measured using a well-known 'capacitance' experiment: A dielectric material is placed between two very thin conductors and subjected to a static electric field (the details of this experiment are explained in the chapter-2). Then the dielectric constant can be obtained from the measured capacitance using the equation

$$C = \varepsilon_0 \varepsilon \frac{A}{d} \qquad eqn\ (1.6)$$

Where C is the capacitance of the material, ε_0 is the permittivity of free space, ε is the dielectric constant of the material, A and d are the surface area and thickness of the dielectric material. In presence of the field, charge separation occurs [25,35,36]. There are many contributions to the total dielectric constant. They are explained as follows.

1.5.1. Electronic polarization (α_e)

On applying an external electric field on a free atom, the atom's nucleus tends to move towards the field and the electrons displace opposite to the field direction. This charge displacement gives rais to a temporary dipole moment. Once the applied field is off, the induced moment becomes zero. The polarization that occurs due to the electrons' displacement can be written as $P_e = \alpha_e E$, α_e is the electronic polarizability of the atom.

1.5.2. Ionic (α_i) and dipolar polarization (α_d)

In real cases, the materials are made up of molecules with cations and anions. In the case of molecules, there are two possibilities:

1. In symmetric ionic molecules like NaCl and CCl_4, there is no permanent dipole moment. However, in the presence of the field, the ions are displaced and the distance between the charge centers may vary owing to the applied field strength. The ionic polarization is an induced effect and is absent without the applied field.
2. Molecules like HCl, H_2O have permanent dipole moments which tend to orient towards the field direction. The dipoles are randomly oriented without any applied field and net polarization is zero, analogous to paramagnetic behavior. This is called dipolar or orientational polarization.

1.5.3. Space charge or the Interface polarization (α_s)

Charge accumulates in the interface region between the electrode and material and at the grain boundaries giving raise to this polarization. On application of electric field, the mobile charges get accumulated at the surfaces. This polarization is observed only in polycrystalline materials.

In actual materials, more than one kind of polarization is observed. The total polarization in a material is given by, $\alpha_{tot} = \alpha_s + \alpha_d + \alpha_i + \alpha_e$.

1.5.4. Dielectric dispersion

The various polarization mechanisms discussed above are concerning the static electric field. Frequency dependence of dielectric permittivity in the material gives an insight into the dispersion in the material when the dielectric material is subjected to ac-field. With increase in the ac field frequency, there is a phase lag between the applied field and the measured polarization. Then, the complex dielectric function can be written as $\varepsilon^* = \varepsilon' - i\varepsilon'',$ where ε' and ε'' are the real and imaginary part of the dielectric function. Different polarizations respond to the field based on the frequency, as shown in figure (1.8) [37]. They can be considered as follows.

1. In the case of dipolar polarization, the dipoles take a specific time to orient along the field direction because of the local viscosity. As the frequency approaches the microwave region (10^{10} Hz), the dipoles fail to follow the frequency change of the ac field.
2. The Ionic polarization cease to follow the electric field above the far-infrared region around (10^{13} Hz).
3. Finally, in the ultraviolet region (10^{15} Hz), the electronic polarization also fails to follow the field.

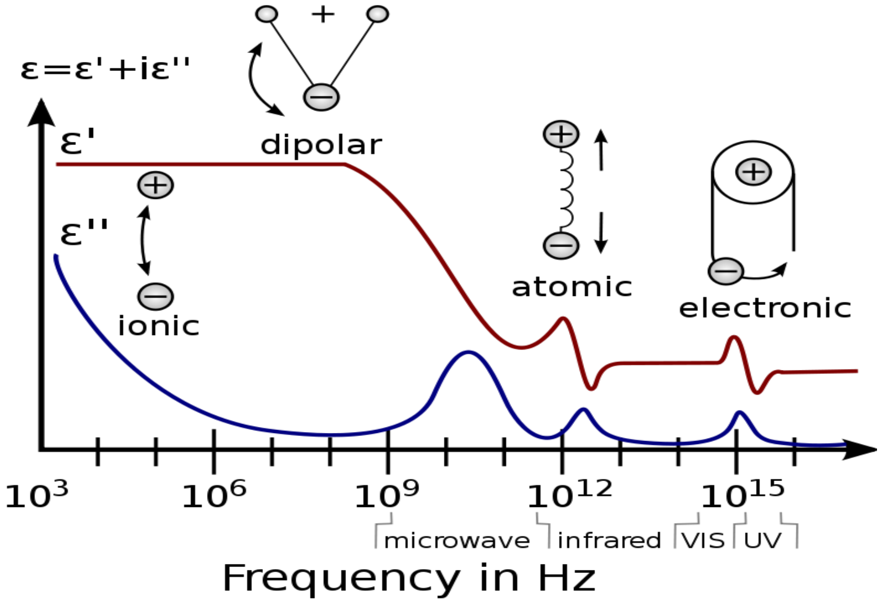

Figure 1.8. Frequency dependence of ε' and ε'' [37].

1.5.5. Dielectric relaxation

Dielectric relaxation is the material's approach to the equilibrium state after the removal of the exciting field that depending on the ac field frequency. The typical behavior of the relaxation that arises from various contributions is given in figure 1.8. There are different kinds of dielectric relaxation.

One such type is Maxwell- Wagner relaxation [38], which contributes from the space charges and becomes essential in the materials with interphase boundaries leading to inhomogeneity. This contribution is orders of magnitude higher at low frequencies than the dipolar or ionic.

Another prime relaxation concerning the dipolar polarization is Debye relaxation [39]. This kind of relaxation suits well for the systems with ideal and non-interacting dipoles. It can be expressed as

$$\varepsilon'(\omega) = \varepsilon_\infty + \frac{\varepsilon_s - \varepsilon_\infty}{1 + \omega^2\tau^2}; \varepsilon''(\omega) = \frac{(\varepsilon_s - \varepsilon_\infty)\omega\tau}{1 + \omega^2\tau^2} \qquad eqn(1.7)$$

Where ε_s and ε_∞ are permittivity at the low and high-frequency limit, respectively. ω and τ are the angular frequency and mean relaxation time. ωτ exhibits a maximum when the angular frequency is 1/τ. In the frequency region below 1/τ, the ε' settles to the static limit, and for the frequencies above 1/τ, the dipoles cannot follow the ac field anymore, thus reducing only to the ionic and electronic contributions. The Debye relaxation is ideal when all the dipoles have the same relaxation time. Systems with distribution in relaxation times, models like Cole-Cole or Cole-Davidson [40–42], can well explain the relaxation.

1.5.6. Ferroelectrics

Polar crystal structures with permanent dipole moments are a necessity but not sufficient for a ferroelectric material [35,36]. The characteristics of a ferroelectric material are;

1. Spontaneous polarization (P_s)
2. Exhibiting hysteresis behavior
3. Paraelectric to ferrolectric transition at Curie temperature (T_C)

Some of the known ferroelectric perovskites are $BaTiO_3$, $PbTiO_3$, $LiNbO_3$. Ferroelectric materials are helpful in memory devices, read-out devices, field-effect transistors.

1.6. Multiferroics

Materials with more than one primary ferroic order, such as ferroelectric, ferromagnetism, and ferroelasticity simultaneously and show coupling between them, are called multiferroic materials [43]. The term multiferroic is first coined by H. Schmidt [44]. Multiferroic materials with linear magneto-electric coupling in which the magnetization can be controlled by its conjugate electric field and vice-versa find application in sensors, magnetic switches, data storage. According to Moore's law, integrated circuits are scaled in terms of the number of logic gates [45]. In this process, integrated circuit technology is encountered by the hurdle of significant power dissipation which can be solved by smart non-volatile devices with lower switching energy. Magneto-electric coupling (ME) based multiferroic materials can significantly help the issues mentioned above [46]. The Landau free energy for the single-phase ME multiferroics can be written as [47]

$$F\ (E,H) = F_0 - P_i E_j - M_i H_j - \frac{1}{2}\ \varepsilon_0 \varepsilon_{ij} E_i E_j - \frac{1}{2}\ \mu_0 \mu_{ij} H_i H_j - \alpha_{ij} E_i H_j - \frac{1}{2}\ \beta_{ijk} E_i H_j H_k \qquad eqn(1.8)$$

Where F is Gibbs free energy, *ijk* are variable components, E and H are electric field and magnetic field, P and M are components of polarization and magnetization, ε_0 and μ_0 are dielectric and magnetic susceptibility of free space, ε and μ and relative permittivity and permeability of the media, α_{ij} is the second-order linear magneto-electric coupling, β_{ijk} is the higher-order coupling parameter. Most of the ME multiferroic materials exhibit linear magneto-electric coupling.

The concept of multiferroics dates back to 1959 when Landau and Lifshitz [48] indicated the presence of two more phenomena, piezomagnetism and magneto-electric behaviour possible only for materials with a particular class of of magnetocrystalline symmetry. The field was renewed with the publication by Nicola A Spaldin [49]. This article discusses the limitations to having simultaneous ferroic orders in a material, along with the ways to overcome those limitations. This article opened up a renewed interest in the field.

1.6.1. Single-phase multiferroics

Materials with the co-existence of electric and magnetic orders are single-phase multiferroic materials with a strict symmetry conditions. Crystals with spontaneous electric polarization (spontaneous magnetization) must be invariant under time reversal symmetry (space inversion symmetry). Out of all 122 possible point groups [50], 13 point groups allow the coexistence of electric and magnetic orders in the same phase (i.e. multiferroic crystals) [51]. Some of the most important single-phase multiferroic materials are Cr_2O_3, $GaFeO_3$, $TbPO_4$, $BiFeO_3$, $HoMnO_3$, $TbMnO_3$, $PbFeTiO_3$ [51]. Single-phase multiferroics are scarce in nature and they are challenging to prepare artificially which have been analyzed by Hill in an excellent article [49].

Single-phase multiferroics are broadly classified into two types: Type-I and Type-II multiferroics. For example, $TbMnO_3$ exhibits magnetic ordering below T_{N1} = 41 K, and below T_{N2} = 28 K, the magnetic structure changes. Only the low-temperature phase exhibits nonzero electric polarization. A study in $TbMnO_3$ showed a strongly influence of magnetic field (applied along a certain direction) on the electric polarization [52]. Similar behavior is observed in $TbMn_2O_5$ [47]. Study of these materials has led to discovery of a number of other multiferroics with strong magneto-electric coupling

1.6.2. Classification of Multiferroics

Khomskii proposed that there are two different types of multiferroics [53]: type-I and type-II. There are many type-I multiferroics. They are, in general, excellent ferroelectrics, magnetic and ferroelectric order occur well above room temperature. However, the coupling between the order parameters is usually relatively weak. The challenge with this type of multiferroics is to enhance this coupling without compromising on other properties. Depending on the ferroelectricity mechanism, type-I multiferroics can be further categorized into three major subclasses. They are lone-pair mechanism, charge ordering, and geometric ferroelectricity. Examples for type-I multiferroics are $BiFeO_3$, $BiMnO_3$, $Pr_{0.5}Ca_{0.5}MnO_3$, $RNiO_3$, $YMnO_3$.

In type-II multiferroics, a particular type of magnetically ordered state induces ferroelectricity. Based on the nature of the multiferroicity, type-II multiferroics is divided into two groups [52,54]: ferroelectric ordering that arises due to a specific kind of magnetic spiral and by collinear magnetic structures. There is a strong magneto-electric coupling in this class of multiferroics, but the magnetic transition is often below room temperature. Also, they exhibit low magnetization and ferroelectric polarization. Some examples are $TbMnO_3$, $Ni_3V_2O_6$, and $MnWO_4$.

1.7. Literature review on $LuFeO_3$

$LuFeO_3$ (LFO) is a prospective room temperature multiferroic and the last candidate in the $RFeO_3$ or orthoferrites family. $RFeO_3$ tend to stabilize in the orthorhombic structure [13]. Since Lu is the smallest among the lanthanides, the distortion in the crystal structure also increases, enabling the formation of a metastable hexagonal phase. Thus, LFO crystallizes into two different crystal structures, orthorhombic (o-LFO) and hexagonal (h-LFO). Cao et al reported o-LFO forms via the formation of hexagonal phase first and as the temperature increases, h-LFO transforms into stable orthorhombic phase [55]. LFO is reported to exhibit multiferroic properties in both the crystal structures.

Hexagonal $LuFeO_3$ with space group $P6_3cm$ (185) is polar in nature and metastable. Due to the metastable nature, the h-LFO is stabilized either in the form of thin films [56–60] or in the nano particle size [61,62] or by substituting a smaller ion such as Sc [63,64], In [65] in place of Lu atom or by substituting Mn [65] or Ni [66] ions in place of Fe. Increase in film thickness and particle size, stabilizes the thermodynamically stable o-LFO [55,67]. The polar and metastable nature of the hexagonal h-LFO makes it challenging to stabilize this compound as a single phase. Wang et al. [68] successfully synthesized h-LFO by growing single-crystalline thin films (of 20 – 60 nm thickness) epitaxially on Al_2O_3 (0001) substrates and reported the coexistence of ferroelectric and antiferromagnetic orders (multiferroicity of type I [69]) with the ferroelectric (FE) Curie temperature $T_{c(FE)}$ ~ 1050 K and the Néel temperature T_N ~ 440 K. However, the claim of multiferroicity at RT in h-LFO [68] was later refuted [70] based on a careful study of magnetic structure and ordering in epitaxially-grown h-LFO thin films, which demonstrated that depending on the film thickness, T_N ranges between ~ 130 K and 150 K. Substituting Cr, Mn and Ni [66,71,72] at Fe site has made it possible to stabilize LFO in the hexagonal structure in the bulk form. Another way of achieving the same result is by substituting atoms with smaller ionic radii, such as Sc and In, for Lu [64,73]. Like h-LFO thin films, the bulk h-LFO systems, involving substitution at Fe or Lu sites [63–66,71,72,74], suffer from low Néel temperature ($T_N \leq 100$ K). h-LFO has a finite dipole moment giving raise to reversible ferroelctric polarization with paraelectric ($P6_3mmc$) to ferroelectric ($P6_3cm$) transition (Tc) around 1050 K [68]. Also, the presence of Fe^{3+}-O^{2-}-Fe^{3+} super-exchange interaction leads to antiferromagnetic interaction in h-LFO. The triangular arrangement of the spin structure in the *ab*-plane gives raise to frustration and long-range magnetic order is observed. Beside exhibiting strong ferroelectric polarization ~22 μC/cm^2 measured at 4 MV/cm [75], h-LFO exhibits weak magnetic moment ~0.09 $\mu_B/f.u.$ at 50 K and T_N ~150 K [76]. Also, the magneto-electro coupling is weak (type-I multiferroics) due to the different origin of the magnetization and the intrinsic ferroelectric polarization. From the above discussion, it can be understood that the T_N and magnetic moment has to be improved to use h-LFO for any practical applications.

By directly measuring the magneto-electric coupling, Chowdhury et al. [15] demonstrated a strong coupling between magnetization and electric polarization (multiferroicity of type II [1]) in bulk orthorhombic o-LFO at RT ($T_{c(FE)}$ ~ 700 K and T_N ~ 600 K) [15] despite its non-polar nature. However, a very low magnetic moment per formula unit ($\mu = 0.24\ \mu_B$/f.u.) at low temperatures in o-LFO due to the canting of Fe^{3+} spins severely limits the use of o-LFO as a smart material. Another limiting feature is that the synthesis of o-LFO in the bulk form requires high annealing temperatures (T_A ~ 1200° C) [5], which results in the formation of undesired Fe-O impurity phases such as Fe_2O_3, Fe_3O_4 [77]. According to Noboru Kimizka et al. [78], the Gibbs free energy change (ΔG°) for chemical reaction Fe+ ½ R_2O_3+ ¾ O_2 of $RFeO_3$ (orthorhombic) system can be minimized in two ways. Either by increasing the atomic radius of R atoms at a constant temperature or increasing the reaction temperature for a particular $RFeO_3$. The ΔG° values calculated [17] at 1100° C for $LuFeO_3$ and $HoFeO_3$ (for example) are - 60.65 kcal/mole and - 63.70 kcal/mole, respectively. This implies that substituting Ho (or R atoms with bigger ionic radius) for Lu in the $LuFeO_3$ system should result in stabilizing the orthorhombic structure at a constant annealing temperature.

1.8. Motivation for this thesis

This work establishes the crystal structure of the $Lu_{1-x}RE_xFeO_3$ (RE = La and Ho) system through an elaborate x-ray diffraction measurement and refinement. RE substitution is expected to affect the structure and multiferroic properties of the $LuFeO_3$ host drastically due to the distortion in the crystal structure. This prompted us to study the structural, magnetic and dielectrical properties with the following objectives in mind.

- The first and foremost aim is to synthesize $LuFeO_3$ in the orthorhombic structure without the formation of Fe-O impurity phases.
- A substantial enhancement in the ground state magnetic moment conducive to multiferroic application is desirable since Lu3+ does not carry any magnetic moment in $LuFeO_3$.
- Systematic study of temperature-dependent magnetization and dielectric permittivity of pure and Ho/La substituted LuFeO3 ceramics to arrive at the true nature of magnetic and dielectric behavior.
- Since the hexagonal phase is polar and orthorhombic has a finite magnetization, it will be interesting to have both the phases together as a natural composite and study their influence on physical properties.

1.9. Organization of the thesis

Chapter-1

In this chapter, a brief introduction to the multiferroic oxides is presented. Various types of magnetic order and interactions relevant to this field are outlined. A brief survey of the literature highlighting the interest in pure and RE doped $LuFeO_3$ is made along with the aim and scope of the thesis.

Chapter-2

In this chapter, the details of synthesis and various experiments carried out in this dissertation are explained.

Chapter-3

Hydrothermal synthesis method is adapted to synthesize nanoparticles at relatively lower temperatures. The higher ionic radius of Ho^{3+} helps to stabilize the orthorhombic structure. This chapter describes the synthesis, structural, microstructure, and Raman spectroscopy studies of $Lu_{1-x}Ho_xFeO_3$ ($0 \leq x \leq 1$) prepared using the hydrothermal method.

Chapter-4

Ho substitution is expected to improve the magnetic properties of the system due to their very high free ion magnetic moment (10.6 μ_B). In this chapter, a detailed analysis of magnetic properties is carried out to bring out the effect of Ho doping in the system.

Chapter-5

In this chapter, the effect of Ho doping is investigated on the dielectric and ferroelectric properties of nanocrystalline $Lu_{1-x}Ho_xFeO_3$ ($0 \leq x \leq 1$). Furthermore, the orthorhombic distortions spontaneously break the centrosymmetry of the underlying cubic lattice and thereby giving rise to dipole moment. Thus, orthorhombic distortions are expected to have a profound effect on the dielectric properties. Accordingly, the static and dynamic dielectric response at RT and also at elevated temperatures has been studied in detail.

Chapter-6

La doping is used to tune the phase fraction and investigate its effect on multiferroic properties. $Lu_{1-x}La_xFeO_3$ nanoparticles with $x = 0$ to 0.25 are synthesized using hydrothermal technique. The magnetic and dielectric properties are correlated to the structural parameters. Since h-LFO exhibits spontaneous polarization ($P = 5\ \mu C/cm^2$) and o-LFO has a finite magnetic moment, $\mu_{eff} = 0.24\ \mu_B/f.u$, it is interesting to have both the phases together as a natural composite and study the influence of varying phase fractions on the physical properties.

Chapter-7

The seventh describes the summary of the present study and also gives some future scope to work on these systems.

References

[1] A.R. Chakhmouradian, P.M. Woodward, Celebrating 175 years of perovskite research: A tribute to Roger H. Mitchell, Phys. Chem. Miner. 41 (2014) 387–391. https://doi.org/10.1007/s00269-014-0678-9.

[2] Goldschmidt V.M., Die Gesetze der Krystallochemie, Naturwissenschaften. 14 (1926) 477–485. https://doi.org/https://doi.org/10.1007/BF01507527.

[3] A.M. Glazer, Perovskites modern and ancient . By Roger H. Mitchell. Thunder Bay, Ontario: Almaz Press, 2002. Price USD 70.00. ISBN 0-9689411-0-9 , Acta Crystallogr. Sect. B Struct. Sci. 58 (2002) 1075–1075. https://doi.org/10.1107/s0108768102020220.

[4] I. Hussain, H.P. Tran, J. Jaksik, J. Moore, N. Islam, M.J. Uddin, Functional materials, device architecture, and flexibility of perovskite solar cell, Emergent Mater. 1 (2018) 133–154. https://doi.org/10.1007/s42247-018-0013-1.

[5] H.D. Megaw, Crystal structure of double oxides of the perovskite type, Proc. Phys. Soc. 58 (1946) 133–152. https://doi.org/10.1088/0959-5309/58/2/301.

[6] P.M. Woodward, Octahedral Tilting in Perovskites. I. Geometrical Considerations, Acta Crystallogr. Sect. B Struct. Sci. 53 (1997) 32–43. https://doi.org/10.1107/S0108768196010713.

[7] A.M. Glazer, The classification of tilted octahedra in perovskites, Acta Crystallogr. Sect. B Struct. Crystallogr. Cryst. Chem. 28 (1972) 3384–3392. https://doi.org/10.1107/s0567740872007976.

[8] J.S. Bechtel, A. Van Der Ven, Octahedral tilting instabilities in inorganic halide perovskites, Phys. Rev. Mater. 2 (2018) 1–13. https://doi.org/10.1103/PhysRevMaterials.2.025401.

[9] A. Filippetti, N.A. Hill, Coexistence of magnetism and ferroelectricity in perovskites, Phys. Rev. B - Condens. Matter Mater. Phys. 65 (2002) 1–11. https://doi.org/10.1103/PhysRevB.65.195120.

[10] A.P. Ramirez, Colossal magnetoresistance, J. Phys. Condens. Matter. 9 (1997) 8171–8199. https://doi.org/10.1088/0953-8984/9/39/005.

[11] J.G. Bednorz, M. Takashige, K.A. Müller, Susceptibility measurements support high-Tcsuperconductivity in the Ba-La-Cu-O system, Prop. Perovskites Other Oxides. 193 (2010) 555–565. https://doi.org/10.1142/9789814293365_0011.

[12] M. Eibschütz, S. Shtrikman, D. Treves, Mössbauer studies of Fe57 in orthoferrites, Phys. Rev. 156 (1967) 562–577. https://doi.org/10.1103/PhysRev.156.562.

[13] R.L. White, Review of recent work on the magnetic and spectroscopic properties of the rare-earth orthoferrites, J. Appl. Phys. 40 (1969) 1061–1069. https://doi.org/10.1063/1.1657530.

[14] T. Yamaguchi, Theory of spin reorientation in rare-earth orthochromites and orthoferrites, J. Phys. Chem. Solids. 35 (1974) 479–500. https://doi.org/10.1016/S0022-3697(74)80003-X.

[15] U. Chowdhury, S. Goswami, D. Bhattacharya, J. Ghosh, S. Basu, S. Neogi, Room temperature multiferroicity in orthorhombic LuFeO3, Appl. Phys. Lett. 105 (2014) 10–14. https://doi.org/10.1063/1.4892664.

[16] U. Chowdhury, S. Goswami, D. Bhattacharya, S.S. Rajput, A.K. Mall, A. Garg, R. Gupta, S.D. Kaushik, V. Siruguri, S. Saravanakumar, S. Israel, R. Saravanan, T. Chatterji, Origin of Ferroelectricity in Orthorhombic LuFeO$_3$, (2017) 1–12. http://arxiv.org/abs/1710.02381.

[17] R.M. Silva, H. Martins, I. Nascimento, J.M. Baptista, A.L. Ribeiro, J.L. Santos, P. Jorge, O. Frazão, Optical current sensors for high power systems: A review, Appl. Sci. 2 (2012) 602–628. https://doi.org/10.3390/app2030602.

[18] R.K. Wahi, W.W. Yu, Y. Liu, M.L. Mejia, J.C. Falkner, W. Nolte, V.L. Colvin, Photodegradation of Congo Red catalyzed by nanosized TiO2, J. Mol. Catal. A Chem. 242 (2005) 48–56. https://doi.org/10.1016/j.molcata.2005.07.034.

[19] Y. Tokunaga, S. Iguchi, T. Arima, Y. Tokura, Magnetic-field-induced ferroelectric state in DyFeO3, Phys. Rev. Lett. 101 (2008) 3–6. https://doi.org/10.1103/PhysRevLett.101.097205.

[20] M. Gateshki, L. Suescun, S. Kolesnik, J. Mais, K. Świerczek, S. Short, B. Dabrowski, Structural, magnetic and electronic properties of LaNi0.5Fe0.5O3 in the temperature range 5-1000 K, J. Solid State Chem. 181 (2008) 1833–1839.

https://doi.org/10.1016/j.jssc.2008.03.041.

[21] S. Acharya, J. Mondal, S. Ghosh, S.K. Roy, P.K. Chakrabarti, Multiferroic behavior of lanthanum orthoferrite (LaFeO3), Mater. Lett. 64 (2010) 415–418. https://doi.org/10.1016/j.matlet.2009.11.037.

[22] S. Blundell, D. Thouless, Magnetism in Condensed Matter, 2001. https://doi.org/10.1119/1.1522704.

[23] W.B. Donald F. Calbreath, CK-12 Chemistry Concepts, (2013). https://www.ck12.org/book/ck-12-chemistry-concepts-intermediate/.

[24] A. Awan, H. Truong, Crystal field theory, (2020) 340–343. https://doi.org/10.1201/b17236-5.

[25] C. Kittel, Introduction to solid state physics, 2005. https://doi.org/10.1016/0022-5096(57)90051-0.

[26] N. Sources, Module 1 : Introduction Lecture 1 : Classes of magnetic materials, 1 (n.d.) 3–4.

[27] Chemistry LibreTexts, The Effects of Temperature on Magnetic Moment , (2020) 2–3. https://chem.libretexts.org/Bookshelves/Inorganic_Chemistry/Map%3A_Inorganic_Chemistry_(Housecroft)/20%3A_d-Block_Metal_Chemistry_-_Coordination_Complexes/20.10%3A_Magnetic_Properties/20.10C%3A_The_Effects_of_Temperature_on_Magnetic_Moment.

[28] H.P. Wu, K.M. Deng, W.S. Tan, C.Y. Xiao, F.L. Hu, Q.X. Li, The structural, electronic, and magnetic properties of SrFeOn (n 2 and 2.5): A GGA+U study, Chinese Phys. B. 18 (2009) 5008–5014. https://doi.org/10.1088/1674-1056/18/11/065.

[29] J.B. Goodenough, Theory of the role of covalence in the perovskite-type manganites [La,M(II)]MnO3, Phys. Rev. 100 (1955) 564–573. https://doi.org/10.1103/PhysRev.100.564.

[30] C. Zener, Interaction between the d-Shells in the Transition Metals. II. Ferromagnetic Compounds of Manganese with Perovskite Structure, 82 (1951) 404.

[31] C. Zener, Interaction Between the d Shells in the Transition Metals *, 81 (1951) 440.

[32] I. Dzyaloshinsky, A THERMODYNAMIC THEORY OF “ WEAK ” OF ANTIFERROMAGNETICS, 4 (1958) 241–255.

[33] T. Moriya, New mechanism of anisotropic superexchange interaction, 4 (1960) 4–6.

[34] T. Moriya, Anisotropic Superexchange Interaction and Weak Ferromagnetism, 120 (1960) 91.

[35] A.J. Dekker, Solid State Physics, 1985th ed., Macmillan, Madras, 1957.

[36] A.R. West, Solid State Chemistry, Second, 4 John Wiley & Sons, Ltd, 2014.

[37] F. Chen, R. Balieu, A state-of-the-art review of intrinsic and enhanced electrical properties of asphalt materials: Theories, analyses and applications, Mater. Des. 195 (2020) 109067. https://doi.org/10.1016/j.matdes.2020.109067.

[38] D. Nachwirkungsvorg, M. Vorstellungen, K.W. Wagner, Erkl/irung der dielektrischen Nachwirkungsvorg/inge auf firund Maxwellscher Vorstellungen., 24 (1913).

[39] A.K. Jonscher, Dielectric relaxation in solids, (1999).

[40] T.P. Iglesias, G. Vilão, J.C.R. Reis, An approach to the interpretation of Cole-Davidson and Cole-Cole dielectric functions, J. Appl. Phys. 122 (2017). https://doi.org/10.1063/1.4985839.

[41] D.W. Davidson, R.H. Cole, Dielectric relaxation in glycerol, propylene glycol, and n-propanol, J. Chem. Phys. 19 (1951) 1484–1490. https://doi.org/10.1063/1.1748105.

[42] K.S. Cole, R.H. Cole, Dispersion and absorption in dielectrics I. Alternating current characteristics, J. Chem. Phys. 9 (1941) 341–351. https://doi.org/10.1063/1.1750906.

[43] S.N. Achary, O.D. Jayakumar, A.K. Tyagi, Multiferroic materials, Elsevier Inc., 2012. https://doi.org/10.1016/B978-0-12-385142-0.00004-0.

[44] H. Schmid, Multi-ferroic magnetoelectrics, Ferroelectrics. 162 (1994) 317–338.

https://doi.org/10.1080/00150199408245120.

[45] G.E. Moore, Cramming more components onto integrated circuits, Proc. IEEE. 86 (1998) 82–85. https://doi.org/10.1109/JPROC.1998.658762.

[46] P.A. Dowben, D.E. Nikonov, A. Marshall, C. Binek, Magneto-electric antiferromagnetic spin-orbit logic devices, Appl. Phys. Lett. 116 (2020). https://doi.org/10.1063/1.5141371.

[47] L.W. Martin, R. Ramesh, Multiferroic and magnetoelectric heterostructures, Acta Mater. 60 (2012) 2449–2470. https://doi.org/10.1016/j.actamat.2011.12.024.

[48] L.D. Landau, E.M. Lifshitz, Electrodynamics of Continuous Media, 1960.

[49] N.A. Hill, Why are there so few magnetic ferroelectrics?, J. Phys. Chem. B. 104 (2000) 6694–6709. https://doi.org/10.1021/jp000114x.

[50] T. Shubnikov, Generalized Symmetry, 16 (1988) 555–562.

[51] H. Schmid, Some symmetry aspects of ferroics and single phase multiferroics, J. Phys. Condens. Matter. 20 (2008). https://doi.org/10.1088/0953-8984/20/43/434201.

[52] T. Kimura, T. Goto, H. Shintani, K. Ishizaka, T. Arima, Y. Tokura, Magnetic control of ferroelectric polarization, Nature. 426 (2003) 55–58. https://doi.org/10.1038/nature02018.

[53] D. Khomskii, Classifying multiferroics: Mechanisms and effects, Physics (College. Park. Md). 2 (2009). https://doi.org/10.1103/physics.2.20.

[54] N. Hur, S. Park, P.A. Sharma, J.S. Ahn, S. Guha, S.W. Cheong, Electric polarization reversal and memory in a multiferroic material induced by magnetic fields, Nature. 429 (2004) 392–395. https://doi.org/10.1038/nature02572.

[55] S. Cao, X. Zhang, K. Sinha, W. Wang, J. Wang, P.A. Dowben, X. Xu, Phase separation in LuFeO3 films, Appl. Phys. Lett. 108 (2016). https://doi.org/10.1063/1.4950991.

[56] X. Zhang, H. Song, C. Tan, S. Yang, Y. Xue, J. Wang, X. Zhong, Epitaxial growth and magnetic properties of h-LuFeO3 thin films, J. Mater. Sci. 52 (2017) 13879–13885. https://doi.org/10.1007/s10853-017-1469-8.

[57] S.M. Disseler, X. Luo, B. Gao, Y.S. Oh, R. Hu, Y. Wang, D. Quintana, A. Zhang, Q. Huang, J. Lau, R. Paul, J.W. Lynn, S.W. Cheong, W. Ratcliff, Multiferroicity in doped hexagonal LuFe O3, Phys. Rev. B - Condens. Matter Mater. Phys. 92 (2015) 1–9. https://doi.org/10.1103/PhysRevB.92.054435.

[58] W. Wang, H. Wang, X. Xu, L. Zhu, L. He, E. Wills, X. Cheng, D.J. Keavney, J. Shen, X. Wu, X. Xu, Crystal field splitting and optical bandgap of hexagonal LuFeO3 films, Appl. Phys. Lett. 101 (2012) 1–5. https://doi.org/10.1063/1.4771601.

[59] S. Cao, X. Zhang, T.R. Paudel, K. Sinha, X. Wang, X. Jiang, W. Wang, S. Brutsche, J. Wang, P.J. Ryan, J.W. Kim, X. Cheng, E.Y. Tsymbal, P.A. Dowben, X. Xu, On the structural origin of the single-ion magnetic anisotropy in LuFeO3, J. Phys. Condens. Matter. 28 (2016) 156001. https://doi.org/10.1088/0953-8984/28/15/156001.

[60] H. Wang, I. V. Solovyev, W. Wang, X. Wang, P.J. Ryan, D.J. Keavney, J.W. Kim, T.Z. Ward, L. Zhu, J. Shen, X.M. Cheng, L. He, X. Xu, X. Wu, Structural and electronic origin of the magnetic structures in hexagonal LuFeO3, Phys. Rev. B - Condens. Matter Mater. Phys. 90 (2014) 1–5. https://doi.org/10.1103/PhysRevB.90.014436.

[61] S. Chaturvedi, S.K. Singh, P. Shyam, M.M. Shirolkar, S. Krishna, R. Boomishankar, S. Ogale, Nanoscale LuFeO 3 : Shape dependent ortho/hexa-phase constitution and nanogenerator application, Nanoscale. 10 (2018) 21406–21413. https://doi.org/10.1039/c8nr07825d.

[62] S. Chaturvedi, P. Shyam, M.M. Shirolkar, S. Krishna, B. Sinha, Tunable magnetization in nanoscale LuFeO 3 : Role of morphology , ortho-hexa phase ratio and local structure, (n.d.) 1–16.

[63] J.C. Leiner, T. Kim, K. Park, J. Oh, T.G. Perring, H.C. Walker, X. Xu, Y. Wang, S.W. Cheong, J.G. Park, Magnetic excitations in the bulk multiferroic two-dimensional triangular lattice antiferromagnet (Lu,Sc)FeO3, Phys. Rev. B. 98 (2018) 1–6. https://doi.org/10.1103/PhysRevB.98.134412.

[64] L. Lin, H.M. Zhang, M.F. Liu, S. Shen, S. Zhou, D. Li, X. Wang, Z.B. Yan, Z.D. Zhang, J. Zhao, S. Dong, J.M. Liu, Hexagonal phase stabilization and magnetic

orders of multiferroic L u1-x S cxFe O3, Phys. Rev. B. 93 (2016) 1–9. https://doi.org/10.1103/PhysRevB.93.075146.

[65] J. Liu, T.L. Sun, X.Q. Liu, H. Tian, T.T. Gao, X.M. Chen, A Novel Room-Temperature Multiferroic System of Hexagonal Lu1−xInxFeO3, Adv. Funct. Mater. 28 (2018) 1–10. https://doi.org/10.1002/adfm.201706062.

[66] P. Suresh, K. Vijaya Laxmi, P.S. Anil Kumar, Enhanced room temperature multiferroic characteristics in hexagonal LuFe1−xNixO3 (x = 0 − 0.3) nanoparticles, J. Magn. Magn. Mater. 448 (2018) 117–122. https://doi.org/10.1016/j.jmmm.2017.05.052.

[67] S. Song, H. Han, H.M. Jang, Y.T. Kim, N.S. Lee, C.G. Park, J.R. Kim, T.W. Noh, J.F. Scott, Implementing Room-Temperature Multiferroism by Exploiting Hexagonal-Orthorhombic Morphotropic Phase Coexistence in LuFeO3Thin Films, Adv. Mater. 28 (2016) 7430–7435. https://doi.org/10.1002/adma.201601989.

[68] W. Wang, J. Zhao, W. Wang, Z. Gai, N. Balke, M. Chi, H.N. Lee, W. Tian, L. Zhu, X. Cheng, D.J. Keavney, J. Yi, T.Z. Ward, P.C. Snijders, H.M. Christen, W. Wu, J. Shen, X. Xu, Room-temperature multiferroic hexagonal LuFeO3 films, Phys. Rev. Lett. 110 (2013) 1–5. https://doi.org/10.1103/PhysRevLett.110.237601.

[69] W. Eerenstein, N.D. Mathur, J.F. Scott, Multiferroic and magnetoelectric materials, Nature. 442 (2006) 759–765. https://doi.org/10.1038/nature05023.

[70] S.M. Disseler, J.A. Borchers, C.M. Brooks, J.A. Mundy, J.A. Moyer, D.A. Hillsberry, E.L. Thies, D.A. Tenne, J. Heron, M.E. Holtz, J.D. Clarkson, G.M. Stiehl, P. Schiffer, D.A. Muller, D.G. Schlom, W.D. Ratcliff, Magnetic structure and ordering of multiferroic hexagonal LuFeO3, Phys. Rev. Lett. 114 (2015) 1–6. https://doi.org/10.1103/PhysRevLett.114.217602.

[71] F. Pomiro, R.D. Sánchez, G. Cuello, A. Maignan, C. Martin, R.E. Carbonio, Spin reorientation, magnetization reversal, and negative thermal expansion observed in R F e0.5 C r0.5 O3 perovskites (R=Lu,Yb,Tm), Phys. Rev. B. 94 (2016) 1–9. https://doi.org/10.1103/PhysRevB.94.134402.

[72] T. Sarkar, K. Manna, S. Elizabeth, P.S. Anil Kumar, Investigation of multiferroicity, spin-phonon coupling, and unusual magnetic ordering close to

room temperature in LuMn0.5Fe0.5O3, J. Appl. Phys. 121 (2017) 0–10. https://doi.org/10.1063/1.4977103.

[73] J. Liu, T.L. Sun, X.Q. Liu, H. Tian, T.T. Gao, X.M. Chen, A Novel Room-Temperature Multiferroic System of Hexagonal Lu1−xInxFeO3, Adv. Funct. Mater. 28 (2018) 1–7. https://doi.org/10.1002/adfm.201706062.

[74] M.Y. Liu, T.T. Gao, X.L. Zhu, X.M. Chen, Ferroelectricity and magnetoelectric coupling in hexagonal Lu0.5In0.5FeO3 ceramics, J. Appl. Phys. 126 (2019) 0–7. https://doi.org/10.1063/1.5117344.

[75] Y.K. Jeong, J.H. Lee, S.J. Ahn, H.M. Jang, Epitaxially constrained hexagonal ferroelectricity and canted triangular spin order in LuFeO 3 thin films, Chem. Mater. 24 (2012) 2426–2428. https://doi.org/10.1021/cm300846j.

[76] J.A. Moyer, R. Misra, J.A. Mundy, C.M. Brooks, J.T. Heron, D.A. Muller, D.G. Schlom, P. Schiffer, Intrinsic magnetic properties of hexagonal LuFeO3 and the effects of nonstoichiometry, APL Mater. 2 (2014). https://doi.org/10.1063/1.4861795.

[77] S. Leelashree, S. Srinath, Investigation of Structural, Ferroelectric, and Magnetic Properties of La-Doped LuFeO 3 Nanoparticles, J. Supercond. Nov. Magn. (2019). https://doi.org/10.1007/s10948-019-5114-4.

[78] N. Kimizuka, A. Yamamoto, H. Ohashi, T. Sugihara, T. Sekine, The stability of the phases in the Ln2O3FeOFe2O3 systems which are stable at elevated temperatures (Ln: Lanthanide elements and Y), J. Solid State Chem. 49 (1983) 65–76. https://doi.org/10.1016/0022-4596(83)90217-7.

CHAPTER 2

Experimental Techniques employed

In this chapter, the details of preparation and various experiments carried out in this dissertation are explained.

2.1. Introduction

This chapter describes the synthesis technique, sample characterization, and physical property measurements used in the present work.

2.2. Synthesis method

There are different synthesis techniques to synthesize perovskite $RFeO_3$ materials and based on the synthesis method, the physical properties of the materials are altered. The most used synthesis method for bulk perovskites is a solid-state reaction that requires high annealing temperature (T_A). As explained in section 1.8, the synthesis of $LuFeO_3$ requires low T_A; thus, wet-chemical synthesis is preferred in the current work. Various wet-chemical synthesis techniques include colloidal [1], sol-gel [2], precipitation [3], and hydrothermal [4,5], are available. The hydrothermal synthesis technique is chosen for its advantages which will be explained in the next section.

2.2.1 Hydrothermal synthesis

In the era of miniaturization, nanomaterials have an extensive variety of applications, and the applications depend on the method of preparation. Hydrothermal is one such method to synthesize $RFeO_3$ nanoparticles with homogeneity [5]. All the materials are synthesized via the hydrothermal (HT) technique in this work. In the HT method, the precursors are mixed in the base liquid water, transferred to a Teflon container, and placed in a closed steel container that can withstand high pressure and temperature for several hours. The cross-section of such an autoclave [6,7] is shown in figure 2.1. The precursors that are not solvable in water under ambient conditions will dissolve at the high pressure created by the vapor inside the autoclave [8]. The formation of nanoparticles in the HT method follows the following steps [9]:

1. The precursors are dissolved in water and enter the solution in the autoclave.
2. A supersaturated solution is formed in the autoclave upon heating.
3. The ions are adsorbed, decomposed, and desorbed at the growth interface.
4. As a final step, the dissolved matter crystallizes.

The morphology of the nanoparticles under the HT method depends on the growth conditions [10]. Under different growth conditions, the exact composition of nanoparticles shows different morphologies [4]. With water as the medium at high temperatures and pressure, the ionic product and ion reaction rates increase exponentially following the

Arrhenius equation. Also, the surface tension and viscosity of water decrease as temperature increases. This significantly increases the mobility of molecules in the solution, promoting the crystallization process [11]. The elevated vapor pressure speeds up the reaction by increasing the probability of collision amongst ions.

Due to the precursor's low solubility, "mineralizers" such as salts, acids, and bases [12,13] are added to the reaction that increases the solubility of the reactants during the crystal growth process. The addition of an appropriate mineralizer boosts the solute's solubility in the hydrothermal solution. The quality and growth rate of the crystal significantly depends on the type of mineralization agent. Different mineralizers help in forming particles with different morphology and crystallite size [14]. Some disadvantages of the conventional hydrothermal methods are high-cost autoclaves and time consumption.

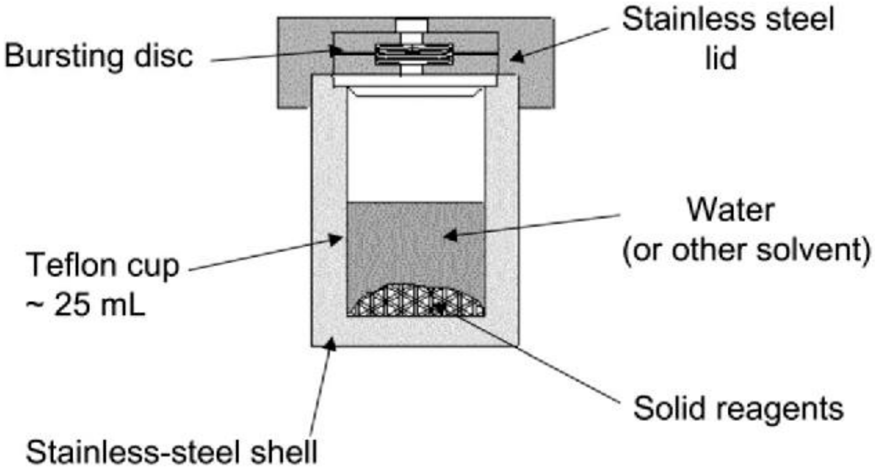

Figure 2.1. A schematic of a Teflons lined stainless steel autoclave typically used for hydrothermal synthesis [7].

In the present work, $Lu(NO_3)_3 \cdot H_2O$, $La(NO_3)_3 \cdot 6H_2O$ (for La-doped systems), $Ho(NO_3)_3 \cdot 5H_2O$ (for Ho-doped systems), $Fe(NO_3)_3 \cdot 9H_2O$ and citric acid are used as precursors for the synthesis of $Lu_{1-x}RE_xFeO_3$ (RE = La, Ho). After dissolving the precursors in double-distilled water, the solution's pH is adjusted to 8 by adding a few drops of NH_3 solution. The liquid is transferred to the autoclave and heated at 200°C for 24 hours. The obtained saturated solution is washed multiple times with ethanol and double-distilled water in a centrifuge at 13,000 rpm. Then the collected sediment is dried at 70°C for 3 hours and found to be amorphous. The powder is annealed at various conditions to optimize the crystallinity.

2.3. Sample Characterization

2.3.1. X-ray Diffraction (XRD)

X-ray Diffraction is an effective tool for phase confirmation and measuring the structural properties such as phase composition, strain component, crystallite size, defects, preferred orientation of these phases [15]. X-ray diffraction (XRD) patterns on the powder samples were measured using PANalytical X'pert Pro-X-ray diffractometer using Cu-Kα source and x-ray wavelength λ = 1.54 Å at room temperature in the Bragg-Brentano geometry (figure 2.2). XRD also helps in determining the thickness of thin films and atomic arrangements in amorphous materials. XRD is a noncontact and non-destructive technique. The XRD intensities consists of information about the atomic arrangements at interfaces in multilayers. Materials with any element can be effectively studied with XRD. Still, it is most sensitive to atoms with relatively higher mass since the diffracted intensity is directly related to the mass of elements. Consequently, the sensitivity of the XRD depends on the constituent atoms of the material.

2.3.1.1. Basic Principles

In an actual experiment, the diffracted intensity is reccorded as a function of 2θ that produces the diffraction pattern [16–22]. The X-ray wavelength (λ) is usually 0.7-2 Å, corresponding to X-ray energies ~ 6 -17 keV [23]. The angle 2θ is the measure between the incident and diffracted X-rays, as displayed in figure 2.2. Prior to considering the conditions for XRD, some essential properties of crystalline materials should be understood. Crystals can be viewed as planes of atoms placed parallel with a distance *d* apart. A coordinate system is introduced for the structure to distinguish between the different *d*-spacings with unit vectors a, b, and c in the edges of the basic unit cell. The *d*-spacing between (*hkl*) planes is denoted as d_{hkl}. The *d*-spacing for a cubic crystal can be calculated using eqn (2.1).

$$d_{hkl} = \frac{a_0}{\sqrt{h^2 + k^2 + l^2}} \qquad eqn\ (2.1)$$

Where a_0 is the lattice constant of the crystal. When there is constructive interference from x-rays scattered by the atomic planes, a diffraction peak is observed. The condition for constructive interference given by Bragg's law [16]

$$\lambda = 2\, d_{hkl}\, \sin\theta_{hkl} \qquad eqn\ (2.2)$$

where θ_{hkl} is the angle between the planes and the incident (or diffracted) X-ray beam, as shown in Figure 2.2 [24]. In the case of a single crystal or epitaxial thin film, the diffraction conditions are satisfied for only one specific orientation for each (hkl) plane.

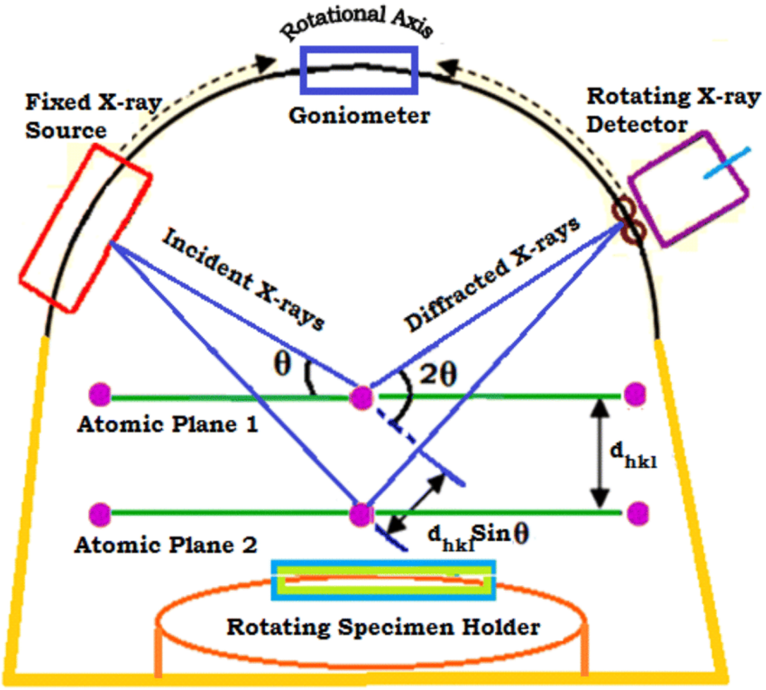

Figure 2.2. Bragg- Brentano geometry and geometrical condition for diffraction from lattice planes [24].

Before considering diffracted intensities, X-ray absorption must be considered, which also plays a role in the observed intensity since all the materials absorb X rays to a certain extent. This results in attenuation of an X-ray beam as it passes through the material. The intensity of the transmitted X-rays deteriorates exponentially with the distance traversed through the specimen and μ measures the linear absorption coefficient, and μ enhances with increasing atomic number and wavelength. For powder diffraction, the intensity of x-rays reflected from *hkl* planes can be expressed as

$$I_{hkl} = K \frac{1 + cos^2 2\theta}{4\, sin^2\theta\; cos\theta} |F_{hkl}|^2 \qquad eqn\ (2.3)$$

Neglecting geometric factors, the structure factor F_{hkl} of integrated X-ray intensity diffracted from the material is written as

$$F_{hkl} = \sum_i f_i \exp[2\pi j\,(hx_i + ky_j + lz_k)] \qquad eqn\ (2.4)$$

The structure factor is interrelated to the plane arrangements in a material. The form factor f_i of ith atom with coordinates x_i, y_j, z_k decreases with an increase in 2θ. Because of this, XRD is more sensitive to materials with higher atomic number.

In the present thesis, the diffraction pattern is obtained using θ - 2θ scanning mode. The sample is fixed in this particular scanning mode, whereas the source and the detector were rotated to the axis perpendicular to the plane containing the x-ray beam. In general, peak position and intensity are collected from a diffraction pattern. Using this information, the crystal structure and symmetry of the contributing phase can be determined.

2.3.1.2. Rietveld Refinement Analysis

The Rietveld analysis is a helpful refining method to analyze diffraction patterns and study crystal and magnetic structures. With initial knowledge of the crystal structure, by considering approximate lattice parameters, the analysis is started, and the diffraction pattern for the system is calculated. Essentially, in this least square method, many parameters including the experimental setup parameters are required to describe the crystal structure. They would be attuned to acquire the best fit between the calculated and observed diffraction patterns. High-score software [25] is used to carry out the Rietveld refinement in our work. All the refinable parameters can be categorized into three major parts: Experimental, Peak function, and structural parameters. There are several parameters for the experimental setup such as: wavelength of the x-ray, scale factor, zero shift for 2θ, specimen displacement, the ratio between K_α / K_β, and eight parameters for a polynomial background. The appropriate peak function among various pseudo-Voigt functions, symmetry parameters of the peak function, the angular dependence of Full Width at Half Maximum parameters such as u, v, and w are some of the parameters related to peak function. The structural parameters refined are lattice parameters, occupation number, isotropic thermal properties (B_{iso}), Wyckoff positions of the R, Fe, and O atoms. A typical $RFeO_3$ (ABO_3) type structure requires most of the parameters mentioned above to be refined to describe the observed XRD pattern. The gradient for the weighted sum of the squared difference between the calculated and measured intensities, R_p, can be determined relative to these parameters. The gradient is then used to change the parameters, and this is repeated until a minimum in the R_p function is reached.

The intensity profile factor is defined as

$$R_p = 100\frac{\sum_{i=1,n}\left|y_i - y_{c,i}\right|}{\sum_{i=1,n} y_i} \qquad eqn(2.5)$$

where y_i is the measured intensity at every step i, $y_{c,i}$ is the corresponding calculated intensity. The goodness of fit (χ^2) and Bragg R- factor is calculated to monitor the quality of the refinement.

The weighted profile factor R_{wp} is given by

$$R_{wp} = 100\left[\frac{\sum_{i=1,n} w_i\left|y_i - y_{c,i}\right|^2}{\sum_{i=1,n} w_i y_i^2}\right]^2 \qquad eqn\ (2.6)$$

The expected profile factor,

$$R_{wp} = 100\left[\frac{n-p}{\sum_i w_i y_i^2}\right]^{1/2} \qquad eqn\ (2.7)$$

The Bragg R-Factor,

$$R_B = 100\ \frac{\sum_h\left|I_{obs,h} - I_{cal,h}\right|}{\sum_h\left|I_{obs,h}\right|} \qquad eqn\ (2.8)$$

The goodness fit can be calculated as

$$\chi^2 = \left[\frac{R_{wp}}{R_{exp}}\right]^2 \qquad eqn\ (2.9)$$

Here, I_{obs} and I_{cal} are the observed and calculated integrated intensities for the different Bragg peaks. 'n' is the number of points observed in the pattern, and 'p' is the total number of refined parameters.

2.3.2. Field Emission Scanning Electron Microscopy (FE-SEM)

The FESEM helps generate a largely magnified image to visualize tiny topographic details on the surface as small as 1 nanometer by using electrons instead of light. A field emission source or an electron gun emits the electrons at the top of the microscope. These electromagnetic lenses in the high vacuum column focusses and deflects the primary electrons and the fine electron beam bombards the sample. The resulting secondary electrons (figure 2.3 (a)) are emitted from the surface the sample. The detector detects the secondary electrons, and by using the angle and velocity, the electronic signal is produced, and the surface structure of the sample is constructed. This electronic signal is amplified and converted to a digital image that can be saved and processed further. A 3D appearance is provided by these images due to the large depth of field of the FESEM and the shadowed relief effect of the contrast of the secondary electron. Figure 2.3 (b) shows the schematic diagram of FESEM explaining the experimental setup [26]. FESEM has a working magnification range of 10 to 100,000 diameter and can focus 300 times better than that of an optical microscope. The 3D images produced facilitate different morphological features to be correctly interrelated and aptly analyzed. The unique advantage of FESEM is that it does not require tedious samples preparation and also the thickness of the specimen is not a constraint. The surface of the pellet or sample can be polished before it is scanned to achieve better surface morphology and grain size data. Carl Zeiss Sigma's Field Emission Scanning Electron Microscope, operated at 5 kV, was used in the present work to study the surface morphology.

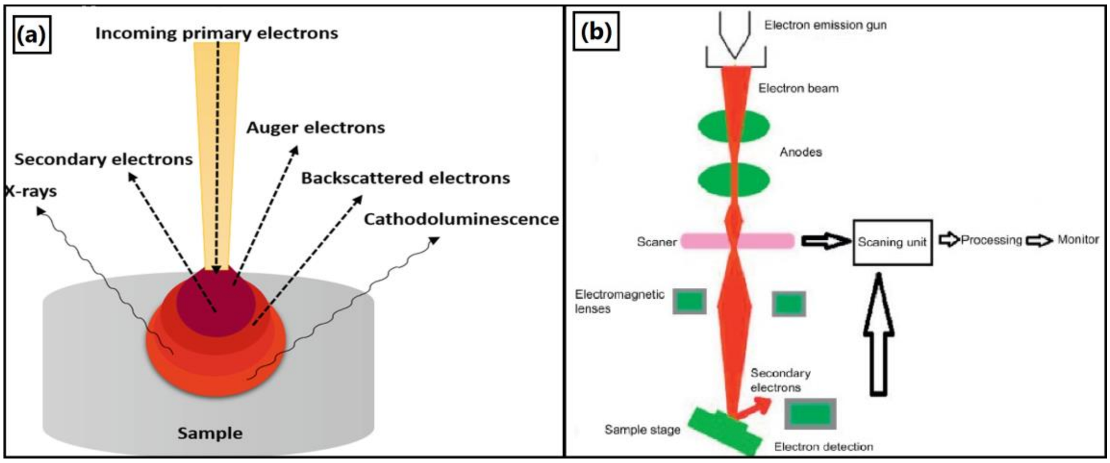

Figure 2.3. (a) Different types of signal generated by the sample after interaction with primary electroms; **(b)** Schematic diagram of FESEM [26].

2.3.3. Energy Dispersive X-Ray Analysis (EDX)

EDX quickly produces data about the elements present as well as their distribution and percentage. This technique is non-destructive and also requires minimal sample preparation. Due to its advantages, EDX analysis has become an essential part of FESEM. In principle, the chemical composition can be measured in the form of elemental mapping and line scans.

When the primary electrons impinges the inner shell of the atom, an electron is ejected, leaving a positively charged vacancy (hole). Due to this, an electron jumps from the outer shell to fill the vacancy releasing an X-ray characteristic of that particular element and transition. The emitted X-rays are collected by a silicon drift detector (SDD) that ensures that only X-rays are trapped, not the electrons. The detector consists of a window comprising of polymers that isolates the detector crystal from the microscope chamber under the high vacuum. Essential electronics are attached to the detector to read the signal, and the signal is interpreted using the software. The SDD detectors are chilled with liquid nitrogen in order to minimize the electronic noise.

2.3.4. Raman Spectroscopy (RS)

Raman spectroscopy is a scattering phenomenon, discovered in 1928 by Sir Chandrasekhara Venkata Raman, which works based on inelastic scattering of the light (monochromatic) incident on a compound, usually from a laser source [27]. Raman Spectroscopy is also a non-destructive technique and gives detailed information on phase and polymorphy, crystallinity, chemical structure, and molecular interactions [28]. RS is essentially based upon the interaction between light and the chemical bonds within a material. The light is reflected, absorbed, or scattered when it is incident on a compound. When the oscillatory electromagnetic (EM) field interacts with matter, it perturbs the matter's charge distribution, leaving it in a modified state [29]. Analyzing the scattered light gives data about the chemical and structural information. Upon releasing photon, the energy states come back to their initial ground state with three different frequencies:

1. Rayleigh scattering: The frequency of the scattered light and the laser source are same.

2. Stokes Raman scattering: The frequency of the scattered light is lesser than the laser source.

3. Anti-Stokes Raman scattering: The frequency of the scattered light is greater than the laser source.

The situation is schematically shown in figure 2.4 [30]. Essentially, these frequencies are associated with rotational, vibrational, and electronic level transitions in a molecular system. The scattered radiation consists of polarization properties different from those of the incident radiation. Depending on the direction of observation, the intensity and polarization of the scattered radiation vary. Raman spectroscopy helps to study structural information such as bond vibrations and various Raman vibrational modes that would arise due to structural distortion in the compound.

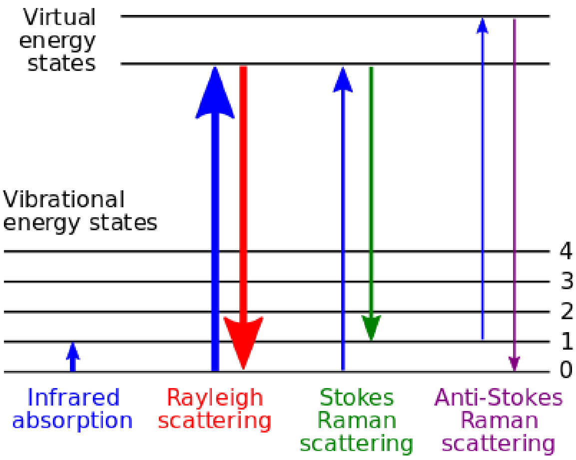

Figure 2.4. Energy-level diagram showing the states involved in Raman spectra [30].

In the current thesis, Raman spectra were recorded at RT using a LabRam HR Evolution (HORIBA Scientific) spectrometer with a laser excitation source of 532 nm and a power of 5 mW for 150 ms. From the Raman scattering experiments carried out at different laser power levels, we find that 5 mW power is low enough to ensure that no overheating of, or damage to, the sample occurs. A microscope with magnification × **50** was used for taking these Raman spectra.

2.4. Physical property measurements

2.4.1. LCR meter for dielectric measurements

Dielectric properties are studied using a parallel plate capacitor attached to LCR meter (Agilent E4109A) precision to measure frequencies ranging between 20 Hz to 2 MHz. The samples were pelletized into a disc shape by applying a pressure of 5-tons. Silver paint is applied on both sides of the pellets to make electrical contact forming a parallel plate capacitor geometry [31] (figure 2.5 (a)). GPIB or LAN interface is used to control the LCR meter remotely. The parameters such as capacitance, inductance, impedance, dissipation factor, admittance, the quality factor can be measured using an LCR meter. A block diagram of a typical LCR meter is shown in figure 2.5 (b) [31].

Every oxide material has a distinctive set of electrical properties, and they can be measured in terms of dielectric permittivity, permeability, resistivity, conductivity, etc. Dielectrics are insulating materials that can store energy with a minimum power dissipation when an external electric field is applied [17,20,32]. The dielectric characteristics of an oxide material are vital in studying the lattice dynamics of the crystal. In general, the dielectric constant is the ratio of the capacitance of metal-insulator-metal to the capacitance of the metal-air-metal configuration. The static dielectric constant, ε' of the sample can be calculated as

$$\varepsilon' = \frac{C}{C_0} \qquad eqn\ (2.10)$$

where C is the measured capacitance and $C_0 = \varepsilon_0 {}^{A}\!/_{t}$ where ε_0 = 8.854×10^{-12} F/m is the dielectric permittivity of free space, 'A' is area of the pellet, and 't' is sample thickness.

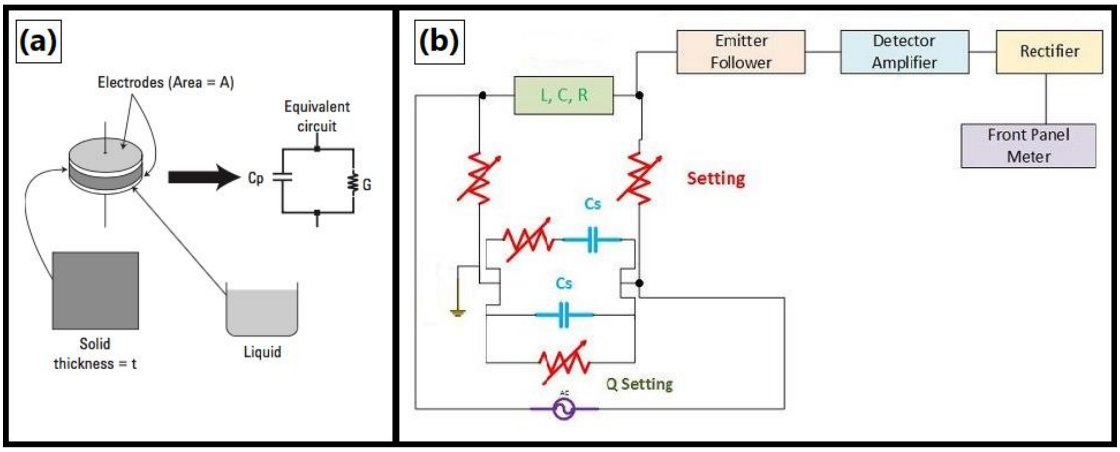

Figure 2.5. (a) Parallel plate capacitor setup; **(b)** Block diagram of LCR meter [31].

It is important to note that permittivity can change with the material's temperature, frequency, and structure. The dielectric properties, their applications, and theories on dielectric behaviour are discussed in detail by many authors [33–36]. When an AC voltage (V) is applied across the capacitor, the resultant will be charging current (I_C) and loss current (I_I) that is related to the dielectric constant. The complex dielectric constant ε* consists of a real part ε' which is a measure of the charge storage capacity of the dielectric and an imaginary part ε'' is the dielectric loss and it measures how dissipative a material is in presence of an external electric field. The loss tangent or tan δ or D denotes dissipation factor, and D is ${}^{\varepsilon''}\!/_{\varepsilon'}$. The LCR meter measures the vector components of capacitance and dissipation, and a connected software program calculates the permittivity and loss tangent. This method is suitable at low-frequency for pellets and liquids.

In this work, the dielectric studies are performed by measuring capacitance, dielectric permittivity, and dielectric loss at room temperature using the Agilent E4908A LCR meter with a specially designed spring-loaded sample holder, in the frequency range from 20 Hz to 2 MHz. The dielectric properties are also studied as a function of temperature from RT to 650 K at 20 frequencies that range from 1 kHz to 2 MHz.

2.4.2. Materials Analyzer for ferroelectric studies

Electric hysteresis loop of polarization P measured against external electric field E is the most crucial characteristic of ferroelectric materials. The standard way of measuring the hysteresis loop is using a modified Sawyer-tower circuit [37,38]. Typical ferroelectric hysteresis (P-E) and remanent hysteresis loops are measured at room temperature and as a function of temperature from 300 K to 600 K with the help of Precision Materials Analyzer from Radiant Technologies, Inc. A system for performing simultaneous P-E measurements is shown schematically in figure 2.6. The P-E loops were measured in the same parallel plate capacitor geometry as used in capacitance measurement. A ferroelectric material exhibits reversible spontaneous electric polarization and a hysteresis loop below the Curie temperature, Tc. Above Tc, the material is paraelectric and exhibits dielectric behavior.

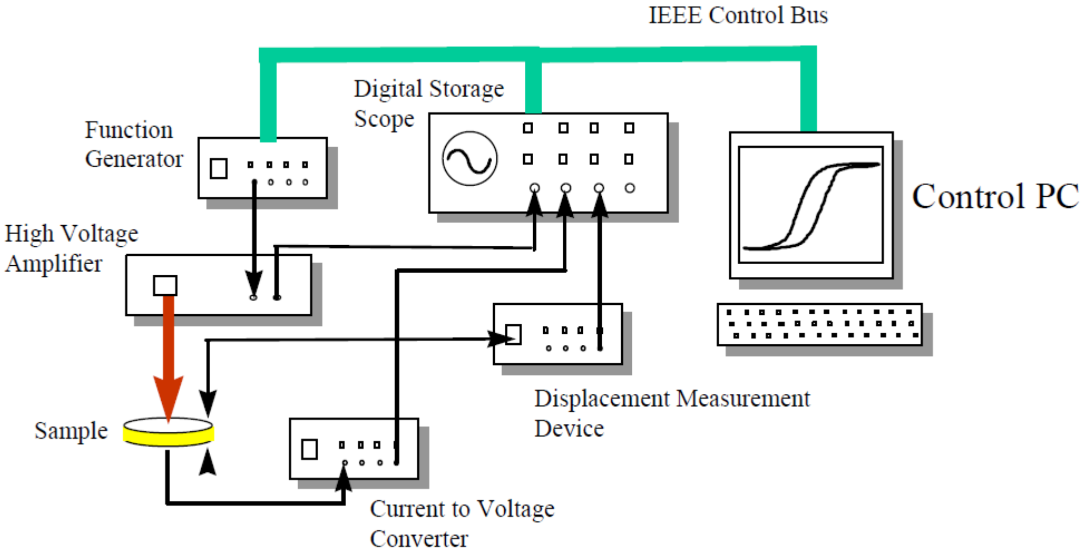

Figure 2.6. Schematic of building blocks in a P-E loop measuremet system [37].

The typical P-E hysteresis loop results from polarization responding to the applied voltage (P(V)). Derivative of polarization with respect to voltage is $\delta P/\delta V = (\delta Q/\delta V)/\text{Area}$, which is the capacitance per unit area [39]. A standard P-E hysteresis test has a preset loop following a delay of the measurement loop. In Radiant P-E loop tracer, the triangular pulses are used because, except at the reversal points, the stimulus has a constant δV/δt.

There exists an unavoidable leakage in $RFeO_3$s, which makes the measured hysteresis loops spurious. The measured polarization has contributions from displacive current and leakage current (caused by the flow of electrons through the sample). Thus, it is impossible to accurately determine the characteristic ferroelectric parameters such as saturation, remanent polarization, and coercivity from this loop [40]. Therefore, it is essential to distinguish intrinsic (remanent polarization) and non-intrinsic components appropriately. There are some correction methods available to remove non-ferroelectric contributions from the P-E loops [41,42].

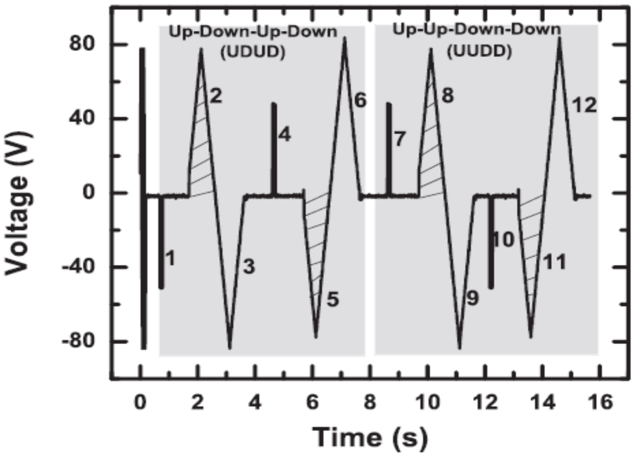

Figure 2.7. The train of voltage pulses used in remanent hysteresis measurement protocol [41,42].

There are different techniques to subtract the leakage and non-ferroelectric components. They are (i) the Dynamic Hysteresis Mode (DHM), (ii) the Dielectric Leakage Current Compensation (DLCC), and (iii) the PUND (Positive Up Negative Down). The 'Remnant Hysteresis' technique is another more detailed protocol to measure polarization as small as ~1 nC/cm^2. The voltage pulse profile with fourteen pulses used for measuring remanent hysteresis loop is shown in figure (2.7) [43]. After two depolarizing pulses, a polarizing pulse is sent, polarizing the domains in a particular orientation. The second pulse switches the domains by 180°, and first-half of the hysteresis loop is measured. The consecutive pulses (3 and 4) orients the domains in opposite directions, and no measurement is carried out. Then, 5th pulse measures the second half of the loop. Repeated domain switching is induced from pulses 1 to 5 in opposite directions continuously. The P-E loop obtained from pulses 2 & 5 consists of contributions from both switchable and nonswitchable polarizations. Owing to its structure, this set of pulses is termed as Up Down Up Down (UDUD).

Similarly, pulses 7–12 measure the contribution from only the nonswitchable component by repeatedly reinforcing the domains along the same direction, and the hysteresis loop has contribution only from nonswitchable polarization. The pulse set 7–12 is termed Up Up Down Down (UUDD). The difference between the loop obtained by UUDD pulses and UDUD pulses gives the intrinsic remanent hysteresis loop.

2.4.3. Vibrating Sample Magnetometer (VSM) for magnetic studies

The Quantum Design Vibrating Sample Magnetometer (VSM) [44] option for the Physical Property Measurement System (PPMS) is a fast and sensitive DC magnetometer works based on the basis of Faraday's Law of Induction. The basic measurement is carried out by vibrating the sample near a pickup coil and measuring the voltage induced. Using a compact gradiometer pickup coil configuration, the system is capable of measuring magnetization changes as low as 10^{-6} emu. The VSM option for the PPMS consists primarily of a VSM linear motor transport (head) for vibrating the sample, a coil set puck for detection, electronics for driving the linear motor transport and detecting the response from the pickup coils, and a copy of the MultiVu software application for automation and control. This system can function in the temperature range between 1.9 K to 400 K over the magnetic field, H = ± 90 kOe.

The basic principle of operation of a vibrating sample magnetometer is that the change in a magnetic flux induces a voltage in a pickup coil. The following equation gives the time-dependent induced voltage

$$V_{coil} = \frac{d\varphi}{dt} = \left(\frac{d\varphi}{dz}\right)\left(\frac{dz}{dt}\right) \qquad eqn\ (2.11)$$

Where φ is the magnetic flux enclosed by the pickup coil, z is the vertical position of the sample with respect to the coil, and *t* is time. For a sample position fluctuating sinusoidally, the induced voltage can be written as

$$V_{coil} = 2\pi f CmA\ \sin(2\pi f t) \qquad eqn\ (2.12)$$

C is a coupling constant, m is the DC magnetic moment of the sample, A is the amplitude of oscillation, and *f* is the frequency of oscillation.

The acquisition of magnetic moment measurements involves measuring the coefficient of the sinusoidal voltage response from the detection coil. Figure 2.8 illustrates the inside view of the PPMS VSM option. The test sample is stick to the end of a sample rod that is moved sinusoidally. When the sample is placed in-between electromagnets that generate a constant uniform magnetic field. If it is a magnetic sample the generated field will cause the alignment of independent magnetic moments causing a magnetization and the magnetic dipole moment in the sample causes a magnetic field around the sample called Stray Magnetic Field. During this, the sample is vibrated vertically (along the *z*-axis) with a vibrating sample holder, resulting in an alternating magnetic field produced by the sample. According to Faraday's Laws of Induction, an alternating magnetic field generates an electric field. These are sensed by the pickup coils equipped near the sample holder and later get processed as the sample's magnetization to a particular applied filed. Then the constant magnetic field is varied over a range, and corresponding magnetization measurements generate the sample's M-H curve.

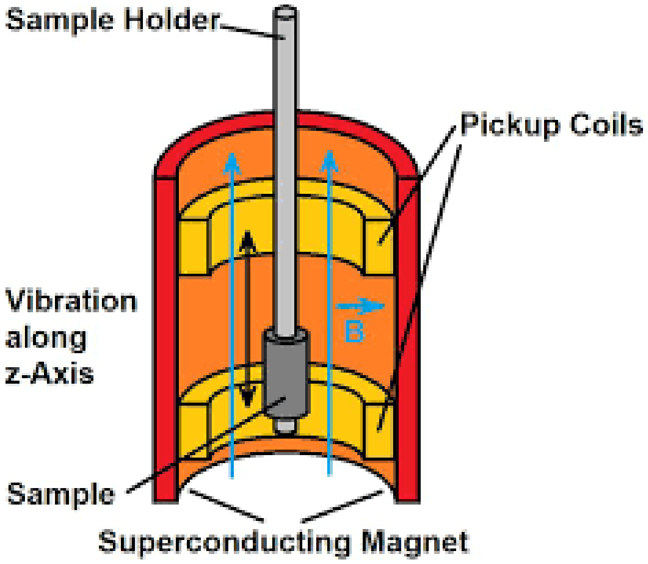

Figure 2.8. Inside view of VSM attached to PPMS [44].

In the present work, the samples pressed into pellets by applying pressure are used for magnetic measurements using VSM attached to QuantumDesign PPMS. Temperature-dependent magnetization (M-T) is measured both in ZFC (zero-field cooled) and FC (field cooled) mode. M-H isotherms are measured at different temperatures in the 5 K–900 K temperature range up to a maximum field of ±9 T.

References

[1] N. Murase, R. Jagannathan, Y. Kanematsu, M. Watanabe, A. Kurita, K. Hirata, T. Yazawa, T. Kushida, Fluorescence and EPR characteristics of Mn2+-doped ZnS nanocrystals prepared by aqueous colloidal method, J. Phys. Chem. B. 103 (1999) 754–760. https://doi.org/10.1021/jp9828179.

[2] P. Suresh, K. Vijaya Laxmi, P.S. Anil Kumar, Enhanced room temperature multiferroic characteristics in hexagonal LuFe1−xNixO3 (x = 0 − 0.3) nanoparticles, J. Magn. Magn. Mater. 448 (2018) 117–122. https://doi.org/10.1016/j.jmmm.2017.05.052.

[3] H.R. Ghorbani, F.P. Mehr, H. Pazoki, B.M. Rahmani, Synthesis of ZnO nanoparticles by precipitation method, Orient. J. Chem. 31 (2015) 1219–1221. https://doi.org/10.13005/ojc/310281.

[4] M. Zhou, H. Yang, T. Xian, J.Y. Ma, H.M. Zhang, W.J. Feng, Z.Q. Wei, J.L. Jiang, Morphology-controlled synthesis of orthorhombic LuFeO3particles via a hydrothermal route, J. Alloys Compd. 617 (2014) 855–862. https://doi.org/10.1016/j.jallcom.2014.08.057.

[5] Z. Zhou, L. Guo, H. Yang, Q. Liu, F. Ye, Hydrothermal synthesis and magnetic properties of multiferroic rare-earth orthoferrites, J. Alloys Compd. 583 (2014) 21–31. https://doi.org/10.1016/j.jallcom.2013.08.129.

[6] R.I. Walton, Subcritical solvothermal synthesis of condensed inorganic materials, Chem. Soc. Rev. 31 (2002) 230–238. https://doi.org/10.1039/b105762f.

[7] L.U. Khan, Z.U. Khan, Bifunctional Nanomaterials : Magnetism , Luminescence and Multimodal Biomedical Applications Bifunctional Nanomaterials : Magnetism , Luminescence and Multimodal Biomedical, 2017. https://doi.org/10.1007/978-3-319-52087-2.

[8] G.W. Morey, P. Niggli, The hydrothermal formation of silicates, A review, J. Am. Chem. Soc. 35 (1913) 1086–1130. https://doi.org/10.1021/ja02198a600.

[9] G. Yang, S.J. Park, Conventional and microwave hydrothermal synthesis and application of functional materials: A review, Materials (Basel). 12 (2019). https://doi.org/10.3390/ma12071177.

[10] R.L. Penn, J.F. Banfield, Morphology development and crystal growth in nanocrystalline aggregates under hydrothermal conditions: Insights from titania, Geochim. Cosmochim. Acta. 63 (1999) 1549–1557. https://doi.org/10.1016/S0016-7037(99)00037-X.

[11] F. Arzilli, M.R. Carroll, Crystallization kinetics of alkali feldspars in cooling and decompression-induced crystallization experiments in trachytic melt, Contrib. to Mineral. Petrol. 166 (2013) 1011–1027. https://doi.org/10.1007/s00410-013-0906-1.

[12] H. Cheng, J. Ma, Z. Zhao, L. Qi, Hydrothermal Preparation of Uniform Nanosize Rutile and Anatase Particles, Chem. Mater. 7 (1995) 663–671. https://doi.org/10.1021/cm00052a010.

[13] G. Dell'Agli, A. Colantuono, G. Mascolo, The effect of mineralizers on the crystallization of zirconia gel under hydrothermal conditions, Solid State Ionics. 123 (1999) 87–94. https://doi.org/10.1016/s0167-2738(99)00109-5.

[14] E. TANI, M. YOSHIMURA, S. SŌMIYA, Formation of Ultrafine Tetragonal ZrO2 Powder Under Hydrothermal Conditions, J. Am. Ceram. Soc. 66 (1983) 11–14. https://doi.org/10.1111/j.1151-2916.1983.tb09958.x.

[15] S. Leelashree, S.N. Kaul, S. Srinath, Effect of progressive substitution of Lu by Ho on the structural and dielectric properties of nanocrystalline LuFeO3 orthoferrite, Mater. Res. Bull. 145 (2022) 111570. https://doi.org/10.1016/j.materresbull.2021.111570.

[16] W.L. Bragg, The diffraction of short electromagnetic waves by a crystal, Proceeedings Cambridge Philos. Soc. 17 (1913) 26. https://doi.org/10.1001/jama.240.8.777.

[17] A.J. Dekker, Solid State Physics, 1985th ed., Macmillan, Madras, 1957.

[18] A.R. Lang, Elementary Crystallography: An Introduction to the fundamental geometrical features of crystals, 1957. https://doi.org/10.1016/0001-6160(57)90175-x.

[19] B.D. CULLITY, Elements of X-ray Diffraction, 1978. https://doi.org/10.1088/0031-9112/29/12/034.

[20] J.I. Gersten, F.W. Smith, The physics and chemistry of materials, JOHN WILEY & SONS, INC, 2001. https://doi.org/10.5860/choice.39-4581.

[21] C. Kittel, Introduction to solid state physics, 2005. https://doi.org/10.1016/0022-5096(57)90051-0.

[22] C. Suryanarayana, M.G. Norton, X-ray diffraction A practical approach, Springer Science+Business Media, LLC, 1998. https://doi.org/10.1007/978-1-4899-0148-4.

[23] J. Epp, X-Ray Diffraction (XRD) Techniques for Materials Characterization, Elsevier Ltd, 2016. https://doi.org/10.1016/B978-0-08-100040-3.00004-3.

[24] G.R. Khan, Crystallographic , structural and compositional parameters of Cu – ZnO nanocrystallites, Appl. Phys. A. 126 (2020) 1–10. https://doi.org/10.1007/s00339-020-03480-y.

[25] T. Degen, M. Sadki, E. Bron, U. König, G. Nénert, The high score suite, Powder Diffr. 29 (2014) S13–S18. https://doi.org/10.1017/S0885715614000840.

[26] C. Ni, Scanning Electron Microscopy (SEM), in: Q.J. Wang, Y.-W. Chung (Eds.), Encycl. Tribol., Springer US, Boston, MA, 2013: pp. 2977–2982. https://doi.org/10.1007/978-0-387-92897-5_1217.

[27] D.A. Long, Handbook of Raman spectroscopy. From the research laboratory to the process line.Edited by Ian R. Lewis and Howell G. M. Edwards. Marcel Dekker, New York and Basel, 2001. Price$225., J. Raman Spectrosc. 35 (2004) 91–91. https://doi.org/10.1002/jrs.1117.

[28] R.R. Jones, D.C. Hooper, L. Zhang, D. Wolverson, V.K. Valev, Raman Techniques: Fundamentals and Frontiers, Nanoscale Res. Lett. 14 (2019). https://doi.org/10.1186/s11671-019-3039-2.

[29] M. Bass, J.M. Enoch, W.L. Wolfe, HANDBOOK OF OPTICS, SECOND, McGraw Hill, 2001. https://doi.org/10.1036/0071414797.

[30] M. M., S. Bahadar, A. Jamal, M. Faisal, A. M., Iron Oxide Nanoparticles, Nanomaterials. (2011). https://doi.org/10.5772/27698.

[31] A. Technologies, Agilent E4980A Peccison LCR meter, (n.d.).

[32] A.R. West, Solid State Chemistry, Second, 4 John Wiley & Sons, Ltd, 2014.

[33] G.S. Perry, A review of the recent literature on the dielectric properties and sintering of alumina, J. Mater. Sci. 1 (1966) 186–198. https://doi.org/10.1007/BF00550106.

[34] A.K. Jonscher, Dielectric relaxation in solids, (1999).

[35] L. Eric Cross, Relaxor ferroelecirics, Ferroelectrics. 76 (1987) 241–267. https://doi.org/10.1080/00150198708016945.

[36] C.M. Kachijava, S.C. Saxena, FEW PROPERTIES OF IONIC CRYSTALS ON THE SHELL MODEL, Indian J. Phys. 41 (1967) 440.

[37] A.M. Glazer, P. Groves, D.T. Smith, Automatic sampling circuit for ferroelectric hysteresis loops, J. Phys. E. 17 (1984) 95–97. https://doi.org/10.1088/0022-3735/17/2/001.

[38] R. Salt, Rochelle salt, Phys. Rev. 35 (1930) 269–276. https://doi.org/https://doi.org/10.1103/PhysRev.35.269.

[39] J. Evans, Characterizing Ferroelectric Materials, Radiant Technol. Inc. (2011) 141. https://www.ferrodevices.com/1/297/support.asp.

[40] J.F. Scott, Ferroelectrics go bananas, J. Phys. Condens. Matter. 20 (2008) 19–21. https://doi.org/10.1088/0953-8984/20/02/021001.

[41] L. Pardo, J. Mendiola, C. Alemany, Theoretical treatment of ferroelectric composites using Monte Carlo calculations, J. Appl. Phys. 64 (1988) 5092–5097. https://doi.org/10.1063/1.342414.

[42] J. Liu, X. Yao, A new digital measuring system of ferroelectric hysteresis loop and field induced strain of ferroelectric materials, Ceram. Int. 30 (2004) 2033–2036. https://doi.org/10.1016/j.ceramint.2003.12.165.

[43] U. Chowdhury, S. Goswami, D. Bhattacharya, A. Midya, P. Mandal, Determination of intrinsic ferroelectric polarization in lossy improper ferroelectric systems, Appl. Phys. Lett. 109 (2016) 1–6. https://doi.org/10.1063/1.4961988.

[44] Q. Design, Vibrating Sample Magnetometer (VSM) Option User’s Manual, Part Number 1096-100, B0. (2011) 1–122.

CHAPTER 3

Synthesis and Structural Characterization of $Lu_{1-x}Ho_xFeO_3$ $(0 \le x \le 1)$

Hydrothermal synthesis method is adapted to synthesize nanoparticles at relatively lower temperatures. The higher ionic radius of Ho^{3+} *helps to stabilize the orthorhombic structure. This chapter describes the synthesis, structural, microstructure, and Raman spectroscopy studies of* $Lu_{1-x}Ho_xFeO_3$ $(0 \le x \le 1)$ *prepared using the hydrothermal method.*

3.1. Introduction

Out of the $RFeO_3$ family, $LuFeO_3$ is of particular relevance/interest to the present work, as elucidated below. $LuFeO_3$ (LFO) crystallizes into two different crystallographic structures: metastable hexagonal ($P6_3cm$) and stable orthorhombic (Pbnm) [1]. The polar and metastable nature of the hexagonal (h-) LFO makes it challenging to stabilize this compound as a single phase. Wang et al. [2] reported the coexistence of ferroelectric and antiferromagnetic orders (multiferroicity of type I [3]) with the ferroelectric (FE) Curie temperature Tc(FE) ~ 1050 K and the Néel temperature T_N ~ 440 K. However, the claim of multiferroicity at RT in h-LFO was later refuted [4] based on a careful study of magnetic structure and ordering in epitaxially-grown h-LFO thin films, which demonstrated that depending on the film thickness, T_N ranges between ~ 130 K and 150 K. By directly measuring the magneto-electric coupling, Chowdhury et al. [5] demonstrated a strong coupling between magnetization and electric polarization (multiferroicity of type II [6]) in bulk orthorhombic (o-) LFO at RT (Tc(FE) ~ 700 K and T_N ~ 600 K) [5,7] despite its non-polar nature. Synthesis of o-LFO in the bulk form requires high annealing temperatures (T_A ~ 1200 ◦C) [5], which results in the formation of undesired Fe–O impurity phases such as Fe_2O_3, Fe_3O_4 [8,9]. In order to overcome this limitation of o-LFO, we have adopted the following strategy. When Ho is progressively substituted for Lu in $LuFeO_3$, the orthorhombic structure can be stabilized at relatively lower temperature [10]. Also, the formation of Fe–O impurity phases can be avoided by synthesizing o- LFO at lower temperatures using the hydrothermal synthesis method and subsequently annealing at an optimum temperature for a specific duration of time. Taking cognizance of the well-known fact that the orthorhombic structure in $RFeO_3$ orthoferrites is stabilized by the rotations (tilts) of the FeO_6 octahedra and that such tilts/rotations give rise to distinct Raman vibrational/rotational modes, we use Raman spectroscopy, in this work, to investigate the lattice distortions and slight changes in octahedral rotations, brought about by the substitution of Lu by Ho in $Lu_{1-x}Ho_xFeO_3$.

3.2. Synthesis of $Lu_{1-x}Ho_xFeO_3$ ($0 \leq x \leq 1$)

The most common synthesis technique used for synthesizing $LuFeO_3$ is solid- state reaction [5,11–13]. This technique requires high annealing temperature as well as tedious synthesis procedure which leads to bigger grain size and inhomogeneity. The higher annealing temperature will facilitate the formation of various Fe-O phases like Fe_3O_4, Fe_2O_3, etc., On the other hand, hydrothermal synthesis can be carried out at relatively low temperatures and has a fairly simple synthesis procedure. Also, using hydrothermal synthesis, smaller grain size can be achieved with a uniform distribution and possibly the formation of impurity phases can be minimized.

Analytical grade chemicals $Lu(NO_3)_3 . H_2O$ (≥ 99.9 %), $Ho(NO_3)_3 . 5H_2O$ (≥ 99.9 %), $Fe(Cl_3)_3 . 6H_2O$ (≥ 95 %), citric acid were used to synthesize $Lu_{1-x}Ho_xFeO_3$ (x = 0.0,0.05, 0.1, 0.2, 0.25, 0.3, 0.4, 0.5, 0.6, 0.8, 1.0) nanoparticles by hydrothermal method. The reagents were dissolved in double distilled water under magnetic stirring. The pH of the solution is changed to 8 by adding a few drops of NH_3. The mixture is then transferred into an autoclave and treated thermally at 200 °C for 24 h. The obtained solution is washed using a centrifuge at 13,000 rpm several times with water and ethanol. The sediment is dried in hot air oven at 70 °C for 3 h. The obtained powder is grounded well and annealed at various temperatures and time periods to optimize the annealing temperature. The procedure is given in the form of a flow chart as shown in figure 3.1.

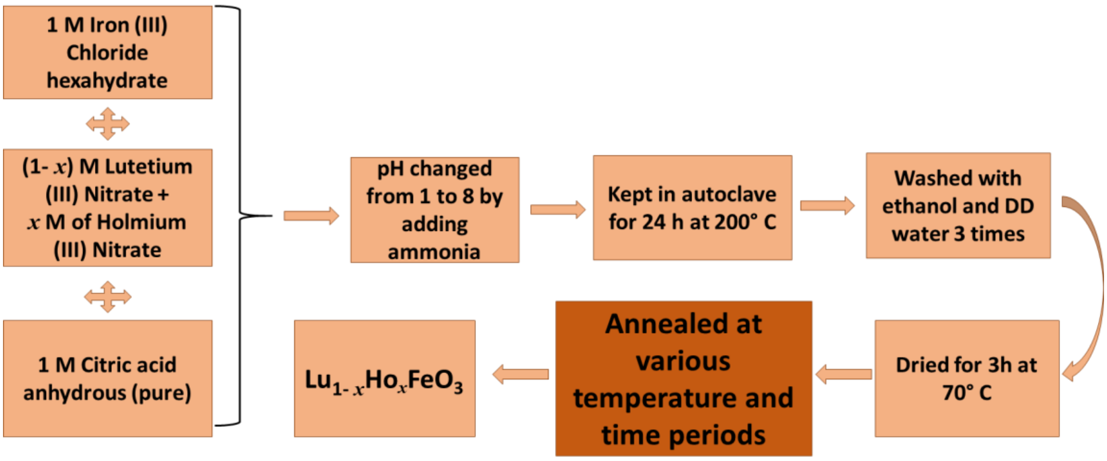

Figure 3.1. Flow chart of the hydrothermal synthesis procedure

3.3. X-ray Diffraction Analysis

3.3.1. Optimization of Annealing temperature

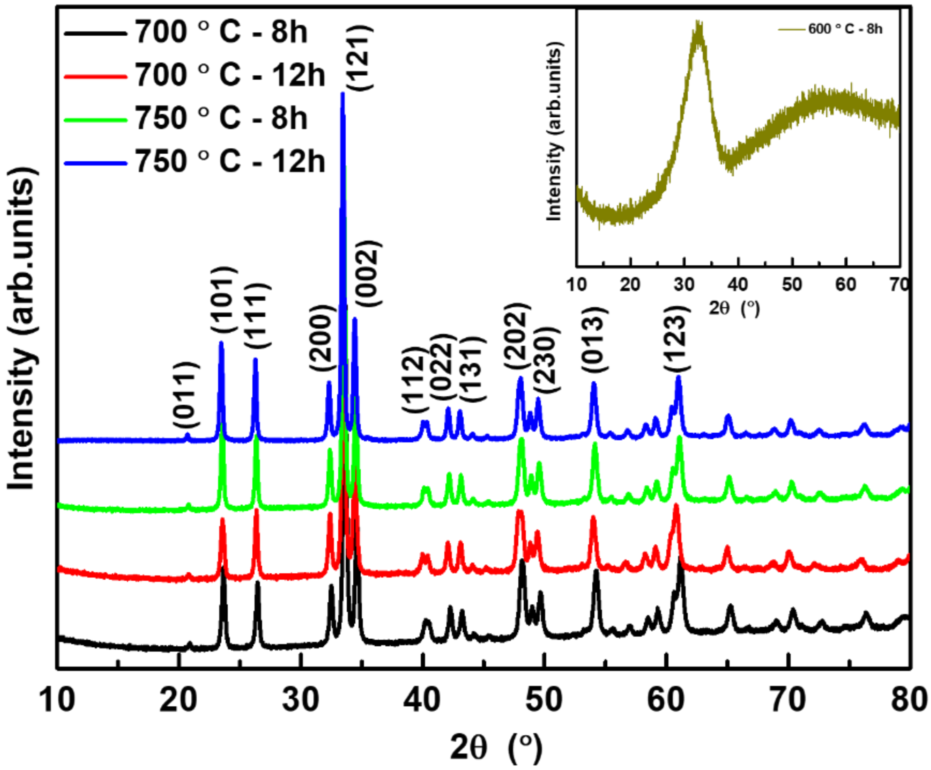

Figure 3.2. XRD patterns of $Lu_{0.9}Ho_{0.1}FeO_3$ synthesized via hydrothermal method at various annealing conditions. Inset: XRD pattern of the sample annealed at 600°C for 8h.

The $Lu_{0.9}Ho_{0.1}FeO_3$ sample synthesized by hydrothermal method was first annealed at 600 °C for 8 hours to confirm the crystallinity of the sample. It is observed that the sample is amorphous (inset of figure 3.2). Then the sample is further annealed at different annealing temperatures and duration for obtaining the crystallinity as shown in figure 3.2. It can be seen in figure 3.2 that orthorhombic $LuFeO_3$ (o- LFO) phase had been stabilized and the peaks are indexed to their (hkl) planes. Annealing for 12 hours at 750 °C started giving rise to Fe_3O_4 phase. The Rietveld refinement is done on the sample annealed at 750 °C for 12 hours and the o- LFO phase fraction is calculated to be 99 % and Fe_3O_4 to be 1 %. The refinement is shown in figure 3.3. Thus, the sample's optimization temperature is fixed to be 750 °C and annealing time is fixed to be 8 hours. In this condition, all the samples ($0 \leq x \leq 1$) are annealed. The synthesized powder is compressed into a pellet form for further characterization.

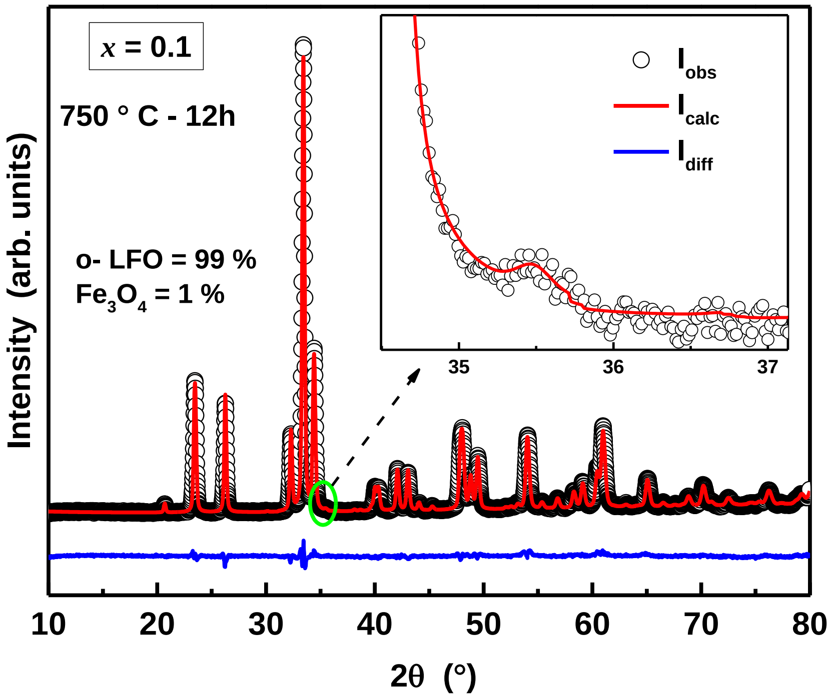

Figure 3.3. Rietveld refinement of $Lu_{0.9}Ho_{0.1}FeO_3$ annealed at 750°C for 12 hours. Inset. A hump observed at 35.5° which corresponds to the Fe_3O_4 phase.

3.3.2. Rietveld refinement analysis of $Lu_{1-x}Ho_xFeO_3$ ($0 \leq x \leq 1$)

Nanocrystalline $Lu_{1-x}Ho_xFeO_3$ (x = 0.0 to 1.0) powders were synthesized by hydrothermal method. The XRD patterns of all the synthesized samples, annealed at 750˚C for 8 hours, are shown in figure 3.4. (a). All the diffraction peaks are indexed using ICDD- 98-002-7285 and ICDD- 98-018-3152 cards for orthorhombic $LuFeO_3$ and hexagonal $LuFeO_3$, respectively. It is evident from figure 3.4. (a) that, in the parent $LuFeO_3$ (x = 0) compound, the majority phase is hexagonal. The distinct Bragg peaks belonging exclusively to the hexagonal phase are denoted by the asterisk '*' symbol. Figure 3.4. (b) provides an enlarged view of the Bragg peak at $2\theta = 40.25^{o}$, highlighted in figure 3.4. (a) by an elliptical curve. The sub-figure 3.4. (b) clearly demonstrates the splitting of this Bragg peak, characteristic of the orthorhombic phase, and the shift of the split peaks to lower angles as the Ho concentration, x, increases. This peak shift is a consequence of the linear increase in the lattice parameters with increasing x, as revealed by the Rietveld refinement of the XRD data.

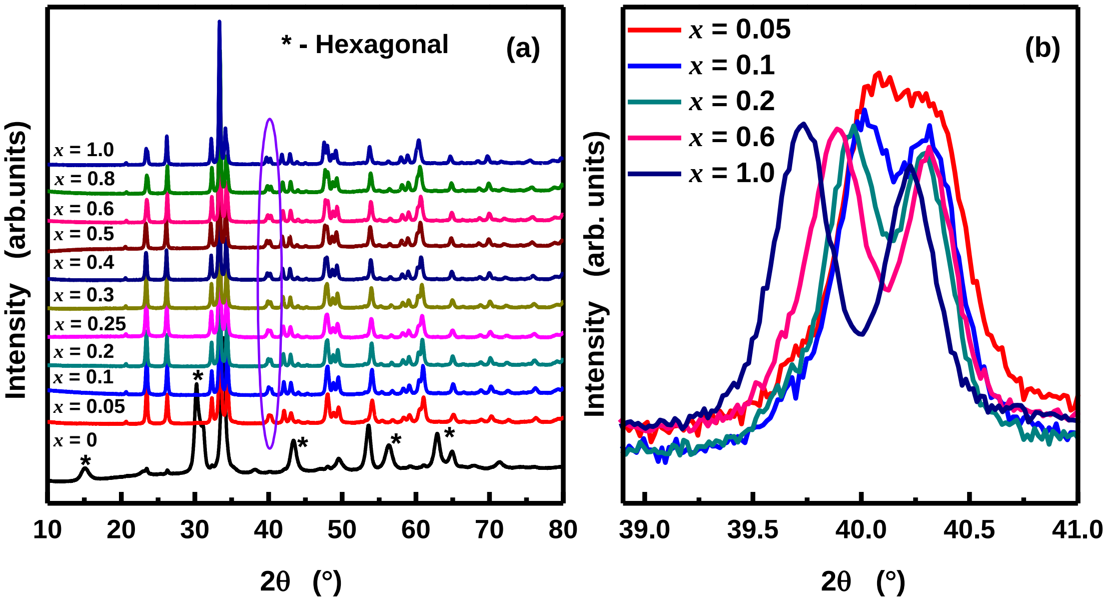

Figure 3.4. (a). Room temperature x-ray diffraction (XRD) patterns of $Lu_{1-x}Ho_xFeO_3$ (x = 0.0 to 1.0). (b). Splitting of the Bragg peak at 40.25° and the shift of the split peaks to lower angles as the Ho concentration increases.

Rietveld refinement of the XRD data was carried out using Highscore Plus software and the resulting Rietveld fits (red curves), typical of all the samples, are shown in figure 3.5. For $x = 0$, the Rietveld refinement yields the phase fractions as 91.5 % hexagonal and 8.5 % orthorhombic. In sharp contrast, as small as 5 at. % Ho substitution (i.e., when $x = 0.05$) tilts the balance in favor of the orthorhombic phase and the phase fraction now stands at 94% orthorhombic and 6% hexagonal. Further doping of Ho, from $x = 0.1$ to 1.0, results in a pure (100%) orthorhombic phase. Note that, for the samples annealed at 750˚C for 8 hours, the Rietveld refinement does not reveal any unaccounted Bragg peaks that could be attributed to the Fe_2O_3 or Fe_3O_4 impurity phase.

Reliable values of the structural parameters such as the lattice parameters, bond angles, bond lengths, etc., yielded by the Rietveld refinement for the hexagonal and orthorhombic phases in $Lu_{1-x}Ho_xFeO_3$ are given in tables 3.1 and 3.2, respectively. The lattice parameters, so obtained, are plotted against the Ho concentration x in figure 3.6 (a). In accordance with Vegard's law [14–16], the lattice parameters increase linearly with the Ho concentration. The validity of Vegard's law asserts that Ho indeed substitutes for Lu in the $Lu_{1-x}Ho_xFeO_3$ nanocrystalline samples. The lattice parameters for the orthorhombic phase of $LuFeO_3$ and $HoFeO_3$, reported in the literature [17,18], are included in figure 3.6 (a) for comparison.

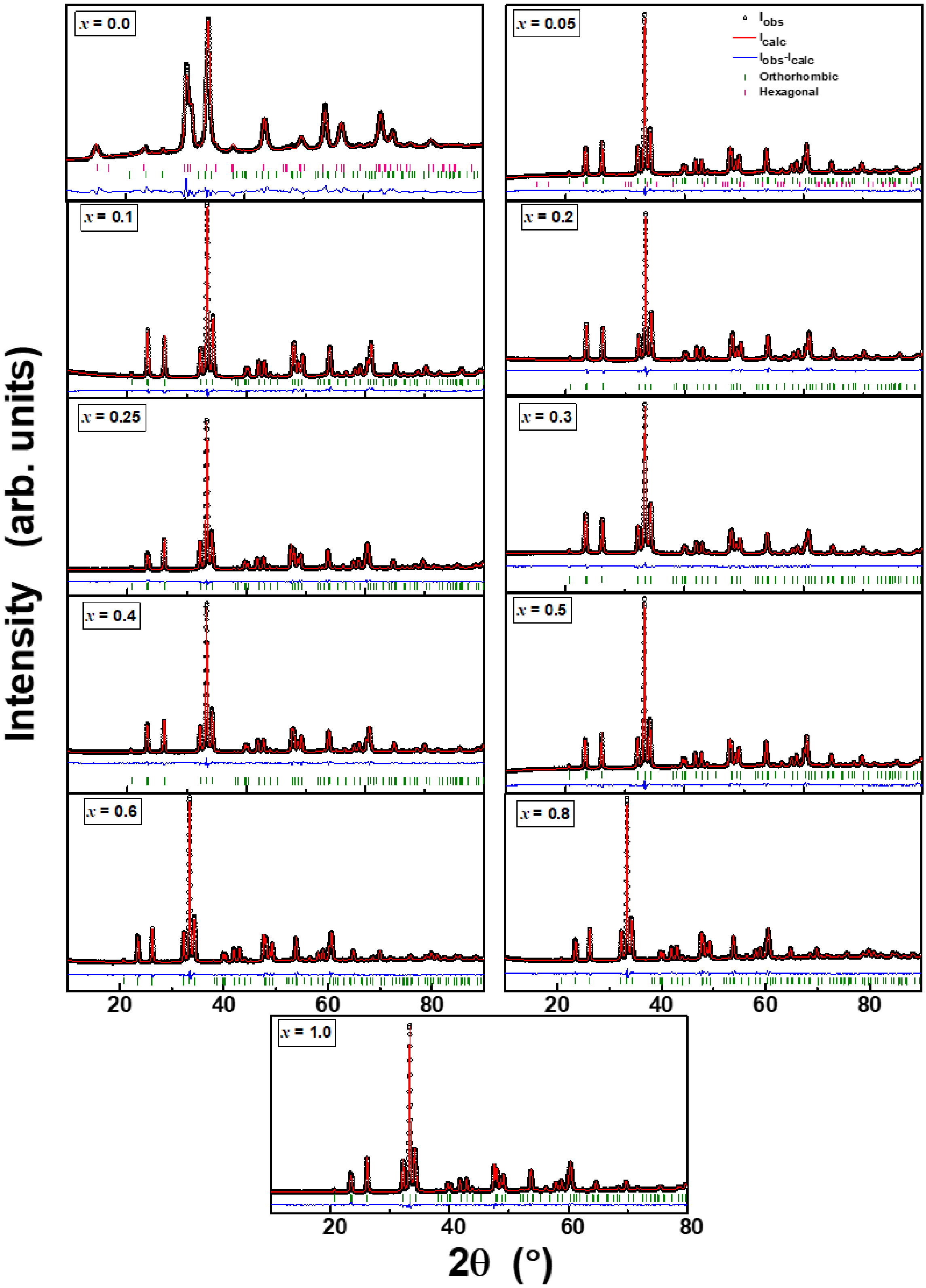

Figure. 3.5. Rietveld-refinement fits to the XRD data taken on $Lu_{1-x}Ho_xFeO_3$ ($0 \leq x \leq 1$) nanoparticles.

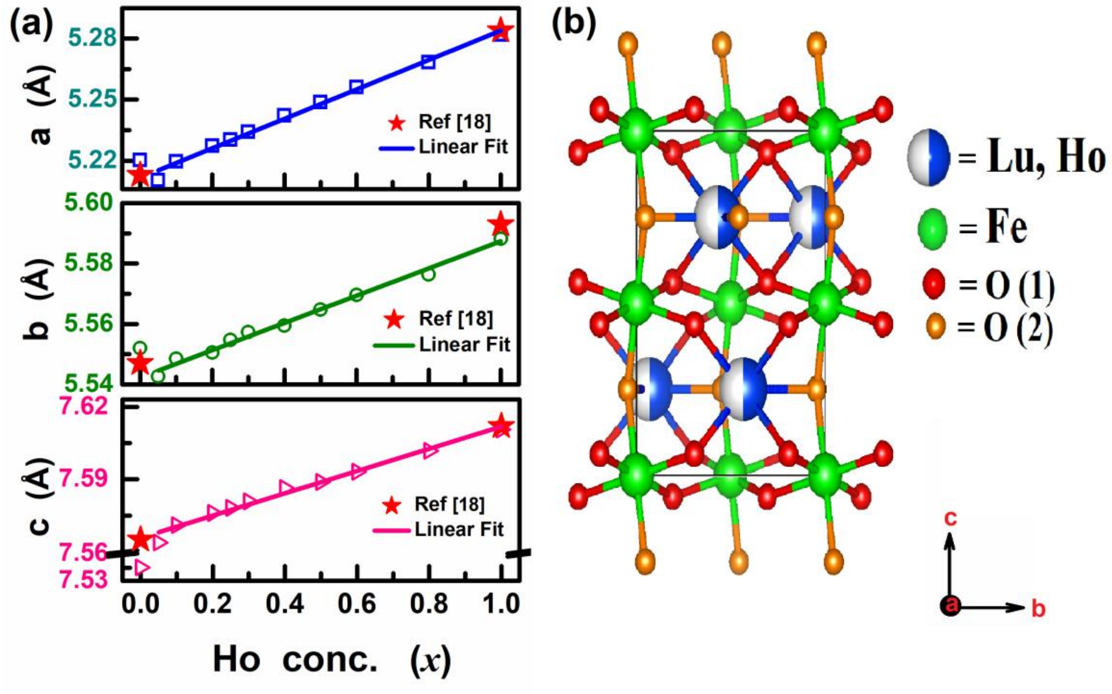

Figure 3.6. (a): Lattice parameters (*a*, *b*, *c*) as functions of the Ho concentration, *x*, and the linear fits to the *a*(*x*), *b*(*x*) and *c*(*x*) data. The asterisk '*' denotes the lattice parameter values for $x = 0.0$ and 1.0 taken from reference [18]. (b): Schematic representation of $Lu_{0.5}Ho_{0.5}FeO_3$ crystal structure.

The $RFeO_3$ crystal structure can be viewed as Fe-O(1) layers, and R-O(2) layers stacked alternately in the *c*-direction. As an illustrative example, a schematic sketch of the $Lu_{0.5}Ho_{0.5}FeO_3$ crystal structure, representative of other compositions as well, is shown in figure 3.6 (b). It is evident from this figure that each Fe^{3+} ion is located at the centre of an octahedral O^{2-} cage consisting of four O(1) ions coplanar (*ab*-basal plane) with Fe^{3+} ion and two out-of-plane apex O(2) ions along the b-axis. On the other hand, each R^{3+} ion is coplanar with two O(2) ions and connected to four O(1) ions in the two adjacent Fe-O(1) layers.

3.3.3. Stabilization of Orthorhombic phase

3.3.3.1. Tolerance factor

In a ABO_3 perovskite structure, A cation is coordinated by 12 oxygen ions and B cation by 6 oxygen ions forming an oxygen octahedra. Generally, when the size of the A cation is comparable to the size of the B cation, the octahedras are parallel to each other forming cubic phase with Pm3m space group, the most stable crystal structure. In the ideal cubic perovskite,

$$r_A + r_O = \sqrt{2}(r_B + r_O) \qquad eqn\ (3.1)$$

where r_A, r_B, r_O are ionic radii of A cation, B cation and oxygen, respectively. When the size of the A ion is larger compared to that of the B ion, the bond B-O-B bends and the octahedral tilts, giving raise to distortion in the unit cell. This distortion forms orthorhombic crystal structure. To accommodate the distortion, a constant 't' is introduced by Goldschmidt [19] in the above equation and given as,

$$r_A + r_O = t\sqrt{2}(r_B + r_O) \qquad eqn\ (3.2)$$

Eqn. (3.2) is rewritten to define tolerance factor 't' to determine the geometrical stability of perovskites is given by

$$t = \frac{r_A + r_O}{\sqrt{2}\,(r_B + r_O)} \qquad eqn\ (3.3)$$

The typical 't' value of the cubic structure is 1. The value of 't' varies between 0.8 and 0.9 for orthorhombic structure. In this work, A ion is Lu and Ho in 3+ valence state, Fe in 3+ valence state is the B ion. Since the ionic radius of Lu and Ho with coordination number 12 is not available in the Shannon table, coordination number 8 [18] is considered to calculate the tolerance factor. The ionic radii 0.977, 1.015, 0.55 and 1.36 Å of Lu, Ho, Fe and O ions, respectively are substituted in eqn.3.3 and the values obtained are included in table 2. Ho substitution in place of Lu increases t linearly from 0.866 to 0.880, confirming the stabilization of orthorhombic structure.

Table 1. Lattice parameters for the hexagonal phase in $Lu_{1-x}Ho_xFeO_3$ (x = 0.0,0.05) yielded by the Rietveld refinement of the XRD data. The values of lattice parameters reported in [21] for hexagonal $LuFeO_3$ are included for comparison. The numbers in the parentheses denote errors in the least significant figure.

Ho conc. *x*	***x* = 0; Ref.** [20]	***x* = 0**	***x* = 0.05**
Hexagonal phase (%)		91.5 (15)	4 (1)
***a* (Å)**	5.965	5.921 (3)	5.914 (1)
***c* (Å)**	11.702	11.739 (2)	12.393 (2)

Table 3.2 (a). Structural parameters for the orthorhombic phase in $Lu_{1-x}Ho_xFeO_3$ yielded by the Rietveld refinement of the XRD data.

Ho conc. *x*	**0**	**0.05**	**0.1**	**0.2**	**0.25**	**0.3**	**0.4**	**0.5**	**0.6**	**0.8**	**1.0**
phase (%)	8.5 (15)	94 (1)	100	100	100	100	100	100	100	100	100
a (Å)	5.5521 (4)	5.5416 (3)	5.5481 (1)	5.5512 (2)	5.5551 (1)	5.5575 (1)	5.5589 (1)	5.5654 (1)	5.5674 (1)	5.5758 (3)	5.5886 (4)
b (Å)	7.5352 (2)	7.5639 (1)	7.5716 (2)	7.5762 (1)	7.5781 (1)	7.5812 (1)	7.5862 (1)	7.5893 (1)	7.5934 (1)	7.6022 (2)	7.6113 (3)
c (Å)	5.2206 (7)	5.2104 (5)	5.2203 (3)	5.2271 (1)	5.2305 (1)	5.2341 (1)	5.2422 (1)	5.2497 (1)	5.2563 (3)	5.2683 (2)	5.2821 (2)
V (Å^3)	218.3	218.4	219.3	219.8	220.2	220.5	221.1	221.7	222.3	223.3	224.6
χ^2	4.5	3.4	2.7	2.83	2.3	2.32	2.4	1.74	2.47	2.35	2.4
R_{wp}	3.2	2.87	2.45	2.48	1.9	1.76	2.2	2.01	2.18	2.17	1.9
Deformation (D)		0.0371	0.0371	0.0371	0.0370	0.0370	0.0370	0.0369	0.0369	0.0368	0.0367
$\Phi_{[010]}$ (°)		13.087	12.885	12.683	12.603	12.507	12.299	12.047	11.825	11.494	11.089
$\Theta_{[101]}$ (°)		19.944	19.833	19.660	19.684	19.644	19.459	19.408	19.323	19.140	19.069
Tolerance factor (t)	0.866	0.867	0.867	0.869	0.870	0.870	0.872	0.873	0.875	0.877	0.880
Crystallite size (nm)	20.8 (1)	30.6 (1)	37.2 (1)	41.7 (5)	42.8 (2)	42.0 (5)	47.4 (3)	42.9 (1)	39.4 (2)	39.1 (2)	42.5 (6)
Strain %	0.097	0.087	0.080	0.057	0.060	0.097	0.078	0.083	0.028	0.010	0.031
Particle size (nm)	31.2 (3)	39.5 (7)	38.4 (6)	41.5 (3)	52.4 (9)	74.4 (9)	82.1(16)	66.9(13)	60.1(19)	45.2(19)	44.3 (5)

Table 3.2 (b). Bond lengths and bond angles for the orthorhombic phase in $Lu_{1-x}Ho_xFeO_3$ obtained from the Rietveld refinement of the XRD data.

Ho conc. *x*	**0.05**	**0.1**	**0.2**	**0.25**	**0.3**	**0.4**	**0.5**	**0.6**	**0.8**	**1.0**
Fe - O(1) (Å)	1.9960 (4)	2.0009 (1)	2.0014 (5)	2.0019 (4)	2.0014 (2)	2.0054 (5)	2.0080 (5)	2.0109 (5)	2.0148 (3)	2.0196 (8)
O(1) - Fe (Å)	2.0223 (3)	2.0259 (2)	2.0264 (4)	2.0263 (5)	2.0264 (7)	2.0293 (5)	2.0319 (3)	2.0342 (5)	2.0372 (1)	2.0417 (5)
Fe - O(2) (Å)	2.0078 (8)	2.0109 (4)	2.0114 (1)	2.0115 (2)	2.0106 (5)	2.0136 (3)	2.0147 (6)	2.0166 (4)	2.0191 (3)	2.0218 (2)
θ_1 = Fe - O(1) - Fe (°)	142.33 (4)	142.35 (3)	142.35 (2)	142.35 (3)	142.36 (1)	142.36 (1)	142.38 (4)	142.39 (1)	142.40 (2)	142.42 (3)
θ_2 = Fe - O(2) - Fe (°)	140.71 (1)	140.66 (1)	140.66 (1)	140.65 (1)	140.65 (1)	140.61 (1)	140.58 (1)	140.56 (1)	140.52 (1)	140.47 (1)
[R- O(1)] (*a*) (Å)	2.2218 (2)	2.2259 (1)	2.2269 (3)	2.2256 (1)	2.2137 (2)	2.2256 (3)	2.2279 (3)	2.2335 (2)	2.2345 (1)	2.2404 (2)
[R- O(2)] (*a*) (Å)	2.3581 (7)	2.2649 (4)	2.2669 (2)	2.2664 (3)	2.2652 (1)	2.2609 (2)	2.2624 (2)	2.2665 (4)	2.2792 (1)	2.2971 (5)
[R- O(2)] (*c*) (Å)	2.0677 (5)	2.1568 (8)	2.1484 (5)	2.1588 (2)	2.1844 (6)	2.1694 (6)	2.1777 (4)	2.1604 (3)	2.1593 (2)	2.1858 (9)

3.3.3.2. Octahedra Tilts

The orthorhombic (Pbnm) structure can be derived by tilting the FeO_6 cages from the parent cubic phase Pm-3m [22]. In $RFeO_3$s, the octahedral tilts are controlled by R^{3+} ionic radius [23]. In $RFeO_3$s, four unit cells form a super cell to describe $RFeO_3$ (Z = 4). Each unit cell (Z = 1) is considered to be pseudo-cubic in which the bond B-O-B is uniform throughout the pseudo-cubic. In pseudo-cubic (pc) settings, the tilt angles θ and φ around $[101]_{pc}$ and $[010]_{pc}$ axes, respectively, are related to the lattice parameters a, b and c by the relations [22,24]

$$a = \sqrt{2}\, a_0 \cos\varphi \qquad eqn\ (3.4)$$

$$b = 2\, a_0 \cos\theta \qquad eqn\ (3.5)$$

$$c = \sqrt{2}\, a_0 \cos\theta \cos\varphi \qquad eqn\ (3.6)$$

Where a_0 is a linear dimension which is related to the B-O bond. In a pseudo- cubic setting,

$$a_0 = 2\,(B - O) \qquad eqn\ (3.7)$$

Considering this relation, the octahedral bond length B-O and the tilt angles θ and φ can be written as

$$B - O = \frac{ab}{4c} \qquad eqn\ (3.8)$$

By substituting equation 3.8 in eqn 3.4 and 3.5 and rearranging, the tilt angles can be obtained as

$$\varphi_{[010]} = cos^{-1}\left({}^{\sqrt{2}c}\!/_{b}\right)\ ;\ \theta_{[101]} = \cos^{-1}({}^{c}\!/_{a}) \qquad eqn\ (3.9)$$

The values for θ and φ, calculated using the presently determined lattice parameter values in eqn. (3.9), are given in table 3.2 (a) and shown in figure 3.7. In an ideal cubic case, there is no rotation (i.e., φ = θ = 0). In the present case, the tilt angle decreases from θ (φ) 19.944° (13.087°) for $x = 0.05$ to 19.069° (11.089°) for $x = 1$. The octahedral tilt/rotation angles are basically controlled by eightfold coordination R^{3+} ionic radius and hence decrease monotonously as the ionic radius increases *linearly* from 0.977 Å for Lu^{3+} to 1.015 Å for Ho^{3+}. This behaviour asserts that the structure becomes more symmetrical and stable with Ho doping.

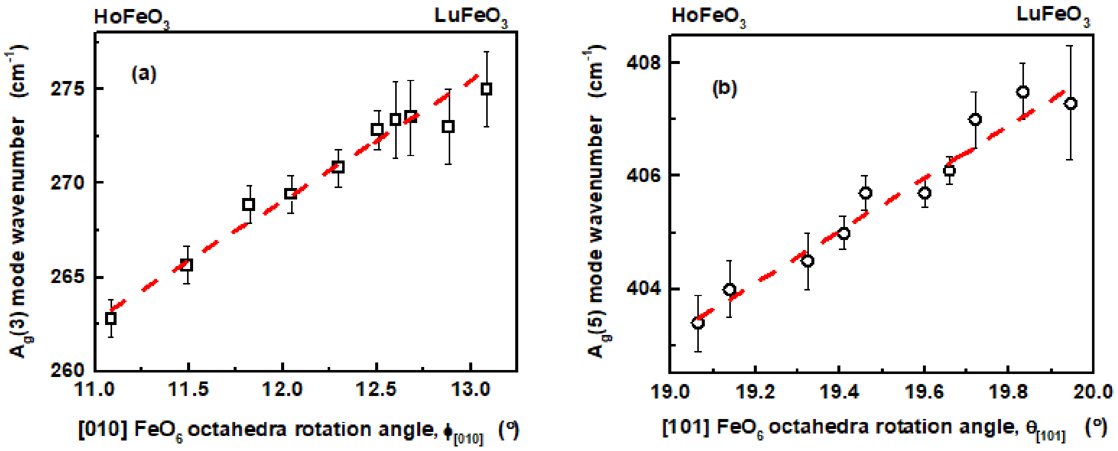

Figure. 3.7. The FeO$_6$ octahedral tilt/rotation angles $\theta_{[101]}$ and $\varphi_{[010]}$ (around the pseudo-cubic (pc) $[101]_{pc}$ and $[010]_{pc}$ axes) as functions of the Ho concentration, *x*.

3.3.3.3. Orthorhombic Deformation

Another measure of the stability of the structure is the orthorhombic deformation (*D*), defined by the following expression [17]

$$D = \frac{1}{3}\sum_{i} \frac{|a_i - \langle a\rangle|}{\langle a\rangle}, \quad \langle a\rangle = \left(\frac{abc}{\sqrt{2}}\right)^{\frac{1}{3}} \qquad eqn\ (3.10)$$

The values of *D* calculated from Eq.(3.10) using the lattice parameters *a*,*b*,*c*, where a_i stands for *a* or *b* or *c*, are also listed in table 3.2 (a) and shown in figure 3.8. The deformation decreases and hence stability of the orthorhombic structure improves with increasing Ho concentration. This inference is consistent with that drawn from the calculated tolerance factor and tilt angle values.

3.3.4. Crystallite size calculation

The peak broadening (ξ) in the XRD peaks can be directly attributed to the crystallite size and the strain induced in the nanocrystals. Along with this contribution, the observed broadening also consists of instrumental broadening [25]. The following equation can correct for instrumental broadening,

$$\xi_d^2 = \xi_o^2 - \xi_i^2 \qquad eqn\ (3.11)$$

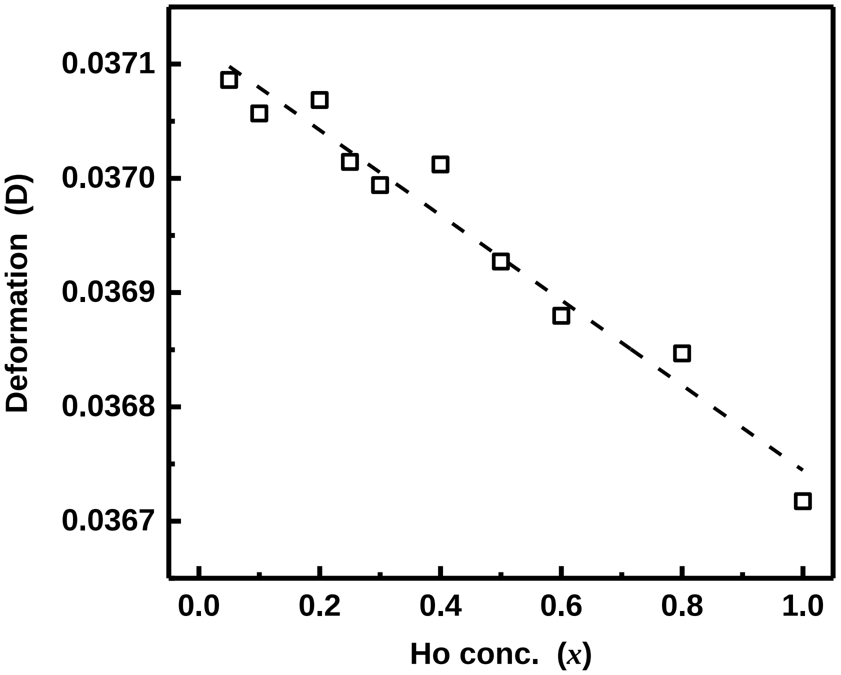

Figure 3.8. Orthorhombic deformation (D) as a function of Ho concentration

Where ξ_d is the broadening after correction, ξ_o is the observed broadening, and ξ_i is the instrumental broadening. The standard Si sample is used for both 2θ position calibration and correcting instrumental broadening in our work.

The Debye- Scherrer method [26] considers only the crystallite size effect on the peak broadening. It doesn't include the contribution from the intrinsic strain components due to the point defects, grain boundary, and stacking faults [25]. The intrinsic strain is also included in Williamson- Hall method [27]. But it considers that the nanocrystals are isotropic. i.e., It assumes that the crystallite size and intrinsic strain are uniform in all the direction. Another assumption is a linear relationship between stress and strain, according to Hook's law. Dislocations and agglomerations create imperfections in the crystals. Thus, in the real crystals, the isotropic behavior and linear relationship cannot be considered.

Halder- Wagner is another method [28,29], which assumes that the XRD peak profile is actually a Voigt function. The peak region of the XRD peak can be described with the Gaussian function, but the peak tail falls quickly, which can be matched with a Lorentzian function. The intrinsic strain is reflected in the Gaussian and the size effect in the Lorentzian function. Thus, to describe the XRD peak profile completely, symmetry Voigt function is assumed in this method. Since the nanocrystals will not be equal in size and shape, all the deformed crystals are approximated to their equivalent spheres, and the volume-weighted mean crystallite size is calculated. The full width at half maximum (FWHM) for a Voigt function can be written as

$$\xi_{hkl}^{2} = \xi_{L}.\xi_{hkl} + \xi_{G}^{2} \qquad eqn\ (3.12)$$

Where ξ_L and ξ_G are contributions from the Lorentzian and Gaussian functions, respectively. This method gives significance to the low and middle range angles where the overlapping of the peak is relatively lesser. Figure 3.9 depict linear Halder-Wagner, $(\xi / \tan\theta)^2$ versus $\xi / (\tan\theta .\ \sin\theta)$, plots, based on the relation

$$\left(\frac{\xi}{tan\theta}\right)^{2} = \frac{k\,\lambda}{d} . \left(\frac{\xi}{tan\theta\ .sin\theta}\right) + 16\,\varepsilon^{2} \qquad eqn\ (3.13)$$

where ξ is the width at half maximum of a Bragg peak, *d* is the volume-weighted mean crystallite diameter (obtained using the lognormal distribution of crystallite diameters), ε is the strain, and *k* is a constant ≈ 1. The values for *d* and ε, computed from the slope and intercept on the ordinate of the linear Halder-Wagner plots, are tabulated in Table 3.2a.

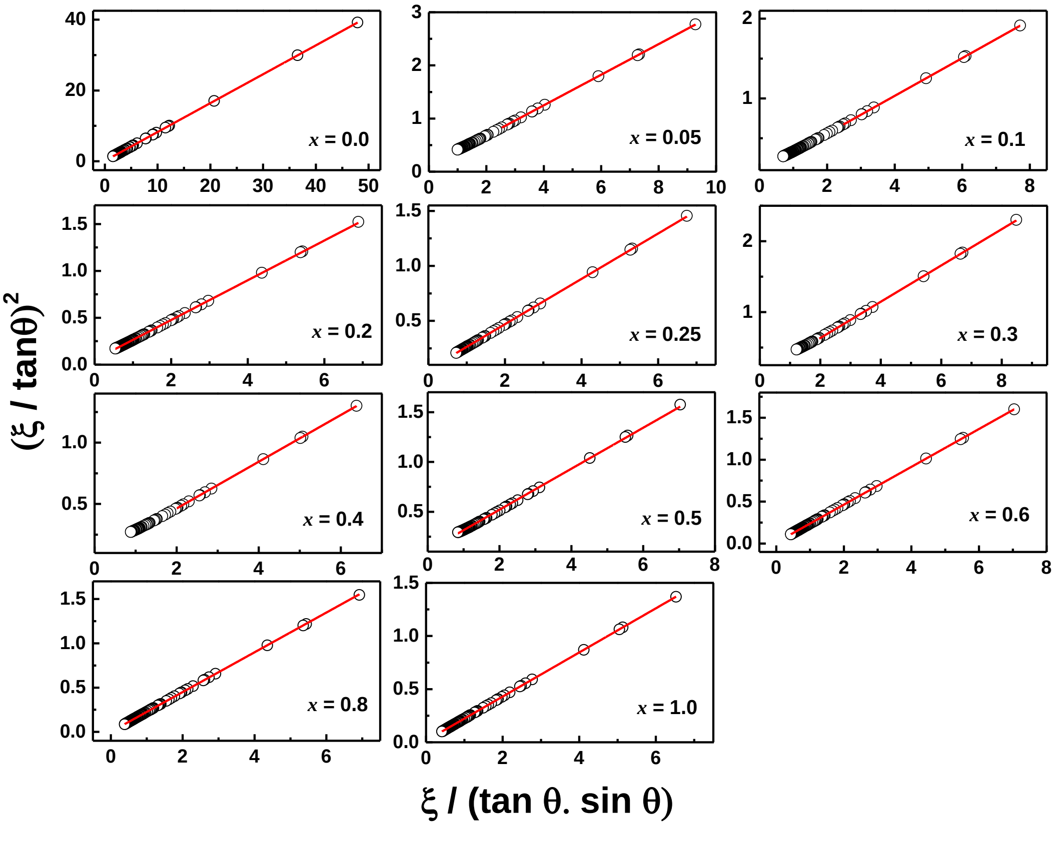

Figure 3.9. The linear Halder-Wagner plots for $Lu_{1-x}Ho_xFeO_3$ $(0 \leq x \leq 1)$ nanoparticles.

3.3.5. Density calculation:

The density measurement is an important part of characterizing a ceramic sample to know the porosity of the sintered pellets. The weight of the $Lu_{1-x}Ho_xFeO_3$ ($0 \leq x \leq 1$) pellets sintered at 750°C at 8 hours is measured in air using a physical balance. Then each pellet is suspended in a beaker of water. The pellets are immersed in water and waited for enough time until all the air bubbles disappear [30,31]. According to Archimedes principle, the experimental density of the pellet can be calculated by equation,

$$\rho_{exp} = \frac{w_a}{w_a - w_{liq}} \rho_{liq} \qquad eqn\ (3.15)$$

Where w_a is weight of the pellet in air, w_{liq} is weight of the pellet in liquid and ρ_{liq} is density of water (0.997 g/m^3). The theoretical density is calculated by

$$\rho_{theo} = \frac{m}{V} = \frac{Atomic\ mass\ of\ Lu_{1-x}Ho_xFeO_3}{a*b*c} \qquad eqn\ (3.16)$$

After calculating the experimental and theoretical density, the relative density is calculated by using equation,

$$Relative\ density = \frac{\rho_{exp}}{\rho_{theo}} \times 100 \qquad eqn\ (3.17)$$

The calculated relative density for $Lu_{1-x}Ho_xFeO_3$ ($0 \leq x \leq 1$) pellets are found to vary between 91.5 to 93.5 %.

3.4. Surface morphology and microstructure

The surface morphology of the samples was examined by FESEM operating at an applied voltage of 5 kV. The microstructural images are shown in figure 3.10. The FESEM images reveal the existence of particles with well-defined boundaries at the pellet surface. The particle-size distributions of $Lu_{1-x}Ho_xFeO_3$ ($0 \leq x \leq 1$) are shown in figure 3.10. The particle sizes in all the samples were measured using ImageJ software. The data have been fitted to a lognormal distribution to obtain the average particle size and the full width at half maximum (FWHM). It is observed from figure 3.11 that the particle-size histograms are described well by the lognormal distribution. The average particle sizes for different *x* are listed in Table 3.2 (a). The average particle size, so obtained from the log-normal distribution is plotted as a function of *x* (figure 3.12) and it is found to be maximum for x = 0.4. The dotted line through the data points is only guide to the eye.

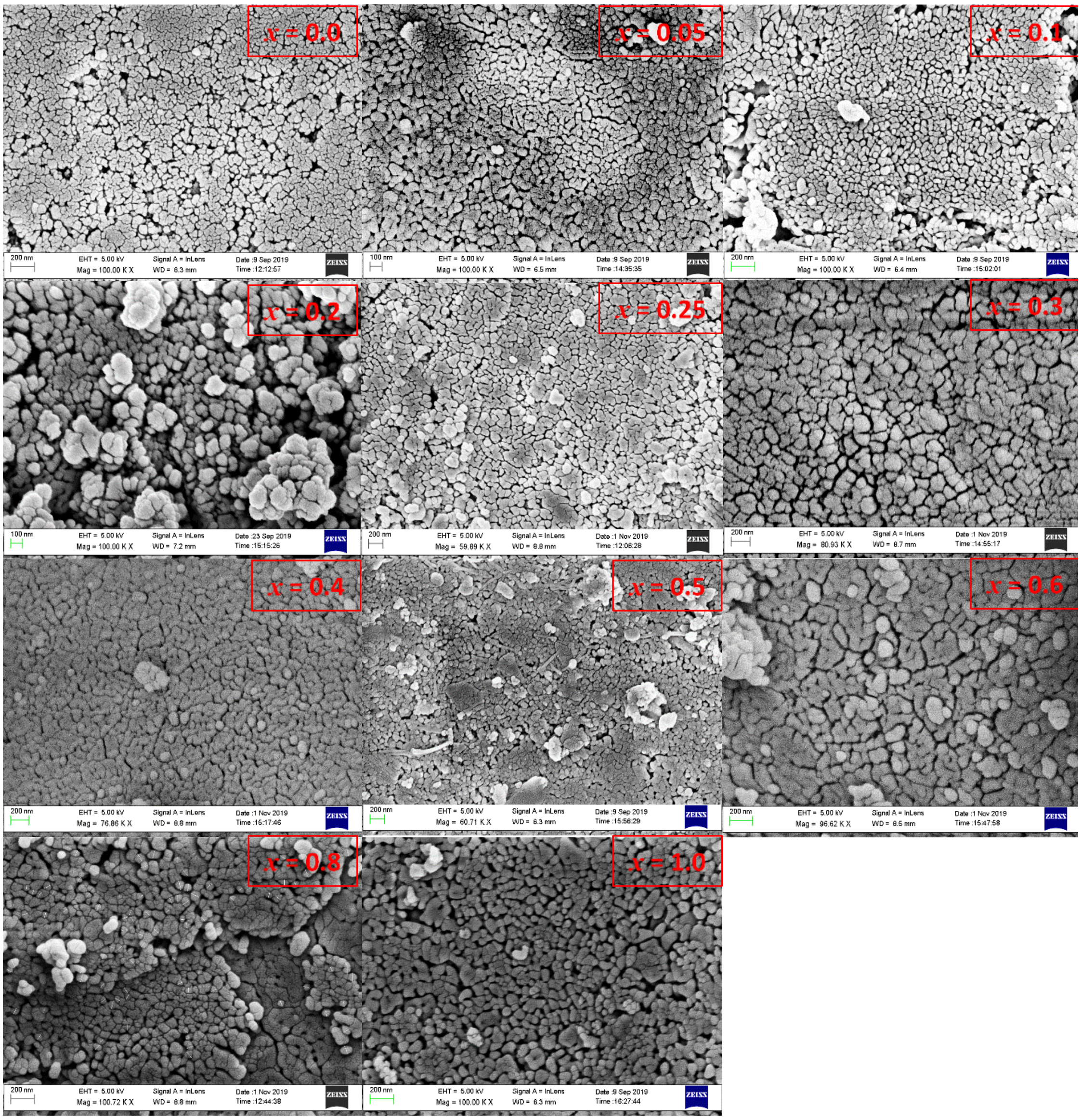

Figure 3.10. FESEM images of $Lu_{1-x}Ho_xFeO_3$ ($0 \leq x \leq 1$)

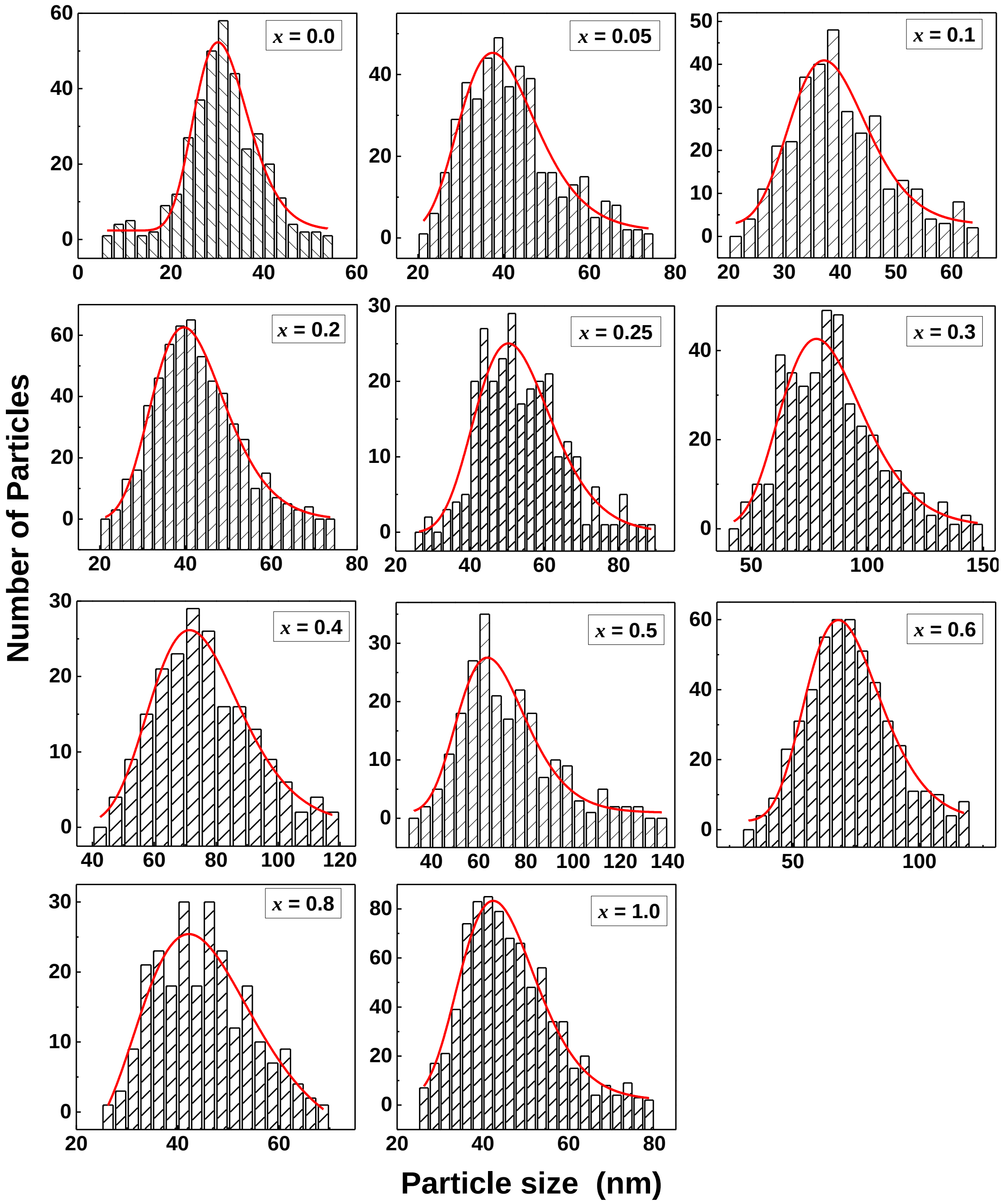

Figure 3.11. Grain size distribution of $Lu_{1-x}Ho_xFeO_3$ ($0 \leq x \leq 1$)

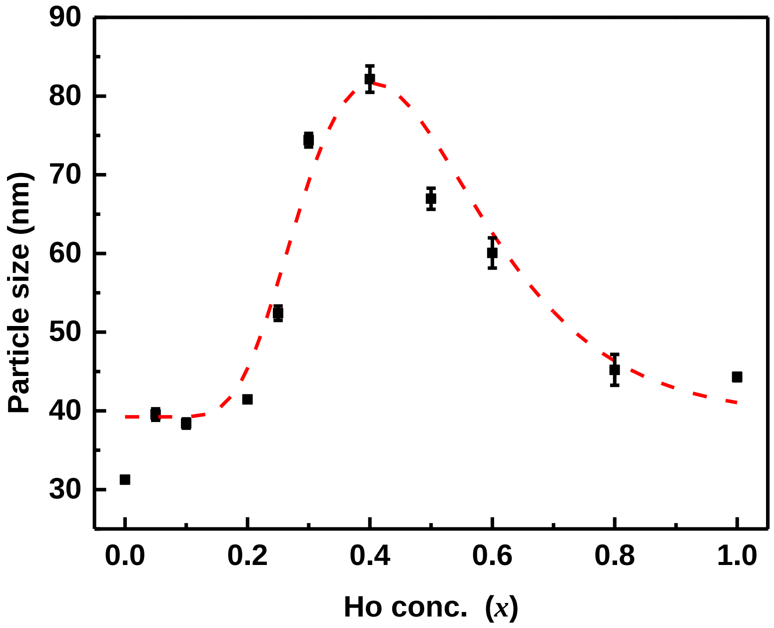

Figure 3.12. Particle size as a function of Ho concentration, *x*.

3.5. Raman spectroscopy

Raman spectra of the pellets of $Lu_{1-x}Ho_xFeO_3$ with $x = 0.0$, 0.05, 0.1, 0.2, 0.25, 0.3, 0.4, 0.5, 0.6, 0.8 and 1.0 (sintered at 750˚C for 8 hours), displayed in figure 3.16, were recorded at room temperature over the wavenumber range extending from 45 cm^{-1} to 800 cm^{-1} on LabRam HR Evolution (HORIBA Scientific) spectrometer that makes use of a 532 nm diode laser with the power level set at 5 mW for 150 seconds. From the Raman scattering experiments carried out at different laser power levels, we find that 5 mW power is low enough to ensure that no overheating of, or damage to, the sample occurs. A microscope with magnification ×50 was used for taking these Raman spectra. The line shapes of the peaks in the Raman spectra are found to be represented well by multiple Lorentzians (red curves through the data (blue open circles) in figure 3.13). Such fits enable a precise determination of the positions, integrated intensities and widths of the Raman peaks. From symmetry considerations, group theory predicts that the hexagonal ($P6_3cm$) structure in $LuFeO_3$ supports 38 RA modes ($\Gamma_H = 9A_1 + 14E_1 + 15E_2$) [32,33], whereas the orthorhombic (Pnma) structure in both $LuFeO_3$ ($x = 0$) and $HoFeO_3$ ($x = 1$) sustains 24 RA modes ($\Gamma_O = 7A_g + 5B_{1g} + 7B_{2g} + 5B_{3g}$) [34–36]. Since Fe^{3+} ions occupy the sites with inversion symmetry in Pnma crystal structure, the vibration modes that include displacements of Fe^{3+} ions are not Raman-active.

3.5.1. Phase confirmation

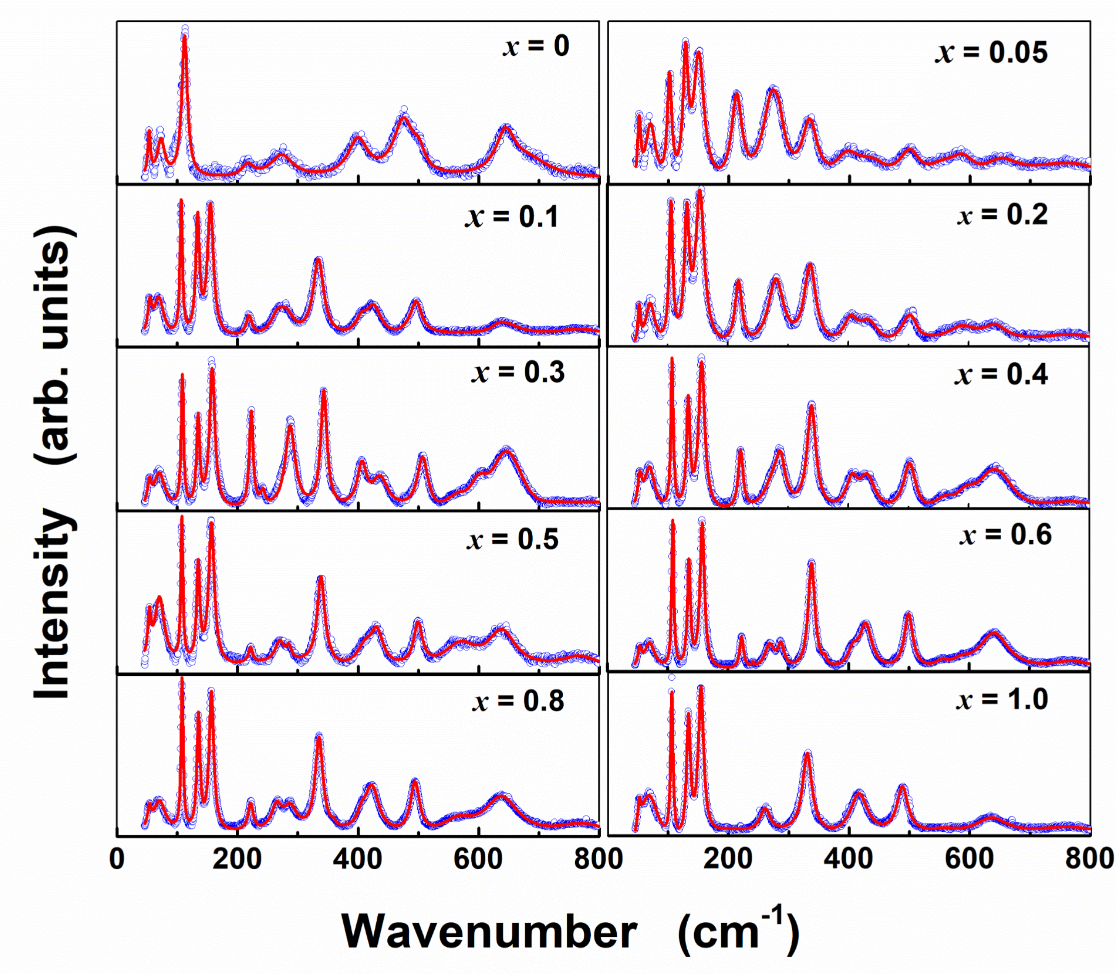

Figure 3.13. Raman intensity plotted against wavenumber over the range from 45 to 800 cm^{-1} for $Lu_{1-x}Ho_xFeO_3$ (x = 0.0 to 1.0) and the multiple Lorentzian fits (red curves) to the data (blue open circles).

The peak positions correspond to Raman-active (RA) vibrational/rotational modes. The Raman modes, so obtained, for hexagonal (H-) and orthorhombic (O-) LFO (x = 0.0, 0.05) are listed in Table 3.3 while those for orthorhombic $Lu_{1-x}Ho_xFeO_3$ (x = 0.05 - 1.0) are tabulated in Table 3.4. The wavenumbers for the Raman-active modes in hexagonal or orthorhombic $LuFeO_3$ and orthorhombic $HoFeO_3$ obtained previously from experiments [36][35] together with those yielded by the density functional theory (DFT) calculations [34] are included in the Tables 3.3 and 3.4 for comparison. Following the assignment of different Raman modes made earlier by Weber et al. [23][37], the main atomic motion associated with a given mode (observed in this work) is also highlighted in the last column of Table 3.4.

Only 9 RA modes are observed for $x = 0$. Among them, 6 RA modes belong to hexagonal phase of $LuFeO_3$ and the one (273 cm^{-1}) is characteristic of the orthorhombic $LuFeO_3$ phase. Apart from these RA modes, two new Raman modes at ≈ 53 cm^{-1} and 69 cm^{-1} (not reported so far) are observed in $LuFeO_3$. These modes are present in all the samples with Ho concentration ranging from $x = 0$ to $x = 1$. For 5 at.% Ho doping ($x = 0.05$), 12 modes are observed. Most of the Raman modes for the hexagonal phase have values not very different from those for the orthorhombic phase. However, the RA mode with wavenumber ≈ 475 cm^{-1}, which is exclusive to the hexagonal structure (observed in $x = 0$) is completely absent in the $x = 0.05$ sample, indicating that 5 at.% Ho solute concentration suffices to stabilize the orthorhombic structure, in agreement with the XRD results. By comparison, RA modes from orthorhombic phases of both $LuFeO_3$ and $HoFeO_3$ are observed in the samples with higher Ho concentrations ($x \geq 0.1$).

Consistent with the conclusion drawn from the Rietveld refinement of the XRD data that the $Lu_{1-x}Ho_xFeO_3$ samples, annealed at 750°C for 8 hours, do not contain Fe_3O_4 or Fe_2O_3 impurity phase, the RA modes at wavenumbers 300 cm^{-1}, 540 cm^{-1}, 669 cm^{-1}, characteristic of Fe_3O_4 phase [38], are completely absent (figure 3.13). The same is true for the Fe_2O_3 phase as well. XRD and Raman scattering data thus completely rule out the presence of these impurity phases.

3.5.2. Observation of two new modes

Use of high-resolution Raman spectrometer, enabled the observation of the two well-resolved new RA modes at ≈ 53 and ≈ 69 cm^{-1} in the wavenumber regime below 100 cm^{-1}, clearly seen in figure 3.13. These modes were neither predicted by the DFT calculations [23,34] nor observed in previous Raman scattering experiments [23,34–36] on $RFeO_3$ orthoferrites including $HoFeO_3$ [35] and $LuFeO_3$ [36]. The existence of new RA modes only in the nanocrystalline samples but not in the bulk counterparts strongly suggests that the origin of these additional RA modes lies in the breaking of symmetry at the surfaces, interfaces and boundaries of nanocrystalline particles. Compared to the symmetric phonon modes A_g, the new RA modes, involving asymmetric vibrations of R^{3+} ions across the surfaces/interfaces/boundaries, cause relatively small changes (higher-order effect) in electric polarizability and hence yield Raman lines of intensity weaker than those corresponding to the A_g phonon modes. This is evident from the Raman spectra shown in figure 3.14.

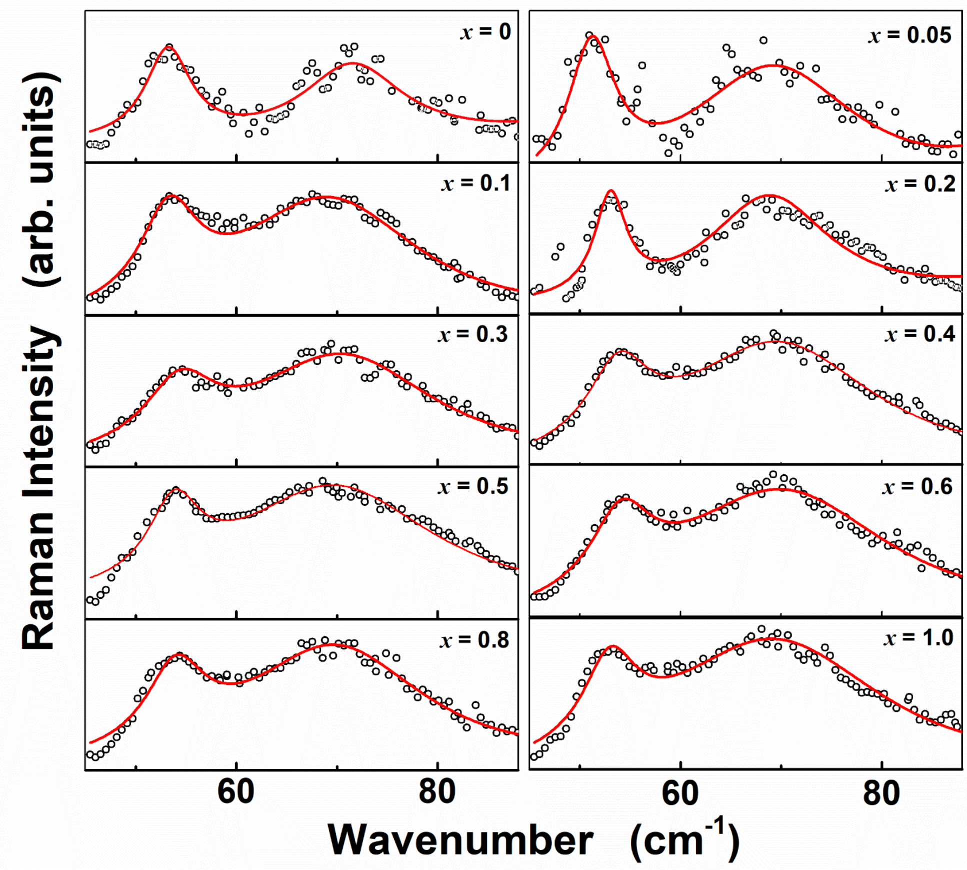

Figure 3.14. The Lorentzian fits to the Raman spectra over the wavenumber range 45 - 90 cm^{-1}.

3.5.3. Effect of Ho doping on Raman modes

In order to bring out clearly the evolution of the Raman-active modes as the Ho concentration x increases from x = 0.05 to x = 1.0 in orthorhombic $Lu_{1-x}Ho_xFeO_3$, the observed Raman modes are individually plotted against Ho concentration x in the (a) and (b) parts of figure 3.15. These sub-figures present the following salient features. For the Raman modes ranging from ≈ 50 to ≈ 250 cm^{-1} (i.e., the modes at ≈ 53 and 69 cm^{-1}, $A_g(1)$, $A_g(2)$, $B_{2g}(2)$, B_{2g} in figure 3.17(a)) and the $A_g(4)$ mode at ~ 335 cm^{-1} (figure 3.15(b)), the wavenumbers 'n' for different x, $n(x)$, corresponding to a given Raman-active mode, go through a broad peak as a function of x at x_{max} ≈ 0.6. By contrast, the RA modes $A_g(3)$, $A_g(5)$, $A_g(6)$, $A_g(7)$ and $B_{3g}(5)$ continuously shift to lower wavenumbers as x increases from 0.05 to 1.0 (figure 3.15(b)).

To unravel the genesis of the Ho doping-induced shift in the wavenumber corresponding to a given RA vibrational mode, we make use of the harmonic oscillator approximation, which relates the vibration frequency (ω) of an atom, belonging to a crystalline structure, to the force constant k and the reduced mass m of the vibrating atom, as $\omega = (k / m)^{1/2}$. Thus, if this approximation holds, the heaviest atom should vibrate at the lowest frequency (wavenumber) and lower the force constant, lower the vibration frequency. In conformity with this expectation, the Raman modes below 250 cm^{-1} (i,e., those at ≈ 53, 69, 107, 133, 155 and 220 cm^{-1}, shown in Figure 3.15(a)) involve primarily the vibrations of heavy rare-earth atoms whereas those ($A_g(3)$ - $A_g(7)$ and $B_{3g}(5)$) with n above ≈ 270 cm^{-1} (i.e., $n \approx$ 284, 337, 405, 429, 499 and 643 cm^{-1} in figure 3.15(b)) have their origin in the FeO_6 octahedra rotation/breathing, $O_1(x)$, $R(-x)$ vibrations (where $O_1 \equiv O(1)$), Fe-O(2) stretching and O(1)-Fe-O(2) scissor-like bending. Note that all these modes are associated with the displacements of oxygen atoms. This assignment of Raman modes is consistent with the general rule that the RA modes that appear below ≈ 300 cm^{-1} pertain to the heavier rare-earth (R) atoms, whereas the vibration modes of lighter oxygen atoms account for the modes above ≈ 300 cm^{-1}.

As the Ho concentration x increases, the reduced mass, m_R, of the rare-earth atoms diminishes and the R-O bond lengths increase due to the higher ionic radius of Ho^{3+}. Considering that the R-O (so also the Fe-O) bonds in $RFeO_3$ are primarily ionic in nature, an increase in the R-O (Fe-O) bond lengths reduces the force constant and shifts the Raman vibrational mode to lower wavenumbers. While a decrease in m_R shifts the Raman mode to higher wavenumbers, an increase in the R-O bond lengths shifts the Raman mode to lower wavenumbers. In an attempt to estimate the contributions made by the changes in m_R and bond length (l) (brought about by the variation in x) to the Raman shifts, we assume that the force constant $k \sim l^{-1}$. Thus, in the harmonic oscillator approximation, the frequency shifts in the R-related vibrational modes should be given by $\omega \sim (l_R\, m_R)^{-1/2}$ whereas such shifts in the RA vibrational modes, associated with oxygen atom displacements, are governed by the relevant bond lengths (l_O) alone since the mass of the oxygen atoms (m_O) does not get affected by the Ho substitution, i.e., in this case, $\omega \sim l_O^{\,-1/2}$.

In order to facilitate a quantitative comparison between the observed Raman shifts and those predicted by these relations, the wavenumber $n(x)$, reduced mass $m(x)$ and bond length $l(x)$ data are normalized to their respective values at $x = 0.05$. These normalized quantities, for a few representative Raman modes, are plotted against the Ho concentration, x, in figure

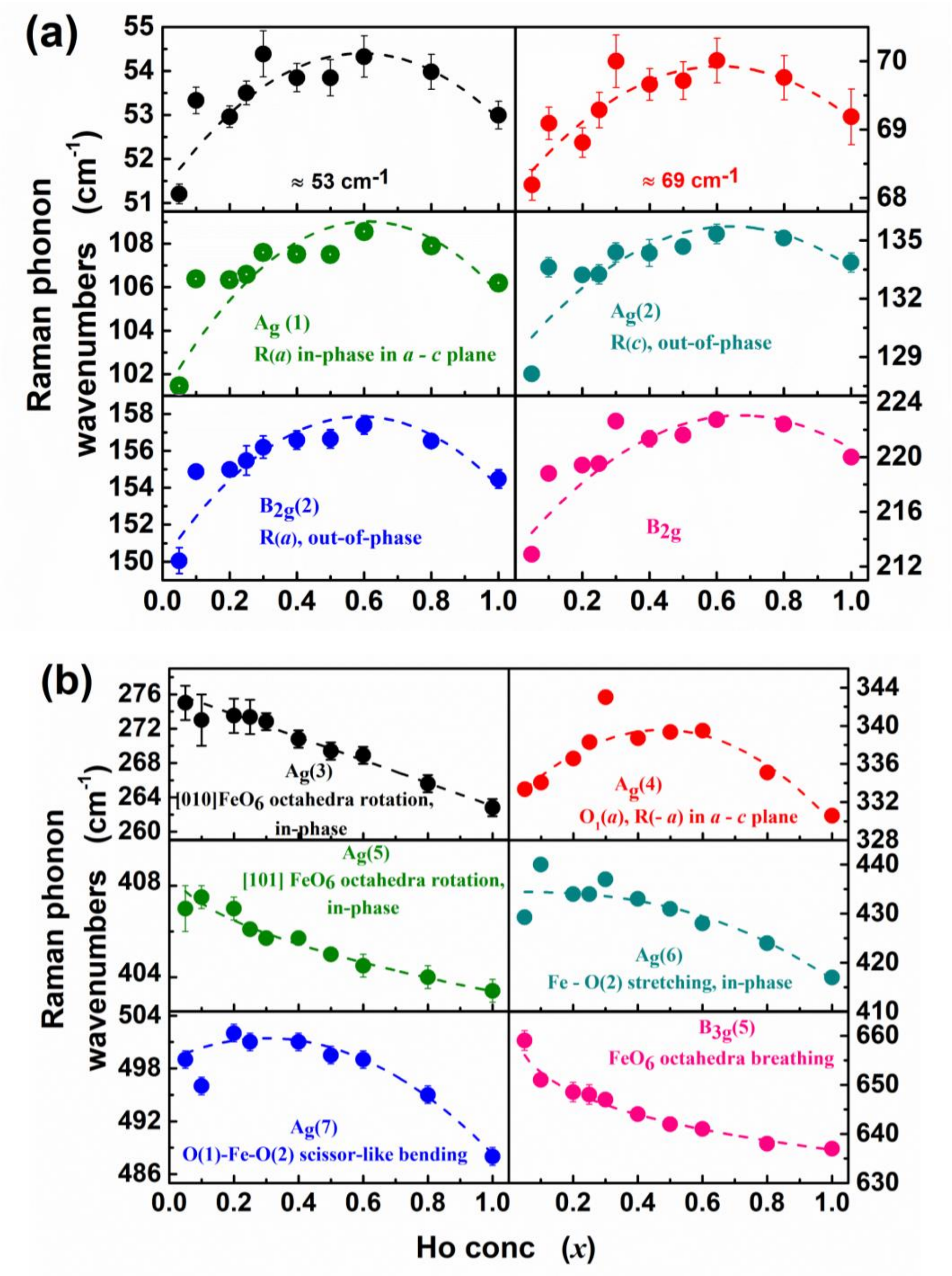

Figure 3.15. Raman modes, observed over the wavenumber range (a) 50 - 250 cm^{-1}, (b) 270 - 650 cm^{-1}, as functions of *x*. The dashed curves (designating the polynomial fits) through the data points (symbols) serve as a guide to the eye.

3.16. For a correct interpretation of the data presented in figure.3.16, it is important to recall that the bond lengths relevant to the RA *vibrational* modes $A_g(1)$, $A_g(2)$, $B_{2g}(2)$, $A_g(4)$, $A_g(6)$ and $B_{3g}(5)$ are R(*a*) ≡ R – O(2) (intraplanar) along *a*-axis, R(*c*) ≡ R – O(2) (intraplanar) along *c*-axis, R(*a*) ≡ R – O(2) (intraplanar) along *a*-axis, O(1) - R (interplanar), Fe – O(2) (interplanar) and Fe – O(1) (intraplanar), respectively; refer to the last column of Table 3.4 and figure.3.6 (b).

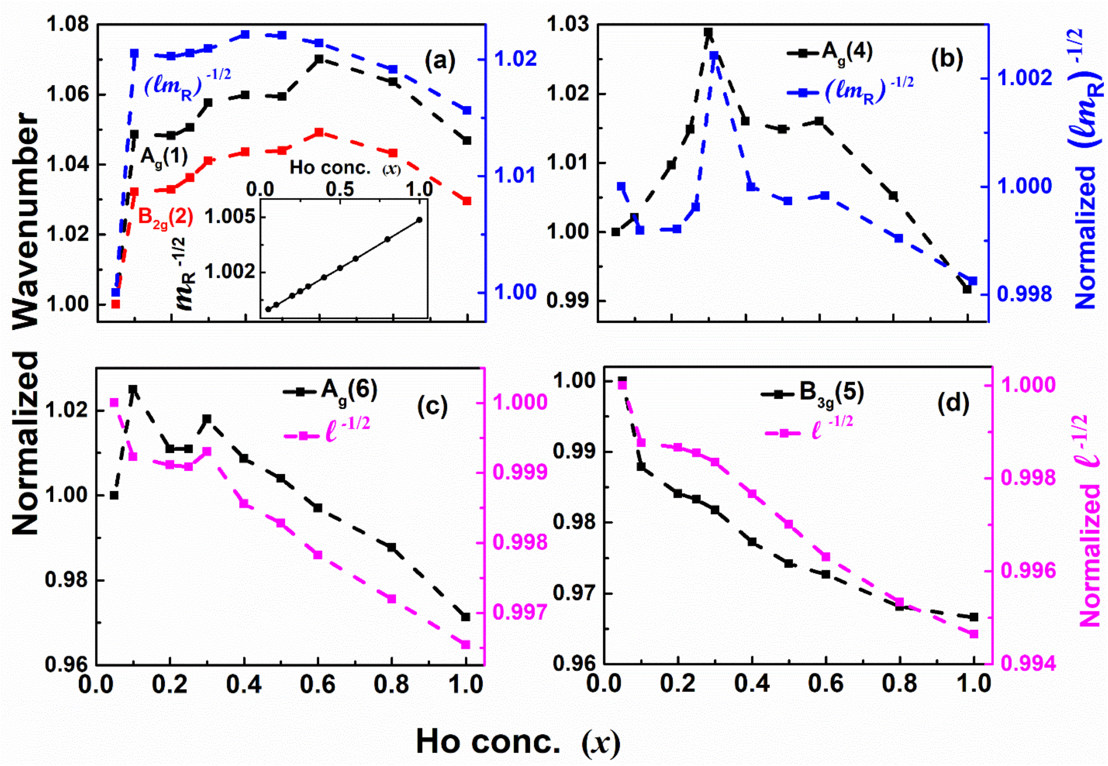

Figure 3.16: The normalized wavenumber (1/square root of the reduced mass of the rare earth atom, $m_R^{-1/2}$, in the inset of panel 8(a)) and square root of the inverse bond length ($l^{-1/2}$) as functions of the Ho concentration, *x*, for the Raman-active *vibrational* modes: (a) $A_g(1)$ and $B_{2g}(2)$, (b) $A_g(4)$, (c) $A_g(6)$ and (d) $B_{3g}(5)$.

From figure.3.16, we infer the following. So far as the shifts in the Raman modes, caused by the change in the Ho concentration, are concerned, (i) a mere increase in $m_R^{-1/2}$ of ~ 0.5 % (inset of figure 3.16(a)) over the entire Ho concentration range (x = 0.0 to 1.0) is practically *of no consequence* and (ii) the bond length contributions $l_R^{-1/2}$ and $l_O^{-1/2}$ correctly capture the overall functional dependence of the R-related and O-related Raman shifts on x but fall short of the observed shifts by an order of magnitude. A striking resemblance between the wavenumber versus x curves of the vibrational modes $A_g(1)$ and $B_{2g}(2)$ (figure 3.16(a)), which involve the same bond length $R(a)$, lends firm support to the inference (ii). To get rid of the discrepancy between the observed and calculated Raman shifts, one probably has to go beyond the harmonic oscillator description and/or to suitably modify the simplistic $k \sim l^{-1}$ relation between k and l. At this stage, it should be emphasized that the above considerations are not applicable to the Raman soft modes $A_g(3)$ and $A_g(5)$, which are basically controlled by the FeO_6 octahedra tilt/rotation angles, as elucidated below.

3.5.4. Evolution of soft modes

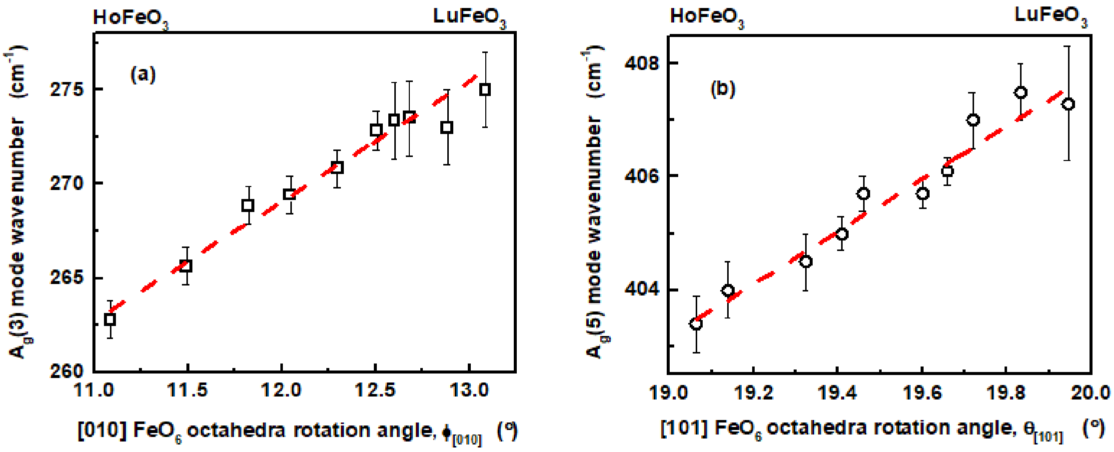

Figure 3.17 (a) The $A_g(3)$ Raman soft mode wavenumbers plotted against the FeO_6 octahedra tilt/rotation angle $\varphi_{[010]}$; (b) The $A_g(5)$ Raman soft mode wavenumbers plotted against the FeO_6 octahedra tilt/rotation angle $[\theta_{[101]}]$.

Figure 3.17 displays the roughly linear decline in the FeO_6 octahedra tilt/rotation angles $\theta_{[101]}$ and $\varphi_{[010]}$ (around $[101]_{pc}$ and $[010]_{pc}$ pseudo-cubic (pc) axes) with increasing Ho concentration, x. The octahedra tilt/rotation angles are basically controlled by eightfold coordination R^{3+} ionic radius and hence decrease monotonously as the ionic radius increases *linearly* from 0.977 Å for Lu^{3+} to 1.015 Å for Ho^{3+}. Following the approach adopted by Weber et al. [23][37], the $A_g(3)$ $[A_g(5)]$ Raman soft mode wavenumbers for various x are plotted against the FeO_6 octahedra tilt/rotation angle $\varphi_{[010]}$ $[\theta_{[101]}]$ in figure 3.17(a) [figure.3.17(b)]. For the compounds belonging to the $RFeO_3$ orthoferrite family, a *linear* increase in the $A_g(3)$ $[A_g(5)]$ wavenumbers, corresponding to different $RFeO_3$ compounds, with increasing $\varphi_{[010]}$ $[\theta_{[101]}]$ has been observed [23][37]. In accordance with this observation, we find that the $A_g(3)$ versus $\varphi_{[010]}$ and $A_g(5)$ versus $\theta_{[101]}$ plots for $Lu_{1-x}Ho_xFeO_3$, with x ranging from 0.05 to 1.0, are *linear*. A direct proportionality between the octahedra tilt/rotation angle and the corresponding frequency/wavenumber of the soft Raman mode is expected only when the soft modes are completely independent of each other without any (mixing) influence from the neighbouring soft modes. The presence of independent $A_g(3)$ and $A_g(5)$ soft RA modes in both pure (undoped) $RFeO_3$ and mixed $Lu_{1-x}Ho_xFeO_3$ compounds is thus clearly borne out by the observations made earlier [23][37] and in this work, respectively.

Table 3.3. Comparison of the observed Raman mode wavenumbers in cm^{-1} for hexagonal (H) $LuFeO_3$ (H-LFO) with those reported in reference [20] . The numbers in the parentheses denote uncertainty in the least significant figure. O stands for the orthorhombic phase.

H-LFO	***x* = 0**		***x* = 0.05**	
Ref [20]	**RA modes (cm^{-1})**	**Phase**	**RA modes (cm^{-1})**	**Phase**
	53.2 (2)		51.2 (2)	
	71.6 (5)		68.1 (4)	
110	112.0 (1)	H	101.5 (5)	O
			128.1 (3)	O
			150.0 (7)	O
223	217.3 (3)	O, H	212.9 (2)	O
268	273.3 (8)	O	275 (2)	O
			333.3 (2)	O
404	399.7 (5)	O, H	407 (1)	O
			429.3 (8)	O
473	475.1 (8)	H		
501	500.7 (12)	O, H	499 (1)	O. H
651	644.7 (4)	O. H	659 (2)	O, H

Table 3.4. The observed Raman-active modes in Lu_{1-x} Ho_xFeO_3 and those reported in the references [36]-[27] for orthorhombic $LuFeO_3$ and $HoFeO_3$. The abbreviations E-, T- and GT stand respectively for experiment, theory and group-theoretical notations for Raman modes. The numbers in the parentheses denote uncertainty in the least significant figure. O stands for the orthorhombic phase.

LFO E- [23]	**LFO T- [25]**	**HFO E- [24]**	**HFO T- [25]**	**GT**	**Ho doping concentration (at. %)**										**Main atomic motion [27]**
					0.05	**0.1**	**0.2**	**0.25**	**0.3**	**0.4**	**0.5**	**0.6**	**0.8**	**1.0**	
					51.2 (2)	53.2 (2)	53.0 (2)	53.5 (2)	53.4 (6)	53.8 (4)	53.8 (4)	53.3 (4)	53.9 (4)	52.9 (4)	-
					68.1 (4)	69.0 (4)	68.8 (4)	69.3 (6)	70.3 (8)	69.6 (4)	69.7 (6)	70.0 (6)	69.8 (6)	69.2 (8)	-
110	110 106	109	111 108	$A_g(1)$ $B_{2g}(1)$	101.5 (5)	106.4 (3)	106.3 (5)	106.6 (4)	107.6 (3)	107.5 (5)	107.5 (3)	108.6 (5)	107.9 (5)	106.2 (2)	R(*a*), in-phase in *a* - *c* plane R(*c*), in-phase in *a* - *c* plane, out-of-phase in *b*
136	133 118	139	135 133	$A_g(2)$ $B_{3g}(1)$	128.1 (3)	133.6 (5)	133.2 (2)	133.2 (5)	134.4 (5)	134.3 (7)	134.7 (3)	135.3 (5)	135.1 (3)	133.9 (5)	R(*c*), out-of-phase R(*b*), out-of-phase in *a* - *c* plane and in *b*
158	161	159	161	$B_{2g}(2)$	150.0 (7)	154.9 (2)	155.0 (2)	155.4 (8)	156.2 (6)	156.6 (5)	156.6 (5)	157.4 (5)	156.5 (3)	154.5 (5)	R(*a*), out-of-phase
		210		B_{2g}	212.9 (2)	218.7 (4)	219.4 (1)	219.5 (4)	222.6 (4)	221.3 (6)	221.6 (2)	222.7 (4)	222.4 (2)	220.0 (4)	-
278	277	270	270	$A_g(3)$	275 (2)	273 (3)	273 (2)	273 (2)	288.2 (1)	287.1 (0)	284.2 (0)	288.0 (0)	286.5 (0)	280.5 (3)	[010] FeO_6 octahedra rotation, in-phase
350	343	340	337	$A_g(4)$	333.3 (2)	334.0 (2)	336.6 (5)	338.3 (2)	343.0 (2)	338.7 (6)	336.5 (2)	335.7 (4)	335.1 (2)	330.6 (2)	$O_1 \equiv O$ (1); O_1 (*a*), R(-*a*) in *a* - *c* plane

	340		321	B_{2g}(3)											[101] FeO_6 octahedra rotation, in-phase
	413 410		400 407	A_g(5) B_{1g}(3)	407 (1)	407.5 (5)	407.0 (5)	406.1 (3)	405.7 (3)	405.7 (3)	405.0 (3)	404.5 (5)	404.0 (5)	403.4 (5)	[101] FeO_6 octahedra rotation, in-phase [101] FeO_6 octahedra rotation, out-of-phase
427	460 423	425	430 414	A_g(6) B_{3g}(4)	429.3 (8)	440 (1)	434 (1)	434 (1)	437 (1)	433 (1)	431 (1)	428 (1)	424 (1)	417 (1)	Fe – O (2) stretching, in-phase O(2)-Fe-O(2) scissor-like bending, out-of-phase
516	517 503	495	494 490	A_g(7) B_{2g}(5)	499 (1)	496 (1)	502 (1)	501 (1)	507 (1)	501 (1)	499.5 (9)	499 (1)	495 (1)	488 (1)	O(1)-Fe-O(2) scissor-like bending O(1)-Fe-O(2) scissor-like bending
654		660		B_{3g}(5)	659 (2)	651 (1)	648 (2)	648 (2)	647 (1)	644 (1)	642 (1)	641 (1)	638 (1)	637 (1)	FeO_6 octahedra breathing

3.6. Summary

In this chapter, an extensive investigation of structural and Raman scattering properties has been carried out at room temperature on nanocrystalline $Lu_{1-x}Ho_xFeO_3$ ($0 \leq x \leq 1$) orthoferrite synthesized by hydrothermal method. Rietveld refinement of the room temperature x-ray diffraction (XRD) data yielded precise values of phase fractions, the lattice parameters a, b, c, bond lengths and bond angles. The lattice parameters are used to calculate the FeO_6 octahedral tilt angles $\theta_{[101]}$ and $\varphi_{[010]}$ around $[101]_{pc}$ and $[010]_{pc}$ pseudo-cubic (pc) axes and the attendant orthorhombic deformation (D) in the crystal structure, both caused by the size of R^{3+} ions. The Raman modes specific to the rotation of FeO_6 octahedra assert that 5 at.% Ho ($x = 0.05$) solute concentration suffices to stabilize the orthorhombic structure at the cost of the hexagonal structure prevalent in the $LuFeO_3$ host.

In addition to the Raman-active modes $A_g(1)$ - $A_g(7)$, $B_{2g}(2)$ and $B_{3g}(5)$, reported previously in the end compounds (crystalline bulk) $LuFeO_3$ and $HoFeO_3$, we observe two new Raman modes at ≈ 53 cm^{-1} and ≈ 69 cm^{-1} in all the compositions ($0 \leq x \leq 1$) in nanocrystalline $Lu_{1-x}Ho_xFeO_3$. These additional RA modes are attributed to the asymmetric vibration of R^{3+} ions across the surfaces/interfaces/boundaries of nanoparticles. The Raman modes below 250 cm^{-1} (i,e., $A_g(1)$, $A_g(2)$, $B_{2g}(2)$ and the new ones at ≈ 53 cm^{-1} and ≈ 69 cm^{-1}) involve primarily the vibrations of heavy rare-earth atoms whereas those ($A_g(3)$ - $A_g(7)$ and $B_{3g}(5)$) with wavenumbers above 270 cm^{-1}, associated with the oxygen atom vibrations/displacements, originate from the FeO_6 octahedra rotation/breathing, O(1) vibration, Fe-O(2) stretching and O(1)-Fe-O(2) scissor-like bending.

As the Ho concentration x increases, the reduced mass, m_R, of the rare-earth atoms decreases while the bond lengths increase due to the higher ionic radius of Ho^{3+}. A decrease in m_R shifts the Raman mode to higher wavenumbers, whereas an increase in the R-O and Fe-O bond lengths shifts the Raman mode to lower wavenumbers. We demonstrate that the contribution to the Raman shifts due to the variations in the R-O/Fe-O bond lengths with x primarily governs the observed functional dependence of the Raman mode wavenumber on x; the m_R-induced Raman shifts are too weak to be visible. The RA mode $A_g(3)$ [$A_g(5)$] wavenumber increases linearly with the FeO_6 octahedra tilt angle $\varphi_{[010]}$ [$\theta_{[101]}$] indicating that these independent modes are sensitive to orthorhombic distortion.

References

[1] S. Cao, X. Zhang, K. Sinha, W. Wang, J. Wang, P.A. Dowben, X. Xu, Phase separation in LuFeO3 films, Appl. Phys. Lett. 108 (2016). https://doi.org/10.1063/1.4950991.

[2] W. Wang, J. Zhao, W. Wang, Z. Gai, N. Balke, M. Chi, H.N. Lee, W. Tian, L. Zhu, X. Cheng, D.J. Keavney, J. Yi, T.Z. Ward, P.C. Snijders, H.M. Christen, W. Wu, J. Shen, X. Xu, Room-temperature multiferroic hexagonal LuFeO3 films, Phys. Rev. Lett. 110 (2013) 1–5. https://doi.org/10.1103/PhysRevLett.110.237601.

[3] W. Eerenstein, N.D. Mathur, J.F. Scott, Multiferroic and magnetoelectric materials, Nature. 442 (2006) 759–765. https://doi.org/10.1038/nature05023.

[4] S.M. Disseler, X. Luo, B. Gao, Y.S. Oh, R. Hu, Y. Wang, D. Quintana, A. Zhang, Q. Huang, J. Lau, R. Paul, J.W. Lynn, S.W. Cheong, W. Ratcliff, Multiferroicity in doped hexagonal LuFe O3, Phys. Rev. B - Condens. Matter Mater. Phys. 92 (2015) 1–9. https://doi.org/10.1103/PhysRevB.92.054435.

[5] U. Chowdhury, S. Goswami, D. Bhattacharya, J. Ghosh, S. Basu, S. Neogi, Room temperature multiferroicity in orthorhombic LuFeO3, Appl. Phys. Lett. 105 (2014) 10–14. https://doi.org/10.1063/1.4892664.

[6] R.L. White, Review of recent work on the magnetic and spectroscopic properties of the rare-earth orthoferrites, J. Appl. Phys. 40 (1969) 1061–1069. https://doi.org/10.1063/1.1657530.

[7] U. Chowdhury, S. Goswami, D. Bhattacharya, S.S. Rajput, A.K. Mall, A. Garg, R. Gupta, S.D. Kaushik, V. Siruguri, S. Saravanakumar, S. Israel, R. Saravanan, T. Chatterji, Origin of Ferroelectricity in Orthorhombic LuFeO$_3$, (2017) 1–12. http://arxiv.org/abs/1710.02381.

[8] S. Leelashree, S. Srinath, Investigation of Structural, Ferroelectric, and Magnetic Properties of La-Doped LuFeO 3 Nanoparticles, J. Supercond. Nov. Magn. (2019). https://doi.org/10.1007/s10948-019-5114-4.

[9] S. Leelashree, P.D. Babu, S. Srinath, Effect of la doping on dielectric and magnetic properties of room temperature multiferroic LuFeO3, AIP Conf. Proc. 1953 (2018) 3–7. https://doi.org/10.1063/1.5033141.

[10] N. Kimizuka, A. Yamamoto, H. Ohashi, T. Sugihara, T. Sekine, The stability of the phases in the Ln2O3FeOFe2O3 systems which are stable at elevated temperatures (Ln: Lanthanide elements and Y), J. Solid State Chem. 49 (1983) 65–76. https://doi.org/10.1016/0022-4596(83)90217-7.

[11] L. Zhang, X.M. Chen, Dielectric relaxation in LuFeO3 ceramics, Solid State Commun. 149 (2009) 1317–1321. https://doi.org/10.1016/j.ssc.2009.05.036.

[12] X.P. Yuan, Y.K. Tang, Y. Sun, M.X. Xu, Structure and magnetic properties of Y 1-xLu xFeO 3 ($0 \leq x \leq 1$) ceramics, J. Appl. Phys. 111 (2012) 1–6. https://doi.org/10.1063/1.3691243.

[13] W. Zhu, L. Pi, S. Tan, Y. Zhang, Anisotropy and extremely high coercivity in weak ferromagnetic LuFeO 3, Appl. Phys. Lett. 100 (2012) 4–8. https://doi.org/10.1063/1.3681789.

[14] H.W. King, Y. Lo Vegard, Yon Lo Vegard., J. Mater. Sci. 1 (1921) 79–90.

[15] C.P. Kempter, Vegard’s “law,” Phys. Status Solidi. 18 (1966) K117–K118. https://doi.org/10.1002/pssb.19660180251.

[16] S. Mukherjee, V. Ranjan, R. Gupta, A. Garg, Composition Dependence of Structural Parameters and Properties of Gallium Ferrite, ArXiv Prepr. ArXiv1107.3623. (2011). http://arxiv.org/abs/1107.3623.

[17] Z. Zhou, L. Guo, H. Yang, Q. Liu, F. Ye, Hydrothermal synthesis and magnetic properties of multiferroic rare-earth orthoferrites, J. Alloys Compd. 583 (2014) 21–31. https://doi.org/10.1016/j.jallcom.2013.08.129.

[18] M. Marezio, J.P. Remeika, P.D. Dernier, The crystal chemistry of the rare earth orthoferrites, Acta Crystallogr. Sect. B Struct. Crystallogr. Cryst. Chem. 26 (1970) 2008–2022. https://doi.org/10.1107/s0567740870005319.

[19] P.K. Nielsen, C. Hemmingsen, S.U. Friis, J. Ladefoged, K. Olgaard, Comparison of straight and curled Tenckhoff peritoneal dialysis catheters implanted by percutaneous technique: A prospective randomized study, Perit. Dial. Int. 15 (1995) 18–21. https://doi.org/10.1177/089686089501500104.

[20] S.M. Disseler, J.A. Borchers, C.M. Brooks, J.A. Mundy, J.A. Moyer, D.A. Hillsberry, E.L. Thies, D.A. Tenne, J. Heron, M.E. Holtz, J.D. Clarkson, G.M.

Stiehl, P. Schiffer, D.A. Muller, D.G. Schlom, W.D. Ratcliff, Magnetic structure and ordering of multiferroic hexagonal LuFeO3, Phys. Rev. Lett. 114 (2015) 1–6. https://doi.org/10.1103/PhysRevLett.114.217602.

[21] E. Magome, C. Moriyoshi, Y. Kuroiwa, A. Masuno, H. Inoue, Noncentrosymmetric structure of LuFeO3 in metastable state, Jpn. J. Appl. Phys. 49 (2010). https://doi.org/10.1143/JJAP.49.09ME06.

[22] Y. Zhao, D.J. Weidner, J.B. Parise, D.E. Cox, Thermal expansion and structural distortion of perovskite - data for NaMgF3 perovskite. Part I, Phys. Earth Planet. Inter. 76 (1993) 1–16. https://doi.org/10.1016/0031-9201(93)90051-A.

[23] M.C. Weber, M. Guennou, H.J. Zhao, J. Íñiguez, R. Vilarinho, A. Almeida, J.A. Moreira, J. Kreisel, Raman spectroscopy of rare-earth orthoferrites RFeO3 (R =La, Sm, Eu, Gd, Tb, Dy), Phys. Rev. B. 94 (2016) 1–8. https://doi.org/10.1103/PhysRevB.94.214103.

[24] M. O’Keeffe, B.G. Hyde, Some structures topologically related to cubic perovskite (E 2 1), ReO 3 (D 0 9) and Cu 3 Au (L 1 2) , Acta Crystallogr. Sect. B Struct. Crystallogr. Cryst. Chem. 33 (1977) 3802–3813. https://doi.org/10.1107/s0567740877012114.

[25] R. Delhez, E.J. Mittemeijer, Determination of Crystallite Size and Lattice Distortions through X-Ray Diffraction Line Profile Analysis, Fresenius’ Zeitschrift Für Anal. Chemie. (1982) 1–16.

[26] P. Scherrer, P. Debye, Werk Übergeordnetes Werk, Nachr. Ges. Wiss. Göttingen, Math.-Physik. Klasse. 2 (1918) 101–120. http://eudml.org/doc/59018.

[27] B.E. Warren, B.L. Averbach, The separation of cold-work distortion and particle size broadening in x-ray patterns [1], J. Appl. Phys. 23 (1952) 497. https://doi.org/10.1063/1.1702234.

[28] N.C. Halder, C.N.J. Wagner, Separation of particle size and lattice strain in integral breadth measurements, Acta Crystallogr. 20 (1966) 312–313. https://doi.org/10.1107/s0365110x66000628.

[29] F. Izumi, T. Ikeda, Implementation of the Williamson – Hall and Halder – Wagner Methods into RIETAN-FP, Adv. Ceram. Res. Cent. Annu. Rep. 3 (2014) 33–38.

[30] M. Kaur, S.P. Singh, D.S. Mudahar, G.S. Mudahar, Structural investigation of B 2O 3- Li 2CO 3-Al 2O 3 glasses by molar volume measurements and FTIR spectroscopy, Mater. Phys. Mech. 15 (2012) 66–73.

[31] W.G. Fahrenholtz, Ceramic Engineering 111 Sintering, Univeristy Missouri-Rolla, Ceram. Eng. Dep. (2004) 20.

[32] T. Sarkar, K. Manna, S. Elizabeth, P.S. Anil Kumar, Investigation of multiferroicity, spin-phonon coupling, and unusual magnetic ordering close to room temperature in LuMn0.5Fe0.5O3, J. Appl. Phys. 121 (2017) 0–10. https://doi.org/10.1063/1.4977103.

[33] P. Suresh, K. Vijaya Laxmi, P.S. Anil Kumar, Enhanced room temperature multiferroic characteristics in hexagonal LuFe1−xNixO3 (x = 0 − 0.3) nanoparticles, J. Magn. Magn. Mater. 448 (2018) 117–122. https://doi.org/10.1016/j.jmmm.2017.05.052.

[34] Z.Q. Wang, Y. Mu, Z.Y. Zeng, X.R. Chen, Q.F. Chen, First-principles study of elastic, dielectric, and vibrational properties of orthoferrites RFeO3 (R= Ho, Er, Tm and Lu), Mater. Res. Express. 6 (2019). https://doi.org/10.1088/2053-1591/ab0694.

[35] S. Venugopalan, M. Dutta, A.K. Ramdas, J.P. Remeika, Magnetic and vibrational excitations in rare-earth orthoferrites: A Raman scattering study, Phys. Rev. B. 31 (1985) 1490–1497. https://doi.org/10.1103/PhysRevB.31.1490.

[36] S. Venugopalan, M.M. Becker, Raman scattering study of LuFeO3, J. Chem. Phys. 93 (1990) 3833–3836. https://doi.org/10.1063/1.458768.

[37] M.C. Weber, J. Kreisel, P.A. Thomas, M. Newton, K. Sardar, R.I. Walton, Phonon Raman scattering of RCrO 3 perovskites (R=Y, La, Pr, Sm, Gd, Dy, Ho, Yb, Lu), Phys. Rev. B - Condens. Matter Mater. Phys. 85 (2012) 1–9. https://doi.org/10.1103/PhysRevB.85.054303.

[38] O.N. Shebanova, P. Lazor, Raman spectroscopic study of magnetite (FeFe2O4): A new assignment for the vibrational spectrum, J. Solid State Chem. 174 (2003) 424–430. https://doi.org/10.1016/S0022-4596(03)00294-9.

CHAPTER 4

Nature of magnetism in $Lu_{1-x}Ho_xFeO_3$ $(0 \leq x \leq 1)$

Ho substitution is expected to improve the magnetic properties of the system due to their very high free ion magnetic moment (10.6 μ_B). In this chapter, a detailed analysis of magnetic properties is carried out to bring out the effect of Ho doping in the system.

4.1. Introduction

In this chapter, we have studied the effect of Ho doping on the synthesized $Lu_{1-x}Ho_xFeO_3$ ($x = 0.0$-1.0) nanoparticles. When Ho is progressively substituted for Lu in $LuFeO_3$, ordering of large magnetic moments (10.6 μ_B) of Ho^{3+} ions at low temperatures due to Ho^{3+} - O^{2-} - Ho^{3+} interaction can lead to a substantial enhancement in the ground state magnetic moment while the Ho^{3+}- O^{2-} - Fe^{3+} interaction should considerably increase the reorientation temperature (T_{SR}) of Fe^{3+} spins. Magnetic measurements were performed on the sintered pellets using the Vibrating Sample Magnetometer (VSM) integrated with the Physical Property Measurement System (PPMS) of Quantum Design make. Using the 'zero-field-cooled' (ZFC) and 'field-cooled' (FC) measurement protocols, magnetization (M) was measured as a function of temperature (T) in the ranges 3- 300 K and 300- 900 K at an external magnetic field (H) of 100 Oe. M-H hysteresis loops were recorded at 3 K, 50 K, 100 K, 200 K, 300 K, 475 K, 650 K and 800 K by varying H within the limits ± 90 kOe.

4.2. 'Zero-field-cooled' and 'field-cooled' thermomagnetic data at $T \leq 300$ K

ZFC and FC magnetizations as functions of temperature, i.e., $M_{ZFC}(T)$ and $M_{FC}(T)$, at H = 100 Oe in the temperature range 3 K - 300 K, are shown in figure 4.1 (a) and (b) for the nanocrystalline samples with $x = 0.0$ to 1.0. The insets of figure 4.1 (a) and (b) mark the temperatures T_{SR}, T_{comp} and T_{Ho} at which the spin reorientation (SR), compensation (comp) of the sub-lattice magnetizations and antiferromagnetic ordering of Ho^{3+} moments occur spontaneously.

4.2.1. Spin reorientation (SR)

Bulk h-$LuFeO_3$ exhibits spin reorientation at $T_{SR} \sim 130$ K [1,2] wherein the magnetic order changes from B_2 to A_2 leading to weak ferromagnetism due to the DM interaction. The present $x = 0$ nanocrystalline sample is made up of 91.5 % hexagonal phase and both $M_{ZFC}(T)$ and $M_{FC}(T)$ go through a peak at $T_{SR} = 115$ K (figure. 4.1 (a)). This peak temperature corresponds to the spin reorientation temperature of h-$LuFeO_3$ [3].

In the present samples with orthorhombic Pbnm crystal structure, at $T < T_N$, Fe^{3+}- O^{2-}- Fe^{3+} superexchange interaction orders Fe^{3+} moments antiferromagnetically in the ab plane, with a net magnetic moment along the c-axis. As the temperature falls below ≈ 100 K, the otherwise paramagnetic Ho^{3+} moments start experiencing the exchange field, generated by the Fe^{3+} moments via the Fe^{3+}- O^{2-}- Fe^{3+} interactions, and tend to get progressively polarized as the Ho^{3+}-O^{2-}-Fe^{3+} interaction picks up slowly. At low temperatures, where Ho^{3+}- O^{2-} -Fe^{3+} interaction becomes stronger than the Fe^{3+}- O^{2-}- Fe^{3+} interaction, the easy axis of the canted Fe^{3+} spins rotates from c-axis to a- axis. This 'spin reorientation' (SR) transition manifests itself as a peak in M_{ZFC}(T) at T = T_{SR}, highlighted by arrows in figure 4.2. The inflexion point of the M_{FC}(T) curve also reflects T_{SR}. o-LFO does not exhibit a SR transition because the Lu^{3+} ions do not carry magnetic moment.

The ZFC magnetization of the samples with x = 0.05 - 1.0, having orthorhombic structure, increases as the temperature decreases from 300 K and goes through a peak at T_{SR}, which increases with the Ho concentration (x) from 3 K to 60 K (figure 4.2). T_{SR} (determined from the M_{ZFC}(T) and M_{FC}(T) curves) plotted against x in figure 4.3 (a), shifts to higher temperatures with increasing x. This shift is a consequence of the enhancement in the Ho^{3+}-O^{2-}- Fe^{3+} interaction strength as the Ho concentration increases. The presently determined value T_{SR} = 57.6 K for x = 1.0 is in close agreement with the value reported [4,5] for $HoFeO_3$.

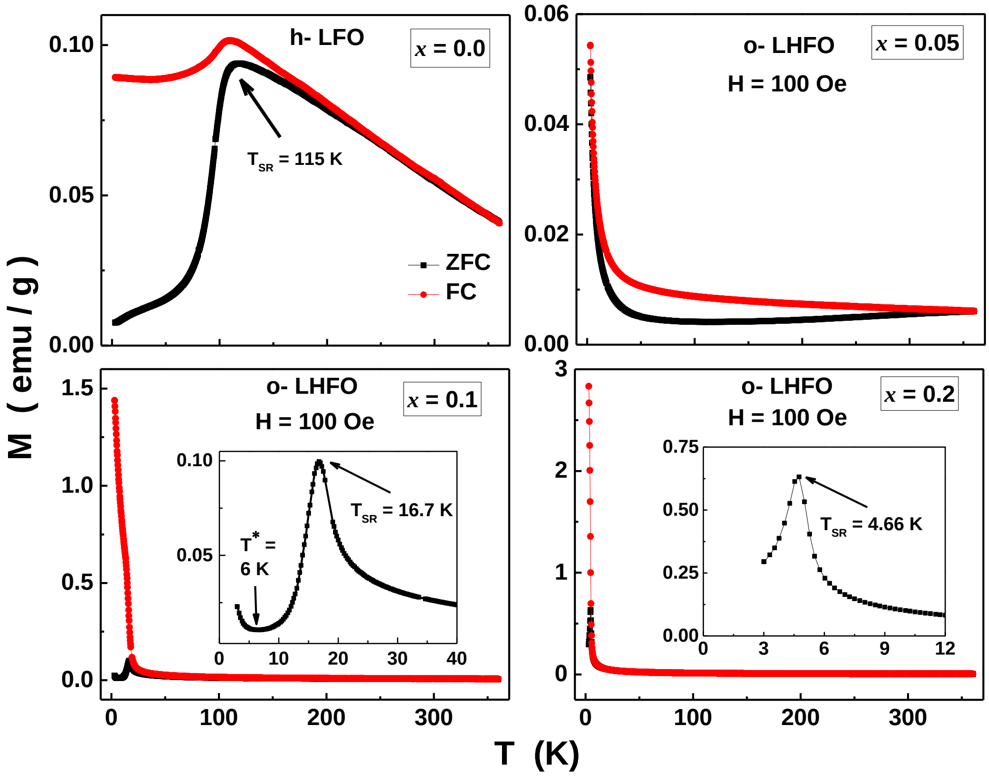

Figure 4.1. (a) M_{ZFC}(T) and M_{FC}(T) measured at H = 100 Oe for $Lu_{1-x}Ho_xFeO_3$ (x = 0.0, 0.05, 0.1, 0.2).

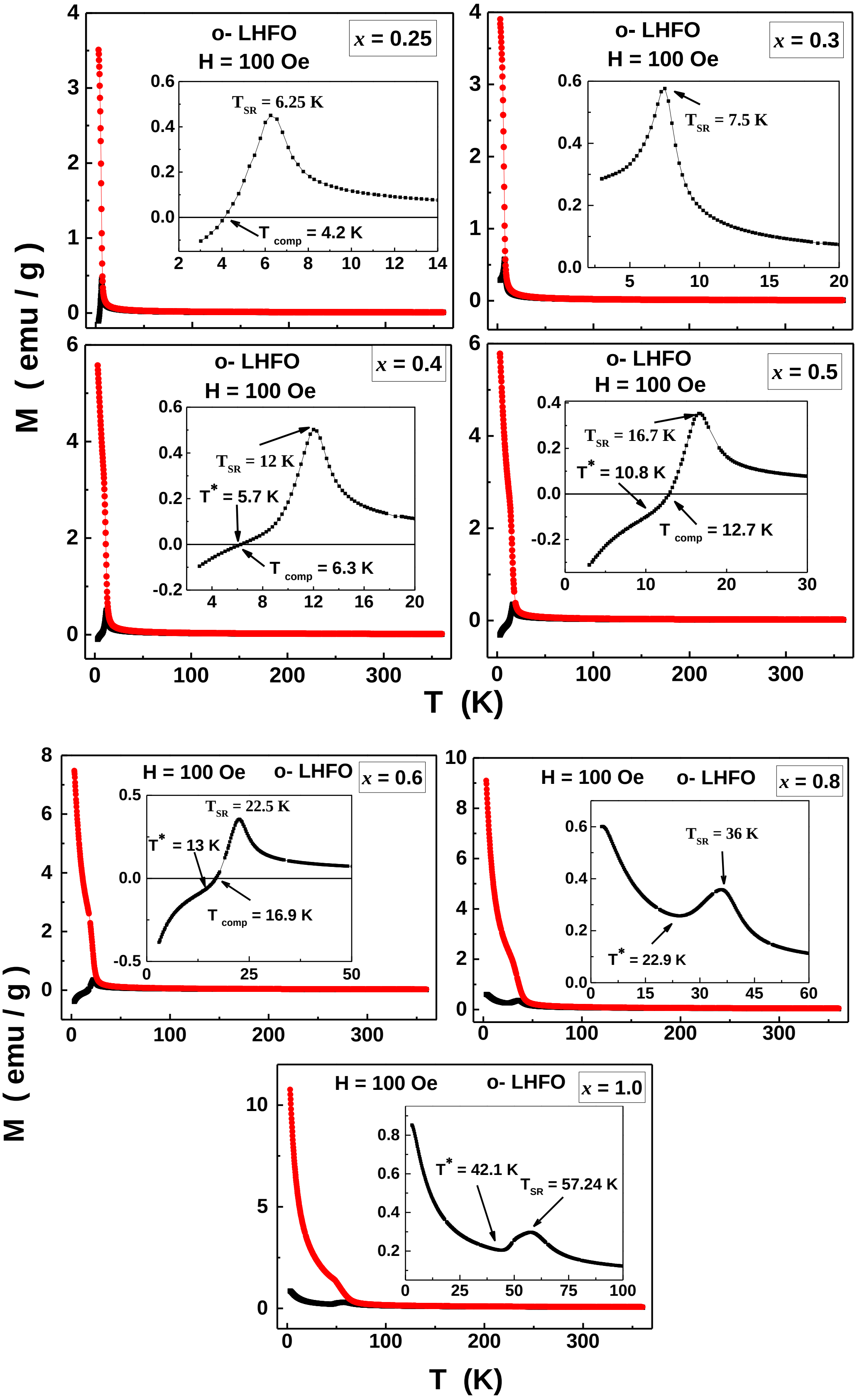

Figure 4.1. (b) $M_{ZFC}(T)$ and $M_{FC}(T)$ measured at H = 100 Oe for $Lu_{1-x}Ho_xFeO_3$ (x = 0.25 to 1.0).

4.2.2. Compensation temperature (T_{comp})

In orthoferrites, below a certain temperature, magnetization of the sublattices, composed of magnetic R^{3+} ions, grows considerably faster than that of the Fe^{3+} sublattices. The R^{3+} sublattice magnetization aligns either parallel or anti-parallel to the Fe^{3+} sublattice magnetization at relatively low temperatures. When, at a given temperature, the sublattice magnetizations of the R^{3+} and Fe^{3+} moments are equal in magnitude but opposite in sign, compensation occurs and the resultant magnetization goes to zero. The temperature at which the compensation occurs is referred to as the compensation temperature (T_{comp}). $RFeO_3$ orthoferrites such as $ErFeO_3$, $NdFeO_3$, $SmFeO_3$ exhibit the phenomenon of compensation. By contrast, no compensation in $PrFeO_3$, $GdFeO_3$, $TbFeO_3$, $DyFeO_3$, $HoFeO_3$ and $TmFeO_3$ occurs, either due to the parallel alignment of the R^{3+} spins with respect to the Fe^{3+} sublattice magnetizations [5,6] or because of the non-magnetic R^{3+} ions.

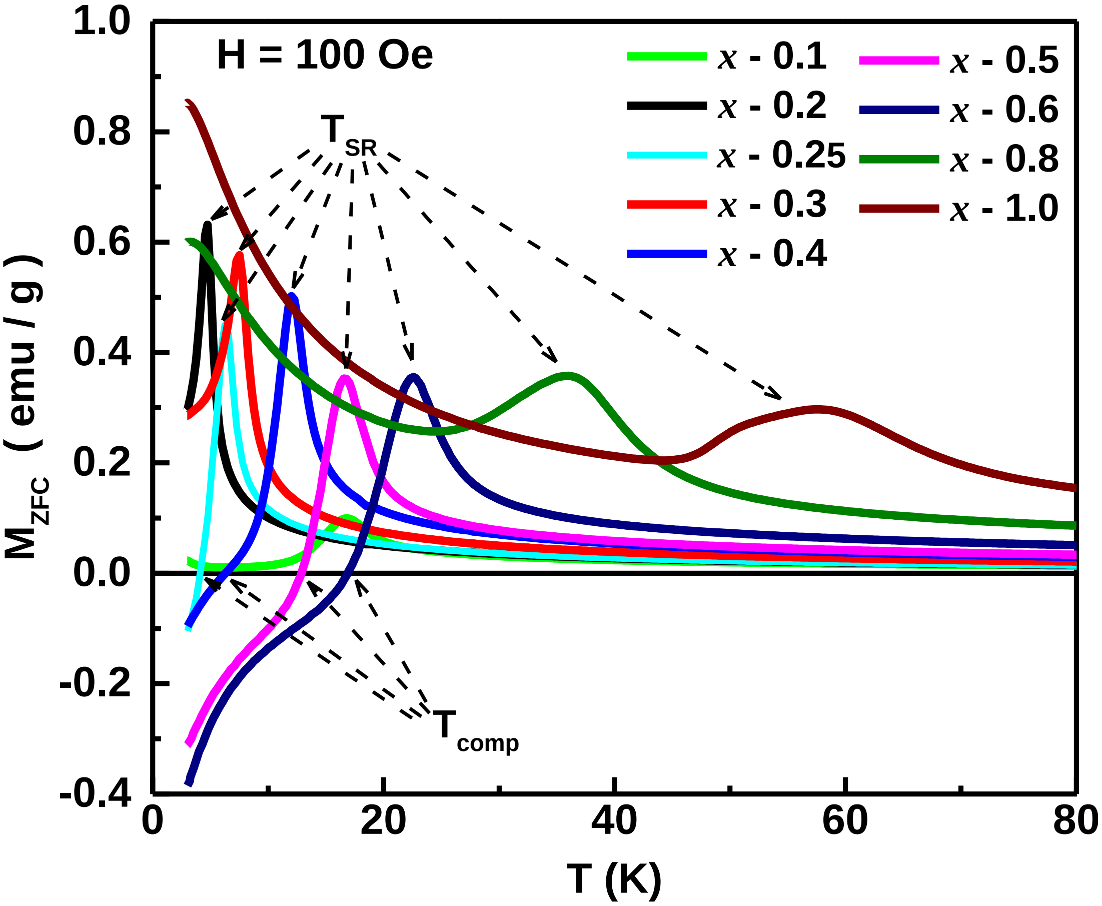

Figure 4.2. Spin reorientation temperature (T_{SR}) and compensation temperature (T_{comp}) as reflected in $M_{ZFC}(T)$.

Depending on the value of x, M_{ZFC}(T) exhibits different characteristic features (figure 4.2) at temperatures below T_{SR}. (i) In x = 0.1, M_{ZFC} is positive and goes through a minimum. (ii) In x = 0.2 and 0.3, M_{ZFC} drops steeply but remains finite and positive even at the lowest measurement temperature (3 K). (iii) In x = 0.25, 0.4, 0.5 and 0.6, M_{ZFC} changes sign at the compensation point (T_{comp}). T_{comp} increases with x, as is shown in figure 4.3 (b). (iv) In x = 0.8 and 1.0, as the temperature is lowered below the SR peak, M_{ZFC} goes on increasing continuously. Above observations (i) - (iv) correspond to the following cases. (a) An upturn in M_{ZFC}(T) at temperatures below the SR peak [findings (i) and (iv)], arises when the single-ion anisotropy (SIA) favors ordering of Ho^{3+} spins on the Ho^{3+} sub-lattice whose magnetization is tilted at an acute angle with respect to the field direction. (b) Since T_{SR} is as low as ~ 10 K for x = 0.2 and 0.3, the SR transition is truncated by the lowest temperature of 3 K [observation (ii)]. (c) The compensation phenomenon is observed [(iii)] because the SIA favors ordering of Ho^{3+} spins on the Ho^{3+} sub-lattice whose magnetization subtends an obtuse angle with H.

4.2.3. Spontaneous ordering of Ho^{3+} moments

As the temperature is lowered below ~ 30 K, the otherwise paramagnetic (PM) Ho^{3+} moments tend to progressively order in an antiferromagnetic (AF) configuration due to the Ho^{3+}- O^{2-}- Ho^{3+} superexchange interaction [6,7]. In figure 4.1, the temperatures that mark the onset of PM behavior are labelled as T^*. The spontaneous ordering of the Ho^{3+} moments at low temperatures ($T < T^*$) is made all the more obvious by the observation of the Curie-Weiss (CW) behavior of M_{FC}(T), or equivalently of the FC susceptibility, $\chi_{FC} = M_{FC}/H$, i.e., $\chi_{FC} = C/(T - \theta_{Ho})$ with $\theta_{Ho} = -4.5 \pm 0.5\,K$, as is shown in figure 4.3 (c). The negative value of θ_{Ho} is indicative of the AF coupling between the Ho^{3+} moments. The temperature range, over which the CW law holds, shrinks rapidly as x decreases so much so that, for Ho concentrations below x = 0.4, the fit range is too narrow to unambiguously assess the validity of the CW law.

M_{FC}(T = 3 K, H = 100 Oe) is plotted as a function of x in figure 4.3 (d). The theoretical fit (red dashed curve), yielded by the relation $M = M^* \times (x - x_c)^n$ with M^*= 11.2(2) emu/g, x_c= 0.049(5) and n = 0.73(3), based on the percolation picture, is found to describe the observed variation of M with x quite well. Agreement between theory and experiment asserts that the percolation of the Ho^{3+} moments on the Ho^{3+} sub-lattices takes place above the threshold concentration of $x_c \approx 0.05$, which is the minimum Ho concentration at which the orthorhombic structure stabilizes in the presently synthesized $Lu_{1-x}Ho_xFeO_3$ nanoparticles.

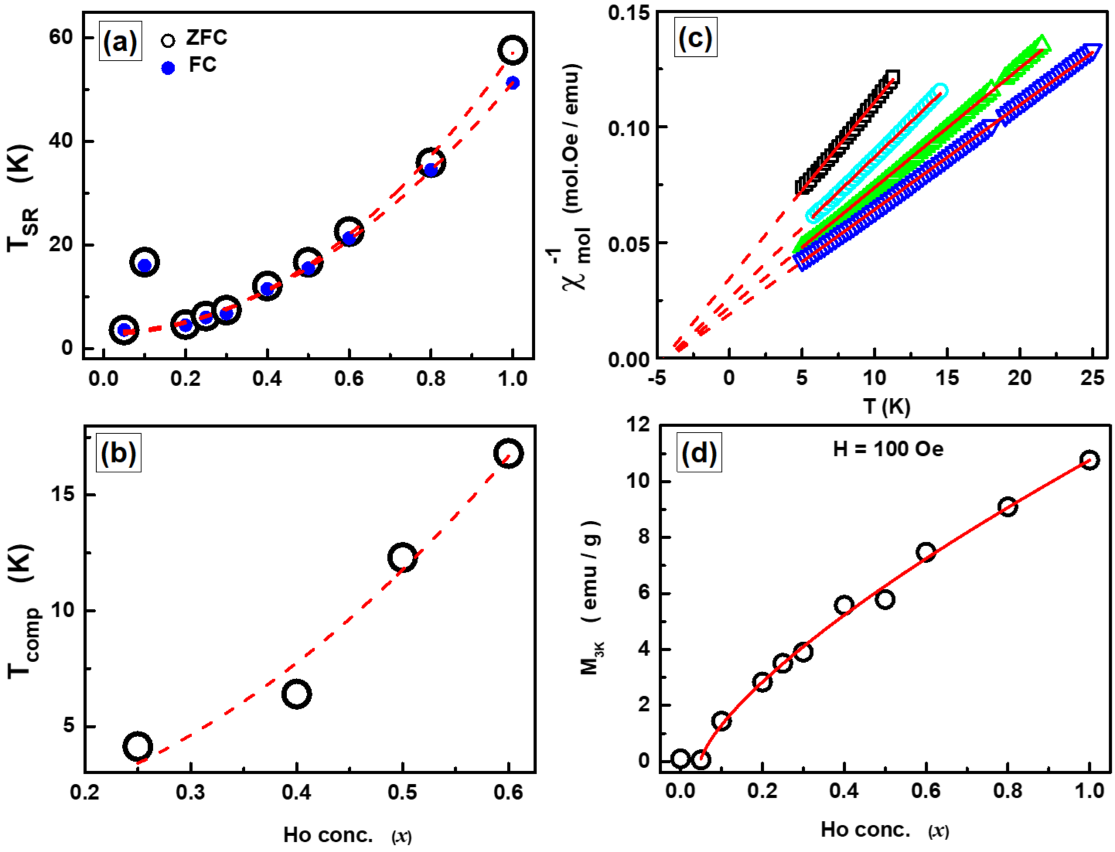

Figure 4.3. Ho concentration variations of **(a).** T_{SR} (K) and **(b)** T_{comp} (K); **(c)** Curie-Weiss law behavior of χ_{mol}^{-1}(T); **(d)** M_{FC}(T = 3 K, H = 100 Oe) as a function of x.

4.3. 'Zero-field-cooled' and 'field-cooled' thermomagnetic data at T ≥ 300 K

4.3.1. Néel temperature, T_N

Figure 4.4 (a) and (b) displays the M_{ZFC}(T) and M_{FC}(T) thermomagnetic curves taken at H = 100 Oe in the temperature range 300 K - 900 K for the $Lu_{1-x}Ho_xFeO$ nanocrystalline samples with x = 0.0 to 1.0. The arrows in the insets of figure 4.4 (a) and (b) mark the Néel temperatures, T_N, as determined from M_{ZFC}(T). For T > T_N, M_{ZFC} goes through a broad peak at ~ 800 K and approaches zero at ~ 850 K while M_{FC} exhibits a Brillouin function-like decrease with increasing temperature and an abrupt slope change at ~620 K before approaching zero at ~ 850 K. By contrast, in x = 1.0, only one peak is observed at 625 K and the peak at ~ 800 K is completely missing in M_{ZFC}(T).

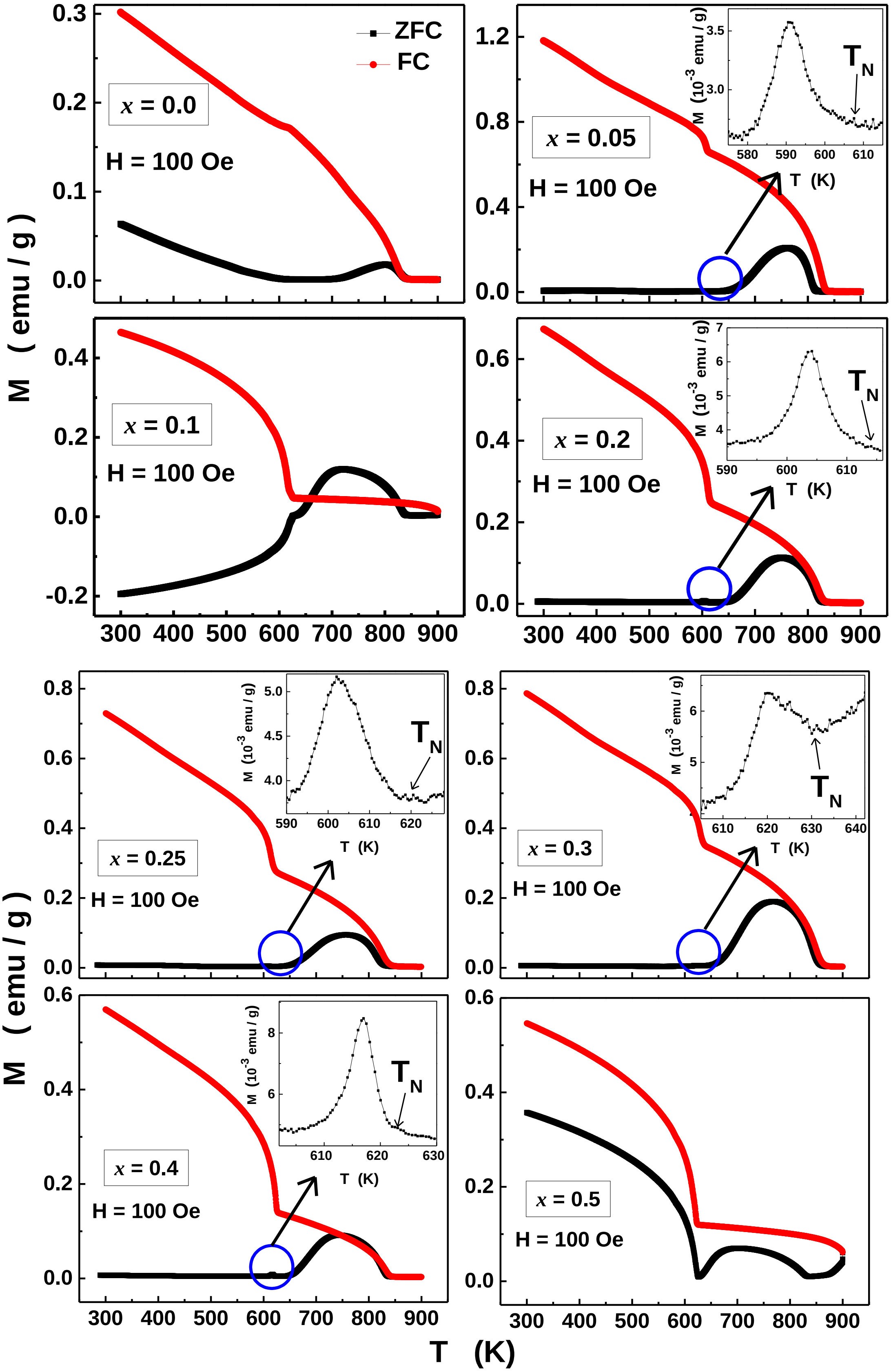

Figure 4.4. (a). M_{ZFC}(T) and M_{FC}(T) thermomagnetic curves in the temperature range 300-900 K for x = 0.0 - 0.5; Inset shows enlarged view of M_{ZFC} at temperatures near T_N.

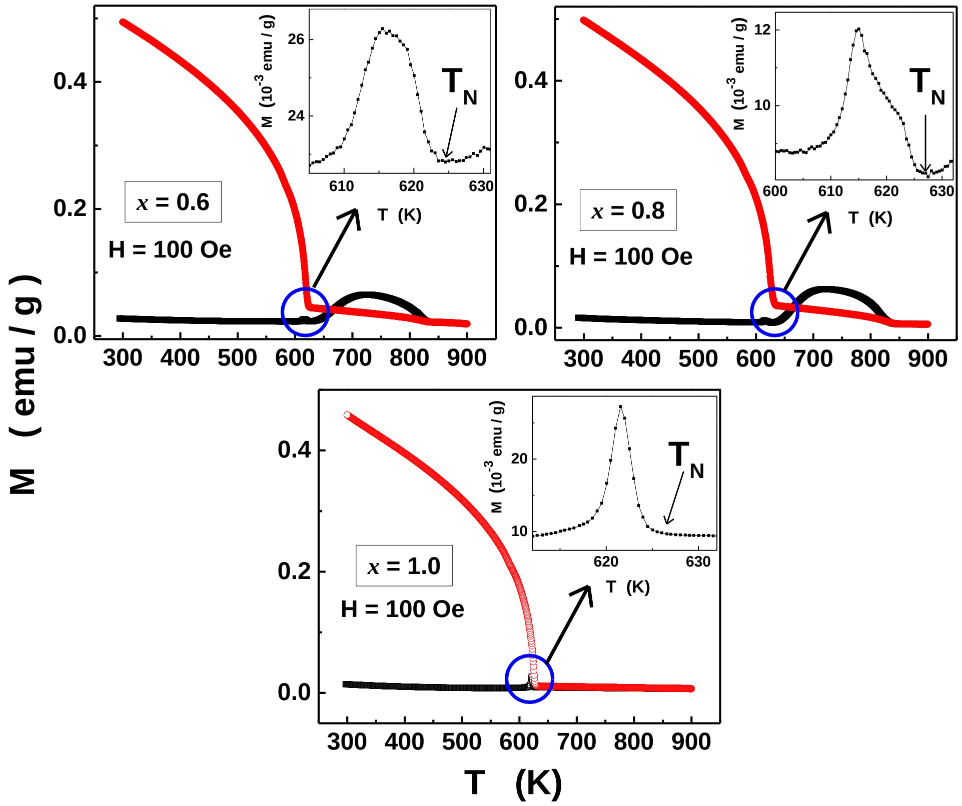

Figure 4.4. (b). M_{ZFC}(T) and M_{FC}(T) thermomagnetic curves in the temperature range 300 K - 900 K for x = 0.6 to 1.0; Inset shows enlarged view of M_{ZFC} at temperatures near T_N.

The variation of T_N with x is shown in the inset of figure 4.5. High T_N reflects a strong interaction between Fe^{3+} ions which increases with x. In the orthorhombic $RFeO_3$ crystal structure, each Fe^{3+} ion is surrounded by six O^{2-} ions forming an octahedral cage. Thus, the interaction between the Fe^{3+} ions operates only through intermediate O^{2-} ion. Depending on the size of the R^{3+} ion, the octahedral cages tilt with respect to each other. Decrease in R^{3+} ion size results in increased octahedral tilt. According to Goodenough-Kanamori [8,9] rules, the indirect exchange interaction is stronger when the bond angle between the Fe^{3+} ions is 180°. In our work, substitutng Ho for Lu, decreases the tilt angle due to the higher ionic radius of Ho. When octahedral tilt decreases, the Fe^{3+}- O^{2-}- Fe^{3+} bond angle increases, resulting in a higher T_N as x increases. Another transition around 850 K is due to the presence of a tiny amount of impurity Fe_3O_4 phase. This impurity phase completely evaded detection in previous x-ray diffraction and Raman scattering experiments [10] but clearly shows up in the thermo-magnetic data because the thermal demagnetization is extremely sensitive to even the trace amounts of magnetic impurities.

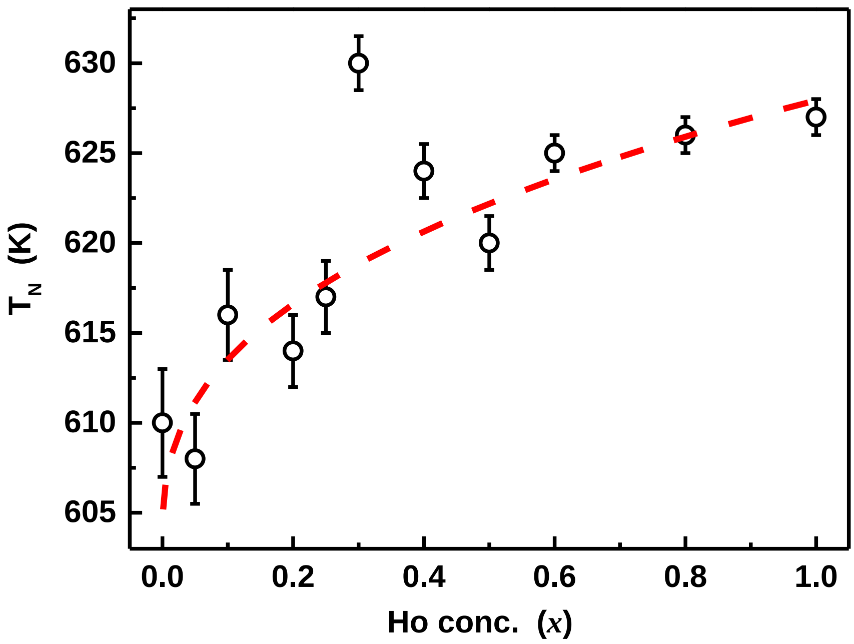

Figure 4.5. The variation of T_N (taken from M_{ZFC} data) as a function of *x*. (The dotted line through the data points is only guide to the eye)

4.4. M-H hysteresis loops at T ≤ 300 K

Typical M-H hysteresis loops, recorded at fixed temperatures (3 K, 50 K, 100 K, 200 K and 300 K) while cycling the magnetic field between the limits H = ± 90 kOe for the samples with *x* = 0.0 to 1.0, are displayed in figure 4.6 (a) and (b). For *x* = 0.0, at the lowest temperature T = 3 K, M does not saturate even in fields as high as H = 90 kOe. Instead, M increases linearly with H at 3 K for $H > 10\ kOe$ and the coercive field, H_c, has a finite value (inset). A strong antiferromagnetic component concomitant with a weak ferromagnetic component (characteristic of weak ferromagnetism) is a consequence of non-collinear antiferromagnetic ordering of Fe^{3+} spins caused by the antisymmetric DM exchange interaction. In LFO, magnetization is solely due to the canted Fe^{3+}- O^{2-}- Fe^{3+} spins because the Lu^{3+} ions are nonmagnetic. When Ho is substituted for Lu, net magnetization of the system increases because of the additional Ho^{3+}- O^{2-}- Fe^{3+} and Ho^{3+}-O^{2-}- Ho^{3+} interactions, and the virgin curves of the M-H hysteresis loops highlight that, at 3 K, M has a tendency to saturate for $H > 20\ kOe$.

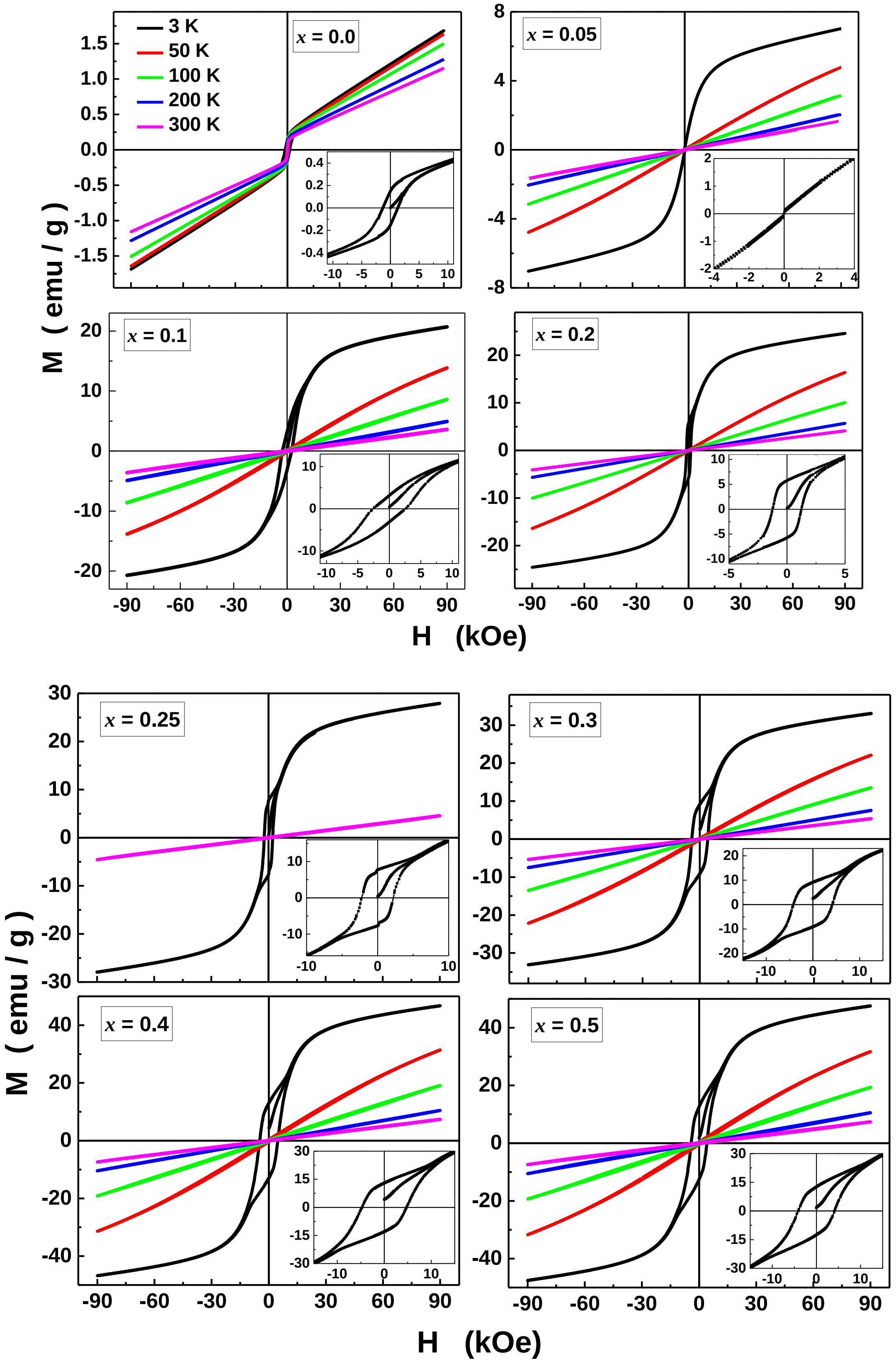

Figure 4.6 (a). Typical M-H hysteresis loops recorded at temperatures in the range 3 K to 300 K for $Lu_{1-x}Ho_xFeO_3$ with x = 0.0 to 0.5.

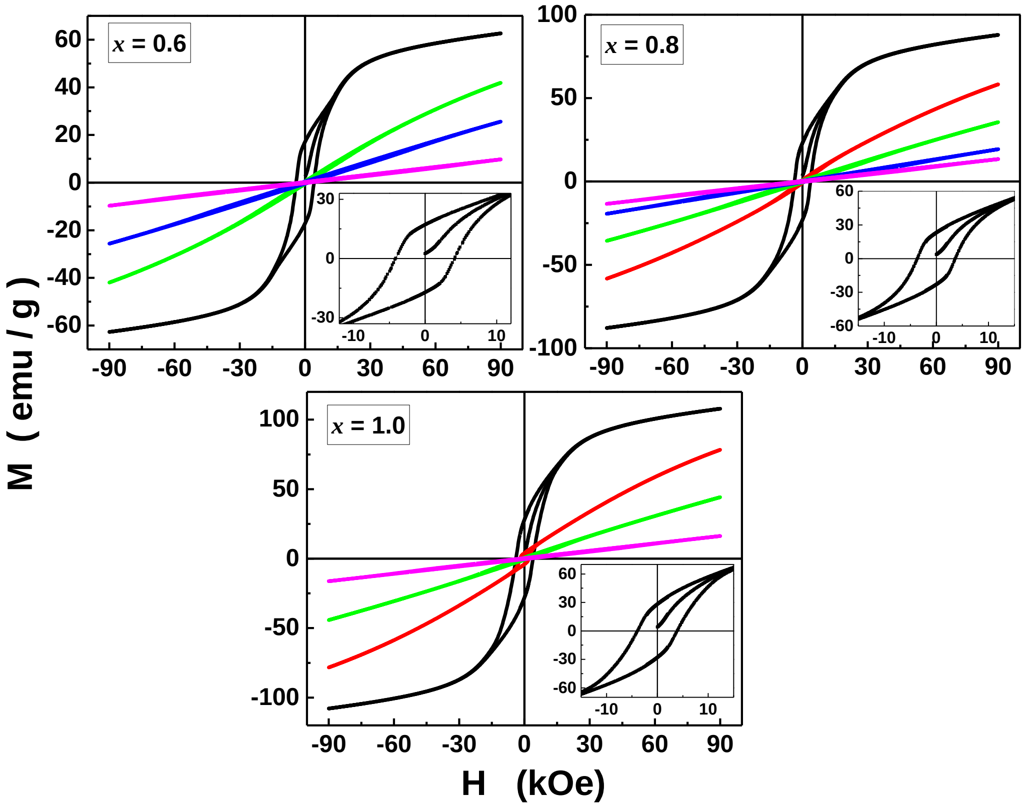

Figure 4.6 (b). Typical M-H hysteresis loops recorded at temperatures in the range 3 K to 300 K for $Lu_{1-x}Ho_xFeO_3$ with $x = 0.6$ to 1.0.

4.4.1. Approach-to-saturation of magnetization at 3 K

The high-field region of a magnetization is determined by a variety of processes like inhomogeneities, anisotropy, and susceptibility [11]. These parameters for a polycrystalline material can be obtained analytically by using law of 'approach-to-saturation' (ATS). By introducing a simple approximation and deriving the contribution of the magnetocrystalline anisotropy for a single crystal, Akulov [12] has first presented the expression for randomly oriented polycrystalline ferromagnets.

In the vicinity of the saturation field, the magnetization vecctor is almost parallel to the applied magnetic field. The component of magnetization along the field can be written as

$$M = M_S \cos\psi$$

$$= M_S\left(1 - \frac{\psi^2}{2}\ldots\ldots\right) \qquad eqn\ (4.1)$$

where 'ψ' is the angle between the magnetizastion and field vectors and it is assumed to be small. The torque exerted by field is counter balances the torque produced by the magnetic anisotropy (E$_a$) which is written as

$$M_S H \sin\psi = -\frac{\partial E_a}{\partial \psi} \qquad eqn\ (4.2)$$

$$M_S H \sin\psi \approx M_S H\,\psi = -\frac{\partial E_a}{\partial \psi} \Rightarrow \psi = \frac{1}{H}\frac{c}{M_S} \qquad eqn\ (4.3)$$

where,

$$c = -\left(\frac{\partial E_a}{\partial \psi}\right)_{\psi\sim 0} \qquad eqn\ (4.4)$$

By substituting eqn (4.3) in eqn (4.1),

$$M = M_S\left(1 - \frac{b}{H^2} - \cdots\right) \qquad eqn\ (4.5)$$

where

$$b = \frac{1}{2}\frac{c^2}{M_S^2} \qquad eqn\ (4.6)$$

The drawback of this theory is that it considers only the effect of crystalline anisotropy on the saturation process of magnetization. It completely ignores the influence of lattice vacancies, distortions, crystalline defects and local concentration fluctuations that impede the motion of domain walls. Later by including the local magnetic inhomogeneities and high-field susceptibility, The Brown-Néel (BN) model yields the following expression for ATS

$$M(H) = M_{sat}\left[1 - \frac{a^*}{H} - \frac{b^*}{H^2}\right] + \chi_{hf} H \qquad eqn\ (4.7)$$

where M_{sat} is the saturation magnetization, the a^*/H term arises from local defects and non-magnetic inclusions, the coefficient b^* is related to the magnetocrystalline anisotropy constant and χ_{hf} is the high-field susceptibility.

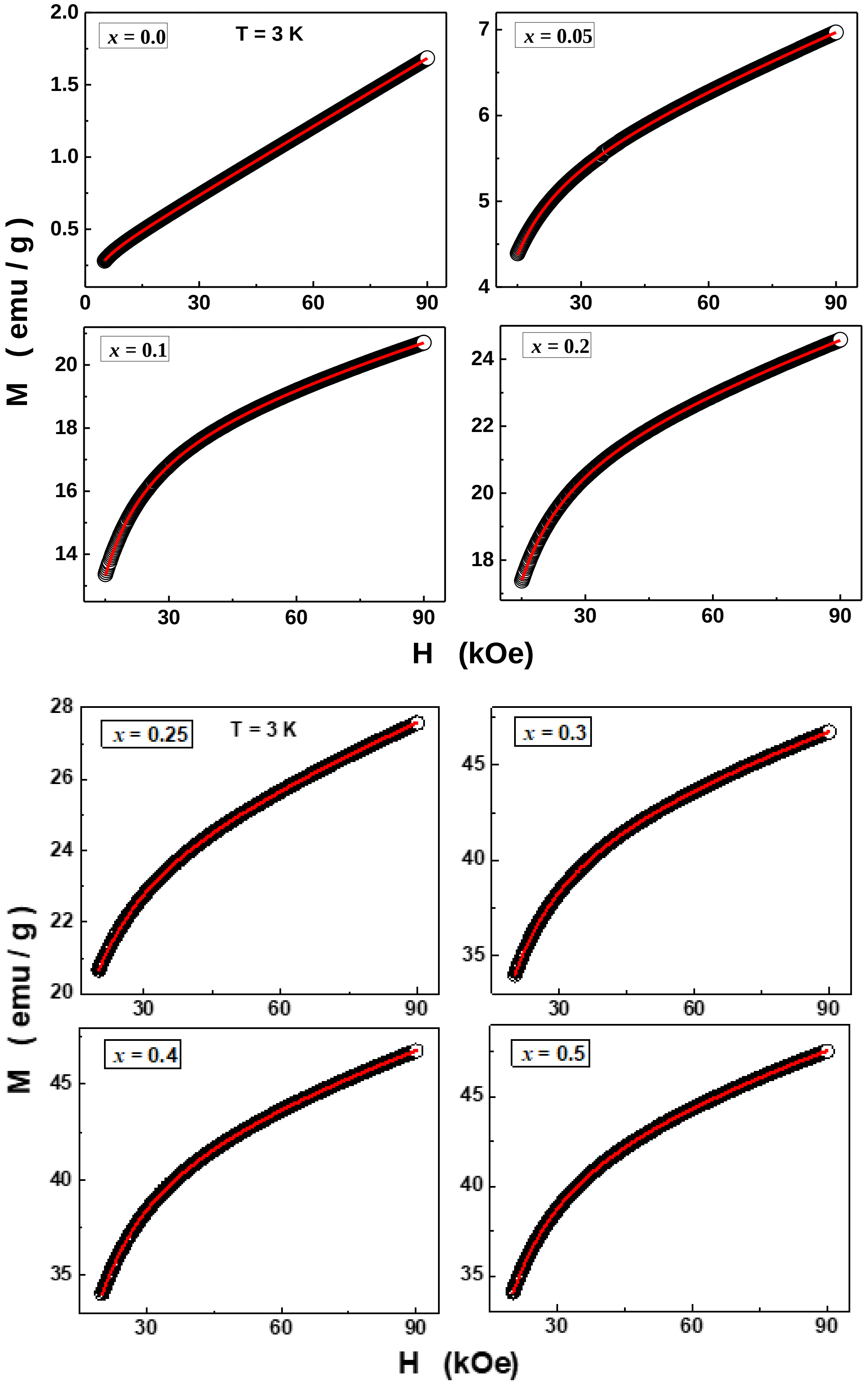

Figure 4.7 (a). Approach-to-saturation fits to the magnetization data, M(H) at 3 K, based on eqn (4.7), for *x* = 0 to 0.5.

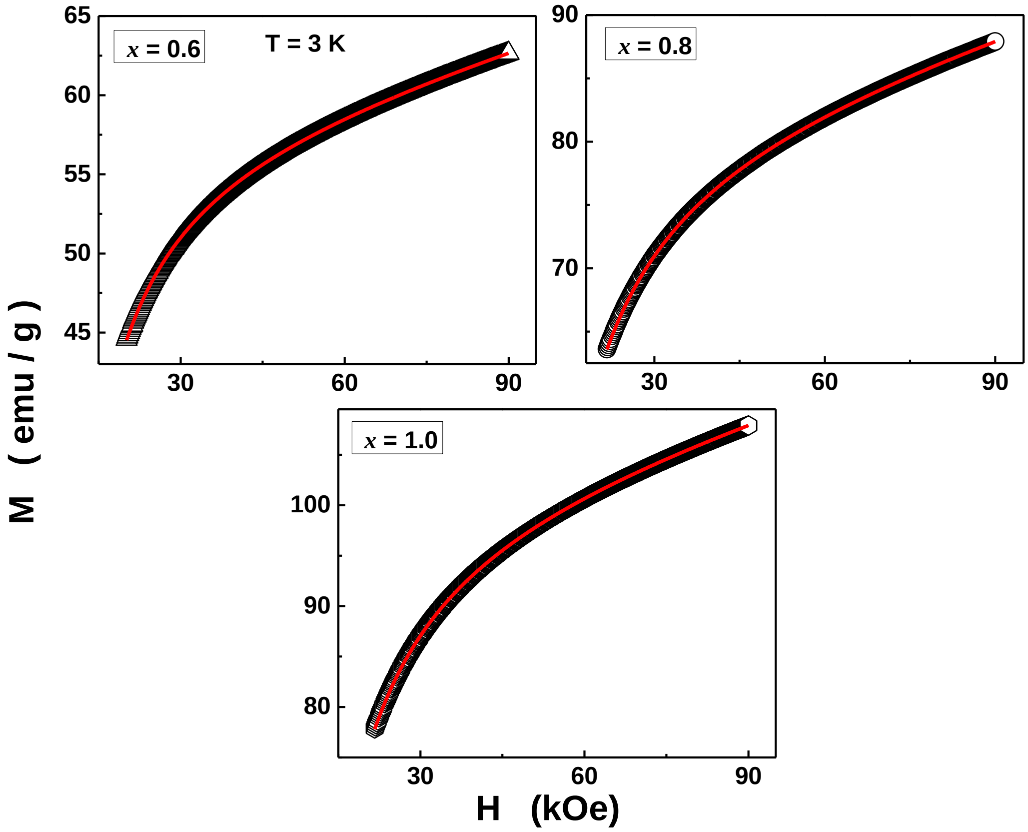

Figure 4.7 (b). Approach-to-saturation fits to the magnetization data, M(H) at 3 K, based on eqn (4.7), for *x* = 0.6 to 1.0.

Out of the theoretical models [13,14] (Brown-Néel [11,15,16], micromagnetic [17] and random anisotropy [18]) proposed for the ATS of magnetization in ferromagnetic systems, the BN model alone closely reproduces the observed ATS in the virgin M-H isotherms taken at 3 K for the $Lu_{1-x}Ho_xFeO_3$ (*x* = 0.0 to 1.0) samples. The ATS fits (red curves through the data points), in the field range $20\ kOe \lesssim\ H\ \leq 90\ kOe$, based on eqn (4.7) for *x* = 0.0 to 1.0, are shown in figure 4.7 (a) and (b). The fit parameters M_{sat}, a^*, b^*, χ_{hf} are plotted against Ho concentration in figure 4.8 (a) – (d). In figure 7(a), M_{sat}, obtained from the ATS fit, is compared with $M_{90\mathrm{kOe}}$, measured at 3 K. A close agreement between $M_{sat}(x)$ and $M_{90\mathrm{kOe}}(x)$ and a linear increase of both the quantities with *x* is evident from this figure. A striking similarity between $b^*(x)$ and $H_C(x)$, measured at 3 K, witnessed in figure 4.8. (d), asserts that the root cause of H_C in the LHFO nanoparticles is magnetocrystalline anisotropy.

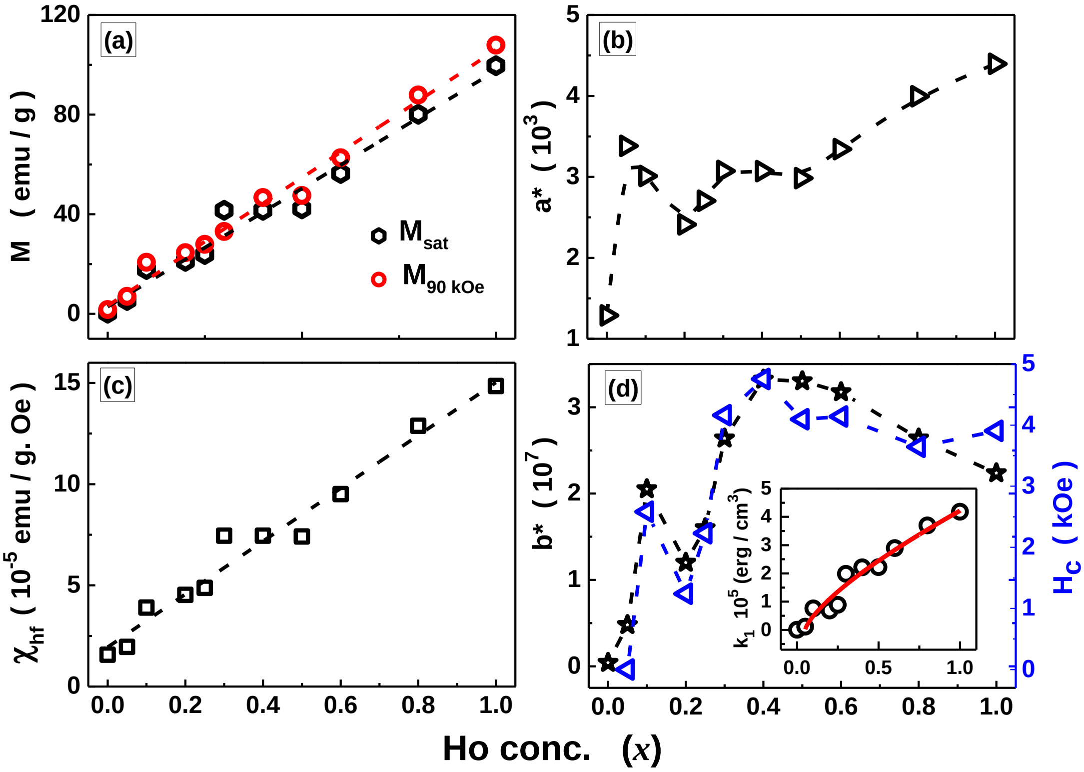

Figure 4.8. The ATS fit parameters M_{sat}, a^*, b^*, χ_{hf} as functions of Ho concentration in $Lu_{1-x}Ho_xFeO_3$. (a) Comparison of M_{sat} with $M_{90\ kOe}$; (d) One-to-one correspondence of the coercive field (Hc) with the coefficient 'b^*', which is a measure of magnetocrystalline anisotropy (MCA); inset of (d) Variation of MCA with *x*.

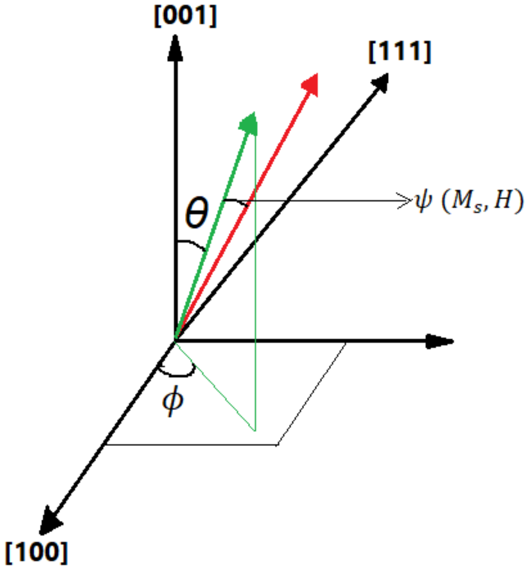

Figure 4.9. Coordinate system used in deriving the relationship between the coefficient of $1/H^2$ term in eqn (4.7) and magnetic anisotropy constant (*K*) [19].

The cubic magnetocrystalline anisotropy can be calculated using ‘b*’ from eqn (4.7) [19]. The magnetization rotates along the maximum gradient of anisotropy energy in the neighborhood of *H*. Using spherical polar coordinates to describe the orientation of the magnetization vector and writing anisotropy energy also in polar coordinates, we obtain,

$$\nabla E_a = \frac{\partial E_a}{\partial r}\,\hat{r} + \frac{1}{r}\,\frac{\partial E_a}{\partial \theta}\,\hat{\theta} + \frac{1}{r\,\sin\theta}\,\frac{\partial E_a}{\partial \phi}\,\hat{\phi} \qquad eqn\ (4.8)$$

Assuming that ∇E_a is pointing already in the radial direction, the component of magnetization in the radial direction experiences a constant force from E_a and hence the first term in the eqn 4.8 becomes zero, with the result

$$c^2 = |\nabla E_a|^2$$

$$= \left(\frac{\partial E_a}{\partial \theta}\right)^2 + \frac{1}{sin^2\theta}\left(\frac{\partial E_a}{\partial \phi}\right)^2 \qquad eqn\ (4.9)$$

and hence,

$$b = \frac{1}{2{M_s}^2}\left[\left(\frac{\partial E_a}{\partial \theta}\right)^2 + \frac{1}{sin^2\theta}\left(\frac{\partial E_a}{\partial \phi}\right)^2\right] \qquad eqn\ (4.10)$$

Rewriting $\frac{\partial E_a}{\partial \theta}$ and $\frac{\partial E_a}{\partial \phi}$ in terms of direction cosines $(\alpha_1 = \sin\theta\,\cos\phi\,, \alpha_2 = \sin\theta\,\sin\phi\,, \alpha_3 = \cos\theta)$ of magnetization with respect to the chosen coordinate system,

$$\frac{\partial E_a}{\partial \theta} = \frac{\partial E_a}{\partial \alpha_1}\,\frac{\partial \alpha_1}{\partial \theta} + \frac{\partial E_a}{\partial \alpha_2}\,\frac{\partial \alpha_2}{\partial \theta} + \frac{\partial E_a}{\partial \alpha_3}\,\frac{\partial \alpha_3}{\partial \theta} \qquad eqn\ (4.11)$$

Similarly,

$$\frac{\partial E_a}{\partial \phi} = \frac{\partial E_a}{\partial \alpha_1}\,\frac{\partial \alpha_1}{\partial \phi} + \frac{\partial E_a}{\partial \alpha_2}\,\frac{\partial \alpha_2}{\partial \phi} + \frac{\partial E_a}{\partial \alpha_3}\,\frac{\partial \alpha_3}{\partial \phi} \qquad eqn\ (4.12)$$

and solving the above expressions, we can obtain

$$b = \frac{1}{2{M_s}^2}\left[\sum_{i=1}^{3}\left(\frac{\partial E_a}{\partial \alpha_i}\right)^2 + \left(\sum_{i=1}^{3}\left(\frac{\partial E_a}{\partial \alpha_i}\right)\alpha_i\right)^2\right] \qquad eqn\ (4.13)$$

For the cubic case, E_a is related to the anisotropy constants K_1 and K_2 as

$$E_a = K_1\,(\alpha_1^2\alpha_2^2 + \alpha_2^2\alpha_3^2 + \alpha_3^2\alpha_1^2) + K_2\,(\alpha_1^2\alpha_2^2\alpha_3^2) + \ldots\ldots\ldots.. \qquad eqn\ (4.14)$$

Considering only the first term in eqn (4.14), we get

$$\frac{\partial E_a}{\partial \alpha_1} = 2\,K_1\alpha_1\,(1-\alpha_1^2\,), \frac{\partial E_a}{\partial \alpha_2} = 2\,K_1\alpha_2\,(1-\alpha_2^2\,), \frac{\partial E_a}{\partial \alpha_3} = 2\,K_1\alpha_3\,(1-\alpha_3^2\,)$$

Then eqn (4.13) becomes,

$$b = \frac{4}{2}\frac{K_1^2}{M_s^2}[(\alpha_1^6 + \alpha_2^6 + \alpha_3^6) - (\alpha_1^8 + \alpha_2^8 + \alpha_3^8) - 2(\alpha_1^4\alpha_2^4 + \alpha_2^4\alpha_3^4 + \alpha_3^4\alpha_1^4)]\,eqn\ (4.15)$$

Assuming random orientation of crystallites/grains for a polycrystalline material, averaging of ‘b’ over all possible directions (by considering the average values of direction cosines over a solid sphere where ‘θ’ ranges from angle 0° to 180° and ‘ϕ’ takes on value 0° to 360°), we obtain

$$\langle b\rangle_{avg} = \frac{4}{2}\frac{K_1^2}{M_s^2}\left\{\frac{3}{7} - \frac{3}{9} - \frac{6}{105}\right\} = \frac{8}{105}\frac{K_1^2}{M_s^2} \qquad eqn(4.16)$$

The cubic magnetocrystalline anisotropy constant (K_1) is calculated from the coefficient b^* using the relation

$$K_1 = \pm\left[\frac{105}{8} \times b^*\right]^{1/2} M_{sat} \qquad (4.17)$$

The inset of figure 4.8 (d) displays the variation of K_1 with Ho concentration (x) along with the theoretical fit (red curve), yielded by the percolation model expression, $K_1 = K_1^* \times (x - x_c)^n$ with K_1^*= 4.3(1)×10^6 erg / cc, x_c= 0.049(7) and n = 0.73(5). It is evident from this inset that, like M_{FC}(T = 3 K, H = 100 Oe), the magneto-crystalline anisotropy constant at 3 K, $K_1(3\,K)$, as a function of x, exhibits percolation behavior in that there exists a percolation threshold Ho concentration, $x_c \approx 0.05$. In this context, it is important to note that x_c and the exponent n have the same values for both M_{FC}(T = 3 K, H = 100 Oe) and $K_1(3\,K)$.

4.5. M-H hysteresis loops at T ≥ 300 K

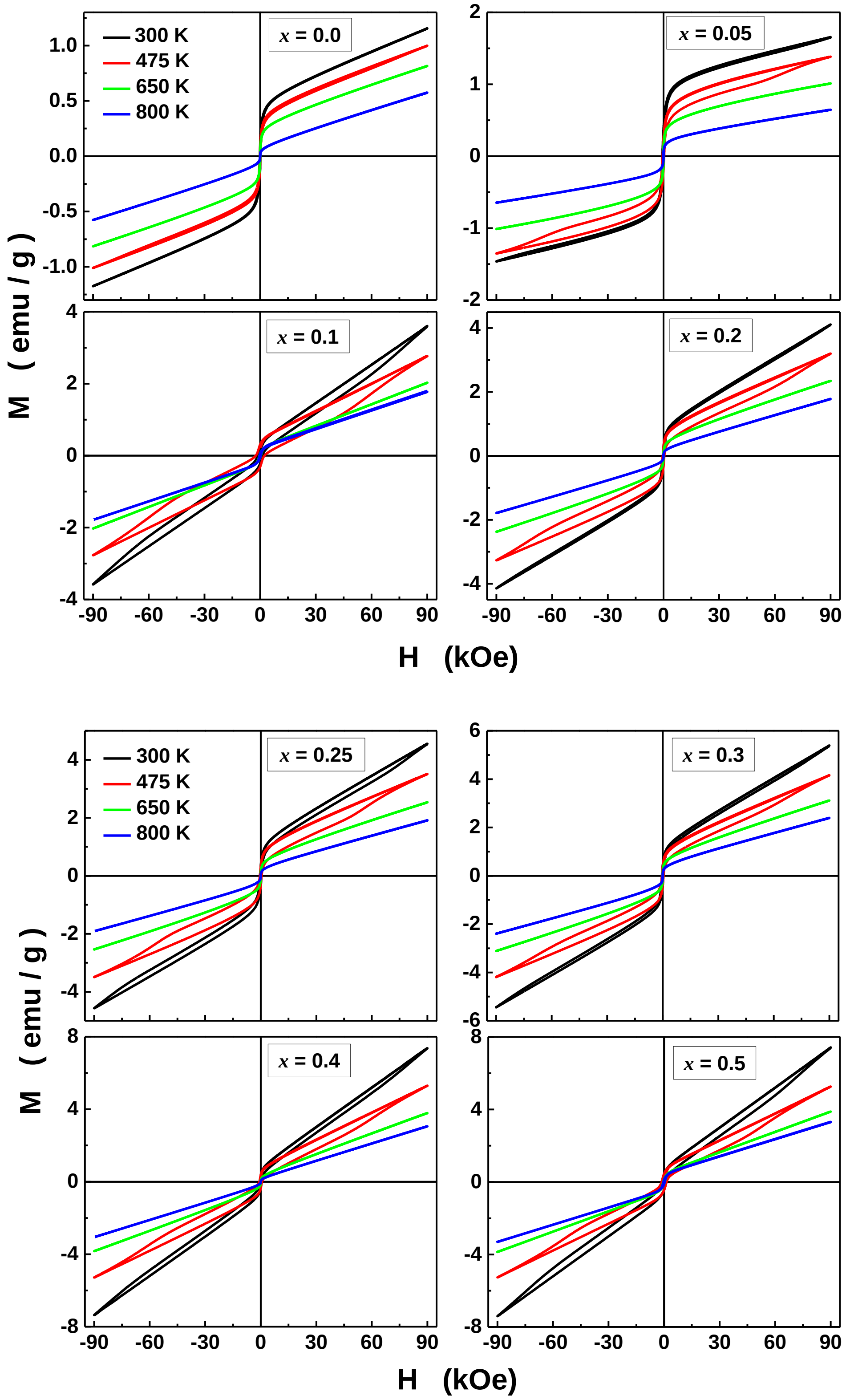

Figure 4.10 (a). M-H hysteresis loops measured at temperatures 300 K, 475 K, 650 K and 800 K for *x* = 0.0 to 0.5.

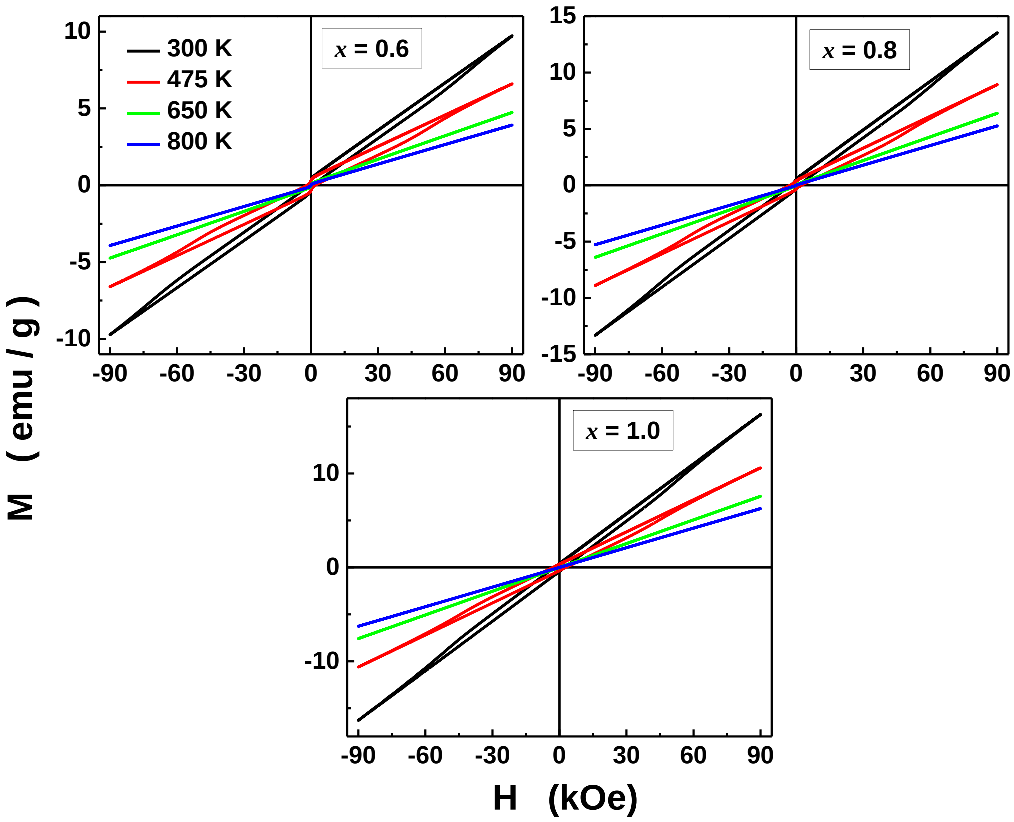

Figure 4.10 (b). M-H hysteresis loops measured at temperatures 300 K, 475 K, 650 K and 800 K for x = 0.6 to 1.0.

The M-H hysteresis loops at fixed temperatures in the range 300 K - 800 K, shown for x = 0.0 to 1.0 in figure 4.10 (a) and (b), are representative of other compositions as well. Irrespective of composition, the hysteresis loops taken at temperatures 300 K and 475 K have features normally associated with the weak ferromagnetism of canted Fe^{3+} spins. Such features, though significantly diminished, persist up to temperatures as high as 800 K ($> T_N = 630\ K$) in the samples with x ranging from 0.0 to 0.5, but are completely absent in x = 0.6, 0.8 and 1.0. This observation basically reflects the presence (absence) of trace Fe_3O_4 phase in $0.0 \leq x \leq 0.5$ ($0.6 \leq x \leq 1.0$). This inference is further supported by the existence of a slight but finite H_C even at a temperature, 800 K, well above T_N in $0.0 \leq x \leq 0.5$, as contrasted with $H_C = 0$ at T = 650 K, which lies just above $T_N = 630\ K$, in $0.6 \leq x \leq 1.0$.

4.6. Functional dependence of $M_{90\ kOe}$ on *x* and T

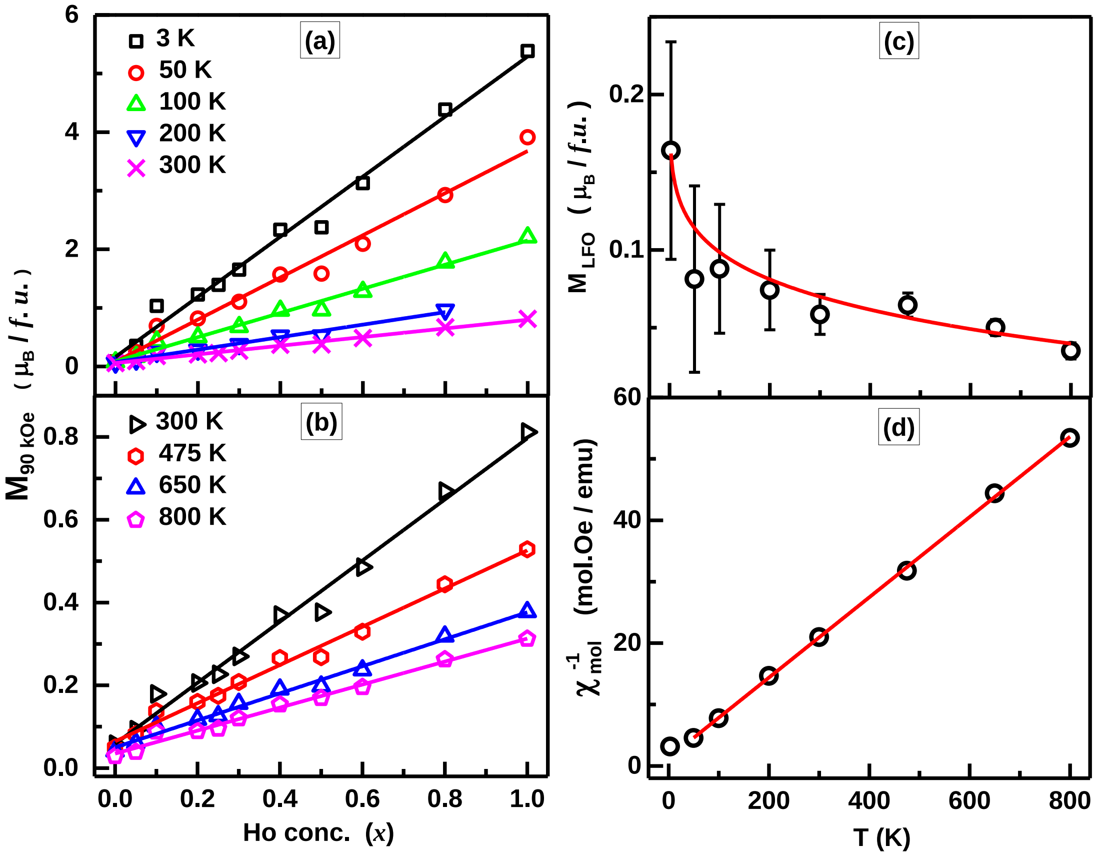

Figure 4.11. (a) & (b). $M_{90\ kOe}$ as a function of Ho concentration, *x*, at fixed temperatures in the range 3 K - 800 K; **(c)** Temperature variation of M_{LFO} (obtained by using eqn (4.18)); **(d)** Curie- Weiss law behavior of χ_{mol}^{-1} (calculated from M_{HFO}).

The value of magnetization at the highest field H = 90 kOe, $M_{90\ kOe}$, is plotted against the Ho concentration, *x*, at fixed temperatures in the range 3 K - 800 K in figure 4.11. At any temperature in this range, $M_{90\ kOe}$ increases linearly with *x*. The straight line fits through the data points are based on the following relation

$$M_{90\ kOe}(T) = (1 - x)\ M_{LFO}(T) + x\ M_{HFO}(T) \qquad (4.18)$$

where M_{LFO} and M_{HFO} are the *LFO* and *HFO* contributions to $M_{90\,kOe}$ at a given temperature. Sub-figures 4.11 (a) and 4.11 (b) clearly bear out that eqn 4.18 forms an adequate description of $M_{90\ kOe}(x)$ at any temperature. Sub-figures 4.11 (c) and 4.11 (d) depict the temperature variations of M_{LFO} and M_{HFO} together with the fits (red curves) yielded by the expressions: $M_{LFO} = a + b\,T^{p}$ with $a = M_{LFO}(T = 0)$ = 0.245 $\pm$ 0.001 μ_B per *f.u.*, *b* = -0.07 $\pm$ 0.02, p = 0.16 $\pm$ 0.04 and $\chi_{HFO}{}^{-1} = H/M_{HFO} = (T - \theta_{Ho})/\,C$ with $\theta_{Ho} =$

$-10 \pm 1\,K$. While the presently determined value of M_{LFO} at $T = 0$ is in perfect agreement with that (0.24 μ_B per *f.u.*) reported [20] previously for bulk o-LFO, χ_{HFO} follows the Curie-Weiss (CW) law in the temperature range $50\,K \leq T \leq 800\,K$ even at fields as intense as 90 kOe and the effective magnetic moment, calculated from the CW constant, C, $\mu_{eff} = 10.9 \pm 0.1\,\mu_B$, has nearly the Ho^{3+} free-ion value of $\mu_{eff} = 10.6\,\mu_B$. The negative value for θ_{HFO} reflects the antiferromagnetic ordering of the Ho^{3+} spins at low temperatures.

4.7. Summary

In this chapter, the effect of Ho substitution on the magnetic properties of $Lu_{1-x}Ho_xFeO_3$ ($0.0 \leq x \leq 1.0$). In order to ascertain the effect of Ho doping, the magnetization of $Lu_{1-x}Ho_xFeO_3$ ($0.0 \leq x \leq 1.0$) was measured as a function of temperature (3 – 350 K) both in zero-field-cooled (ZFC) and field-cooled (FC) modes at a magnetic field of 100 Oe, using PPMS-VSM of Quantum Design. In $RFeO_3$ system, due to the DM interaction of R^{3+} with Fe^{3+} moments, the easy axis of magnetization rotates from c to a- axis exhibiting a spin reorientation (SR) at T_{SR}. The occurrence of SR and the magnitude of T_{SR} depends on the nature of R^{3+} and the coupling with Fe^{3+} moments. T_{SR} is plotted against x and it is found to increase with x. For $x = 0.3$ to 0.6, Ho^{3+} and Fe^{3+} moments point in opposite directions and when their magnitudes are equal at T_{comp}, M ~ 0. Below T_{comp}, ordering of Ho^{3+} spins opposite to Fe^{3+} results in $M < 0$. M exhibits a change in slope at T with a sharp increase in magnetization at low temperatures. This study establishes that the Ho doping stabilizes o-structure beyond $x > 0.05$ and increases the T_{SR} from 0 in O-LFO to 57.8 ± 0.2 K in o-HFO.

The T_{SR} and T_{comp} shifts to higher temperature indicating the growing interaction strength between Ho^{3+} and Fe^{3+} ions. From the Curie-Weiss fit of χ_{FC} , θ_{Ho} is found to be negative indicating the antiferromagnetic coupling between Ho^{3+} ions. M_{3K}(FC) increases with Ho conc, exhibits percolation behavior. $x = 0.05$ is the threshold concentration for percolation which is also the concentration required for orthorhombic stabilization. The antiferromagnetic to paramagnetic transition (T_N) shifts from 610 K to 630 K with increase in Ho concentration. Another transition is observed ~850 K that arises due to the trace amount of Fe_3O_4 present which was not deductible in both X-ray diffraction and Raman spectroscopy measurements carried out at room temperature.

M-H hysteresis loops measured at 3 K approaches saturation for $x = 0.05$ to 1.0 due to the ordering of Ho^{3+} moments. Canting of Fe^{3+} spins, caused by the D-M interaction, gives rise to finite coercivity (H_C) at 3 K and weak ferromagnetism. M-H hysteresis measured at T > 3 K doesn't saturate even at H = 90 kOe exhibiting strong antiferromagnetic coupling between Fe^{3+} spins. The Brown-Néel model closely reproduces the observed 'approach-to-saturation' in the virgin M-H isotherms taken at 3 K. Similarity between b* and Hc indicates, that the magnetocrystalline anisotropy is the root cause of Hc. M-H isotherms measured at 800 K shows finite Hc and M_R for x = 0.0 to 0.5 indicating the presence of Fe_3O_4. For x = 0.6 to 1.0, the M-H loop is linear showing the suppression of Fe_3O_4.

At any temperature, $M_{90\ kOe}$ increases linearly with x. MLFO and MHFO is separated out and found to be matching with the literature value. From the straight line fits through the data points, M_{LFO} and M_{HFO} are extracted at a given temperature. the value of M_{LFO} at $T = 0$ calculated from the temperature variation of M_{LFO} is in perfect agreement with that (0.24 μ_B per *f.u.*) reported previously for bulk o-LFO. χ_{HFO} follows the Curie-Weiss (CW) law in the temperature range $50\,K \le T \le 800\,K$ even at fields as intense as 90 kOe and the effective magnetic moment, calculated from the CW constant, C, $\mu_{eff} = 10.9 \pm 0.1\ \mu_B$, has nearly the Ho^{3+} free-ion value of $\mu_{eff} = 10.6\ \mu_B$. The negative value for θ_{HFO} reflects the antiferromagnetic ordering of the Ho^{3+} spins at low temperatures.

References

[1] W. Wang, J. Zhao, W. Wang, Z. Gai, N. Balke, M. Chi, H.N. Lee, W. Tian, L. Zhu, X. Cheng, D.J. Keavney, J. Yi, T.Z. Ward, P.C. Snijders, H.M. Christen, W. Wu, J. Shen, X. Xu, Room-temperature multiferroic hexagonal LuFeO3 films, Phys. Rev. Lett. 110 (2013) 1–5. https://doi.org/10.1103/PhysRevLett.110.237601.

[2] J. Liu, T.L. Sun, X.Q. Liu, H. Tian, T.T. Gao, X.M. Chen, A Novel Room-Temperature Multiferroic System of Hexagonal Lu1−xInxFeO3, Adv. Funct. Mater. 28 (2018) 1–7. https://doi.org/10.1002/adfm.201706062.

[3] J. Liu, T.L. Sun, X.Q. Liu, H. Tian, T.T. Gao, X.M. Chen, A Novel Room-Temperature Multiferroic System of Hexagonal Lu1−xInxFeO3, Adv. Funct. Mater. 28 (2018) 1–10. https://doi.org/10.1002/adfm.201706062.

[4] E. Balykina, E. Gan'shina, G. Krinchik, Magnetooptic properties of rare-earth orthoferrites in the region of spin reorientation transitions, Zh. Éksp. Teor. Fiz. 93 (1987) 1879–1887.

[5] Z. Zhou, L. Guo, H. Yang, Q. Liu, F. Ye, Hydrothermal synthesis and magnetic properties of multiferroic rare-earth orthoferrites, J. Alloys Compd. 583 (2014) 21–31. https://doi.org/10.1016/j.jallcom.2013.08.129.

[6] H.J. Zhao, J. Íñiguez, X.M. Chen, L. Bellaiche, Origin of the magnetization and compensation temperature in rare-earth orthoferrites and orthochromates, Phys. Rev. B. 93 (2016) 1–5. https://doi.org/10.1103/PhysRevB.93.014417.

[7] T. Chatterji, M. Meven, P.J. Brown, Temperature evolution of magnetic structure of HoFeO3 by single crystal neutron diffraction, AIP Adv. 7 (2017). https://doi.org/10.1063/1.4979710.

[8] J.B. Goodenough, Theory of the role of covalence in the perovskite-type manganites [La,M(II)]MnO3, Phys. Rev. 100 (1955) 564–573. https://doi.org/10.1103/PhysRev.100.564.

[9] J. Kanamori, Superexchange interaction and symmetry properties of electron orbitals, J. Phys. Chem. Solids. 10 (1959) 87–98. https://doi.org/10.1016/0022-3697(59)90061-7.

[10] S. Leelashree, S.N. Kaul, S. Srinath, Effect of progressive substitution of Lu by Ho

on the structural and dielectric properties of nanocrystalline LuFeO3 orthoferrite, Mater. Res. Bull. 145 (2022) 111570. https://doi.org/10.1016/j.materresbull.2021.111570.

[11] L. Néel, Relation entre la constante d'anisotropie et la loi d'approche à la saturation des ferromagnétiques, J. Phys. Le Radium. 9 (1948) 193–199. https://doi.org/10.1051/jphysrad:0194800906019300.

[12] N. Akulov, Zur Atomtheorie des Ferromagnetismus, Zeitschrift Für Phys. 54 (1929) 582–587. https://doi.org/10.1007/BF01338489.

[13] S.P. Mathew, S.N. Kaul, Magnetization processes in nanocrystalline gadolinium, J. Phys. Condens. Matter. 24 (2012). https://doi.org/10.1088/0953-8984/24/25/256008.

[14] S.N. Kaul, U. Messala, Chirality-driven intrinsic spin-glass ordering and field-induced ferromagnetism in Ni3Al nanoparticle aggregates, J. Magn. Magn. Mater. 401 (2016) 539–558. https://doi.org/10.1016/j.jmmm.2015.10.058.

[15] W.F. Brown, Theory of the approach to magnetic saturation, Phys. Rev. 58 (1940) 736–743. https://doi.org/10.1103/PhysRev.58.736.

[16] J. William Fuller Brown, The Effect of Dislocations on Magnetization Near Saturation, 60 (1941) 1–9.

[17] H. Kronmuller, Micromagnetism in Amorphous Alloys, IEEE Trans. Magn. 15 (1979) 1218–1225. https://doi.org/10.1109/TMAG.1979.1060343.

[18] E. M. Chudnovsky and R. A. Serota, Spin-glass and ferromagnetic states in amorphous solids, Phys. Rev. B. 26 (1982) 2697–2699.

[19] S. Chikazumi, Physics of Ferromagnetism, Second, Oxford University Press, New York, 2005.

[20] U. Chowdhury, S. Goswami, D. Bhattacharya, J. Ghosh, S. Basu, S. Neogi, Room temperature multiferroicity in orthorhombic LuFeO3, Appl. Phys. Lett. 105 (2014) 10–14. https://doi.org/10.1063/1.4892664.

CHAPTER 5

Dielectric polarization and relaxation in $Lu_{1-x}Ho_xFeO_3$ $(0 \leq x \leq 1)$

In this chapter, we have investigated the effect of Ho doping on the dielectric and ferroelectric properties of nanocrystalline $Lu_{1-x}Ho_xFeO_3$ $(0 \leq x \leq 1)$*. Furthermore, the orthorhombic distortions spontaneously break the centrosymmetry of the underlying cubic lattice and thereby giving rise to dipole moment. Thus, orthorhombic distortions are expected to have a profound effect on the dielectric properties. Accordingly, the static and dynamic dielectric response at room temperature and as a function of temperature has been studied in detail.*

5.1. Introduction

In the previous chapter, the structural properties of the hydrothermally synthesized $Lu_{1-x}Ho_xFeO_3$ are studied. The crystallite size and particle size are also calculated and found that they are nanosized. The size of the crystallite and particle is expected to have profound effects on the dielectric properties. In this chapter, the structural and size effects on the dielectric and ferroelectric properties are studied. Accordingly, the static and dynamic dielectric response has also been studied in detail.

5.2. Electric polarization – electric field hysteresis loops

5.2.1. Room temperature studies

It is customary to measure the electric polarization (P) versus electric field (E) hysteresis loop of a ferroelectric material and such P-E loops, taken over different electric field ranges, for the nanocrystalline $Lu_{1-x}Ho_x$FeO3 samples are displayed in figures 4.1 (a) and (b) These loops were measured by applying standard bipolar triangular voltage pulses in the Sawyer-Tower circuit. E is kept constant for a time period (tmeas) at each step, ranging from 1 ms to 50 ms in different experimental runs. This measurement protocol works well for materials with high electric polarization. Figures 5.1 (a) and (b) bear out clearly that the polarization does not saturate even when voltages close to the breakdown voltage are applied.

The maximum value of polarization, P_{max}, corresponding to the maximum electric field that could be applied just before the electrical breakdown occurs, is plotted as a function of Ho concentration in figure 5.2 (a). This behaviour is well represented by the power-law expression, $y = a + b x^c$, (red curve through the data) with the parameters a = 1.8 (2), b = -1.7 (3) and c = 0.33. The breakdown field for the samples with different Ho concentrations is also shown in figure 5.2 (b); the sample with $x = 0.1$ is found to have the highest breakdown field.

The P-E loops, so measured, are a cumulative response of linear components, e.g., resistance, capacitance, etc., and non-linear elements such as remanent polarization and non- remanent polarization. The non-remanent contributions is from the electric charge leakage currents caused by conducting particle surfaces/interfaces and particle boundaries. It is observed that increasing the time period increases the loop area, indicating an increase in the leakage component. The polarization, P_m, measured at the highest electric field, E_m, to which

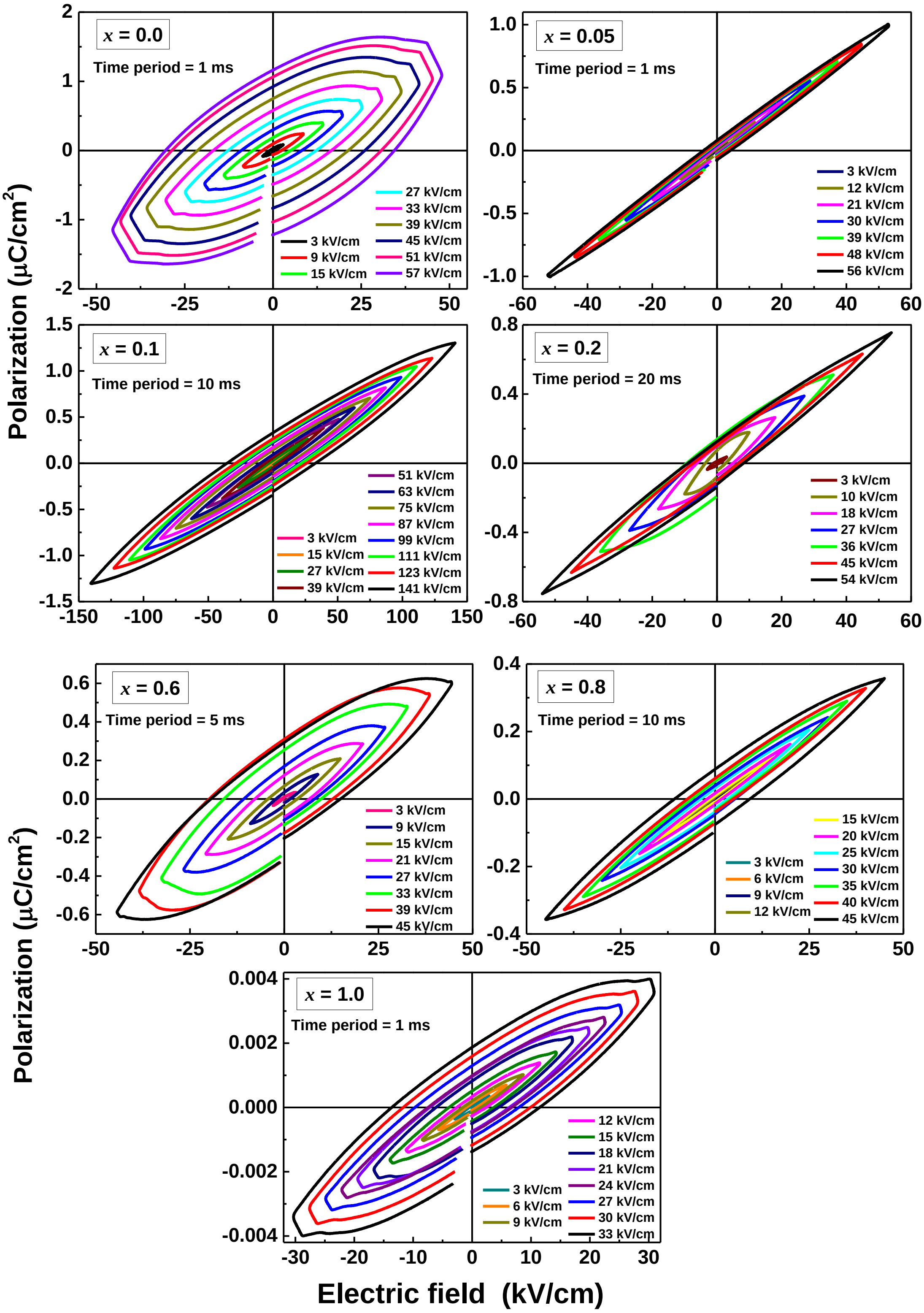

Figure 5.1 (a). Room temperature P-E hysteresis loops for the compositions, $0.0 \leq x \leq 0.5$

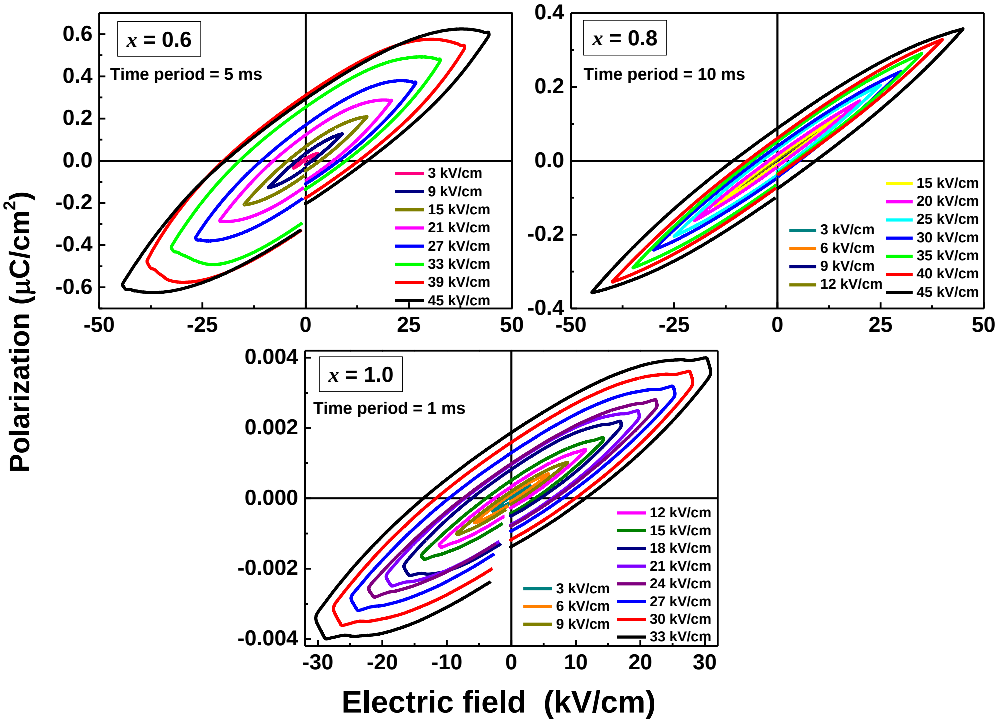

Figure 5.1 (b). Room temperature P-E hysteresis loops for the compositions, *x* = 0.6, 0.8, 1.0.

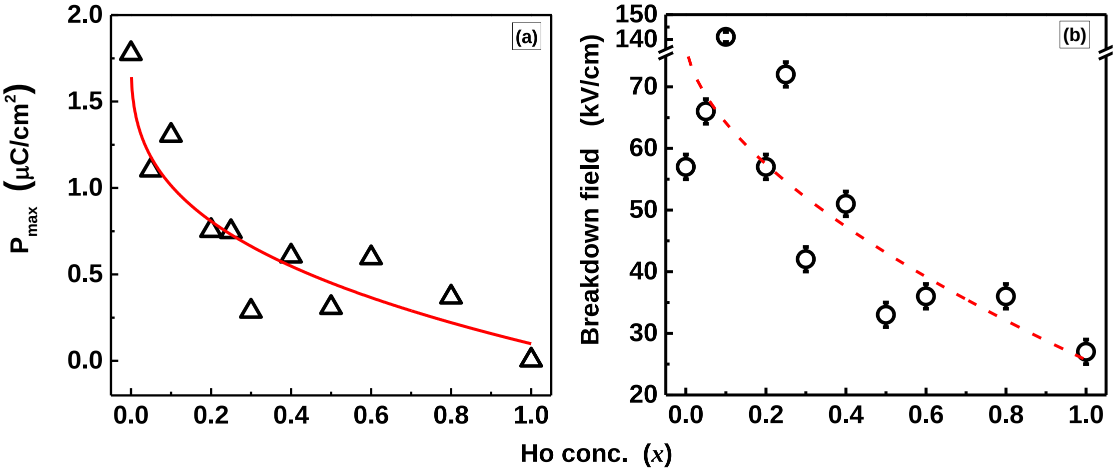

Figure 5.2. (a) Maximum polarization (P_{max}) measured at a field very close to the breakdown field; **(b)** Breakdown field as a function of the Ho concentration, *x* (the red dotted line through the data is only guide to the eye).

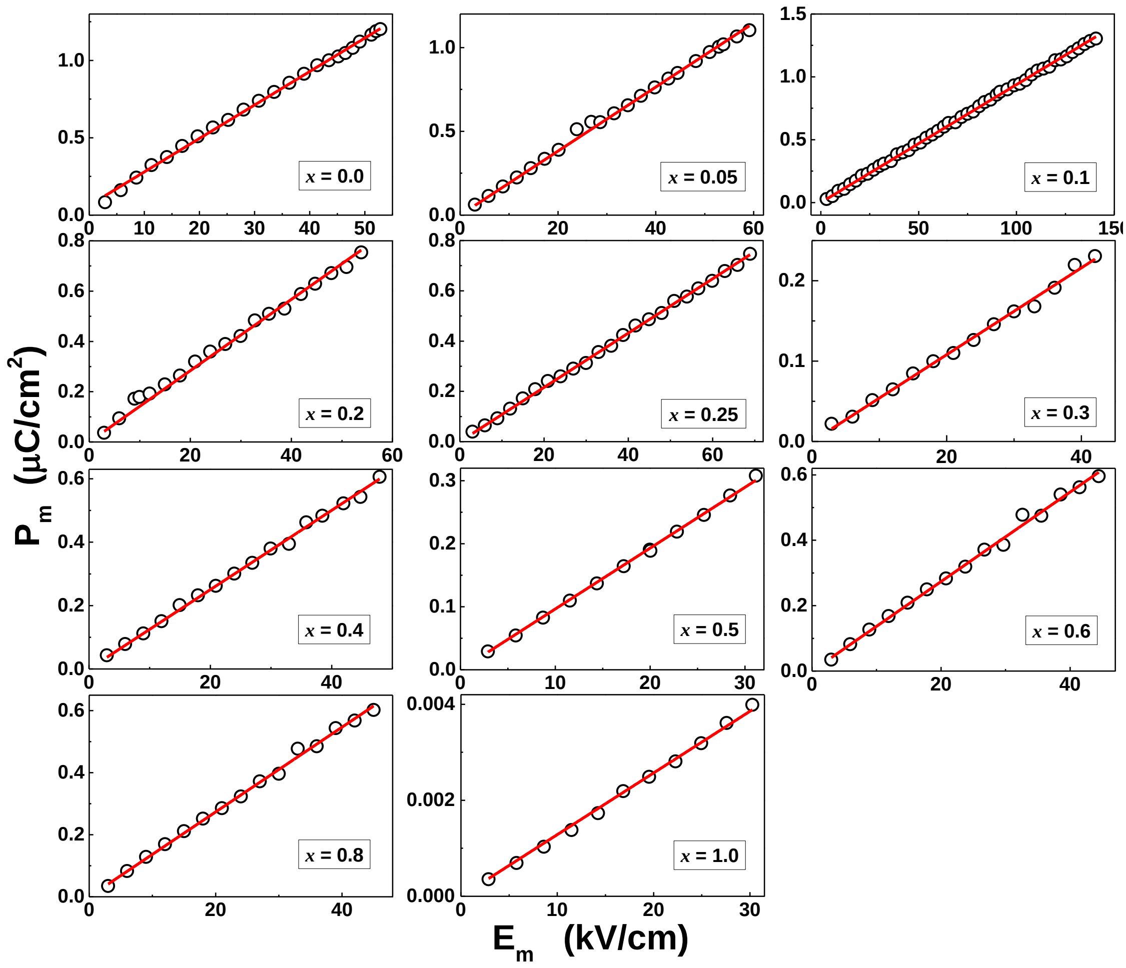

Figure 5.3. A linear relation between maximum polarization, P_m, and maximum field, E_m.

the sample is cycled while tracing a P-E loop, is plotted against E_m in figure 5.3. A linear relation between P_m and E_m indicates that the linear components give dominating contributions, and hence the non-linear part has to be separated out to study the intrinsic polarization behavior of the nanocrystalline samples in question.

To get rid of the non-remanent contributions and thereby arrive at the true intrinsic remanent hysteresis loop, the measurement protocol, detailed in reference [1,2], has been used. The remanent hysteresis loops are measured with the help of Vision Data Acquisition and Management Software in Precision Materials Analyzer from Radiant Technologies. An example of the effect of the measurement time (t_{meas}) on the shape of the remanent Pint – E hysteresis loops is given in figure 5.5. The intrinsic polarization, P_{int}, versus electric field, E, P_{int}-E loops, shown in 5.4 for x = 0.2 and measured at time periods 10 ms, 20 ms, 30 ms, serve to bring out the effect of time period on the P_{int}-E loops. With increasing time period, the area of the hysteresis loop increases and a steeper drop in P_{int} occurs as the field approaches its highest value; P_{int} has a nearly time-independent value at the highest applied field of 35 kV/cm. Sharper drop in P_{int} as E nears 35 kV/cm with increasing t_{meas} reflects the increasing contribution from leakage currents.

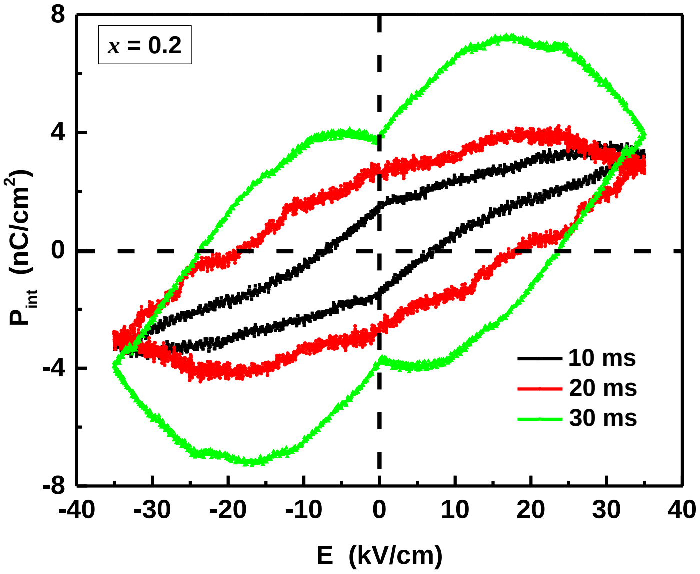

Figure 5.4. Intrinsic polarization measured as a function of electric field at measurement times 10 ms, 20 ms, and 30 ms.

The P_{int} – E hysteresis loops, optimized with respect to t_{meas} (t_{meas} = 20 ms) and typical of nanocrystalline $Lu_{1-x}Ho_xFeO_3$, are shown in figures 5.5 (a) and (b). Such loops establish the existence of permanent electric dipole moments and ferroelectric order in the present nanocrystalline samples at room temperature. The saturation intrinsic dielectric polarization, P_{int}^{sat}, obtained from the P_{int} – E hysteresis loops, is plotted against the Ho concentration, *x*, in the lower panel of figure 5.8. As *x* increases from *x* = 0 to *x* = 1, P_{int}^{sat} presents an overall decreasing trend with a dip at *x* = 0.4. The decrease in P_{int}^{sat} with increasing *x* can be qualitatively understood in terms of (i) the increase in the unit cell volume (Table 3.2) and (ii) the reduction in the electric dipole moment consequent upon the decline in orthorhombic distortion (Table 3.2), or equivalently in the FeO_6 octahedral tilt angles $\theta_{[101]}$ and $\varphi_{[010]}$ around $[101]_{pc}$ and $[010]_{pc}$ pseudo-cubic (pc) axes (Figure 3.7), caused by the higher ionic radius of Ho^{3+} compared to that of Lu^{3+}.

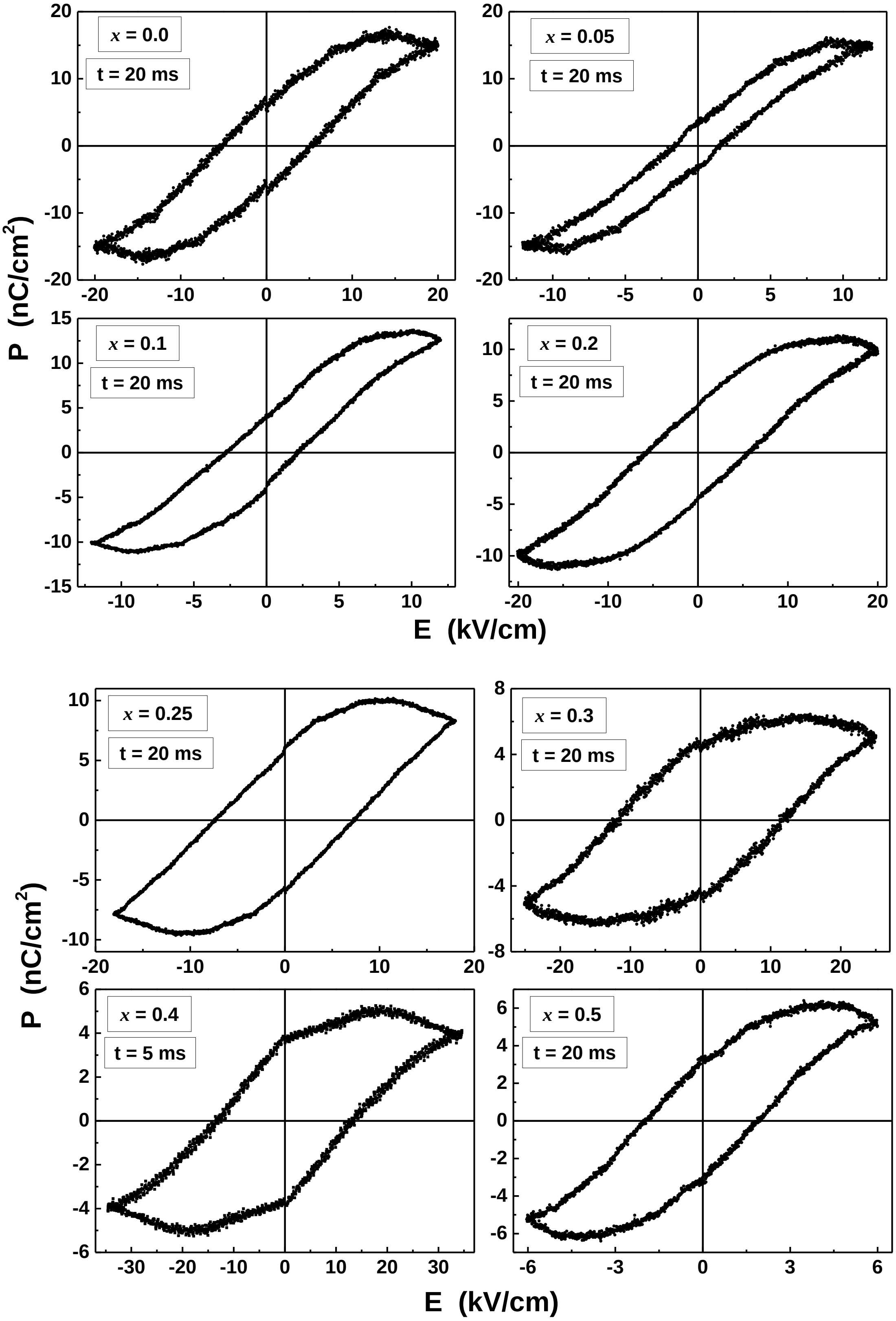

Figure 5.5 (a). Intrinsic Polarization (P_{int}) versus electric field hysteresis loops (measurement time = 20 ms) for the compositions x = 0.0 to 0.5.

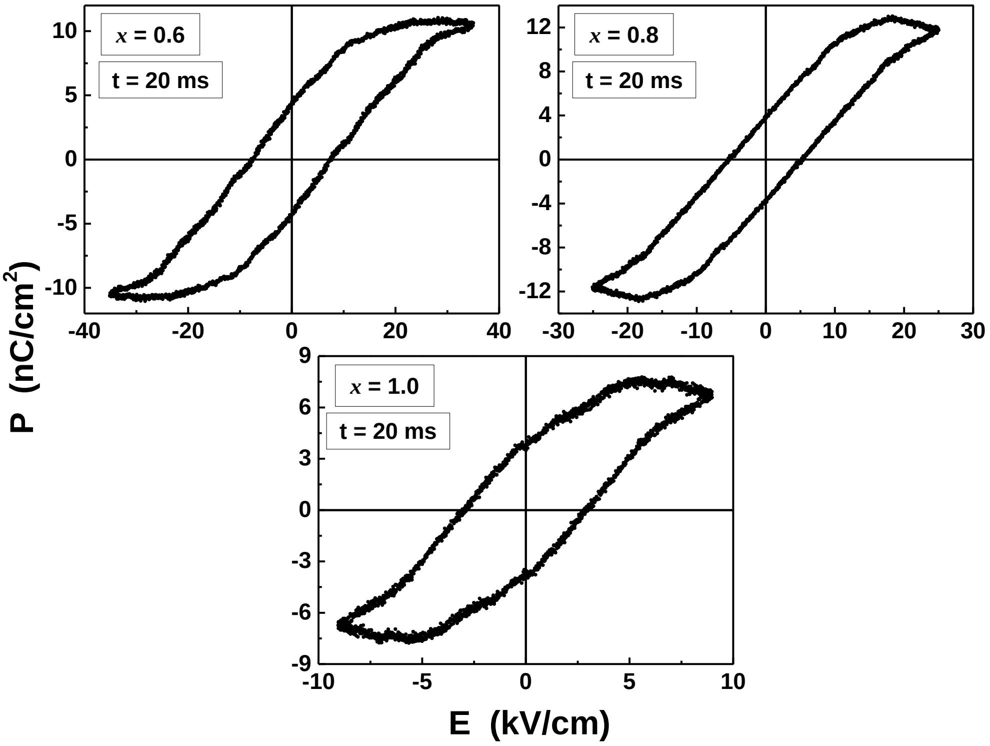

Figure 5.5 (b). Intrinsic Polarization (P_{int}) versus electric field hysteresis loops (measurement time = 20 ms) for the compositions x = 0.6, 0.8 and 1.0.

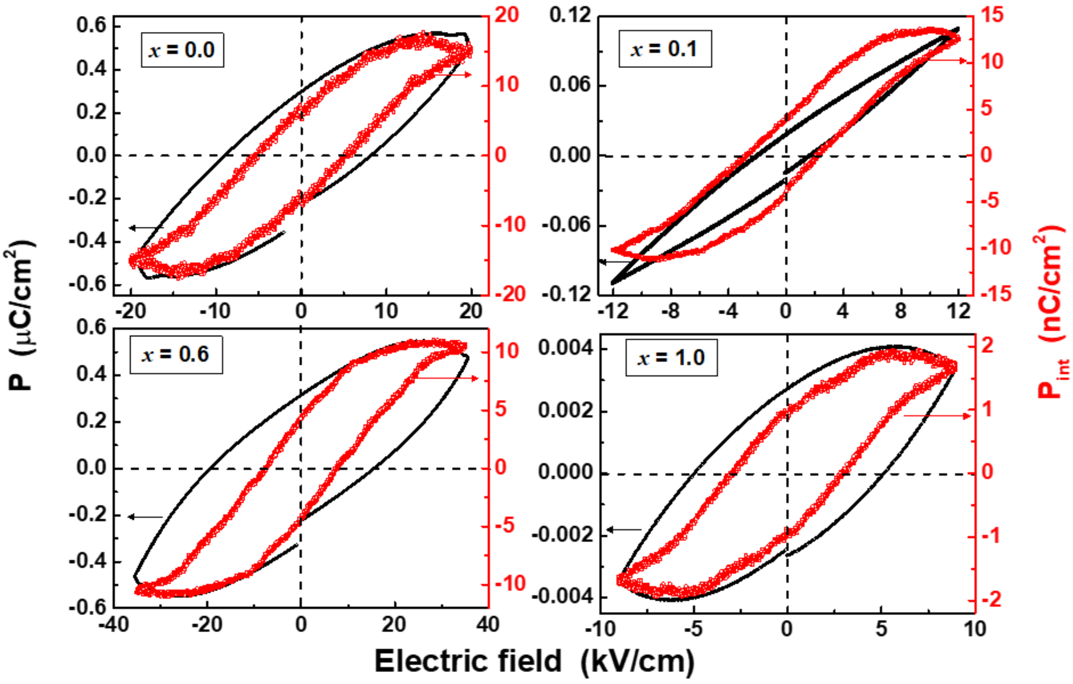

Figure 5.6. Comparison of the ordinary P-E loops with intrinsic P_{int}-E loops.

Figure 5.6 directly compares the intrinsic remanent (t_{meas}= 20 ms) and ordinary ferroelectric hysteresis loops for *x* = 0.0, 0.1, 0.6 and 1.0. From such a comparison, it is evident that the intrinsic remanent polarization is at least two orders of magnitude smaller. The larger magnitude of the total polarization in P-E loops is due to overwhelming contributions from non-remanent, non-switchable polarization.

5.2.2. Ferroelectric transition, T_c

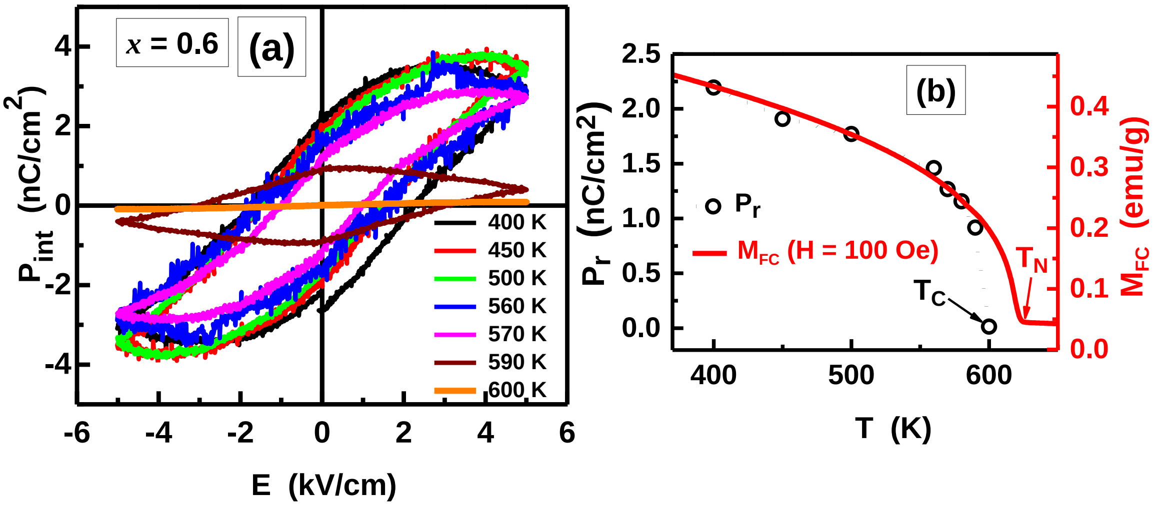

Figure 5.7. (a) Temperature dependent P_{int}-E loops; **(b)** Comparison between P_r and M_{FC} measured at H = 100 Oe.

In order to verify the Ferroelecric – Paraelectric transition temperature, T_c , the intrinsic electric polarization (P_{int}) versus electric field (E) hysteresis loops were measured at fixed temperatures within the range 300 K - 600 K. A typical example of the P_{int} – E hysteresis loops, so obtained, at a few selected temperatures is given for $x = 0.6$ in figure 5.7 (a). The temperature variation of remanent intrinsic polarization ($P_r = P_{in}$ at E = 0), in the range 400 K – 600 K, is shown in figure 5.7 (b). Like the spontaneous polarization (order parameter), P_r drops rapidly for temperatures above ~ 560 K and falls to a minute but finite value at T = 600 K. The P_{int} – E hysteresis loops couldn't be measured beyond T = 600 K because the sample broke down. This temperature is close to T_c = 625 K (figure 5.10 (c)) at which a peak in ε′(T) for $x = 0.6$ occurs. Similar agreement between the values of T_c, deduced from ε′(T) and P_r(T), is found in other compositions as well.

5.3. Dielectric properties

5.3.1. Room temperature studies

The real (ε′) and imaginary (ε″) parts of the complex dielectric permittivity, $\varepsilon* = \varepsilon' - i\,\varepsilon''$, have been measured at room temperature over the ac electric-field frequency range, 20 Hz $\leq f \leq$ 2 MHz, in order to study the dielectric relaxation [3–9] in nanocrystalline $Lu_{1-x}Ho_xFeO_3$. Essentially, two different types of frequency variations of the dispersion ε′(*f*) and absorption ε″(*f*) components of the ac-dielectric response have been observed on $\log_{10} f$ abscissa scale (refer to figure 5.17 and 5.19). Type-I: as a function of *f*, ε″ goes through a peak at f_{max} while ε′ increases with decreasing *f* and approaches a constant but composition-dependent value (20 – 50) at low frequencies in the compositions $0.2 \leq x \leq 0.8$. Type-II: both ε′ and ε″ increase with decreasing *f* and exhibit a very steep rise when *f* falls below ≈ 1 kHz reaching values as high as $10^3 – 10^s$ as *f* approach the lowest measurement frequency of 20 Hz, in Ho concentrations $0 \leq x \leq 0.1$ and 1.0.

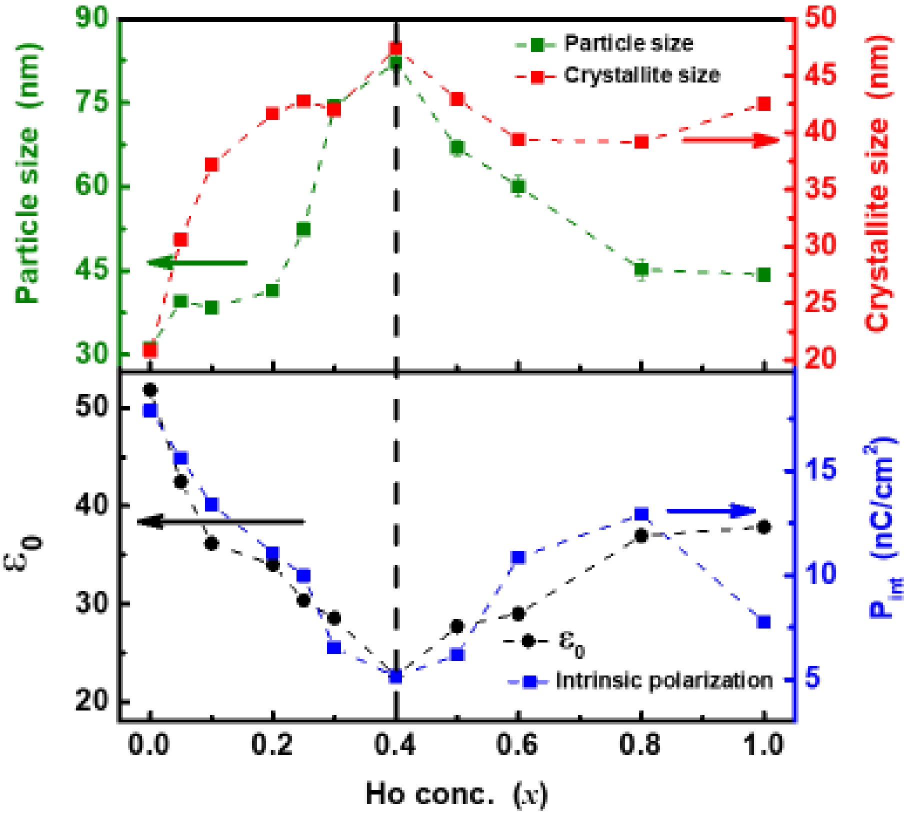

Figure 5.8. Top panel: particle size and crystallite size as a function of *x*. **Bottom panel:** static dielectric permittivity, determined from the fits based on eqns. (5.2) and (5.3) for *x* = 0.2 to 0.8 and intrinsic polarization (P_{int}) as a function of *x*, for all the

The dip in the $P_{int}^{sat}(x)$ and static dielectric permittivity, $\varepsilon_0(x)$, (for $\varepsilon_0(x)$, refer to the following subsection) at $x = 0.4$ is related to the peak in the crystallite/particle size (d) at $x = 0.4$ since smaller (larger) the d, larger (smaller) the crystallite/particle surface area and hence the accumulation of charge carriers [3] at the crystallite/particle surfaces/interfaces and boundaries. Thus, the peak in the crystallite/particle size at $x = 0.4$ (top panel in figure 5.8) accounts for the dip in both $P_{int}^{sat}(x)$ and $\varepsilon_s(x)$ (or even in $\varepsilon'(x)$ at any given frequency, see figure 5.9) at the same Ho concentration.

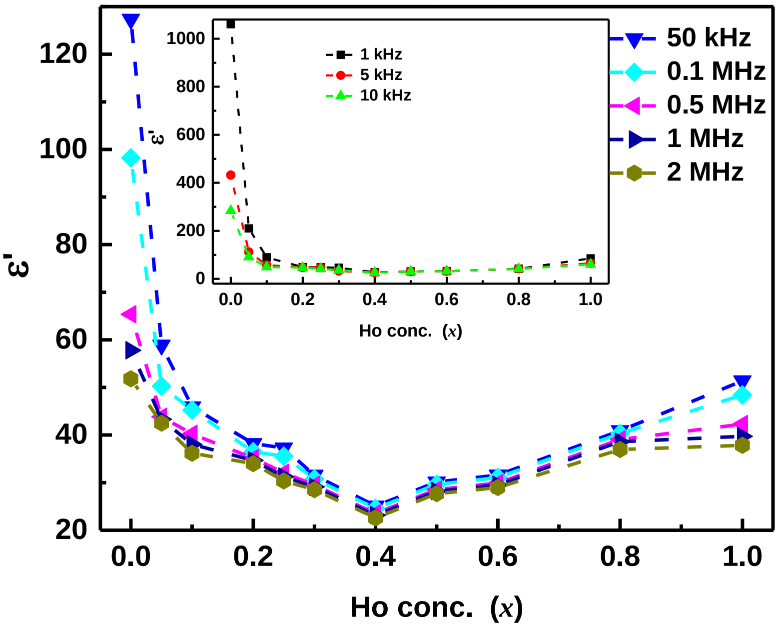

Figure 5.9. Real part of dielectric permittivity (ε′), measured at frequencies 50 kHz, 0.1 MHz, 0.5 MHz, 1 MHz and 2 MHz, plotted against Ho concentration. Inset: ε′ at 1 kHz, 5 kHz and 10 kHz as a function of Ho concentration.

5.3.2. High temperature studies

The real (ε') and imaginary (ε") parts of the complex dielectric permittivity, $\varepsilon * = \varepsilon' - i\,\varepsilon''$, have been measured over the ac electric-field frequency range, 1 kHz ≤ f ≤ 2 MHz, at temperatures 300 K ≤ T≤ 750 K on the nanocrystalline $Lu_{1-x}Ho_xFeO_3$ ($x = 0.0 - 1.0$) samples. ε′(T) and ε″(T) data are shown for $x = 0.0$ to 1.0 at different frequencies in figure 5.10 (a-c). ε′(T) goes through a broad peak at the ferroelectric (FE) – paraelectric (PE) transition temperature, T_c, which shifts to higher temperatures as the frequency increases. For the end compounds, $x = 0.0$ and $x = 1.0$, the shift in T_c, ΔT_c, is less than 1 % over the entire frequency range. For the intervening compositions, ΔT_c is very small (< 1 %) up to

100 kHz but becomes appreciable (~ 4 %) from *f* = 100 kHz to 2 MHz. In a conventional FE material, T_c is independent of frequency. The frequency-induced shift in T_c is a characteristic feature [5,8,10] of relaxor ferroelectrics. The variation of T_c (the temperature at which ε′(T) peaks) at the frequency *f* = 10 kHz (note that up to this frequency hardly any shift in the peak is observed) with *x* is compared with that of T_N in figure 5.11. We shall discuss the implications of such a comparison between T_c and T_N at a later stage in the text.

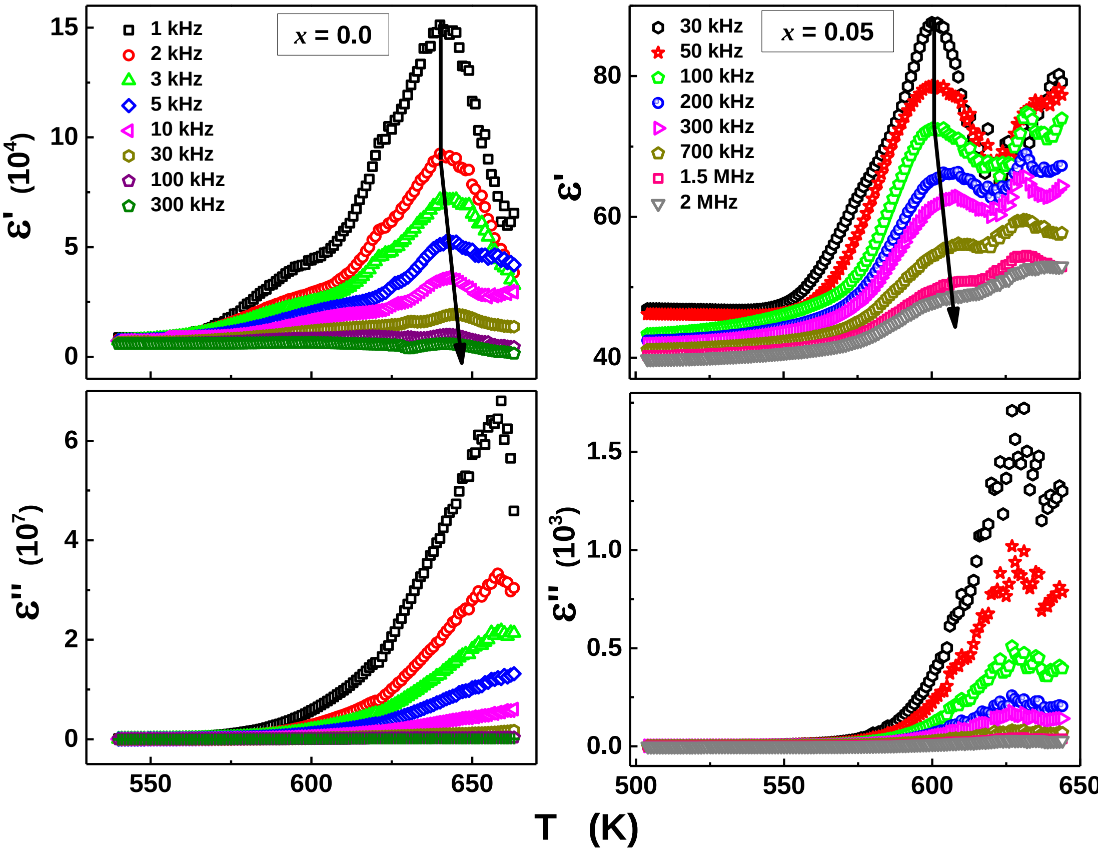

Figure 5.10. (a) $\boldsymbol{\varepsilon'}$ and $\boldsymbol{\varepsilon''}$ as a function of temperature for *x* = 0 and 0.05.

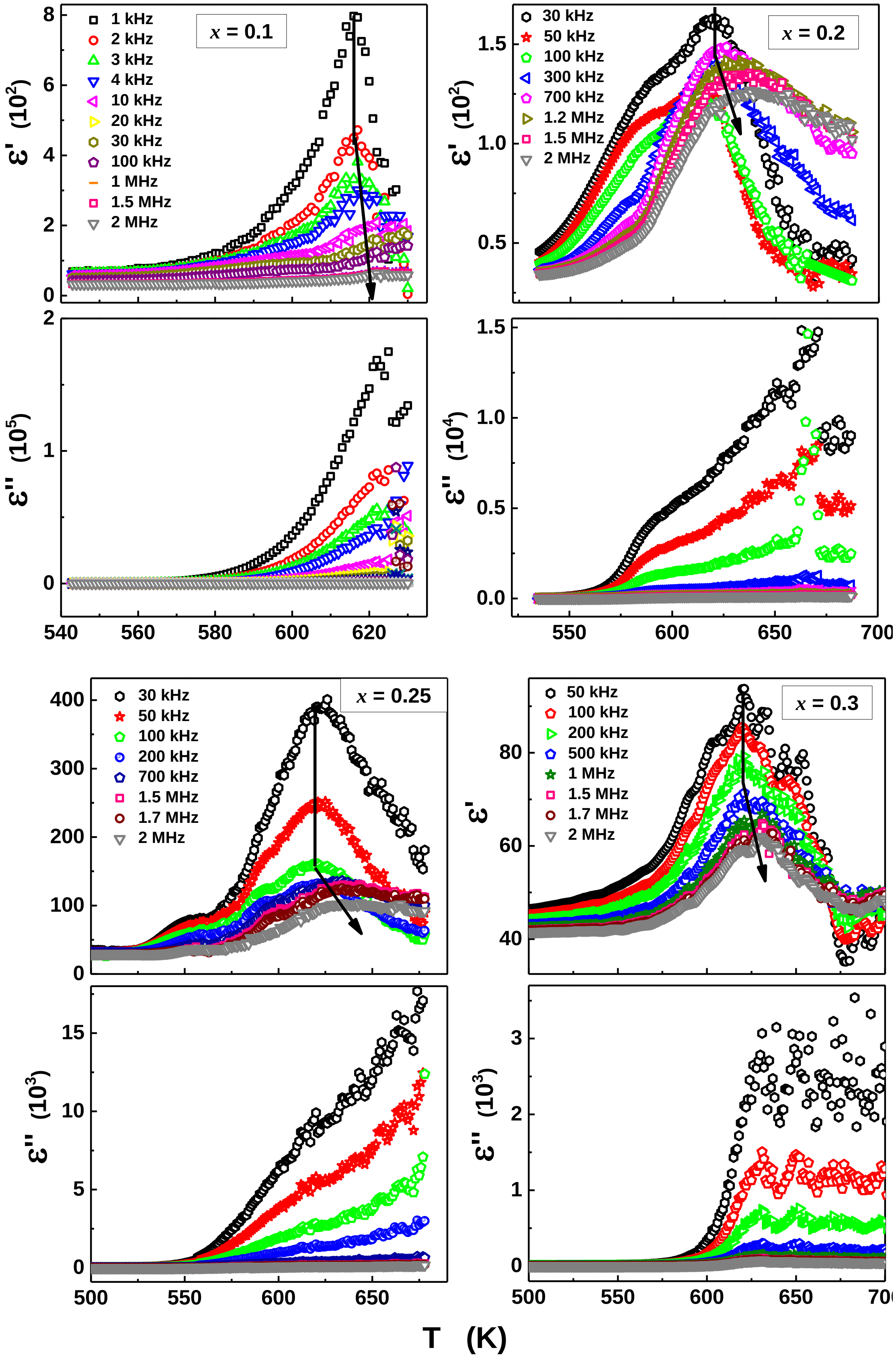

Figure 5.10. (b) ε' and ε'' as a function of temperature for $x = 0.1$ to 0.3.

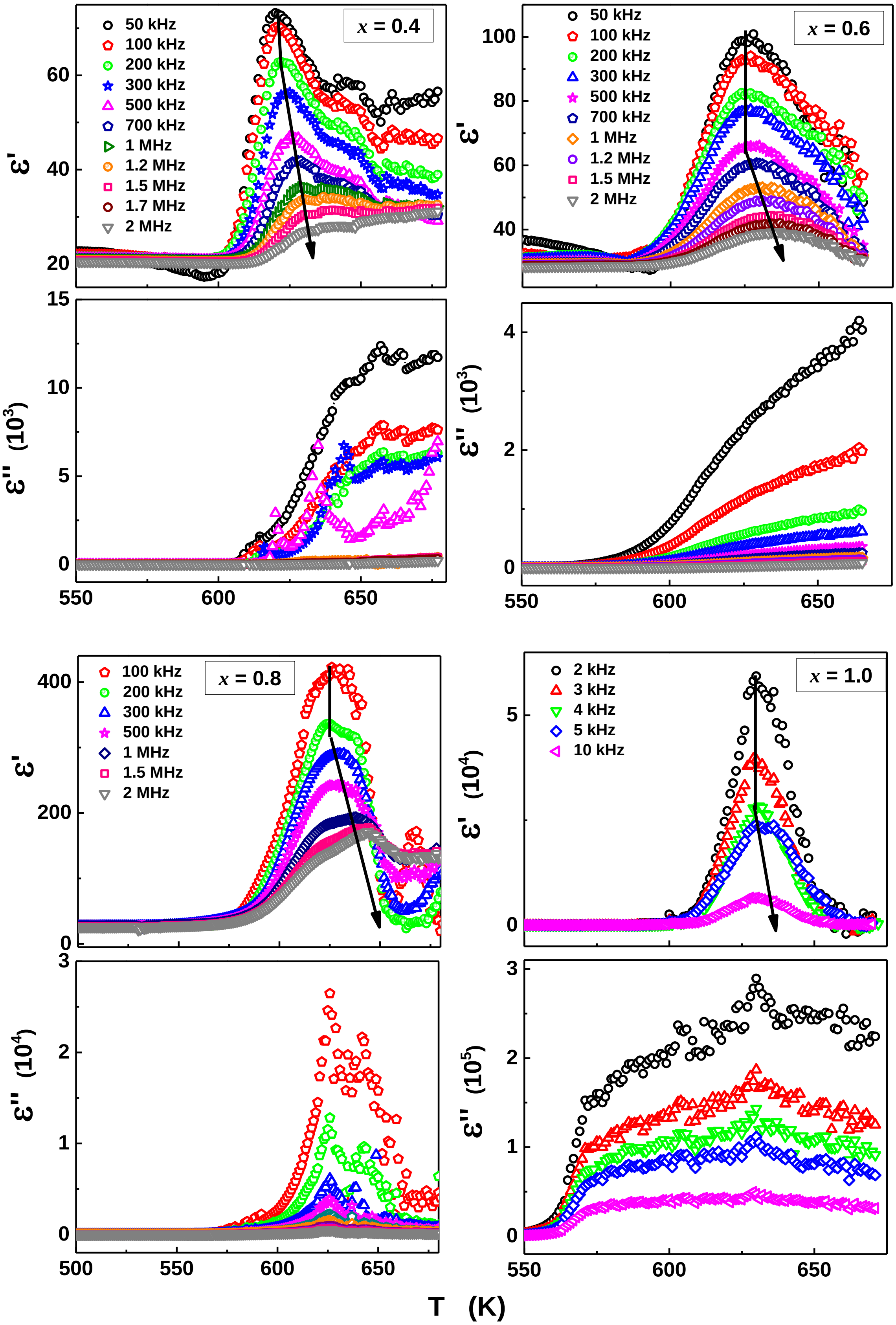

Figure 5.10. (c) $\boldsymbol{\varepsilon}'$ and $\boldsymbol{\varepsilon}''$ as a function of temperature for $x = 0.4$ to 1.0.

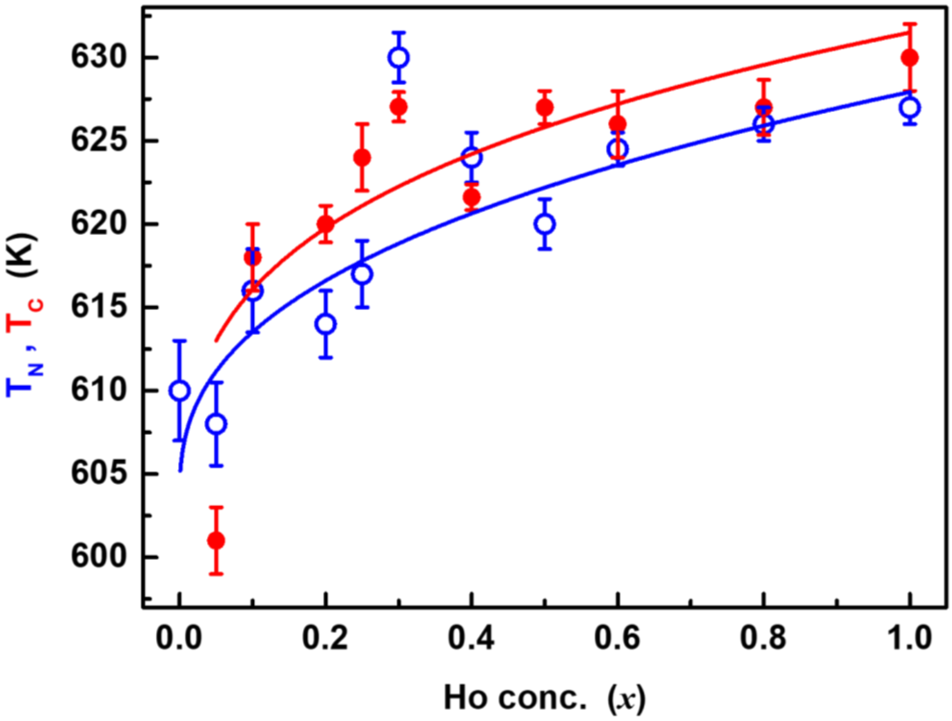

Figure 5.11. Variation of T_N and T_C with *x*.

5.3.3. Relevant structural features

To ascertain whether or not the FE – PE phase transition is associated with a structural phase transition, x-ray diffraction (XRD) patterns were measured on powder samples at fixed temperatures in the range 300 K to 835 K. Before recording the XRD spectra, thermodynamic equilibrium was ensured by maintaining the sample temperature constant (to within ± 1 K) for half an hour at a given predetermind value. The XRD spectra alog with Rietveld refinement for $x = 0.2$ at all temperatures are shown in figure 5.13 (a-c). XRD data were taken at closer temperature intervals (~ 5 K) over the temperature range 600 K – 630 K near T_c = 620 K / T_N = 614 K (Fig.5.11) of $x = 0.2$ and at temperatures (800 K – 835 K), well above T_c / T_N, where the sample is in the paraelectric (PE) / paramagnetic (PM) state. Rietveld refinement of the XRD spectra reveals the following. (i) Orthorhombic structure (for reference, a schematic representation of the orthorhombic crystal structure, belonging to the Pbnm space group, is shown in the figure 3.6 (b)) is retained over the entire temperature range covered in the present XRD experiments. This implies that the FE – PE (AF – PM) phase transition at T_c (T_N) is not accompanied by a structural phase transition. (ii) As functions of temperature, the lattice parameters a, b, c and the unit cell volume go through a shallow dip at T ≈ 610 K, which lies just below T_N =

614 K (figure 5.14 and its insets). (iii) A dip in the Fe – O(1), O(1) – Fe and Fe – O(2) bond lengths (figure 5.15(a) and 15(b)) occurs at a temperature which is closer to T_c = 620 K than T_N = 614 K. (iv) Such features in the temperature variations of the lattice parametrs, unit cell volume and Fe – O bond lengths are accompanied by a sharp peak (minimum) at T_c = 620 K in the Fe - O(1) – Fe (Fe – O(2) - Fe) bond angle, as is evident from figure 5.15(c) and its inset (figure 5.15(d)).

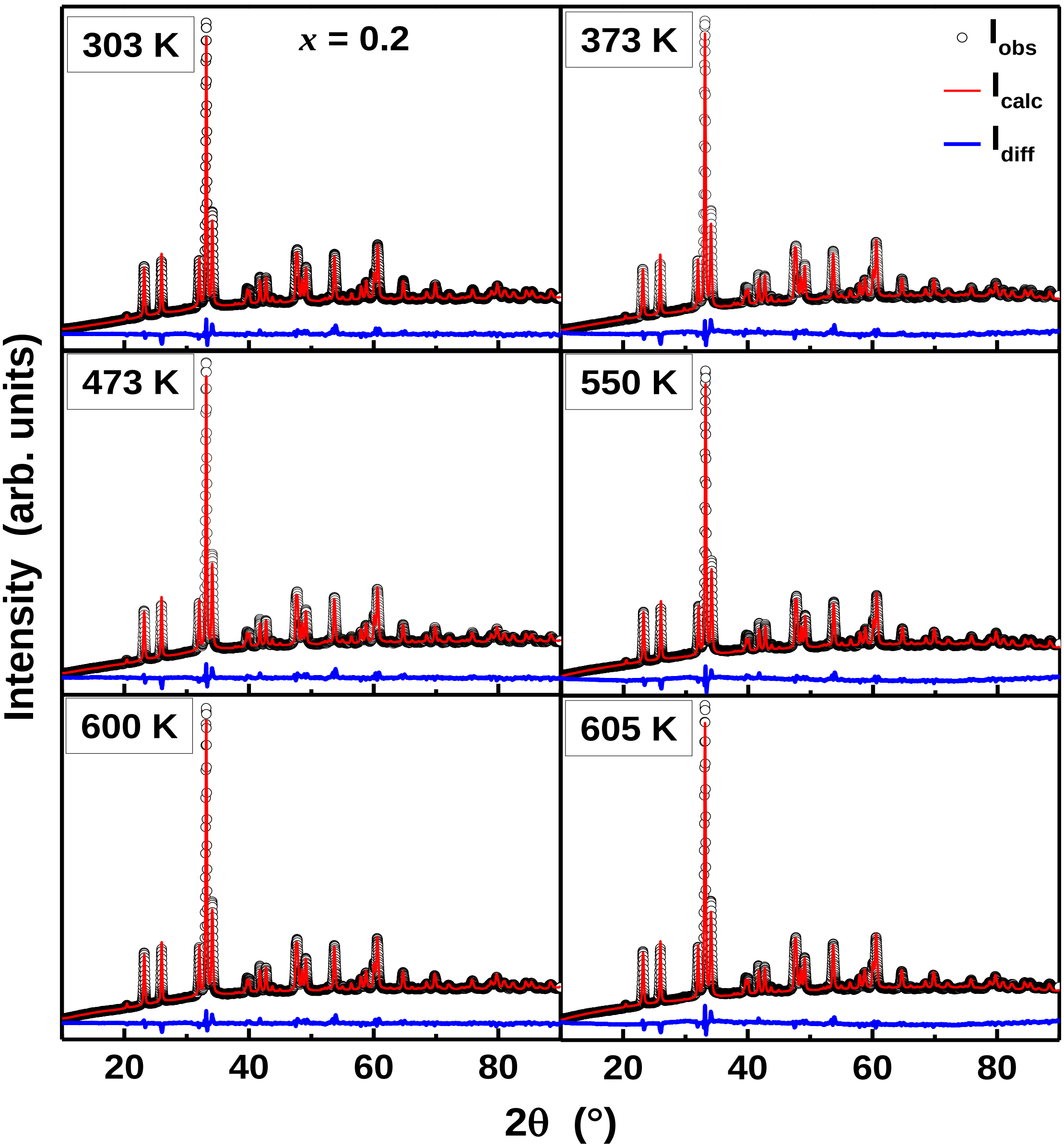

Figure 5.13. (a) Rietveld refinement of x = 0.2 at T = 303 K, 373 K, 473 K, 550 K, 600 K, 605 K.

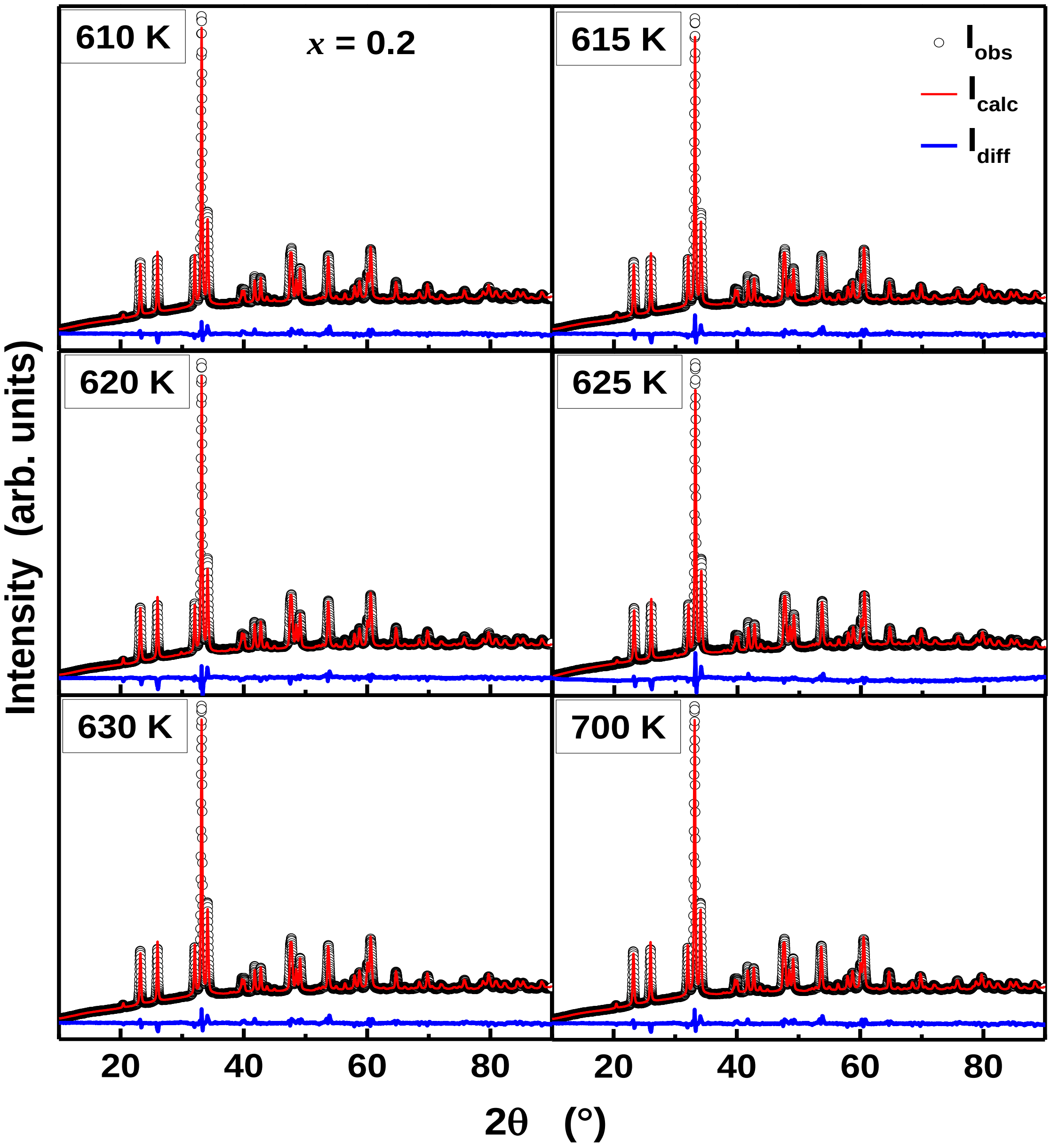

Figure 5.13. (b) Rietveld refinement of $x = 0.2$ at T = 610 K, 615 K, 620 K, 625 K, 630 K, 700 K.

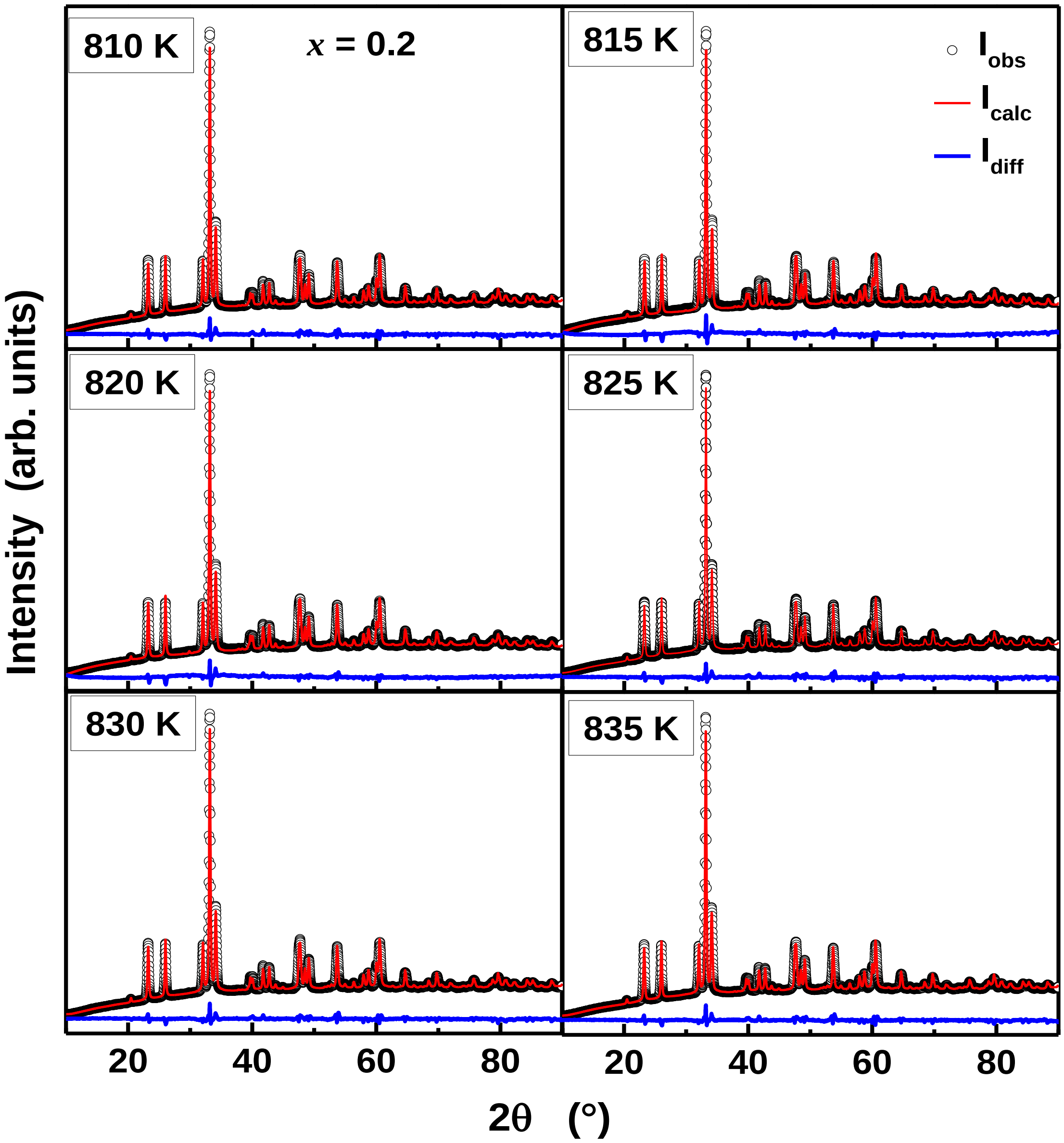

Figure 5.13. (c) Rietveld refinement of x = 0.2 at T = 810 K, 815 K, 820 K, 825 K, 830 K, 835 K.

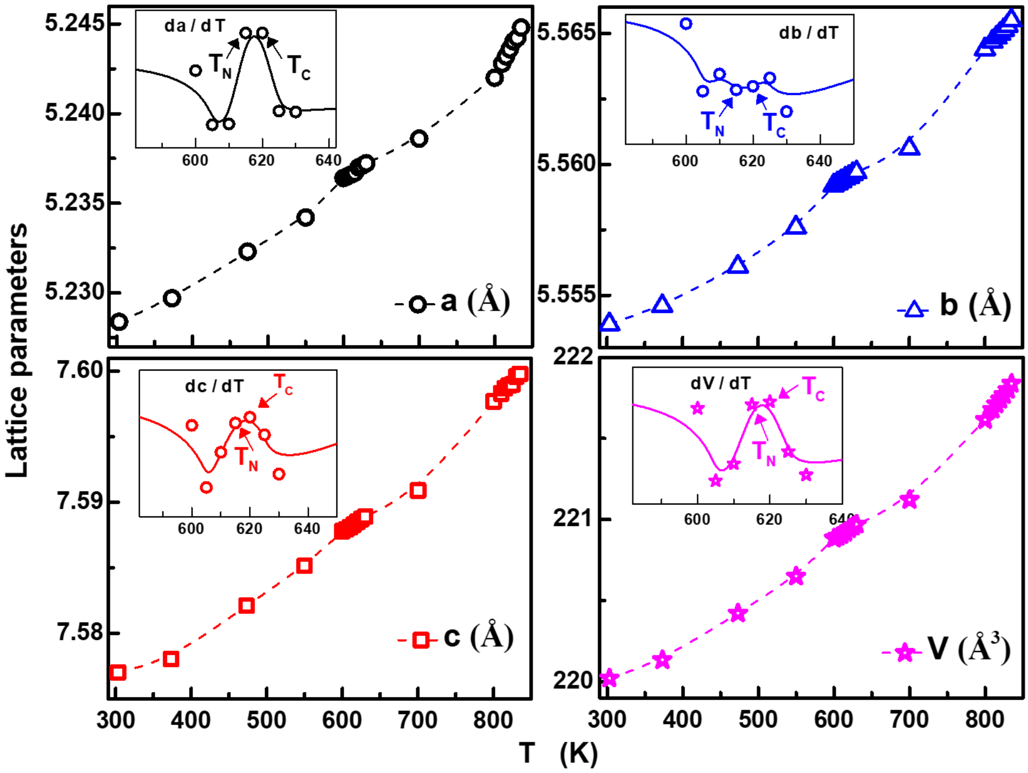

Figure 5.14. Variation of lattice parameters (a,b,c) and unit cell volume (V) as a function of T; **Inset.** Derivatives with respect to T.

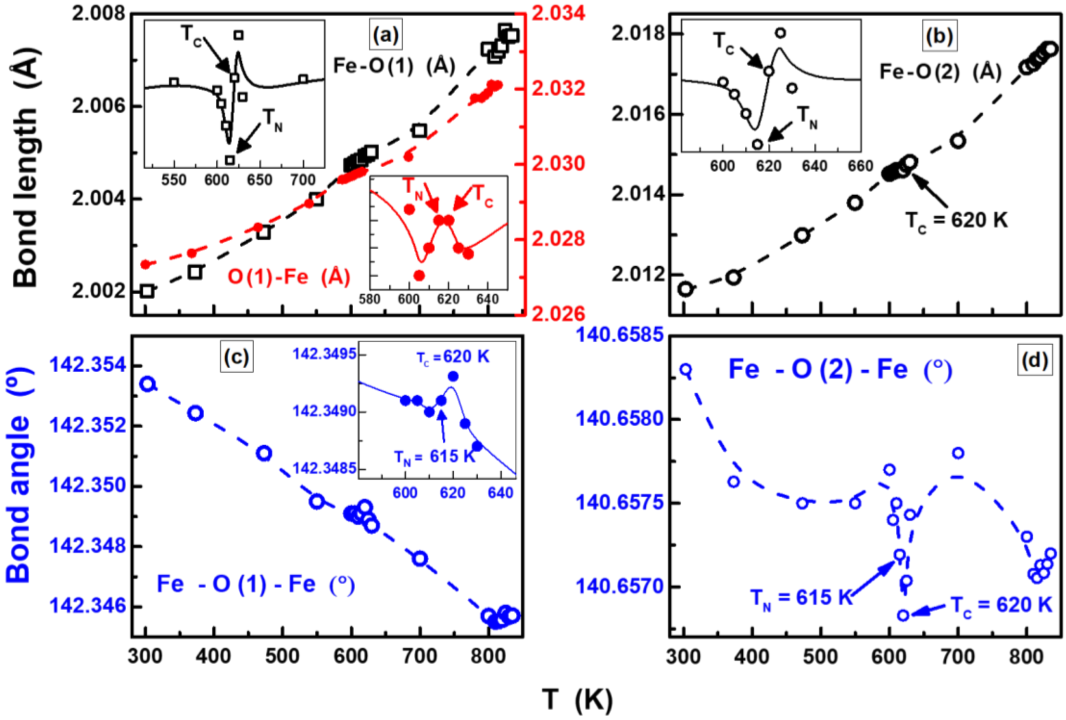

Figure 5.14. Variation of bond lengths and bond angles as a function of T; **Insets of (a & b).** Derivatives with respect to T. **Insets of (c).** Enlarged view around T_N and T_C.

That T_N tracks T_c (apparent in figure 5.11), is clearly brought out by a direct comparison between $M_{ZFC}(T)$, measured at H = 100 Oe, and $\varepsilon'(T)$ at f = 10 kOe, as shown for a few representative compositions in figure 5.16. This finding asserts that a magneto-electric coupling exists between the magnetic and ferroelectric order parameters.

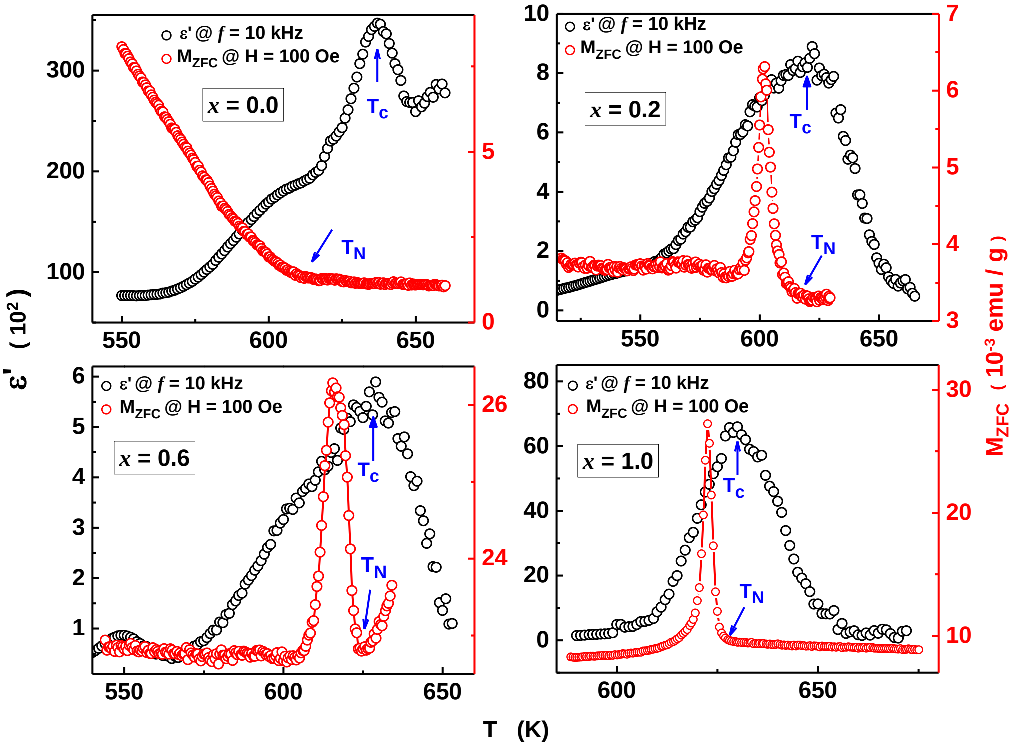

Figure 5.16. Real part of dielectric permittivity (ε′) measured at frequency 10 kHz is plotted along with M_{ZFC} measured at 100 Oe against temperature for x = 0.0, 0.2, 0.6, 1.0.

5.4. Dielectric relaxation

5.4.1. Ho Functional dependence

To analyze the ε′(f) and ε″(f) data measured at room temperature, use has been made of the modified Debye expressions that take into account the Cole-Cole distribution of relaxation times [7].

$$\varepsilon^* = \varepsilon' - i\,\varepsilon'' = \varepsilon_\infty + \frac{(\varepsilon_0 - \varepsilon_\infty)}{1 + (i\omega\tau)^{1-\alpha}} \qquad eqn\ (5.1)$$

with

$$\varepsilon'(\omega) = \varepsilon_\infty + \frac{(\varepsilon_0 - \varepsilon_\infty)\left(1 + \cos\left(\frac{\beta\pi}{2}\right)(\omega\tau)^\beta\right)}{1 + 2\,(\omega\tau)^\beta \cos\left(\frac{\beta\pi}{2}\right) + (\omega\tau)^{2\beta}} \qquad eqn\ (5.2)$$

$$\varepsilon''(\omega) = (\varepsilon_0 - \varepsilon_\infty)\,\frac{(\omega\tau)^\beta \sin\left(\frac{\beta\pi}{2}\right)}{1 + 2\,(\omega\tau)^\beta \cos\left(\frac{\beta\pi}{2}\right) + (\omega\tau)^{2\beta}} \qquad eqn\ (5.3)$$

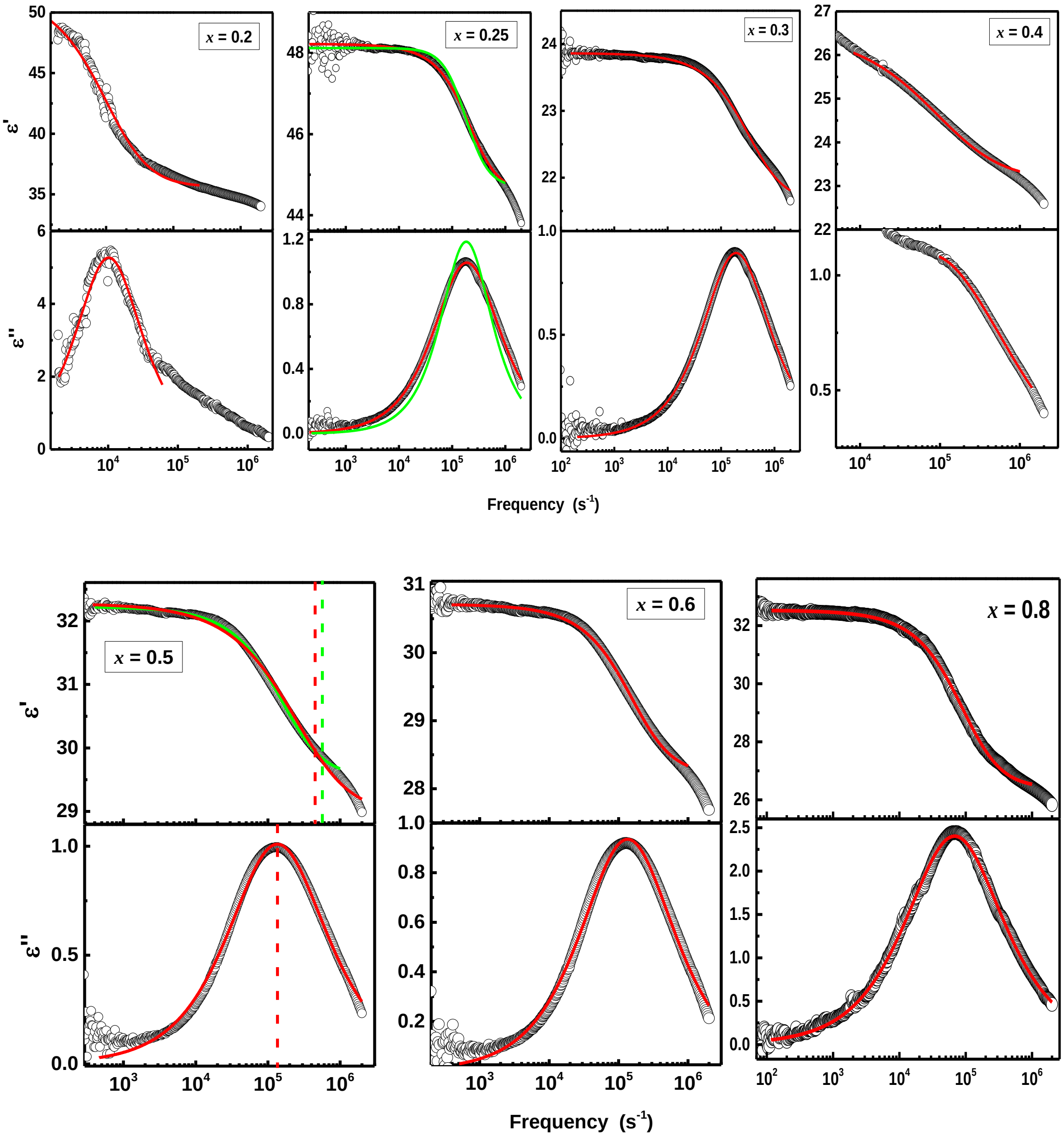

Figure 5.17. Frequency variations of the real (ε′) and imaginary (ε″) parts of dielectric permittivity characteristic of type-I relaxation behaviour for x = 0.2 to 0.8)

In eqns.(5.1) – (5.3), $\omega = 2\pi f$, ε_0 is static (limit $\omega \rightarrow 0$) permittivity, ε_∞ is the permittivity at extremely high frequencies (limit $\omega \rightarrow \infty$), τ is characteristic mean relaxation time, and $\beta = 1 - \alpha$. For $\alpha = 0$ or $\beta = 1$, eqns. (5.1) – (5.3) reduce to the well-known Debye expressions for the relaxation of non-interacting identical elementary electric dipoles all having the same value of τ. The deviation of α from zero in the range $0 < \alpha < 1$, or equivalently, β from unity in the range $0 < \beta < 1$, thus signals a non-Debye relaxation behavior in which the elementary dipoles interact with one another and different dipoles have different relaxation times. eqns. (5.2) and (5.3) predict (i) a peak in $\varepsilon''(f)$ at $f_{max} = 1 / 2\pi\tau$ and a step-like frequency variation of ε', and (ii) smaller the value of β compared to 1, broader the dispersion region of $\varepsilon'(f)$ and lower the height of the absorption peak in $\varepsilon''(f)$ at $\omega = 1/\tau$. The optimal fits (continuous red curves) to the $\varepsilon'(f)$ and $\varepsilon''(f)$ data (open circles), based on eqns. (5.3) and (5.3), with ε_0, ε_∞, τ and β as free-fitting parameters, displayed in figure 5.17 for a few representative compositions, clearly demonstrate that the type-I dielectric relaxation behavior, found in the compositions $0.2 \leq x \leq 0.8$, conforms well with both the above-mentioned theoretical predictions (i) and (ii).

The main observations made from such a comparison between theory and experiment are as follows. The theoretical fits, based on eqn.(5.3) that closely reproduce the peak in $\varepsilon''(f)$ at $f_{max} = 1 / 2\pi\,\tau$ (i.e., $\omega\,\tau = 1$) accurately determine both τ and β. By contrast, the parameters ε_0, ε_∞, τ and β, appearing in eqn.(5.2), are extremely sensitive to the frequency range chosen to fit the $\varepsilon'(f)$ data. To illustrate this, we treat the sample with $x = 0.5$ as an example. For this sample, the theoretical fit to $\varepsilon'(f)$, based on eqn.(5.2), yields $\tau_1 = 2.77 \times 10^{-7}$ sec. ($\tau_2 = 3.68 \times 10^{-7}$ sec.) and $\beta_1 = 0.901(3)$ ($\beta_2 = 0.763(5)$) in the frequency range 200 Hz $\leq f \leq$ 1 MHz (200 Hz $\leq f \leq$ 2 MHz). The green (red) vertical line marks the frequency $f_1 = 1 / 2\pi\,\tau_1$ ($f_2 = 1 / 2\pi\,\tau_2$) for the fit obtained in the frequency range 200 Hz $\leq f \leq$ 1 MHz (200 Hz $\leq f \leq$ 2 MHz). Evidently, as the upper bound of the frequency range is increased from 1 MHz to 2 MHz, τ increases ~ 1.3 times and tends to approach its correct value $\tau = 1.17 \times 10^{-6}$ sec., corresponding to the peak in $\varepsilon''(f)$. Thus, for extracting a reliable value of τ from the $\varepsilon'(f)$ data, measurements need to be extended to very high frequencies so as to cover the frequency range over which ε'' falls to very low values (≈ zero). To highlight the deviations observed from the Debye relaxation, the green curves in figure 5.17 for $x = 0.25$, obtained by setting $\beta = 1$ (Debye relaxation) in eqns. (5.2) and (5.3) are included in figure 5.17 for comparison. Such deviations are illustrative of the non-Debye relaxation behavior found in other compositions in the range $0.2 \leq x \leq 0.8$ as well.

The values of τ and β, determined from the ε″(*f*) data taken in the composition range $0.2 \leq x \leq 0.8$, are plotted against the Ho concentration, *x*, in figure 5.18. The overall increasing (decreasing) trend of τ (β) with increasing *x* can be qualitatively understood as follows. In this context, we recall that the mean relaxation time τ associated with the electric dipole orientation process is related to the mean height of the potential barrier, E_b, (which the elementary dipoles have to overcome to flip in the electric field direction) via the relation $\tau = \tau_0 \, exp(E_b/k_B T)$, where $1/\tau_0$ is the attempt frequency of the dipoles between the flips. According to the above expression, a distribution in relaxation times translates into distribution in the barrier heights. Smaller the value of β, the larger the width of the distribution. Thus, as *x* increases, the antisite-disorder-induced width of the E_b distribution increases while E_b shifts to higher values with the result that τ also shifts to higher values.

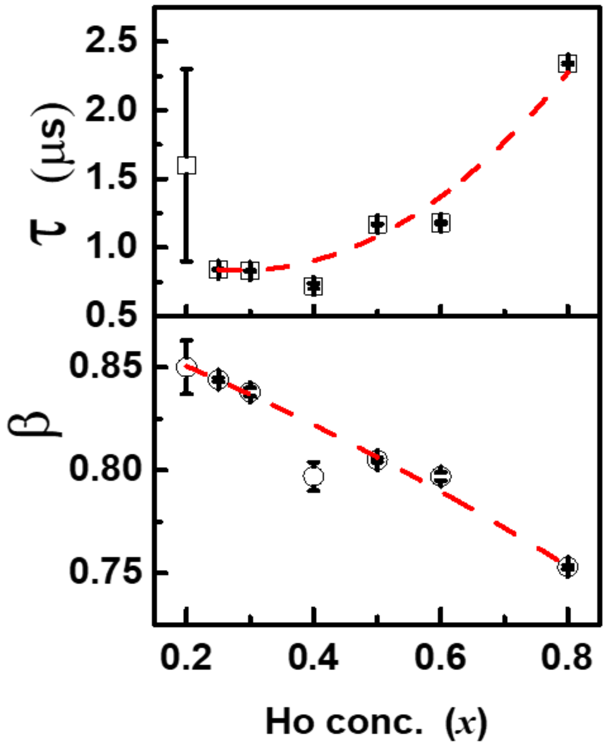

Figure 5.18. The variations of the relaxation time, τ and the exponent β, appearing in the eqns. (5.2) and (5.3), with the Ho concentration, *x*, in the range $0.2 \leq x \leq 0.8$. The red dashed curves through the data serve as a guide to the eye.

In sharp contrast with the type-I relaxation, the type-II dielectric relaxation (i.e., a steep "exponential-like" drop-in ε′ and ε″ with increasing *f*), observed in Ho concentrations $0 \leq x \leq 0.1$ and 1.0, does not directly follow from eqns. (5.2) and (5.3). Only when the condition $f >> 1/\, 2\pi\, \tau$ is satisfied do these equations predict a power-law behavior $\varepsilon'(f) \sim \varepsilon''(f) \sim \omega^{-\beta}$, which could describe the ε′(*f*) and ε″(*f*) observed in the frequency range 20 Hz $\leq f \leq$ 2 MHz. Thus, in the present case, the peak in ε″(*f*) and plateau in ε′(*f*) should lie well below the lowest measurement frequency of 20 Hz. Consistent with this expectation, the fits based on eqns.(5.2) and (5.3) yield the values of relaxation time τ (sec.) = 0.04(1), 0.055(2), 0.080(3) and 0.020(2) in the samples with x = 0.0, 0.05, 0.1 and 1.0, respectively, if the fit range is restricted to frequencies 20 Hz $\leq f \leq$ 10 kHz. Note that the fits to the ε′(*f*) and ε″(*f*) data over the entire frequency range 20 Hz $\leq f \leq$ 2 MHz give unphysically large parameter values with huge error bars (e.g., $\tau = 10^6 \pm 10^{10}$ sec.). The above-stated values of τ are several orders of magnitude larger than those characterizing the samples that exhibit Type-I relaxation. Considerably long relaxation times assert that the electric dipoles find it difficult to keep pace with the time variations of the applied electric field. Consequently, the orientational dipolar polarization makes only a small contribution to ε′(*f*) and ε″(*f*). Thus, dipolar polarization alone cannot account for the huge low-frequency (f = 20 Hz) values ($10^3 - 10^4$) of both ε′ and ε″ and hence of the dielectric loss, tanδ = ε″ / ε′.

By contrast, the relaxation associated with the hopping of charge carriers (electrons) between various localized states in the presence of an external ac-electric field can explain such high values of ε′ and ε″. The contributions to ε′ and ε″ due to this mechanism are given by [5]

$$\varepsilon'(f) = c' + A\ \tan\left(\frac{n\pi}{2}\right)\ \omega^{n-1} \qquad eqn\ (5.4)$$

$$\varepsilon''(f) = c'' + A\ \omega^{n-1} \qquad eqn(5.5)$$

where $0 < n < 1$. It is evident from figure 5.19 that eqns. (5.4) and (5.5) (continuous blue curves) adequately describe the Type-II relaxation behavior of ε′(*f*) and ε″(*f*), exemplified by the compositions x = 0.0 and 1.0, in the entire frequency range 20 Hz $\leq f \leq$ 2 MHz covered in the present experiments. These fits are far superior to those yielded by eqns. (5.2) and (5.3) for the dipolar relaxation in the same frequency range and give physically meaningful parameter values; the errors, in the worst case do not exceed 5 %, e.g., $n - 1$ = - 0.959(3), - 0.890(4), - 0.626(9) and - 0.541(6) for x = 0.0, 0.05, 0.1 and 1.0, respectively.

From these findings, we conclude that the dominant contribution to the type-II dielectric relaxation comes from the relaxation mechanism that sets in when the electron hopping time is larger than the time period of the ac driving electric field. This is the case in the pure LFO and HFO compounds (i.e., when x is close to 0 or 1) where the least disorder levels permit electron hopping. In the intermediate Ho concentration range $0.2 \leq x \leq 0.8$, the disorder, brought about by random occupation of Lu sites by Ho, tends to localize the electrons and block the electron hopping process. Consequently, the orientational dipolar polarization (type-1) relaxation takes over at such Ho concentrations.

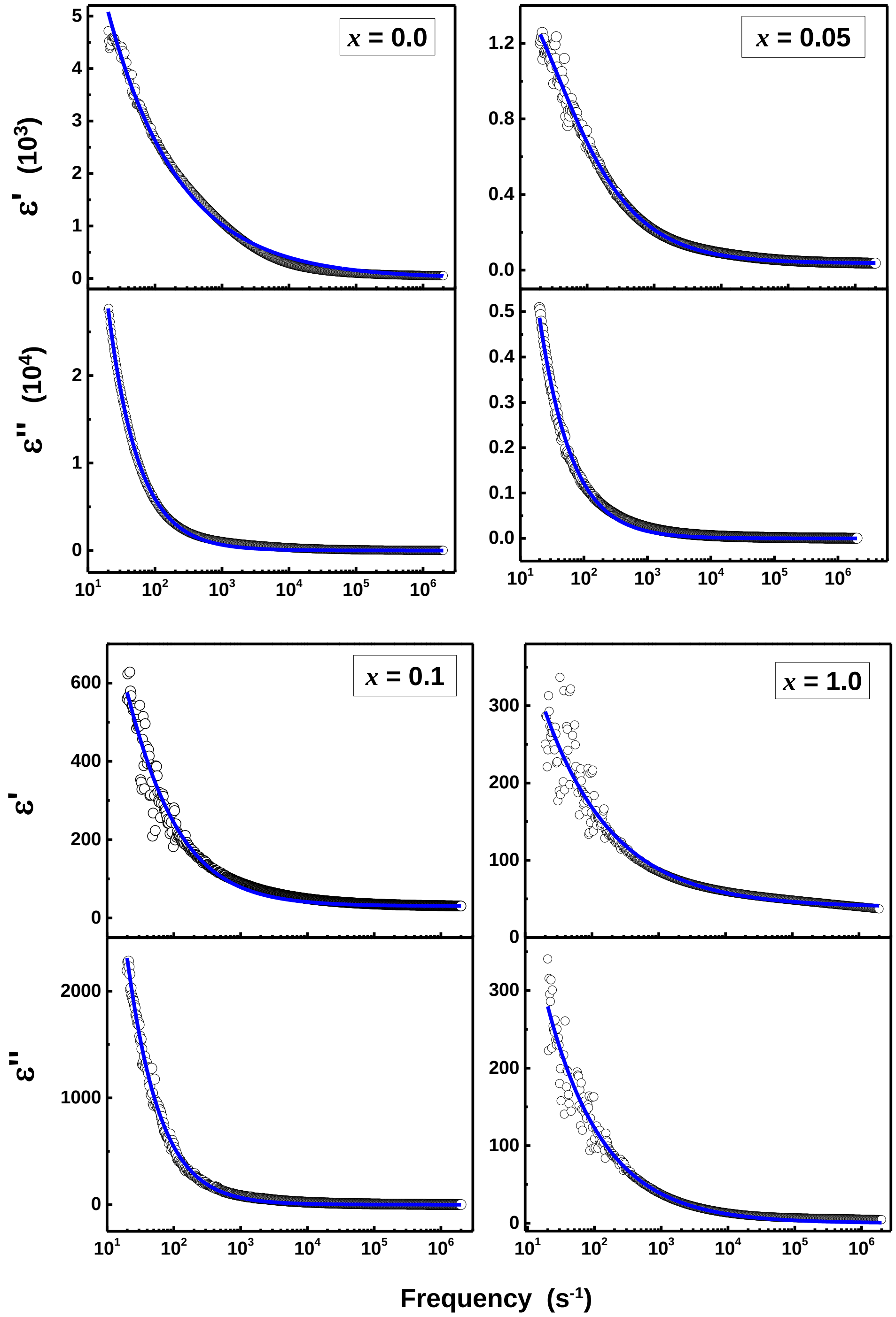

Figure 5.19. Type-II relaxation behavior for x = 0.0, 0.05, 0.1 and 1.0.

5.4.2. Thermal evolution of dielectric relaxation

Earlier ε′(*f*) and ε″(*f*) data, taken at room temperature over the ac electric-field frequency range, 20 Hz $\le f \le$ 2 MHz, unraveled two strikingly different types of frequency variations of ε′ and ε″ in nanocrystalline $Lu_{1-x}Ho_xFeO_3$. To unravel the effect of temperature on dielectric relaxation, the above-mentioned analysis of the ε′(*f*) and ε″(*f*) data, in terms of the Cole-Cole (CC) dipolar relaxation and the hopping charge (HC) relaxation models, is extended to temperatures as high as 750 K. Consistent with the earlier findings, at a given temperature, the type-1 and type-II frequency variations of ε′ and ε″ are described quite well by eqns (5.2) – (5.5) as shown in figures 5.20 and 5.21.

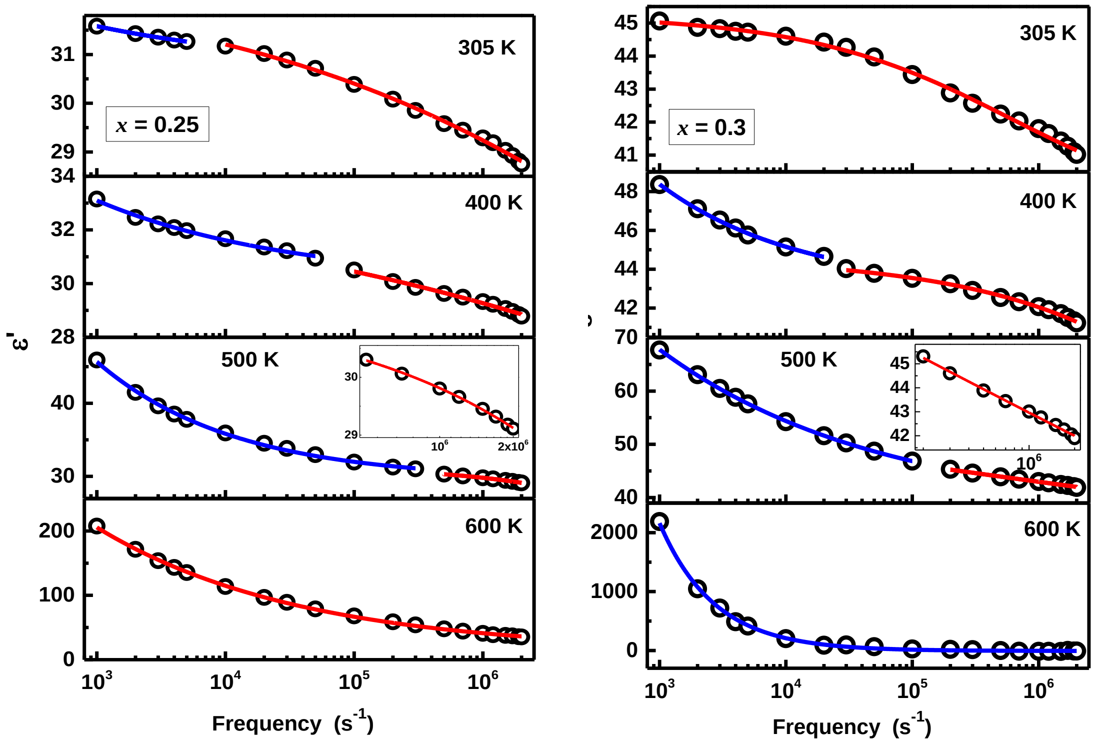

Figure 5.20 (a). Thermal evolution of Type-I and Type-II dielectric relaxation observed in ε′(*f*) for $x = 0.25$ and 0.3.

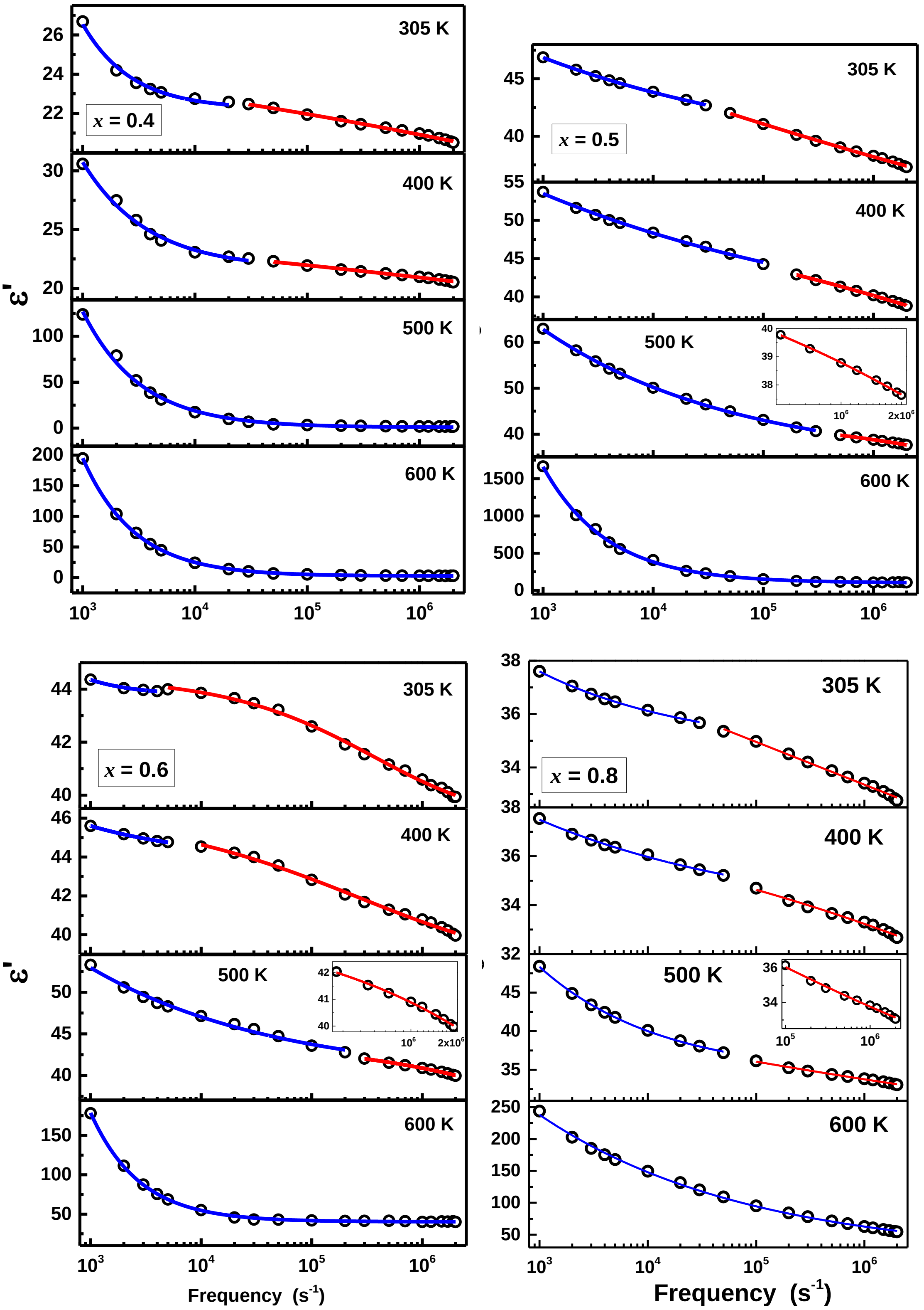

Figure 5.20 (b). Thermal evolution of Type-I and Type-II dielectric relaxation observed in ε′(*f*) for *x* = 0.4 and 0.8.

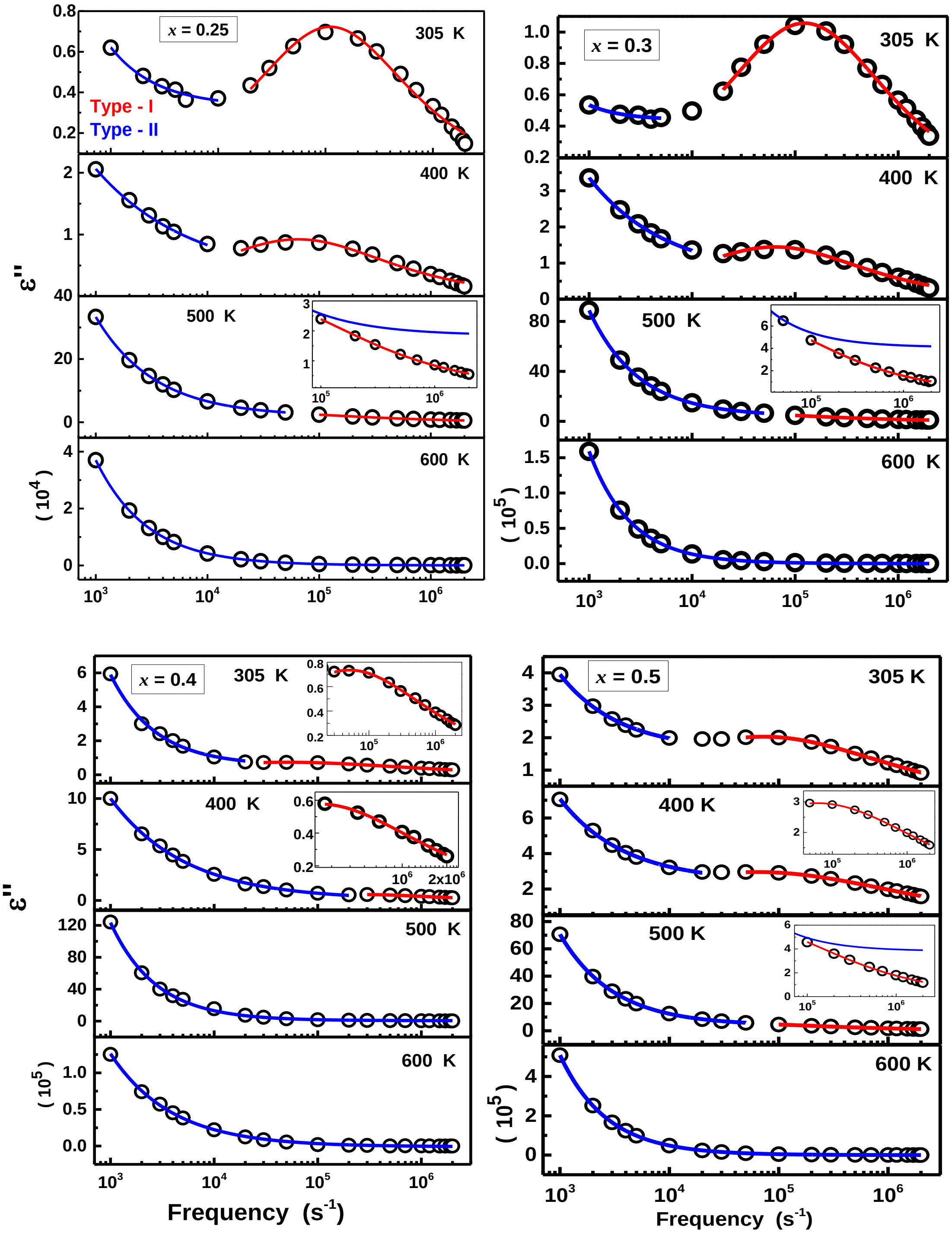

Figure 5.21 (a). Thermal evolution of Type-I and Type-II dielectric relaxation observed in ε″ (*f*) for *x* = 0.25 to 0.5.

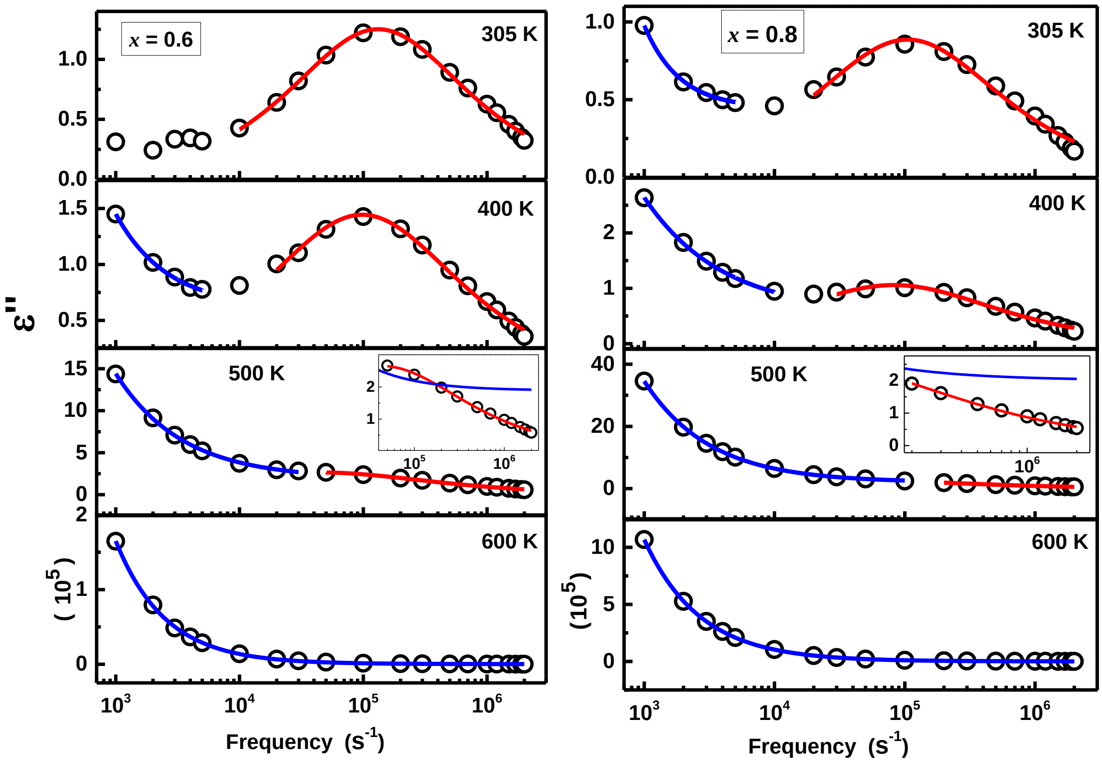

Figure 5.21 (b). Thermal evolution of Type-I and Type-II dielectric relaxation observed in ε″ (*f*) for *x* = 0.6 to 0.8.

Figure 5.20 and 5.21 highlights the thermal evolution of the relaxation types I and II observed over different frequency ranges in the compositions *x* = 0.25 - 0.8. The red and blue fits (curves) through the data (open circles), based on eqns.(5.2) and (5.3), correspond to the type-I and type-II relaxation behaviors, respectively. At a given temperature, a crossover from type II to type I behavior occurs at a frequency, f_{CO}, which increases with increasing temperature, so much so that only type-II behavior prevails over the entire frequency range above ~ 530 K. This indicates that, at such temperatures (above T ~530 K), charge carrier hopping is the only mechanism for dielectric relaxation. To show the validity of CC relaxation behaviour, insets are added. This clearly indicates at 500 K, though not dominating, but still dipolar relaxation persists. By contrast, the samples with *x* = 0.0, 0.05, 0.1 and 1.0 exhibit the type II relaxation behavior in the entire frequency range at any given temperature consistent with the observations made at room temperature which is shown in figure 5.22 and 5.23.

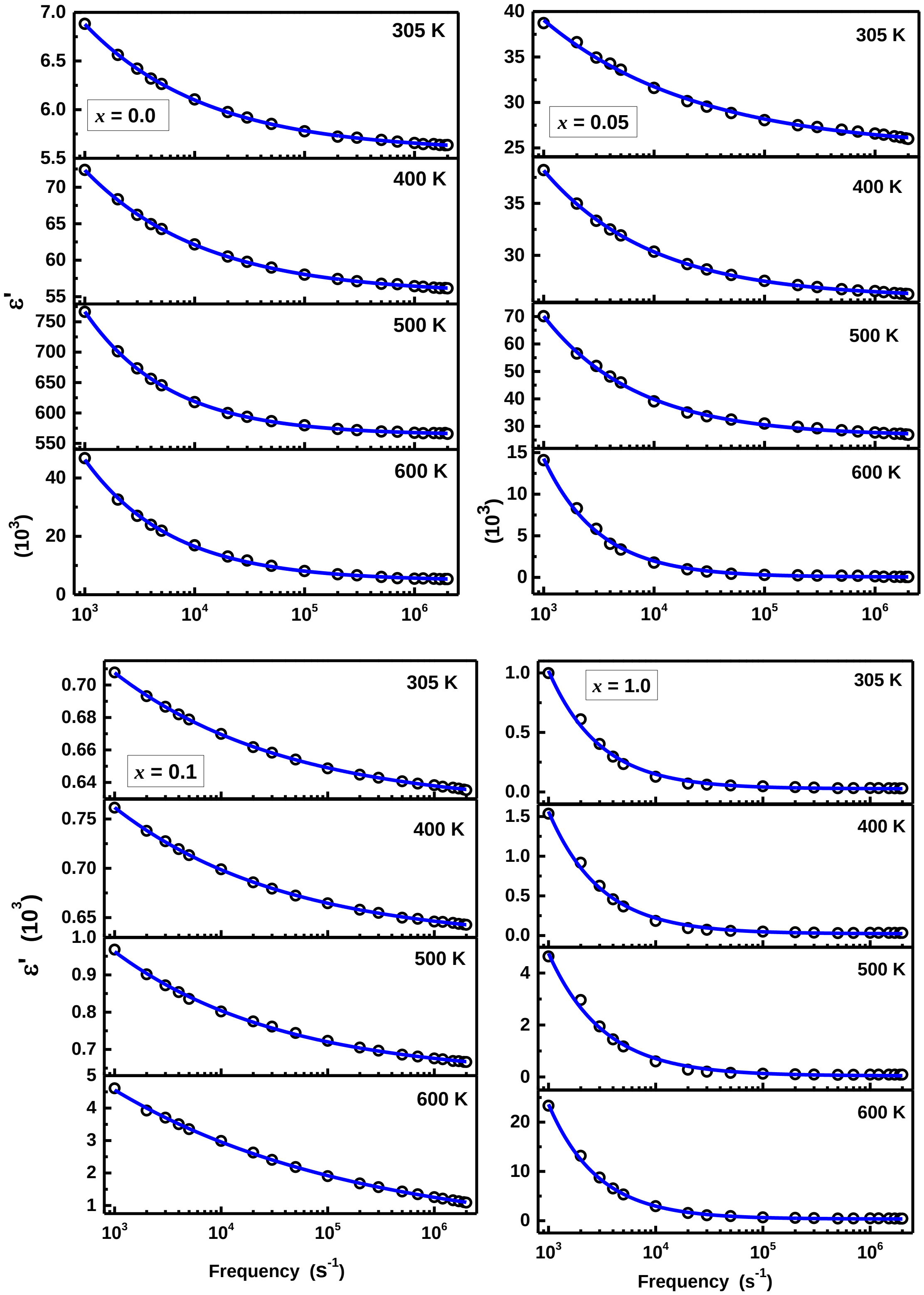

Figure 5.22. Thermal evolution of Type-II dielectric relaxation observed in ε′ (*f*) for *x* = 0.0, 0.05, 0.1 and 1.0.

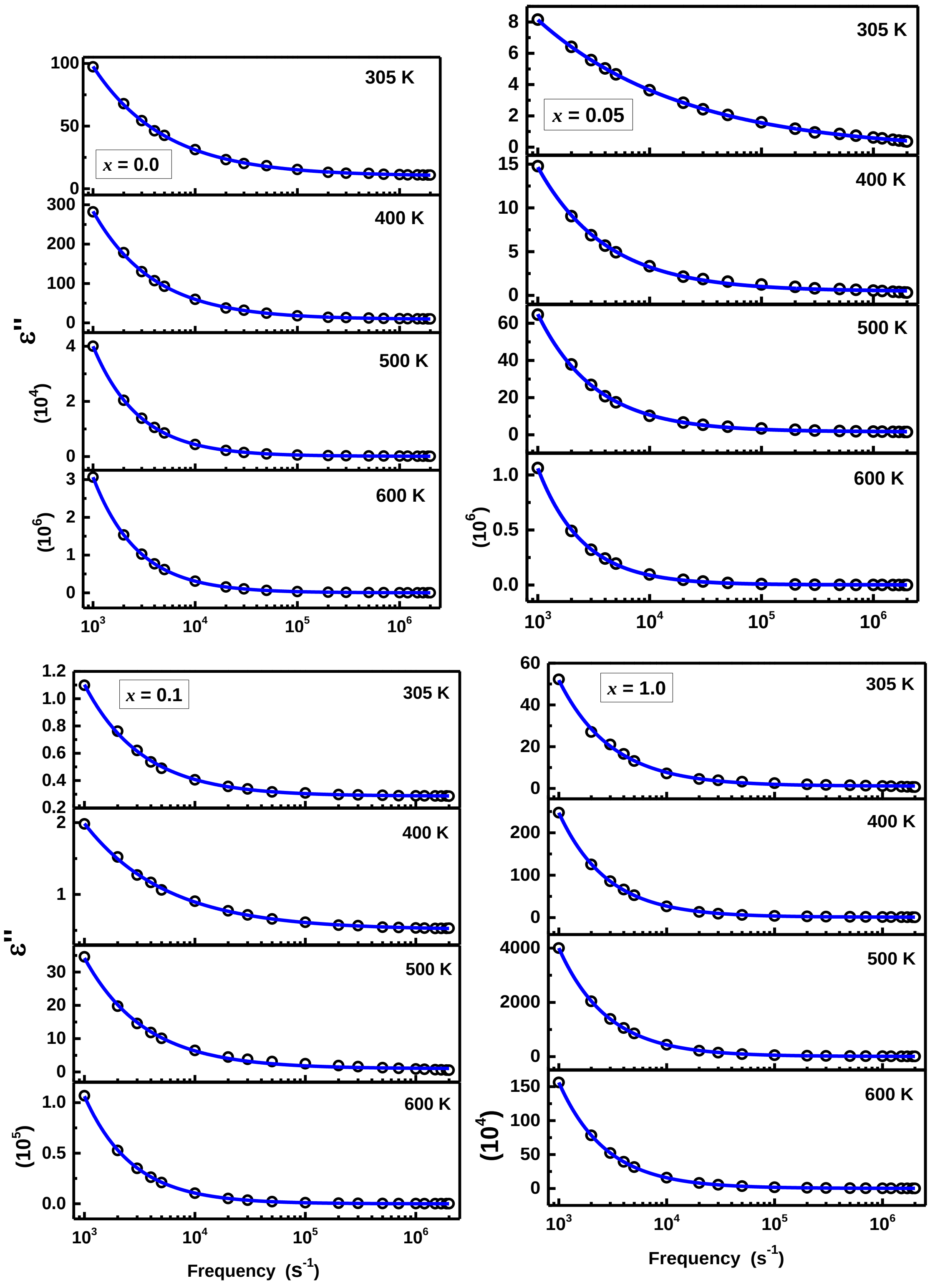

Figure 5.23. Thermal evolution of Type-II dielectric relaxation observed in ε″ (*f*) for *x* = 0.0, 0.05, 0.1 and 1.0.

5.5. Summary

The intrinsic switchable polarization, P_{int}, versus the electric field, E, hysteresis loops, measured using an experimental protocol that gets rid of the nonremanent contributions arising from the electric leakage currents and non-switchable polarization, provide conclusive evidence for the existence of permanent electric dipole moments in, and ferroelectric nature of, the nanocrystalline $Lu_{1-x}Ho_xFeO_3$ ($0 \leq x \leq 1$) samples at room temperature. As x increases from $x = 0$ to $x = 1$, the saturation value of intrinsic polarization, P_{int}^{sat}, presents an overall decreasing trend with a dip at $x = 0.4$. While the decrease in P_{int}^{sat} with increasing x is a consequence of the increase in the unit cell volume and reduction in the electric dipole moment due to decline in orthorhombic distortion, the peak in the crystallite/particle size at $x = 0.4$ is shown to account for the dip in the $P_{int}^{sat}(x)$ and in the static dielectric permittivity, $\varepsilon_0(x)$, at $x = 0.4$.

Direct comparison between the $\varepsilon'(T)$ and $M_{ZFC}(T)$, the peak or dip observed at T_N and T_C in the Fe-O(1)-Fe, Fe-O(2)-Fe bond length and bond angle measured from the high temperature XRD data assesrts the magneto-electro coupling present in the system.

The real (ε') and imaginary (ε'') parts of the complex dielectric permittivity, measured at room temperature over the ac electric-field frequency range, 20 Hz $\leq f \leq$ 2 MHz, unravel two different types of frequency variations of ε' and ε'' in nanocrystalline $Lu_{1-x}Ho_xFeO_3$. In type-I, ε'' goes through a peak as a function of f at f_{max} while ε' increases with decreasing f and approaches a constant but composition-dependent value (20 – 50) at low frequencies in the compositions $0.2 \leq x \leq 0.8$. By contrast, in type-II, both ε' and ε'' increase with decreasing f and exhibit a very steep rise when f falls below $\approx$ 1 kHz reaching values as high as 10^3 – 10^4 as f approaches the lowest measurement frequency of 20 Hz, in Ho concentrations $0 \leq x \leq 0.1$ and 1.0. The type-I frequency variation has been understood in terms of the non-Debye relaxation of elementary electric dipoles which interact with one another and have different relaxation times and the type-II relaxation is associated with the hopping of charge carriers between various localized states in the presence of a time-varying external electric field.

References

[1] U. Chowdhury, S. Goswami, D. Bhattacharya, A. Midya, P. Mandal, Determination of intrinsic ferroelectric polarization in lossy improper ferroelectric systems, Appl. Phys. Lett. 109 (2016) 1–6. https://doi.org/10.1063/1.4961988.

[2] U. Chowdhury, S. Goswami, D. Bhattacharya, J. Ghosh, S. Basu, S. Neogi, Room temperature multiferroicity in orthorhombic LuFeO3, Appl. Phys. Lett. 105 (2014) 10–14. https://doi.org/10.1063/1.4892664.

[3] I.I. Makoed, N.A. Liedienov, A. V. Pashchenko, G.G. Levchenko, D.D. Tatarchuk, Y. V. Didenko, A.A. Amirov, G.S. Rimski, K.I. Yanushkevich, Influence of rare-earth doping on the structural and dielectric properties of orthoferrite La0.50R0.50FeO3 ceramics synthesized under high pressure, J. Alloys Compd. 842 (2020). https://doi.org/10.1016/j.jallcom.2020.155859.

[4] K.S. Cole, R.H. Cole, Dispersion and absorption in dielectrics I. Alternating current characteristics, J. Chem. Phys. 9 (1941) 341–351. https://doi.org/10.1063/1.1750906.

[5] D.W. Davidson, R.H. Cole, Dielectric relaxation in glycerol, propylene glycol, and n-propanol, J. Chem. Phys. 19 (1951) 1484–1490. https://doi.org/10.1063/1.1748105.

[6] S. Havriliak, S. Negami, A complex plane analysis of α-dispersions in some polymer systems, J. Polym. Sci. Part C Polym. Symp. 14 (2007) 99–117. https://doi.org/10.1002/polc.5070140111.

[7] L. Zhang, X.M. Chen, Dielectric relaxation in LuFeO3 ceramics, Solid State Commun. 149 (2009) 1317–1321. https://doi.org/10.1016/j.ssc.2009.05.036.

[8] A.A. BOKOV, Z.-G. YE, Dielectric Relaxation in Relaxor Ferroelectrics, J. Adv. Dielectr. 02 (2012) 1241010. https://doi.org/10.1142/s2010135x1241010x.

[9] T.P. Iglesias, G. Vilão, J.C.R. Reis, An approach to the interpretation of Cole-Davidson and Cole-Cole dielectric functions, J. Appl. Phys. 122 (2017). https://doi.org/10.1063/1.4985839.

[10] A.K. Jonscher, Dielectric relaxation in solids, (1999).

CHAPTER 6

Structural, Dielectric and Magnetic properties of $Lu_{1-x}La_xFeO_3$ $(0 \leq x \leq 0.25)$

La doping is used to tune the phase fraction and investigate its effect on multiferroic properties. $Lu_{1-x}La_xFeO_3$ nanoparticles with $x = 0$ to 0.25 are synthesized using hydrothermal technique. The magnetic and dielectric properties are correlated to the structural parameters. Since h-LFO exhibits spontaneous polarization ($P = 5\ \mu C/cm^2$) and o-LFO has a finite magnetic moment, $\mu_{eff} = 0.24\ \mu_B/f.u$, it is interesting to have both the phases together as a natural composite and study the influence of varying phase fractions on the physical properties.

6.1. Introduction

The previous chapters describe as to how $LuFeO_3$ is stabilized in a single orthorhombic phase by substituting more than 5 at. % of Lu by Ho and provide a detailed account of their properties. In this chapter, the effect of having a mixed-phase consisting of hexagonal (-h) and orthorhombic (-o) $LuFeO_3$ (LFO) is studied. The hexagonal phase exhibits a spontaneous polarization as large as $P = 5\ \mu C/cm^2$ due to its polar nature but has a very small net magnetization. The reported ferroelectric-paraelectric transition is ~ 1000 °C and the paramagnetic-to-antiferromagnetic transition (T_N) is ~ 440 K, which makes the system multiferroic at room temperature (RT) [1]. However, the recent works on h-LFO do not support RT multiferroicity since they yield T_N that lies well below RT [2]. The polar and metastable nature of h-LFO makes it challenging to stabilize this compound as a single phase. By directly measuring the magneto-electric coupling, Chowdhury et al. [3] demonstrated a strong coupling between magnetization and electric polarization (multiferroicity of type II) in bulk o-LFO at RT ($T_{c(FE)}$ ~ 700 K and T_N ~ 600 K) [3] despite its non-polar nature. However, a very low magnetic moment per formula unit ($\mu = 0.24\ \mu_B$/f.u.) at low temperatures in o-LFO (due to the canting of Fe^{3+} spins) severely limits the use of o-LFO as a smart material. Since the hexagonal phase exhibits higher electric polarization while the orthorhombic phase has higher magnetization, it is interesting to have both the phases together as a natural composite and study the influence of the coexisting hexagonal and orthorhombic phases on the physical properties. Song et al. [2] reported successful growth of morphotropic phase mixture of hexagonal and orthorhombic phases in thin films by controlling the annealing conditions and thickness of the film. Likewise, Chaturvedi et al. [4] reported the synthesis of mixed phases of h-LFO and o-LFO via wet chemical method by controlling particle size and shape. In the light of these reports, in this work, we tune the hexagonal/orthorhombic phase fraction by substituting La for Lu and study the effect of La substitution on the physical properties.

6.2. Hydrothermal synthesis

$Lu_{1-x}La_xFeO_3$ (x = 0, 0.05, 0.1, 0.15, 0.2, 0.25) nanoparticles were synthesized via hydrothermal method. Stoichiometric ratios of $Lu(NO_3)_3{\cdot}H_2O$, $La(NO_3)_3{\cdot}6H_2O$, and $Fe(Cl_3)_3{\cdot}\ 9H_2O$ and citric acid were dissolved in double distilled water under magnetic stirring. The pH of the solution is adjusted to 8 by adding a few drops of NH_3. The mixture is then transferred into an autoclave and treated thermally at 200 °C for 24 h. The obtained solution is washed using a centrifuge at 13,000 rpm several times with water and ethanol. The sediment is dried in hot air oven at 70 °C for 3 h. The powder, so obtained, is grounded well and annealed at various temperatures for different time periods. The procedure is represented as flow chart in figure 6.1.

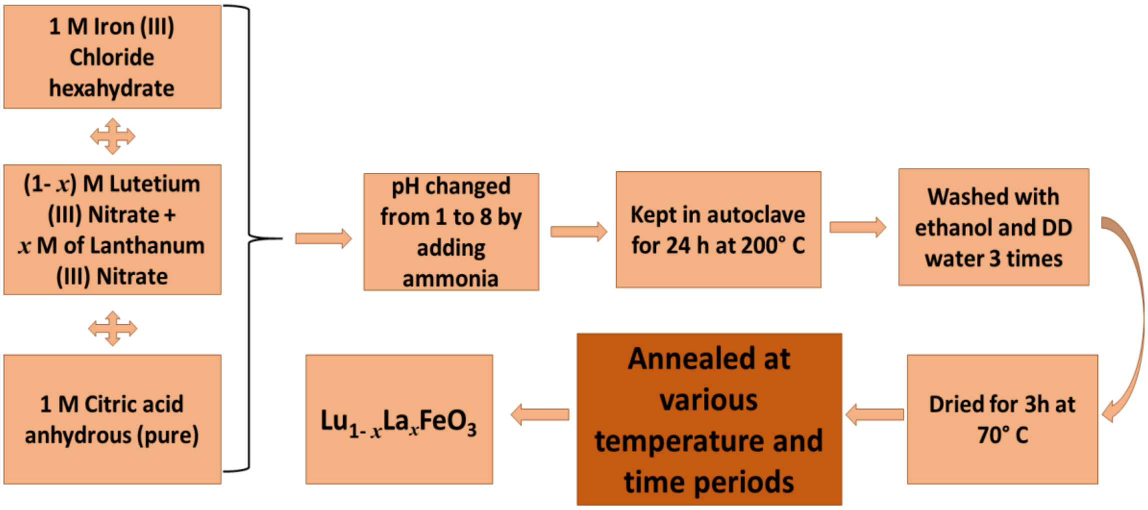

Figure 6.1. Flow chart of hydrothermal synthesis for $Lu_{1-x}La_xFeO_3$ (x = 0, 0.05, 0.1, 0.15, 0.2, 0.25)

6.3. X-ray diffraction Analysis

6.3.1. Optimization of annealing temperature

The as- synthesized $LuFeO_3$ sample and the samples annealed at temperatures ranging from 300°C to 900°C for time periods 4h, 8h and 12h are shown in fig 6.2. The as- synthesized sample and samples annealed at 300°C and 600°C for 8h are found to be amorphous (figure 6.2 (a)). Further increase in annealing temperature to 700°C for 8h exhibited diffraction peaks for both h- LFO and o- LFO with less crystallinity. When the sample is annealed at 820°C for 8 h, the crystallinity is observed to improve. The annealing conditions 820°C for 12 h and 900°C for 8 h gave raise to Fe_3O_4 peaks. Thus, the annealing conditions for the $Lu_{1-x}La_xFeO_3$ (x = 0, 0.05, 0.1, 0.15, 0.2, 0.25) samples is fixed to be 820°C for 8 h.

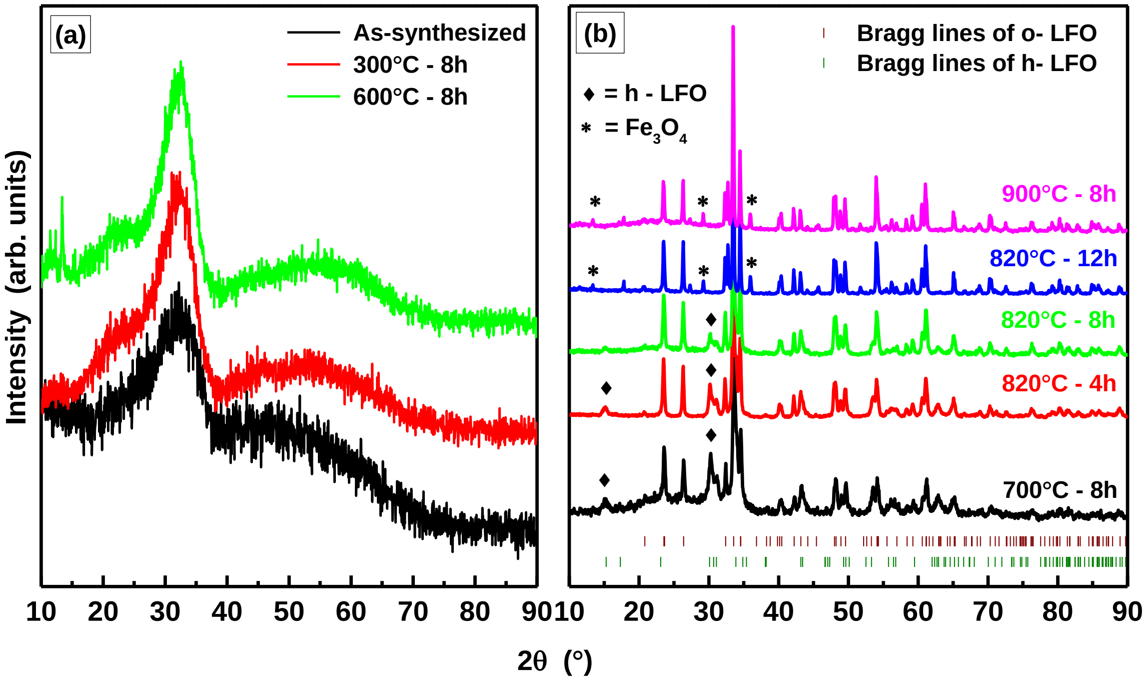

Figure 6.2. X-ray diffraction patterns of $LuFeO_3$ taken under different annealing conditions

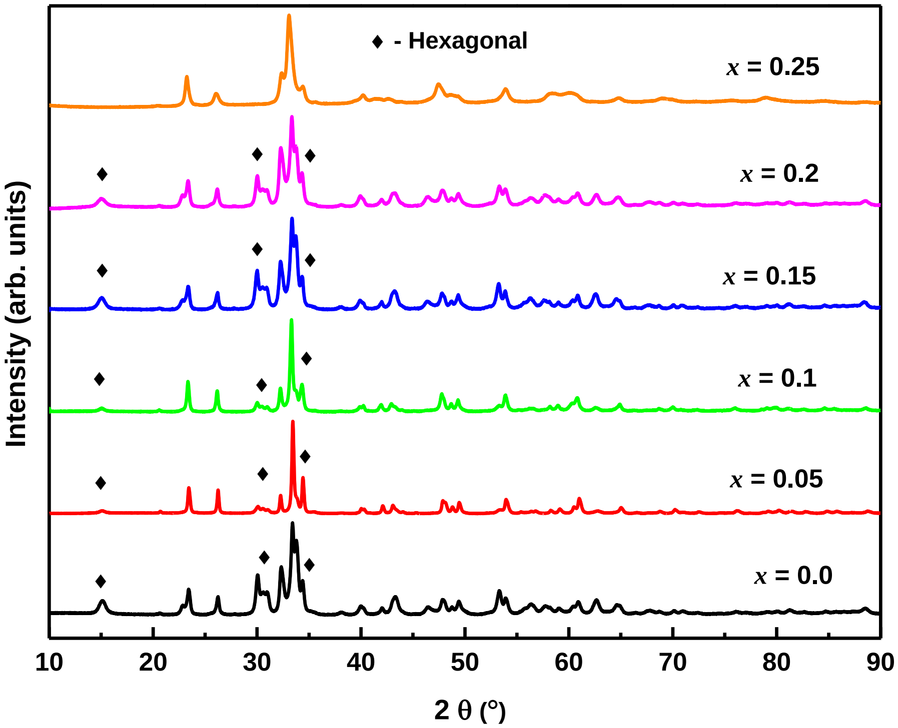

Figure 6.2. X-ray diffraction patterns of $Lu_{1-x}La_xFeO_3$ (x = 0 to 0.25) prepared at 820°C for 8 h.

6.3.2. Rietveld Refinement Analysis

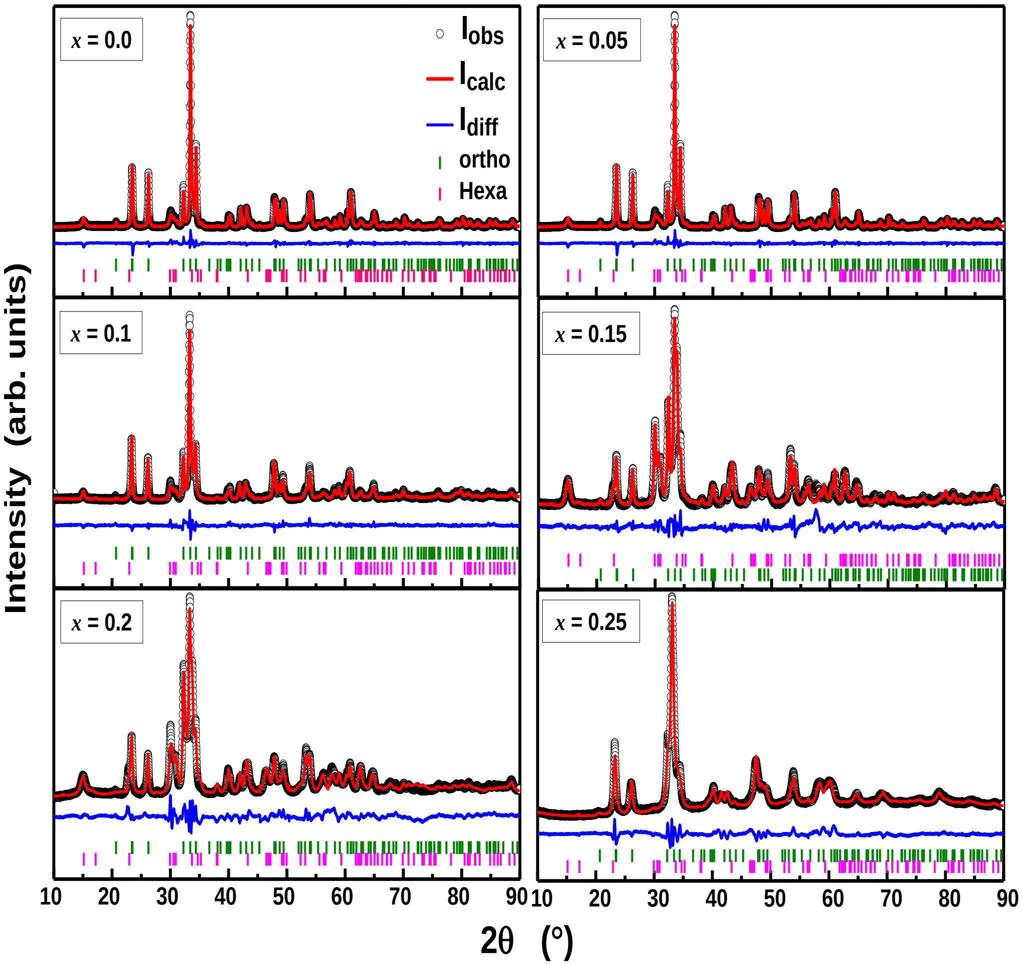

Figure 6.4. Rietveld refinement of $Lu_{1-x}La_xFeO_3$ (x = 0 to 0.25) samples.

The x-ray diffraction patterns of the as-prepared and annealed samples $Lu_{1-x}La_xFeO_3$ (x= 0.0, 0.05, 0.1, 0.15, 0.2, 0.25) are shown in Figure 6.3. The observed diffraction peaks are indexed based on the reflections expected for the hexagonal (ICDD:98-018-3152) and orthorhombic (ICDD:98-002-7285) phases of $LuFeO_3$ with space group $P6_3cm$ (185) and Pbnm (62), respectively. For the La concentration ranging from 0.0 to 0.2, both the hexagonal and orthorhombic phases exist. Further increase in La concentration to 0.25, the hexagonal phase is completely suppressed and only the orthorhombic phase is present. This is clearly evident from the Bragg peak at 15.19°, which is characteristic of the hexagonal phase. The stabilization of single-phase orthorhombic phase with the increase in La doping can be understood in terms of tolerance factor t (explained in section 3.3.3.1). La (1.36 Å) has a larger ionic radius compared to Lu (1.2 Å). Substituting Lu with an element of larger (smaller) ionic radius, stabilizes the orthorhombic (hexagonal) structure [5–7].

In view of the above observations, Rietveld refinement of the XRD data was carried out (using Highscore Plus software) by considering either a hexagonal/orthorhombic phase alone or both the hexagonal and orthorhombic phases together. The resulting Rietveld fits (red curves) are shown in figure 6.4. The hexagonal/orthorhombic phase fraction and the corresponding lattice parameters are listed in table 6.1. It can be seen from this table that the percentage of phase fraction does not vary systematically with increasing *x*. For the La concentration of $x = 0.05$, there is a great reduction in the hexagonal phase fraction. The hexagonal phase fraction increases as *x* increases from 0.05 to 0.15 but, at higher *x*, drops steeply so as to reach zero at $x = 0.25$.

Table 6.1. Lattice parameters and phase fractions of $Lu_{1-x}La_xFeO_3$ samples obtained from Rietveld refinement.

La conc. (*x*)	**Orthorhombic** [8]				**Hexagonal** [9]				**Fe_3O_4 %**	**χ^2**
	Phase %	**a (Å)**	**b (Å)**	**c (Å)**	**Phase %**	**a (Å)**	**b (Å)**	**c (Å)**		
Ref	-	5.2176	5.5556	7.5749	-	5.9652	5.9652	11.7022	-	-
0.0	74.5	5.2123 (3)	5.5488 (2)	7.65 (7)	24.9	5.9467 (2)	5.9467 (2)	11.716 (6)	0.6	2.6
0.05	88.2	5.2314 (4)	5.5457 (3)	7.585 (3)	10.2	6.1645 (4)	6.1645 (4)	12.1456 (8)	1.6	2.9
0.1	80.3	5.2266 (7)	5.5467 (4)	7.5886 (3)	19.5	5.9493 (9)	5.9493 (9)	11.7367 (4)	0.2	2.9
0.15	49	5.1933 (6)	5.5433 (3)	7.6345 (2)	50.7	6.1827 (5)	6.1827 (5)	12.1706 (4)	0.3	3.7
0.2	58	5.2188 (4)	5.5397 (1)	7.5987 (2)	39.5	5.9479 (3)	5.9479 (3)	11.7755 (1)	2.5	3.9
0.25	99.6	5.2866 (3)	5.5456 (9)	7.6804 (7)	0	-	-	-	0.4	3.4

Table 6.2. Bond lengths and bond angles for h- LFO and o- LFO in $Lu_{1-x}La_xFeO_3$ obtained after the Rietveld refinement.

Bond information for o-LFO	**La concentration (*x*)**					
	0.0	**0.05**	**0.1**	**0.15**	**0.2**	**0.25**
Fe-O1 (Å)	2.012	2.0138	2.0109	2.0121	2.0134	2.0151
Fe-O2 (Å)	2.007	2.0167	2.0105	2.0125	2.0101	2.0293
Average bond (Å)	2.0095	2.01525	2.0107	2.0123	2.01175	2.0222
Fe-O1-Fe (°)	142.3608	142.3227	142.8856	142.4006	142.1345	144.0065
Fe-O2-Fe (°)	140.6784	140.6864	141.3434	140.3572	141.6854	139.6281
Crystallite size (nm)	22 (4)	25 (2)	20.5 (2.5)	17 (1)	19 (1.5)	27.3 (2)
Strain (%)	4.3	22.2	5.8	1	7.5	24.2
Bond information for h-LFO						
Fe-O1 (Å)	1.9932	2.0678	2.0803	1.98557	1.9915	-
Fe-O2 (Å)	2.0072	2.0939	2.0572	2.00493	2.0071	-
Fe-O3 (Å)	1.9712	2.1032	1.8939	2.10782	2.0245	-
Fe-O4 (Å)	1.8154	1.8455	2.1581	2.03072	1.9420	-
Average bond (Å)	2.0002	2.08085	2.06875	1.99525	1.9993	-
Fe-O1-Fe (°)	119.013	119.4722	115.9308	119.8065	116.1506	-
Fe-O2-Fe (°)	117.383	116.8945	119.5741	117.6390	119.9648	-
Crystallite size (nm)	14.7 (1.3)	9 (1)	12.2 (8)	13.6 (6)	12.6 (5)	-
Strain (%)	-8.9	-22.1	-12.6	-6.8	-11.08	-

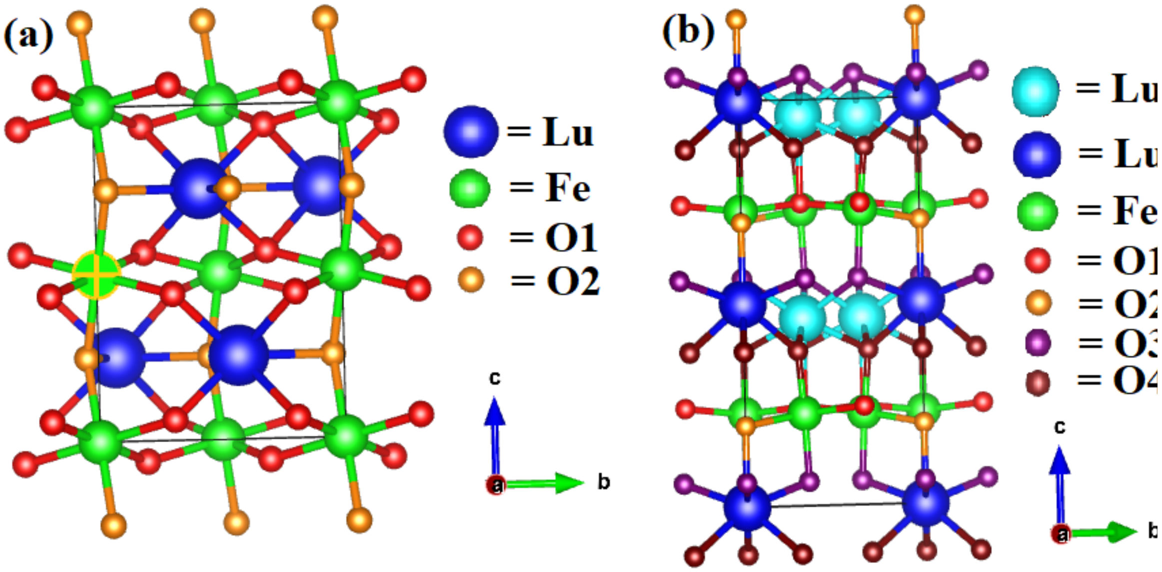

Figure. 6.5. Schematic representation of (a) orthorhombic and (b) Hexagonal $LuFeO_3$ crystal structure

$LuFeO_3$ belongs to the $RFeO_3$ family which has orthorhombic crystal structure as stable structure. LFO is the last member of the $RFeO_3$ family and has the highest distortion. Earlier investigations have revealed [4,10–12] that, as the annealing progresses, at first the hexagonal phase forms and then the orthorhombic phase nucleates and grows at the expense of the hexagonal phase. h-LFO is thus an intermediate phase between the amorphous phase and the o-LFO phase. To stabilize LFO in the metastable hexagonal structure or to the reduce the Gibbs free energy (ΔG), several ways can be followed. They are

1. Wet chemical synthesis procedures
2. Under cooling from a melt
3. Depositing epitaxial thin films on substrates with trigonal symmetry
4. By substituting with an element of smaller ionic radius at the Lu site or Fe site

Among the above mentioned methods, by controlling the interface energy between the amorphous phase and hexagonal phase, hexagonal structure can be successfully stabilized by employing 1-3 methods. Either by increasing temperature or by increasing the thickness of the film or by increasing the particle size, orthorhombic phase grows. When the transition occurs from amorphous state to the crystalline phase, there is a competition between the energy gain because of the formation of crystalline phase and the energy loss in the interface energy between the amorphous and crystalline phase. This results in a critical size above which orthorhombic phase grows. The energy barrier for the critical size to cross and for orthorhombic nucleation to happen is defined as

$$\Delta G^{*} = \frac{16\pi\sigma^{3}\vartheta_{c}^{2}}{3\Delta\mu^{2}}$$

Where ΔG – change in Gibbs free energy, σ – surface energy, υ_c – molar volume, and Δμ - change in chemical potential [4]. The molar volume of h- LFO is more than o- LFO. Since o- LFO is the stable phase, the chemical potential $\Delta\mu^2$ is larger for amorphous to orthorhombic phase. These two parameters favor the formation of o- LFO. The parameter that can be controlled to form h- LFO is surface energy. The h- LFO will have the smaller size and leads to more surface energy but the chemical potential will be more. Because the h- LFO has higher symmetry than o- LFO, the interface energy for amorphous to hexagonal phase is smaller than amorphous to orthorhombic phase. This results in a temperature window in which the h- LFO can be stabilized. The temperature window depends on the size of R^{3+} atom. Smaller the size of R^{3+} atom, larger the temperature window and in $RFeO_3$s, it is larger in case of $LuFeO_3$. From the above discussion, it can be understood that the intermediate h- LFO could be stabilized in nano size. Increase in size will lead to growth in all 3-dimensions and underplays the role of interface, thus resulting in formation of o- LFO.

In the hydrothermal synthesis, when the R^{3+} (La^{3+}/Lu^{3+}) is dissolved in water, it forms $R(OH)_3$. Adding NH_3, dissolves $R(OH)_3$ and forms $R(OH)_4^-$. The solubility of $R(OH)_3$ in the alkaline medium depends on the size of R^{3+} ion. The alkalinity of the synthesis medium controls the dissolution, formation and nucleation process of $RFeO_3$ formation. When the alkalinity of the medium is less, it gives raise to the formation of rare earth oxides and iron oxides. Hence in the hydrothermal synthesis, the formation of $RFeO_3$ is a result of competition between the alkalinity and R^{3+} size. In this work, the autoclave temperature, annealing temperature and alkalinity is fixed and the only changing parameter is the La doping. From the Rietveld analysis, it is observed that the phase fraction of o- LFO and h-LFO is not following any trend. Also, a small fraction of Fe_3O_4 is present. This can be understood in terms of competition between the alkalinity, annealing temperature and the size of R^{3+} ions.

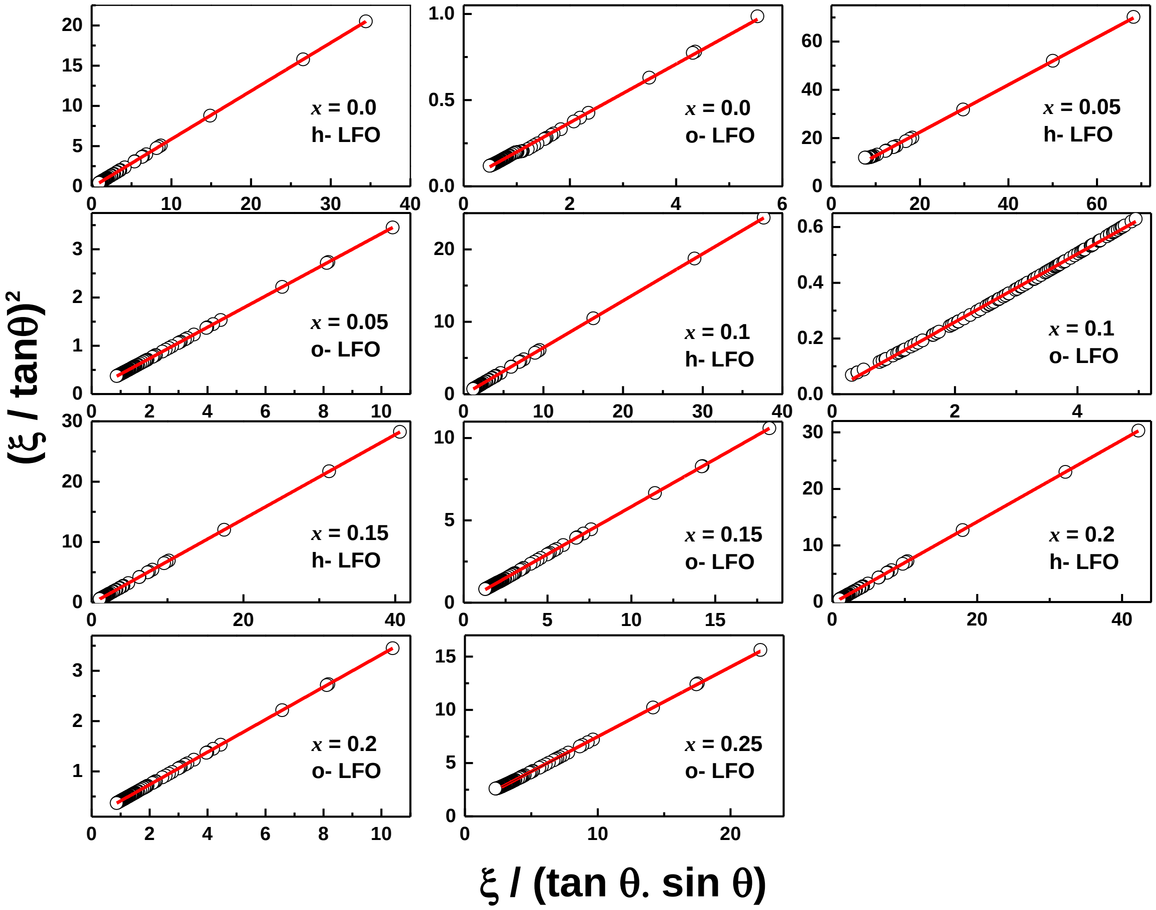

Figure 6.6. Linear Halder- Wagner plots of h- LFO and o- LFO for Lu$_{1-x}$La$_x$FeO$_3$ (x = 0, 0.05, 0.1, 0.15, 0.2, 0.25) samples.

The crystallite size and strain for both h- LFO and o- LFO is calculated using the Halder-Wagner method (3.3.4) and listed in table in 6.2. The strain calculated for hexagonal phase is negative [13] and found to increase with the phase fraction of increase in hexagonal phase. The crystallite size also increases with increase in h- LFO %. Whereas for the orthorhombic phase also, the crystallite size and strain (positive) increases with increase in o- LFO %. The strain of h-LFO and crystallite size of o-LFO is anti-correlated. It means that orthorhombic phase grows by compressing the h-LFO. Also, it is found that the crystallite size of h-LFO is always smaller than the o- LFO for each concentration as expected. The compression of h- LFO unit cell and growth of o- LFO strongly affects the local structure of the unit cell. To study this local structure distortions, bond angles and bond lengths are yielded by Rietveld refinement for both the hexagonal and orthorhombic phase and included in table 6.2. The effect of these parameters on the physical properties will be discussed later in detail.

The crystal structure for all the samples is simulated using Vesta software [14] directly by importing the respective crystallographic information file (CIF). As an illustrative example, a schematic sketch of the $LuFeO_3$ crystal structure, representative of other compositions as well, is shown in 6.5 (a) and (b). The orthorhombic (Pbnm) crystal structure can be viewed as Fe-O(1) layers, and Lu-O(2) layers stacked alternately in the c-direction. It is evident from this figure that each Fe^{3+} ion is located at the center of an octahedral O^{2-} cage consisting of four O(1) ions coplanar (*ab*-basal plane) with Fe^{3+} ion and two out-of-plane apex O(2) ions along the c-axis. On the other hand, each R^{3+} ion is coplanar with two O(2) ions and connected to four O(1) ions in the two adjacent Fe-O(1) layers.

In the hexagonal ($P6_3cm$) structure. The trivalent Fe ions are surrounded by trigonal bipyramidal, 5- fold oxygen environment. Two O(1) atoms and one O(2) are linked to each Fe^{3+} ion in the *ab*- basal plane. O(3) and O(4) atom occupies the apex positions along the *c*-axis. Lu(1) and Lu(2) occupies two independent Wyckoff positions surrounded by eight oxygen atoms. The layers of Lu-O and Fe-O are stacked alternately in the *c*-direction. A typical hexagonal crystal structure of $LuFeO_3$ is shown in figure 6.5(b). With doping, La partially occupies the position of the Lu depending on the doping concentration.

6.4. Surface morphology and microstructure

The average particle size measured from FESEM images for the samples $x = 0.0$, 0.05, 0.1, 0.15, 0.2, 0.25 are 34 ± 4, 38 ± 2, 25 ± 1, 24 ± 1, 28 ± 2, 43 ± 3 nm. The sizes measured from FESEM images are bigger than the crystallite sizes calculated from Halder-Wagner method indicating agglomeration of the nanoparticles. The Energy Dispersive X-ray spectroscopy revealed that the stoichiometry is in good agreement with the nominal composition.

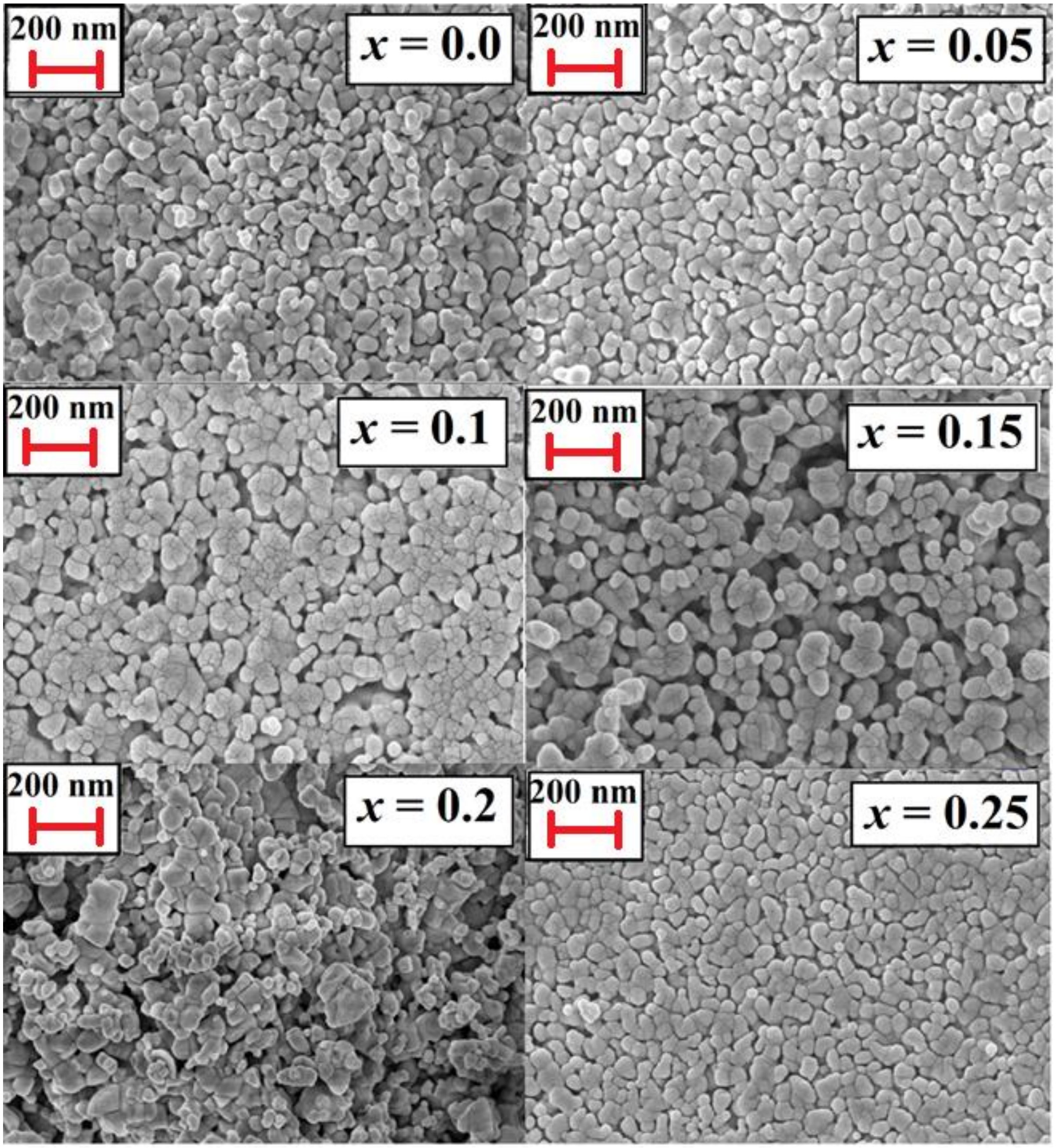

Figure. 6.7. Microstructural images of $Lu_{1-x}La_xFeO_3$ (x = 0, 0.05, 0.1, 0.15, 0.2, 0.25)

6.5. Raman spectroscopy

Raman spectra of the pellets of $Lu_{1-x}La_xFeO_3$ with $x = 0.0, 0.05, 0.1, 0.15, 0.2, 0.25$ (sintered at 820˚C for 8 hours) are shown in figure 6.8, were recorded at room temperature over the wavenumber range extending from 50 cm^{-1} to 1000 cm^{-1} The line shapes of the peaks in the Raman spectra are found to be represented well by multiple Lorentzians (red curves through the data (blue open circles) in figure 6.8). Such fits enable a precise determination of the positions, integrated intensities and widths of the Raman peaks. The peak positions correspond to Raman-active (RA)

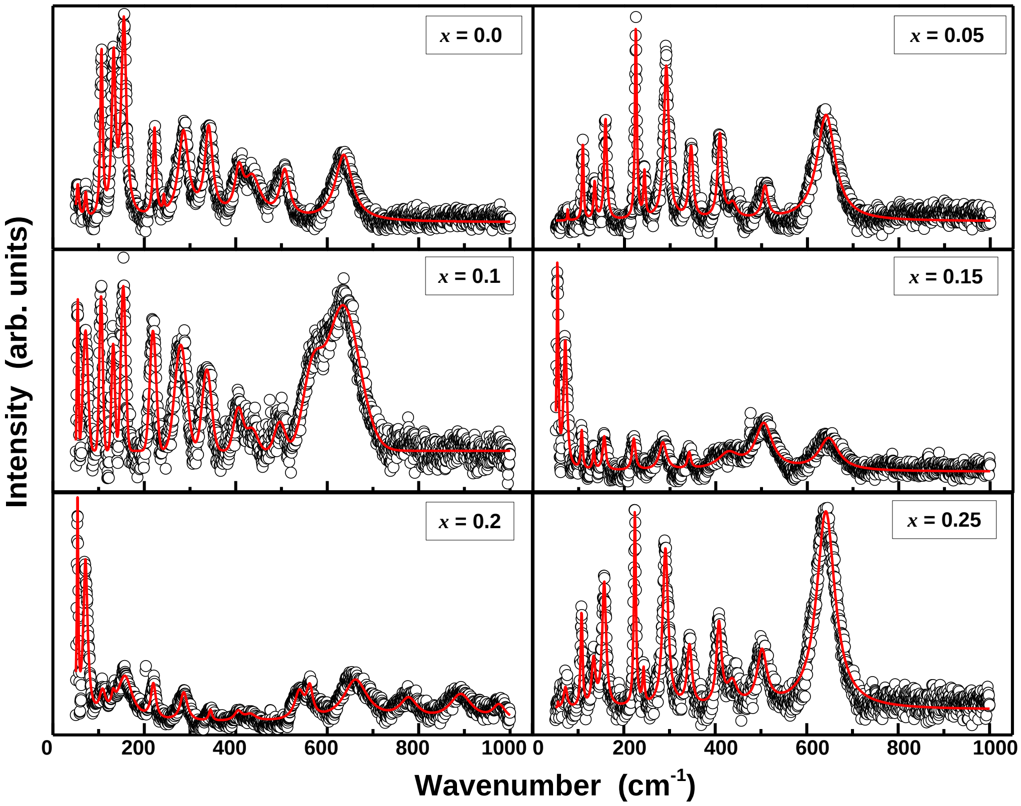

Figure. 6.8. Raman spectra along with multiple Lorentzian fit for $Lu_{1-x}La_xFeO_3$ ($x = 0$, 0.05, 0.1, 0.15, 0.2, 0.25) samples.

Table 6.3. Raman-active modes observed in $Lu_{1-x}La_xFeO_3$ (x = 0 to 0.25) compared with the references [15] [16] [17].

Hexagonal		Orthorhombic			La concentration. (x)					
$LuFeO_3$	**GT**	**$LuFeO_3$**	**$LaFeO_3$**	**GT**	**0.0**	**0.05**	**0.1**	**0.15**	**0.2**	**0.25**
-	-	-	-	-	54.3 (3)	56.3 (4)	54.2 (1)	53.7 (1)	53.9 (1)	56.2 (9)
-	-	-	-	-	71.7 (4)	75.7 (5)	71.3 (2)	70.7 (1)	71.2 (1)	72.3 (8)
110	E_2	110	84	$A_g(1)$	106.4 (1)	108.8 (1)	105.3 (1)	106.7 (2)	108.4 (6)	107.6 (1)
-	-	136	135	$A_g(2)$	132.7 (1)	134.6 (3)	131.8 (1)	132.9 (4)	131.9 (8)	133.8 (4)
-	-	158	143	B_{2g} (2)	155.1 (1)	158.4 (1)	153.8 (1)	155.8 (3)	157.3 (6)	156.9 (1)
284	A_1	278	186	$A_g(3)$	285.6 (2)	291.4 (1)	279.6 (3)	284.1 (5)	286.3 (5)	290.9 (1)
346	E_1	350	274	$A_g(4)$	340.8 (2)	345.6 (2)	336.6 (3)	341.6 (6)	344.6 (9)	343.6 (3)
404	E_2	410	449	$A_g(5)$	406.9 (6)	408.7 (2)	405.3 (8)	405.4 (4)	405.2 (7)	408.1 (3)
448	A_1	427	303	$A_g(6)$	436.5 (9)	436.9 (9)	434.7 (9)	427.6 (9)	432.5 (9)	437.2 (8)
501	E_2	516	433	$A_g(7)$	507.1 (9)	507.2 (3)	496.4 (9)	505.1 (5)	508.9 (6)	502.1 (5)
651	A_1	654	641	B_{3g} (5)	636.2 (4)	640.9 (3)	634.6 (8)	647.1 (7)	645.9 (5)	641.8 (2)

vibrational/rotational modes. The Raman modes, so obtained, for hexagonal (H-) and orthorhombic (O-) LFO phases of $Lu_{1-x}La_xFeO_3$ with x = 0.0, 0.05, 0.1, 0.15, 0.2, 0.25 are listed in Table 6.3. The wavenumbers for the Raman-active modes in hexagonal [15] or orthorhombic $LuFeO_3$ [16] and orthorhombic $LaFeO_3$ [17] obtained previously from experiments are included in the Table 6.3 for comparison.

Totally 12 RA modes are observed for all the samples. Most of the Raman modes from 110 cm^{-1} to 650 cm^{-1} for the hexagonal phase have values not very different from those for the orthorhombic phase. Two modes at 136 cm^{-1} and 156 cm^{-1} which is exclusive to orthorhombic phase is observed across all the concentrations. Unfortunately, no distinct peak for hexagonal phase (~ 475 cm^{-1}) is observed. Apart from these RA modes, two new Raman modes at ≈ 54 cm^{-1} and 70 cm^{-1} (not reported in previous literature) are observed. These modes are observed in Ho- substituted samples as well. The origin of the new modes is attributed to the symmetry breaking at the surfaces/ interfaces/ boundaries that arises due to the nano size of the samples.

6.6. Dielectric Properties

6.6.1. Ambient temperature studies

The dielectric studies were carried out on $Lu_{1-x}La_xFeO_3$ (x = 0, 0.05, 0.1, 0.15, 0.2, 0.25) samples at room temperature in the frequency range 500 Hz to 2 MHz at 1 kV/cm electric field. The real (ε') and imaginary (ε'') part of the dielectric function is measured as a function of frequency and shown in figure 6.9. With increase in frequency, the dielectric constant (ε') decreases sharply at low and mid frequency range and exhibits a Debye-like dispersion at higher frequencies. The decrease in dielectric constant can be explained using the active polarization mechanism: When the frequency of the applied ac electric field is low, the dipoles can follow and this gives raise to higher polarization leading to increase in dielectric constant. As the frequency increases, the dipoles cannot orient with the rapidly flipping ac filed. Thus, decrease in dielectric constant is observed. This behavior is observed across all the samples. On the other hand, the dielectric loss behavior can be categorized into two behaviors: 1. Decrease in dielectric loss throughout the frequency range, indicating the hopping charge carriers is the dominating mechanism (Type-II). The type-II behavior is observed for the samples, x = 0.05, 0.1 and 0.25 for which the orthorhombic phase fraction is more. 2. Decrease in dielectric loss till mid frequencies (~ 4 x 10^4 cm^{-1}) and exhibiting a peak like behavior at

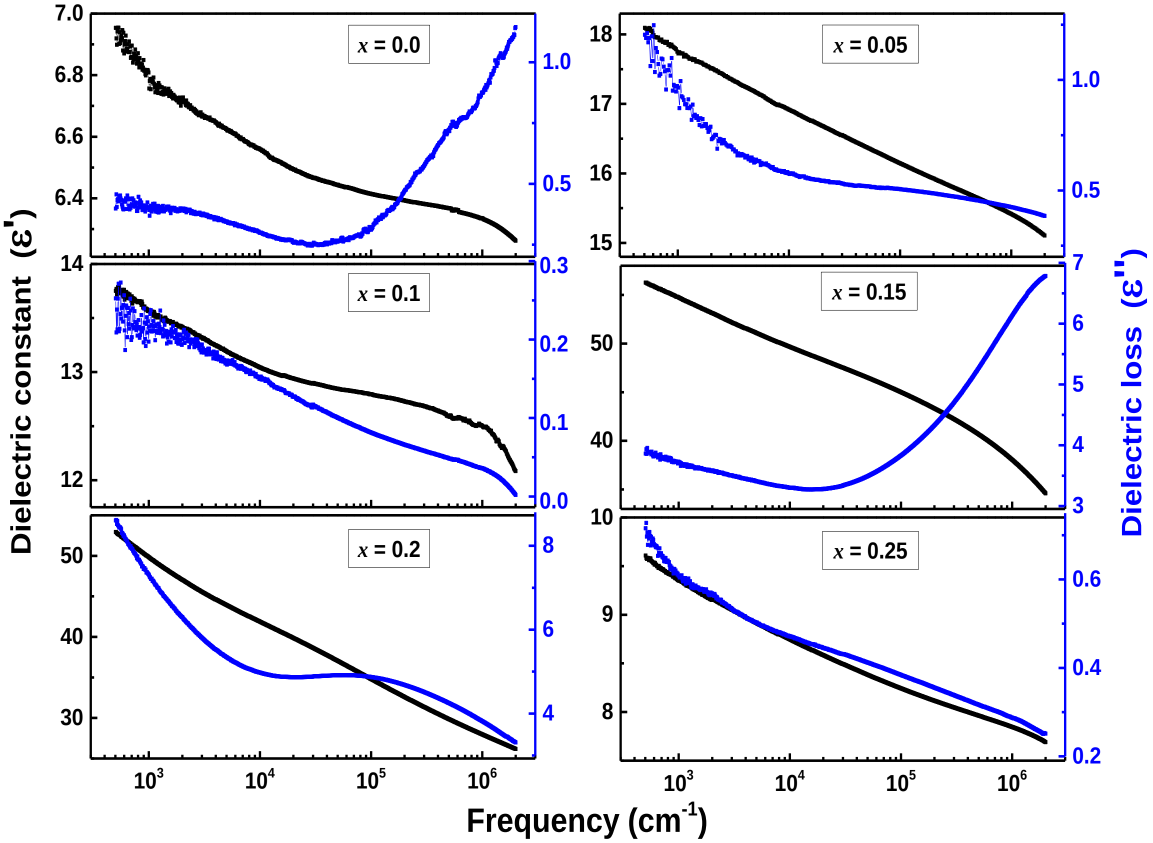

Figure. 6.9. Dielectric constant and dielectric loss measured as a function of frequency at room temperature for $Lu_{1-x}La_xFeO_3$ (x = 0, 0.05, 0.1, 0.15, 0.2, 0.25) samples

high frequency range, ~ 4 x 10^4 cm^{-1} to ~ 2 x 10^6 cm^{-1}. Since the peaks are not complete in the measured frequency range, the relaxation time couldn't be calculated precisely. A peak like behavior is observed in x = 0.0, 0.15 and 0.2 samples, indicating the domination of dipolar/orientation polarization (Type-I). Incidentally, in these samples hexagonal phase fraction is more compared to the orthorhombic phase.

The dielectric constant measured at various frequencies is plotted as a function of La doping concentration (x) and shown in fig. 6.10 (a). Dielectric constant is observed to decrease with increase in frequency for all the La doping concentrations. It can be seen for the samples x = 0.15 and 0.2, the dielectric constant increases throughout the measured frequency range. This is in agreement with the Rietveld refinement wherein for these compositions an increase in hexagonal phase (polar in nature) is observed. For other concentrations, the dielectric constant decreases which can be correlated to an increase in orthorhombic (non-polar) phase. In order to bring out the role of phase fraction, ε' measured at 2 MHz (representative of all other frequencies) is plotted against the hexagonal phase percentage. It can be clearly seen that the dielectric constant is increasing linearly with increase in phase %.

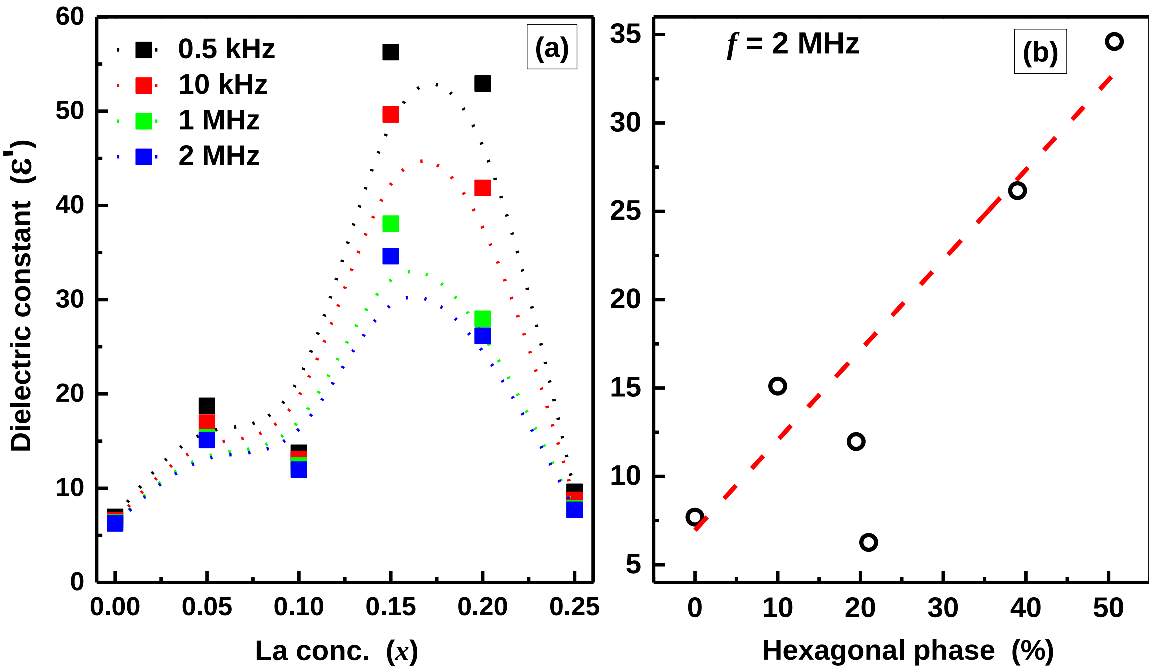

Figure 6.10. Dielectric constant plotted as a function of (a) La doping concentration (*x*); (b) Hexagonal phase fraction.

6.6.2. Temperature dependent studies

Dielectric constant and dielectric loss are also measured as a function of temperature at various frequencies ranging from 1 kHz to 2 MHz. In the figure 6.11 and 6.12, ε' and tanδ are plotted against temperature at frequencies 50 kHz, 100 kHz, 200 kHz, 300 kHz, 500 kHz, 700 kHz and 1 MHz for all concentrations. The temperature at which maximum dielectric constant (ε'_{max}) observed is termed as T_C indicating ferroelectric to paraelectric transition. The common observations made for each sample's data are 1. ε'_{max} decreases with increasing in frequency, 2. T_C (temperature at which ε' is maximum) is fairly independent of frequency at low frequencies and shifts to higher temperature at high frequencies (above 1 MHz), 3. Peaks become broader with increase in frequency. 4. The apparent T_C observed from tanδ differs from the T_C observed from ε'.

When there is distribution in the nano crystallites [18] and there is internal stress in the unit cell due to the multiple occupation at A and/or B site in ABO_3 perovskites [19], the T_C is not sharply defined and thus deviate from Curie-Weiss behavior. This type of phase transitions can be termed as "Diffusive Phase Transitions" (DPT) or relaxor ferroelectrics [20]. The DPT phenomena explains that there are nano polar regions in the sample caused by the local distortions. These nano polar regions have their own local T_C and ε'_{max}. The experimentally observed T_C and ε'_{max} is an average of all the nano polar regions' contributions. This results in a diffusive transition peak. Sharp decrease in ε'_{max} with increasing frequency and difference in T_C observed from ε' and tanδ plots are also indication of relaxor ferroelectric behavior [21].

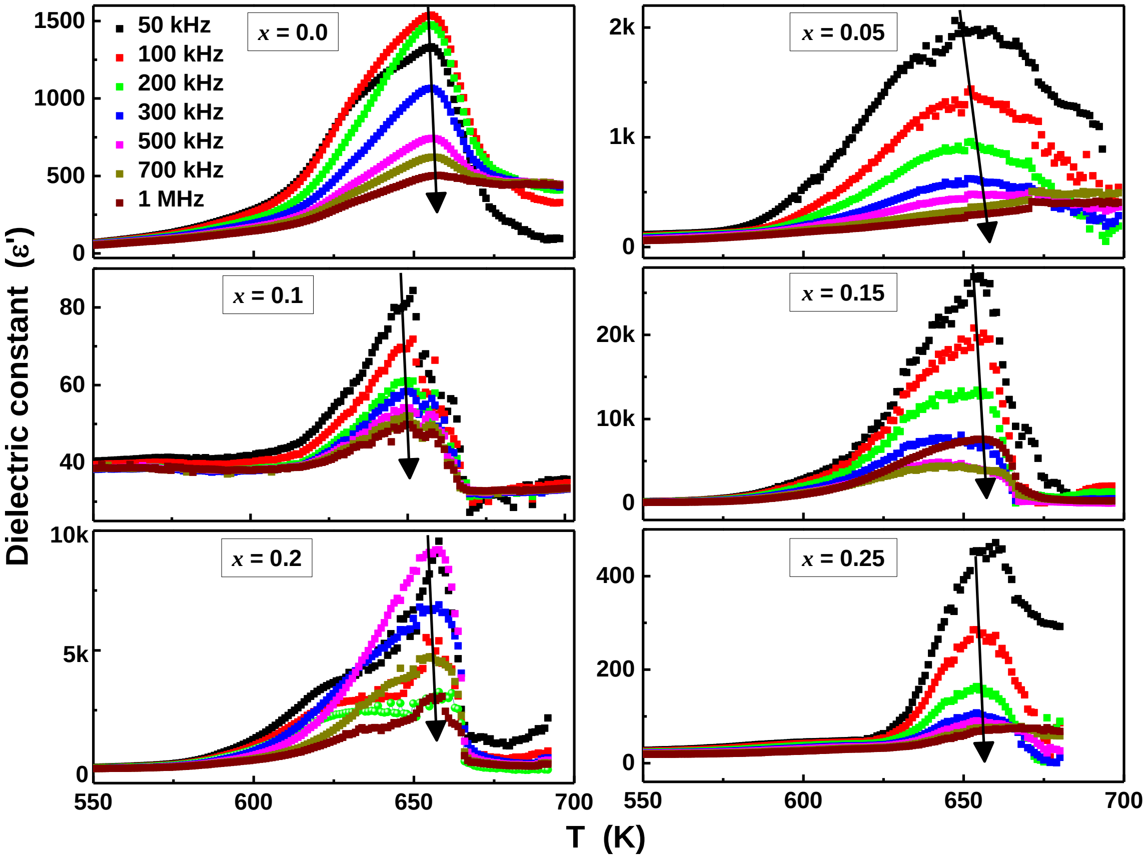

Figure. 6.11. Dielectric constant plotted against temperature at various frequencies for $Lu_{1-x}La_xFeO_3$ (x = 0, 0.05, 0.1, 0.15, 0.2, 0.25) samples

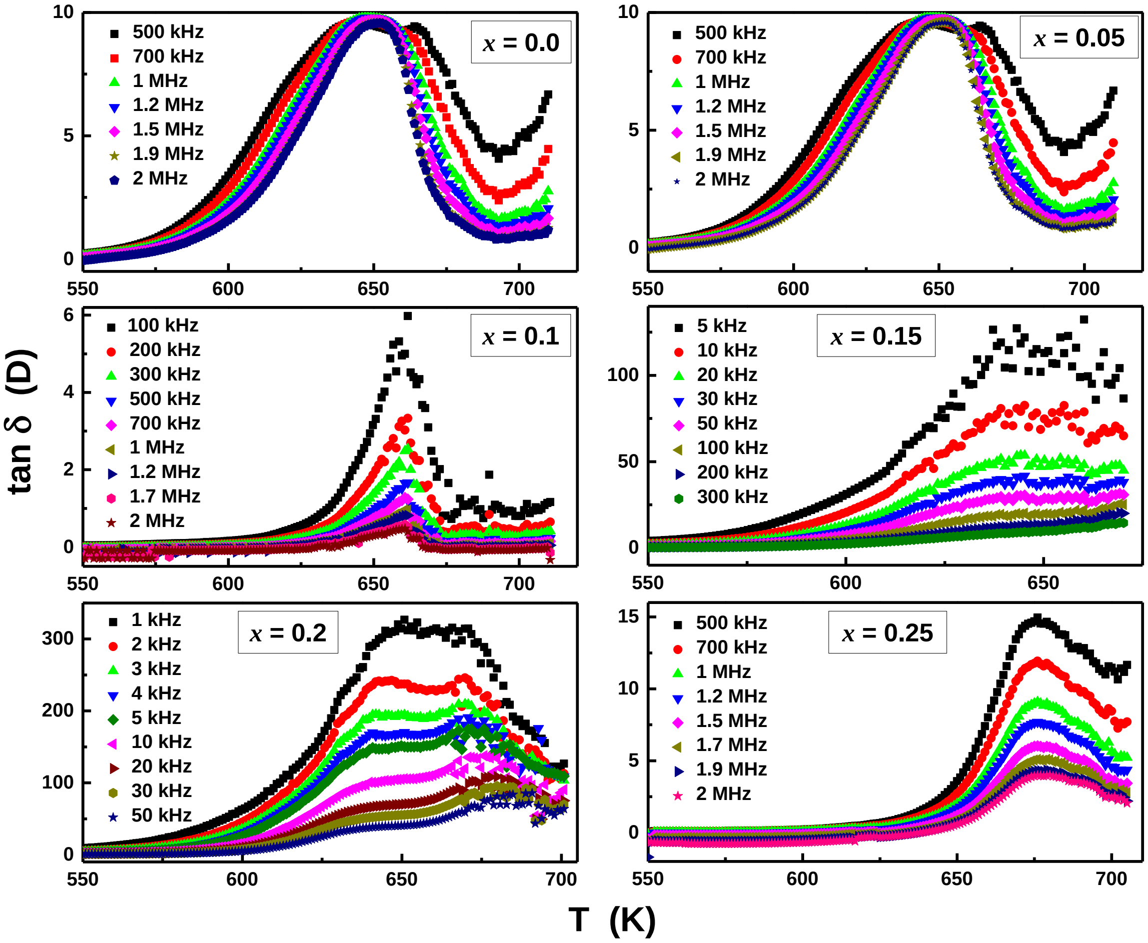

Figure 6.12. Dielectric loss plotted against temperature at various frequencies for $Lu_{1-x}La_xFeO_3$ (x = 0, 0.05, 0.1, 0.15, 0.2, 0.25) samples.

The dielectric properties strongly depend on nature of the dipoles and the local structure (grains and grain boundaries). Park *et al* studied the effect of average crystallite size on the diffusiveness as well as the T_C of the transition peak on $PbSc_{0.5}Ta_{0.5}O_3$ system. They observed that with increase in crystallite size, diffusiveness decreases and the T_C shifts to higher temperature [20]. To understand the variation of T_C in the present work, ε' measured as a function of temperature at 700 kHz is considered for all the samples. Crystallite size calculated using the Halder-Wagner method (table 6.2) from the XRD data is plotted along with the T_C measured from ε' at 700 kHz (as representative) and shown in figure 6.13. It is found that the variation in T_C follows the same behavior of the crystallite size of the orthorhombic phase. All these correlations conclude that the observations made above strongly suggests that $Lu_{1-x}La_xFeO_3$ (x = 0, 0.05, 0.1, 0.15, 0.2, 0.25) samples belong to relaxor ferroelectrics.

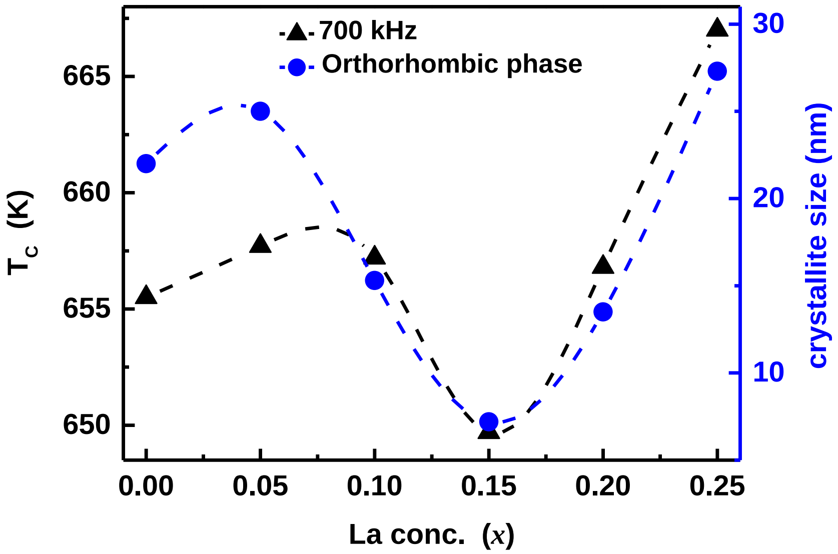

Figure. 6.13. Tc (K) and crystallite size calculated from XRD pattern plotted as a function of La concentration.

6.6.3. Ferroelectric Properties

To further investigate the ferroelectric nature of these samples, Polarization (P) is measured as a function of applied electric field (E) with time period = 20 ms at RT. The P-E loops for x = 0, 0.05, 0.1, 0.15, 0.2 and 0.25 are shown in figure 6.14. The measured P-E loops are not saturating even at the highest applied field before that the breakdown occurs. The loops for x = 0.0, 0.05, 0.1 appear to exhibit lossy capacitor [22] behavior. In the lossy capacitor behavior, the area of the loop gives loss tangent and the slope gives capacitance of the system. Increase in La doping concentration resulted in relaxor-type P-E loops. In this type of loops, the maximum polarization is not observed at the maximum electric field as expected in ideal ferroelectric P-E loop. Instead, the polarization increases with increase in electric field and after a certain field, P decreases which is a typical behavior for a relaxor-type ferroelectric. The P-E loops don’t close indicating the presence of leakage current [13].

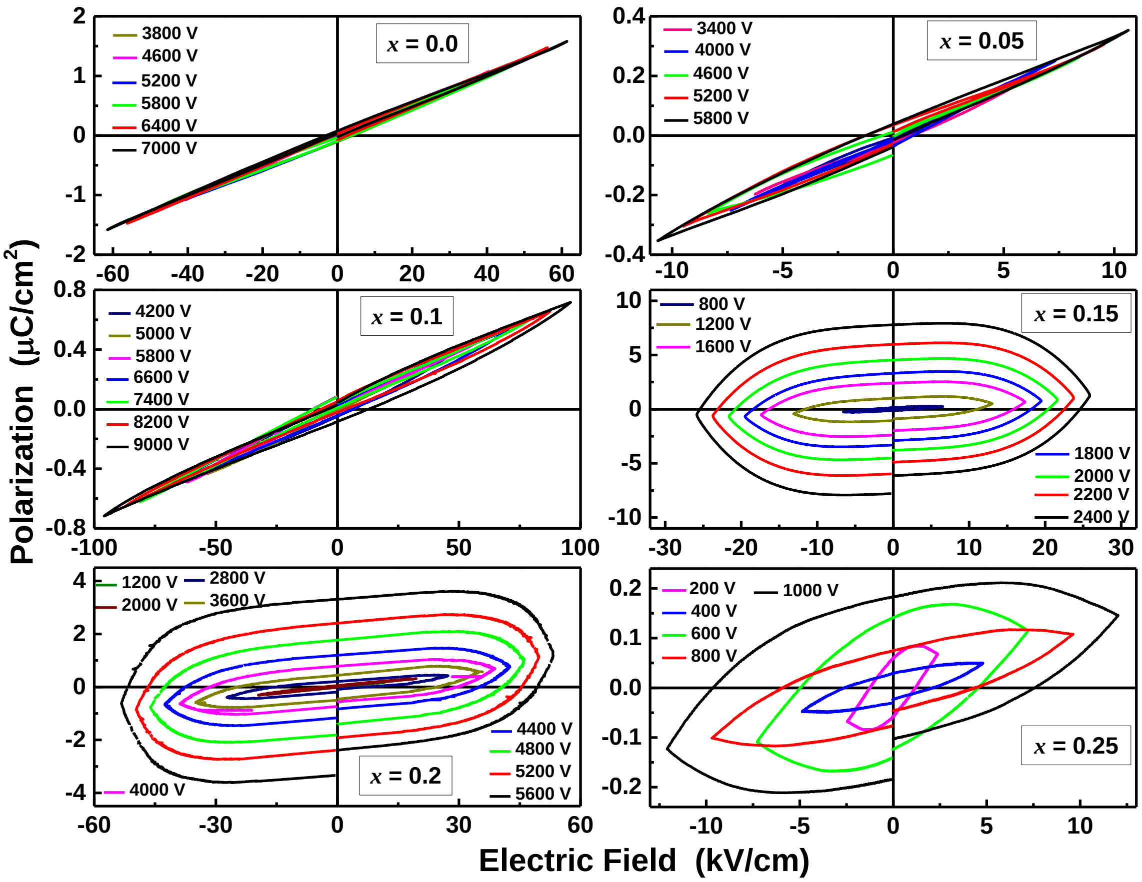

Figure 6.14. P-E loops measured at RT with time period t = 20 ms for all La doping concentrations.

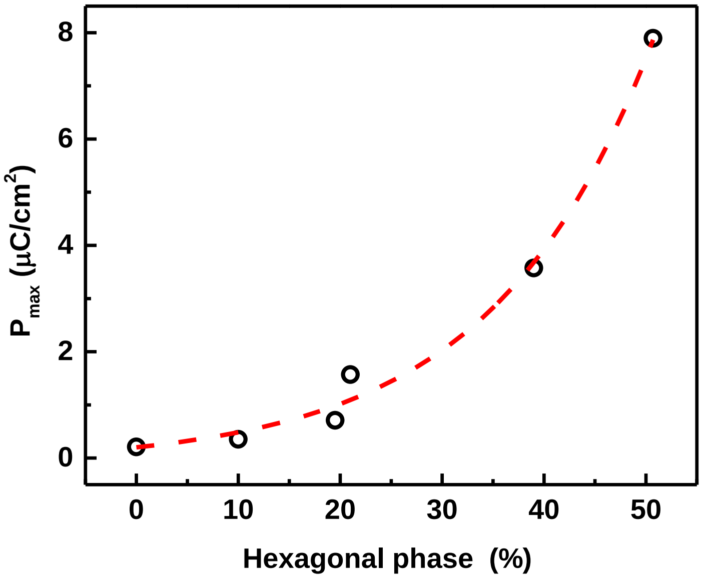

Figure 6.15. P_{max} (μC/cm^2) plotted as a function of hexagonal phase %.

The parent compounds $LuFeO_3$ and $LaFeO_3$ belong to centrosymmetric Pbnm space group which isn't supposed to exhibit spontaneous polarization. However, in these materials the spin-orbit coupling breaks the inversion symmetry and results in a finite polarization [3]. Observation of ferroelectric hysteresis loops at room temperature in $LuFeO_3$ [3,23] and $LaFeO_3$ [24,25] in the previous reports suggest that they are ferroelectric in nature. Moreover, in the present work, along with the orthorhombic phase, non-centrosymmetric hexagonal phase also coexists which has finite intrinsic polarization. In the literature, the maximum polarization reported for the parent compounds h- $LuFeO_3$, o- $LuFeO_3$ and o- $LaFeO_3$ are 4 $\mu C/cm^2$ at 200 kV/cm [26], 0.5 $\mu C/cm^2$ at 1.5 kV/cm [3] and 0.17 $\mu C/cm^2$ at 40 kV/cm [24]. To understand the ferroelectric behavior in the La doped $LuFeO_3$, the maximum polarization (P_{max}) observed just before the electrical breakdown occurs is taken and plotted as a function of hexagonal phase percentage. It can be observed from figure 6.15 that the polarization increases exponentially with increase in hexagonal phase %. The maximum value of 7.89 $\mu C/cm^2$ for 50.7 % of hexagonal phase is observed which is twice the literature value and can be explained by the smaller crystallite size (13.6 nm) [27]. The least polarization value observed is 0.21 $\mu C/cm^2$ for $x = 0.25$ (100 % o- LFO). The decrease in the P_{max} is expected because La doping reduces the FeO_6 octahedra rotation which is responsible for the polarization observed in the system [17].

6.7. Magnetic properties

Magnetic measurements were done on $Lu_{1-x}La_xFeO_3$ ($x = 0, 0.05, 0.1, 0.15, 0.2, 0.25$) pellets using VSM attached to Quantum Design PPMS.

6.7.1. Low-temperature studies

Temperature-dependent magnetization (M-T) was measured on all the samples both in ZFC (zero-field-cooled) and FC (field- cooled) mode. Figure 6.16 shows the M-T data measured at H = 500 Oe for $x = 0.0, 0.15, 0.25$ and at H = 100 Oe for $x = 0.05, 0.1, 0.2$ samples. It can be seen that $x = 0.0$ sample shows the expected SRT (spin reorientation temperature) close to T = 130 K. The transition is usually referred due to the transition of magnetization from c- axis to a-axis and termed as B_2 to A_2 in hexagonal unit cell [28]. With La doping, for even $x = 0.05$, the anomaly related to the spin reorientation transition is completely suppressed. It can also be observed that M increases with decrease in temperature for $x = 0.0$ and 0.25. The behavior looks identical apart from the SR. For x = 0.05 and 0.1, decrease in T raises M in FC mode and lowers M in ZFC mode. It should be noted that the applied field is only 100 Oe. With increase in field, x = 0.05 and 0.1 also would have followed the same trend as x = 0.0 and 0.25. It should be noted that these samples have orthorhombic phase and indicates that 500 Oe is enough to overcome the anisotropy in the system.

To further investigate the magnetic nature of these samples, M-H measurements are carried out at different temperatures in the temperature range of 5 K–300 K up to a maximum field of 90 kOe and shown in figure 6.17. All the samples show non-linear M-H curves which do not saturate even up to the maximum measurement field ± 90 kOe. The loops show pinching effect

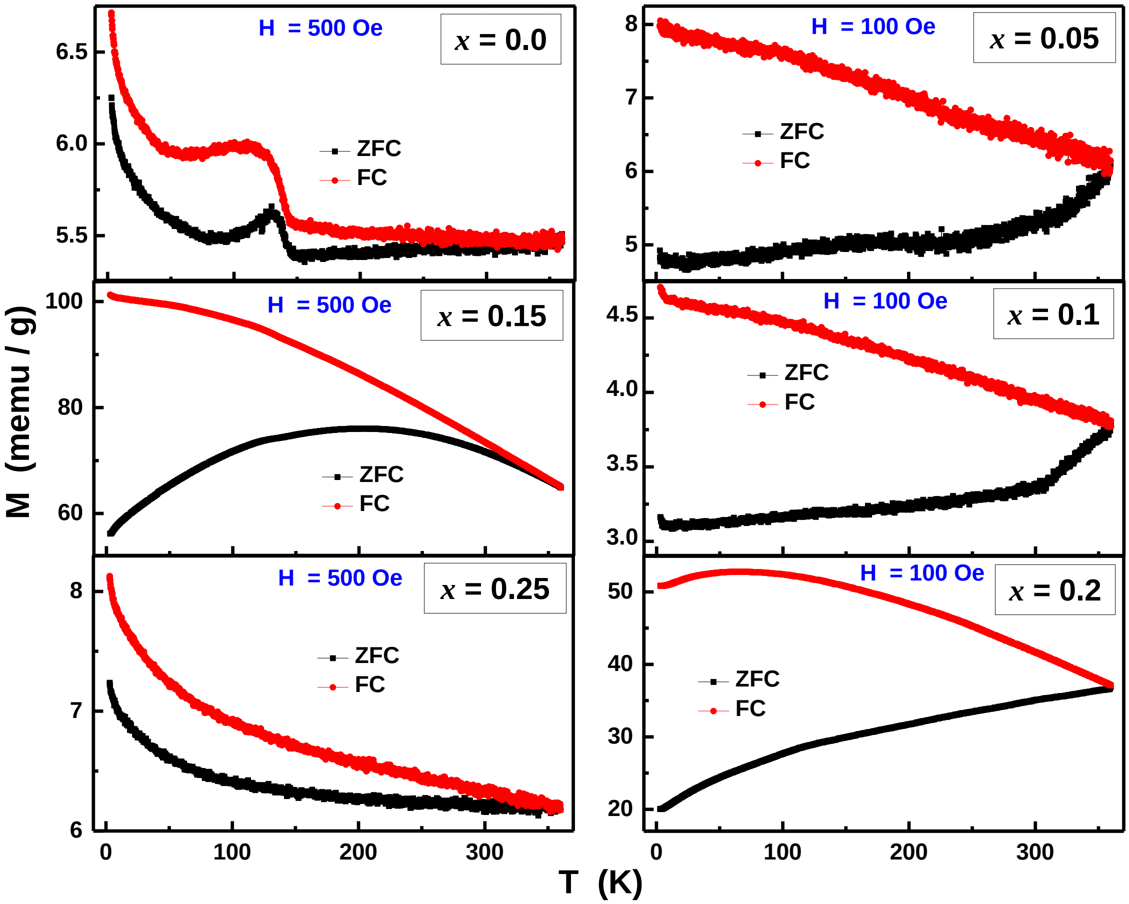

Figure 6.16. Magnetization vs temperature measured at ZFC and FC mode at H= 100 / 500 Oe for $Lu_{1-x}La_xFeO_3$ (x =0.0, 0.05, 0.1, 0.15, 0.2, 0.25)

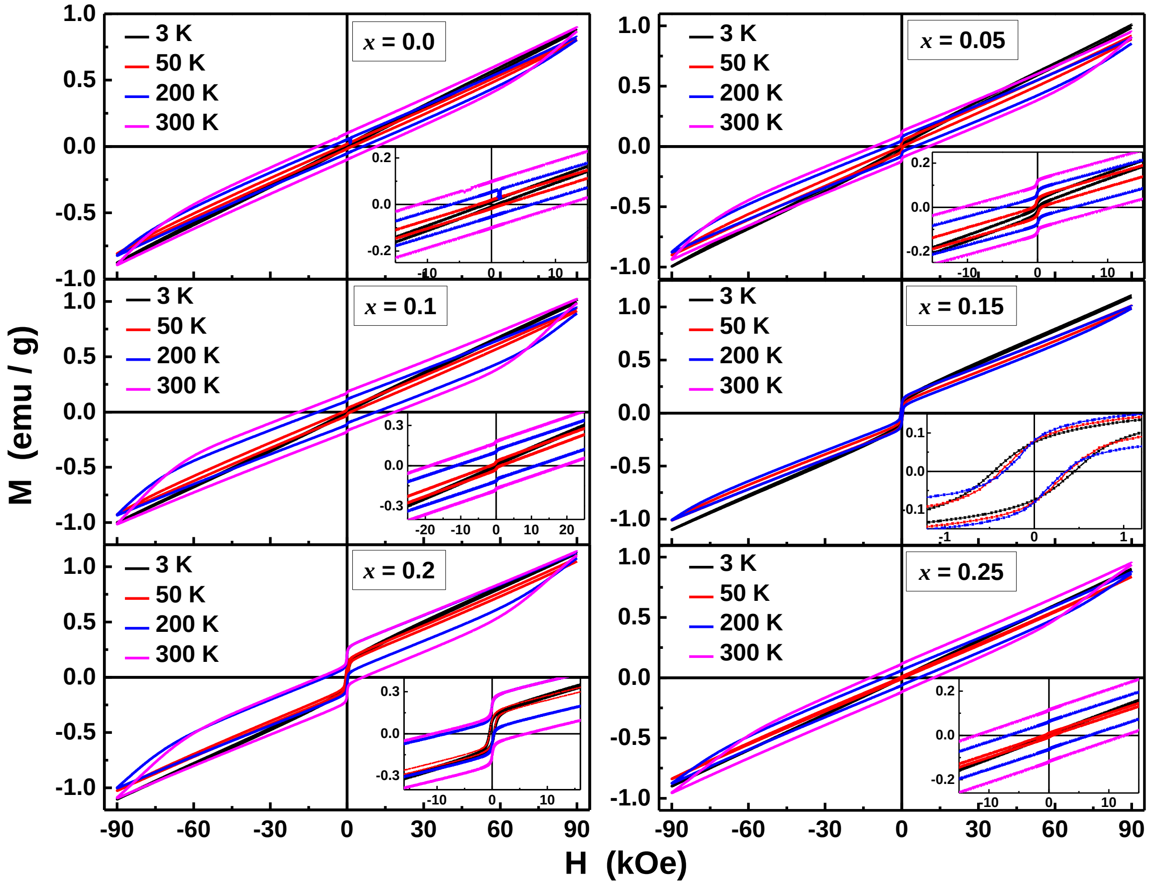

Figure. 6.17. Magnetization vs field measured at 3 K, 50 K, 200 K and 300 K for $Lu_{1-x}La_xFeO_3$ (x = 0, 0.05, 0.1, 0.15, 0.2, 0.25) samples.

close to H = 0 Oe. The non- saturating loops with the finite coercivity and pinching effect establish the presence of competing ferromagnetic (FM) and antiferromagnetic (AFM) interaction in this system. The M-H loops show vertical shift without much of a horizontal shift. In general, the shift in M-H loops from the origin (both horizontal as well as vertical) is associated with the presence of exchange bias in the system arising due to the competing FM-AFM interactions. To observe the horizontal shift and to quantify the amount of exchange bias present in the system, in general, one has to cool the system from T > T_N in the presence of a bias field and measure the M- H. The shift in the loop, exchange field (HE) is in general proportional to the amount of bias field. However, in the present case, since the T_N is above RT, no such bias field could be applied and the M-H loops are measured without the application of any bias field. This protocol resulted in nearly zero horizontal shifts but with a large shift in vertical axis.

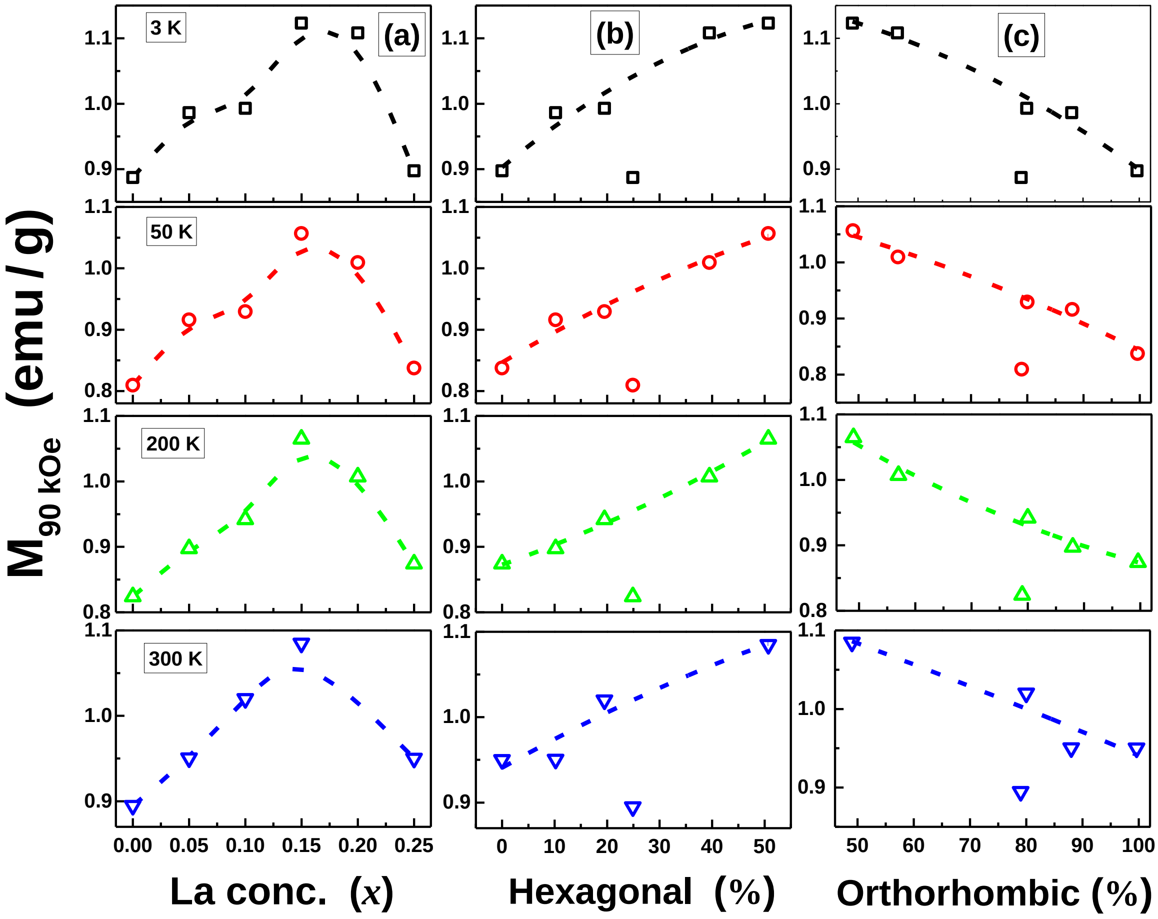

Figure 6.18. (a) $M_{90\ kOe}$ plotted against La concentration at T = 3 K, 50 K, 200 K, 300 K; **(b)** $M_{90\ kOe}$ plotted against hexagonal phase %. **(c)** $M_{90\ kOe}$ plotted against orthorhombic phase %.

As discussed in XRD analysis part (section 6.3.3), the hexagonal structure consists of four distinct oxygen positions, two La/Lu positions and one Fe position. This leads to various interactions: Fe-O1-Fe, Fe-O2-Fe, Fe-O3-La/Lu, Fe-O4-La/Lu. Out of these, only Fe-O1-Fe, Fe-O2-Fe contributes for magnetic interaction as La and Lu are diamagnetic in nature. Similarly, in orthorhombic phase also Fe-O1-Fe, Fe-O2-Fe are the only magnetic interactions. The Fe^{3+} ions mediate through O2- ions and gives raise to ground state antiferromagnetic interactions. However, due to the Dzyaloshinskii–Moriya (DM) interactions, the spins deviate slightly from their anti- parallel configuration and results in weak ferromagnetism. The canted spin configuration manifests itself as tilt in the FeO_6 octahedra and FeO_5 trigonal bipyramid in the orthorhombic and hexagonal structure, respectively.

In order to understand the magnetic behavior due to La doping, the maximum magnetization measured at 90 kOe ($M_{90\ kOe}$) for all the doping concentrations at all temperatures is plotted against La doping concentration. It can be seen from figure 6.18 that $M_{90\ kOe}$ peaks at $x = 0.15$. To understand this behavior, $M_{90\ kOe}$ is also plotted against hexagonal phase percentage. It can be clearly observed that $M_{90\ kOe}$ is increasing almost linearly with increase in hexagonal %. From literature, it is known that h- LFO (0.1 μ_B/*f.u*) is less magnetic than the o-LFO (0.24 μ_B/*f.u*). Whereas in our work, the magnetization is observed to strongly depends on the hexagonal phase %. In general, La doping is expected to increase the lattice parameters due to the bigger ionic radius of La compared to Lu. In the present work, due to the nano size of the samples the strain created in the nano crystallites play an important rule. It can be understood that the negative strain, calculated for hexagonal phase from Halder- Wagner method, compresses the unit cell such that the characteristic bond lengths, Fe-O(1) and Fe-O(2) shortens and results in smaller bond length compared to the orthorhombic counterparts (Table 6.2). Thus, the presence of h-LFO enhances the magnetization. Similar results have been reported by Smita Chaturvedi et al [29].

One more possibility that the net magnetization follows the hexagonal phase could be because of the interfaces between the two phases. Cao et el showed that the o- LFO planes near the boundary of h- LFO phase tends to align with the h- LFO planes. This could orient the magnetization towards the hexagonal easy axis and enhance the magnetization. The increase in H_C is observed with increase in temperature from 3 to 300 K. (inset of figure 6.17). This unusual behavior of increase in H_C with an increase in temperature is previously reported in Mn-doped $LuFeO_3$ system [30]. The anomalous enhancement of H_C with an increase in T is observed in a number of multiferroic systems [31,32] wherein the variation is explained in terms of the competition between the magnetic anisotropy and magneto electric coupling [31,32]. In the present system, the observation of finite P-E loops, M-H loops along with the observation of dielectric peak around the T_N temperature indicates the indirect presence of magneto- electric coupling which may explain the observed variation of H_C with T.

6.7.2. High-temperature studies

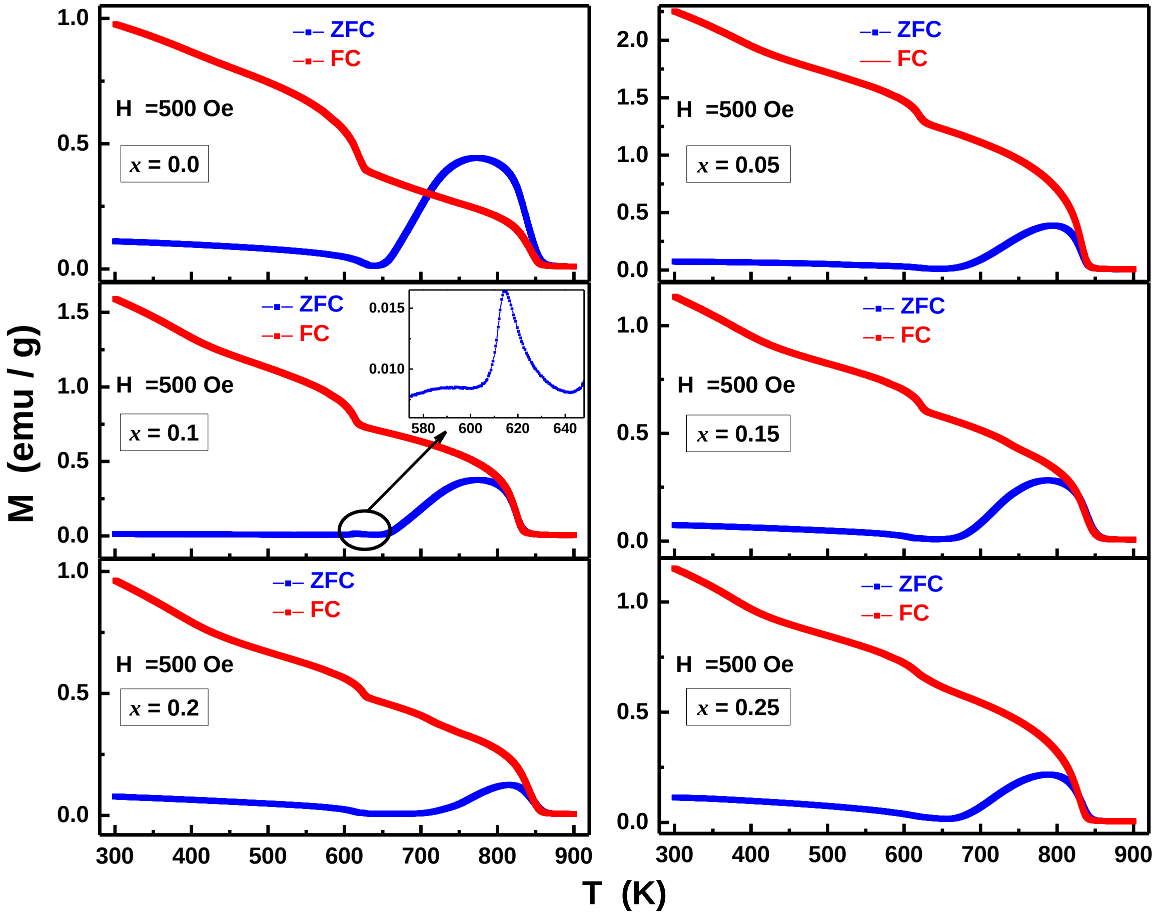

Figure 6.19. M-T curves of La doped $LuFeO_3$ for $x = 0.0$ to 0.25 in ZFC and FC mode measured at 500 Oe.

The presence of M-H hysteresis measured at T = 300 K and the bifurcation in ZFC and FC (fig 6.16) starting from 360 K for all the samples indicate the presence of competing interactions even above RT. To further study about the T_N, M-T measurement is carried out from 300 K to 900 K in FC and ZFC mode in presence of 500 Oe field and shown in figure 6.19. The magnetic transition from antiferromagnetic to paramagnetic transition of o-LFO is observed ~630 K and is matching with the literature [3,8]. With increasing in La doping concentration, the T_N shifts from 634 K for $x = 0.0$ to 656 K for $x = 0.25$. This behavior is expected as the T_N of $LaFeO_3$ is 750 K. Another peak ~850 K is observed which belongs to Fe_3O_4 phase.

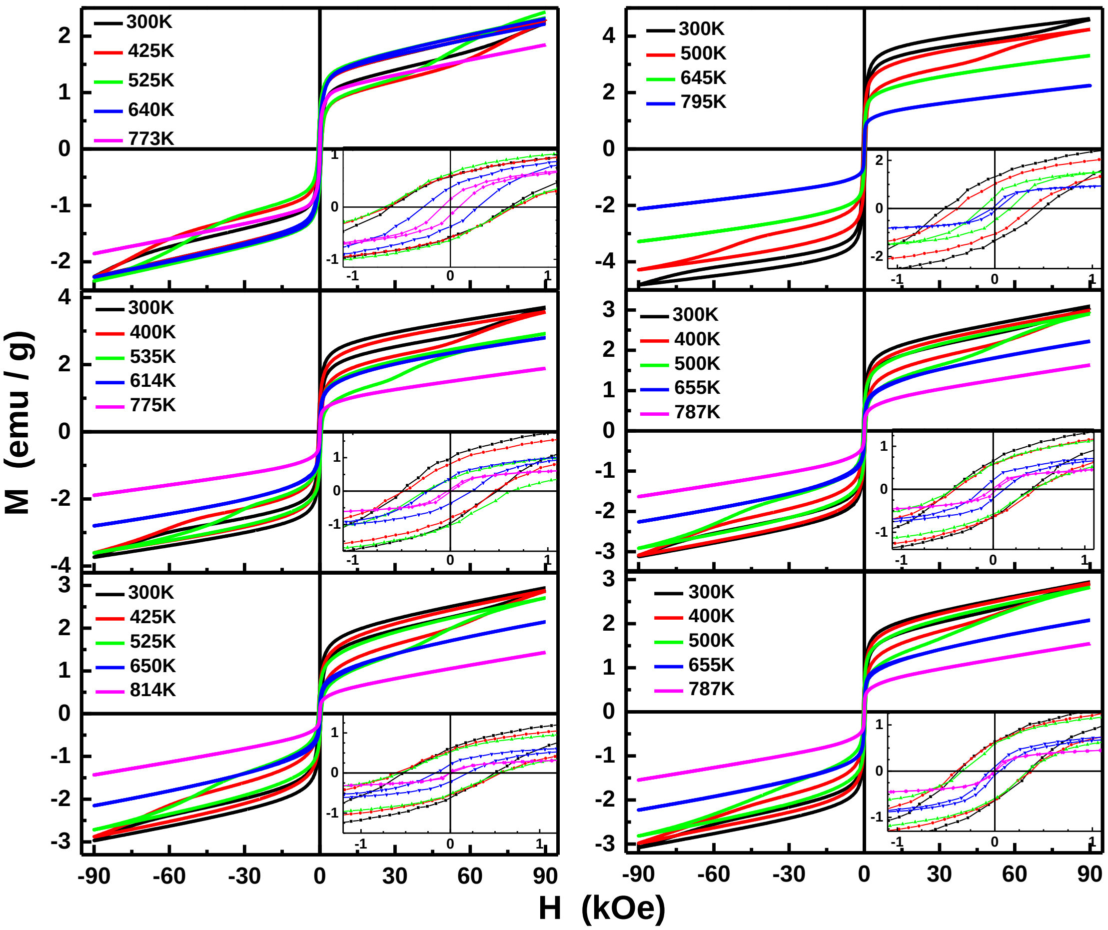

Figure 6.20. M-H hysteresis of La doped $LuFeO_3$ for all the doping concentrations at various temperatures.

Magnetization hysteresis loops are measured as a function of temperature at various temperatures ranging from 300 K to 800 K and shown in figure 6.20. $M_{90\ kOe}$, H_C and M_r are observed to decrease with increase in temperature. This shows that the temperature is randomizing the spins as it approaches T_N. But a clear observation of hysteresis around 800 K indicates that still magnetic interaction persists which is due to the presence of Fe_3O_4 phase.

That T_N tracks T_c (similar to figure 5.16), is clearly brought out by a direct comparison between $M_{ZFC}(T)$, measured at H = 100 Oe, and ε′(T) at *f* = 10 kOe, as shown for a *x* = 0.0 to 0.25 compositions in figure 6.21. This finding asserts that a magneto-electric coupling exists between the magnetic and ferroelectric order parameters.

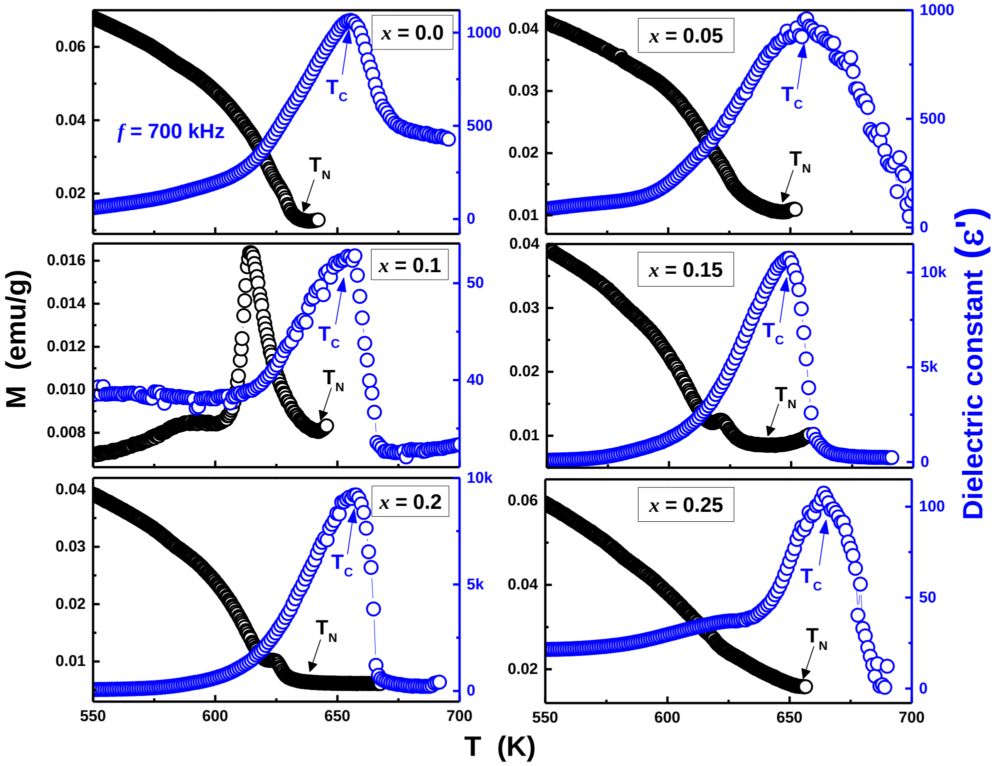

Figure 6.21. Real part of dielectric permittivity (ε′) is plotted along with M_{ZFC} measured at 100 Oe against temperature for x = 0.0 to 0.25.

6.8. Summary

$Lu_{1-x}La_xFeO_3$ (x = 0, 0.05, 0.1, 0.15, 0.2, 0.25) nanoparticles are synthesized using the hydrothermal method and individual hexagonal and orthorhombic phase fractions are estimated using Rietveld refinement. Crystallite size and strain are calculated using Halder- Wagner method. Raman spectra also confirms the presence of the mixed phases. The real part of dielectric permittivity increases with the increase in h- LFO phase % due to its polar nature. The peak observed in the high temperature dielectric constant and tanδ follows the same trend as the h- LFO crystallite size confirming that the ferroelectric transition is a 'diffusive phase transition'. The bulk polarization measured from P-E loops also increases with increase in h-LFO%. The spin reorientation observed at 130 K is suppressed by La doping. h- LFO % strongly influences $M_{90\ kOe}$. Due to the compressive strain on h-LFO, the bond length shortens and reduces below the bond length of o- LFO, thus enhancing the magnetization. The T_N of o-LFO is observed to increase with La doping as expected. M-H loop at ~800 K and a peak in M-T curve around ~850 K confirms the presence of Fe_3O_4.

References

[1] W. Wang, J. Zhao, W. Wang, Z. Gai, N. Balke, M. Chi, H.N. Lee, W. Tian, L. Zhu, X. Cheng, D.J. Keavney, J. Yi, T.Z. Ward, P.C. Snijders, H.M. Christen, W. Wu, J. Shen, X. Xu, Room-temperature multiferroic hexagonal LuFeO3 films, Phys. Rev. Lett. 110 (2013) 1–5. https://doi.org/10.1103/PhysRevLett.110.237601.

[2] J. Liu, T.L. Sun, X.Q. Liu, H. Tian, T.T. Gao, X.M. Chen, A Novel Room-Temperature Multiferroic System of Hexagonal Lu1−xInxFeO3, Adv. Funct. Mater. 28 (2018) 1–10. https://doi.org/10.1002/adfm.201706062.

[3] U. Chowdhury, S. Goswami, D. Bhattacharya, J. Ghosh, S. Basu, S. Neogi, Room temperature multiferroicity in orthorhombic LuFeO3, Appl. Phys. Lett. 105 (2014) 10–14. https://doi.org/10.1063/1.4892664.

[4] S. Chaturvedi, S.K. Singh, P. Shyam, M.M. Shirolkar, S. Krishna, R. Boomishankar, S. Ogale, Nanoscale LuFeO 3 : Shape dependent ortho/hexa-phase constitution and nanogenerator application, Nanoscale. 10 (2018) 21406–21413. https://doi.org/10.1039/c8nr07825d.

[5] L. Lin, H.M. Zhang, M.F. Liu, S. Shen, S. Zhou, D. Li, X. Wang, Z.B. Yan, Z.D. Zhang, J. Zhao, S. Dong, J.M. Liu, Hexagonal phase stabilization and magnetic orders of multiferroic L u1-x S cxFe O3, Phys. Rev. B. 93 (2016) 1–9. https://doi.org/10.1103/PhysRevB.93.075146.

[6] M.Y. Liu, T.T. Gao, X.L. Zhu, X.M. Chen, Ferroelectricity and magnetoelectric coupling in hexagonal Lu0.5In0.5FeO3 ceramics, J. Appl. Phys. 126 (2019) 0–7. https://doi.org/10.1063/1.5117344.

[7] J. Liu, T.L. Sun, X.Q. Liu, H. Tian, T.T. Gao, X.M. Chen, A Novel Room-Temperature Multiferroic System of Hexagonal Lu1−xInxFeO3, Adv. Funct. Mater. 28 (2018) 1–7. https://doi.org/10.1002/adfm.201706062.

[8] Z. Zhou, L. Guo, H. Yang, Q. Liu, F. Ye, Hydrothermal synthesis and magnetic properties of multiferroic rare-earth orthoferrites, J. Alloys Compd. 583 (2014) 21–31. https://doi.org/10.1016/j.jallcom.2013.08.129.

[9] E. Magome, C. Moriyoshi, Y. Kuroiwa, A. Masuno, H. Inoue, Noncentrosymmetric structure of LuFeO3 in metastable state, Jpn. J. Appl. Phys. 49 (2010). https://doi.org/10.1143/JJAP.49.09ME06.

[10] S. Song, H. Han, H.M. Jang, Y.T. Kim, N.S. Lee, C.G. Park, J.R. Kim, T.W. Noh, J.F. Scott, Implementing Room-Temperature Multiferroism by Exploiting Hexagonal-Orthorhombic Morphotropic Phase Coexistence in LuFeO3Thin Films, Adv. Mater. 28 (2016) 7430–7435. https://doi.org/10.1002/adma.201601989.

[11] X. Xu, W. Wang, Multiferroic hexagonal ferrites (h-RFeO3, R = Y, Dy-Lu): A brief experimental review, Mod. Phys. Lett. B. 28 (2014) 1–27. https://doi.org/10.1142/S0217984914300087.

[12] W. Wang, J. Wang, Phase separation in LuFeO 3 films, (2016).

[13] R S Arun Raj, Study of the modified magnetic, dielectric, ferroelectric and optical properties in Ni substituted GdFe1-xNixO3 orthoferrites, Nanotechnology. 11 (2021) 5035–5040. https://doi.org/10.1016/j.matdes.2020.109338.

[14] K. Momma, F. Izumi, VESTA 3 for three-dimensional visualization of crystal, volumetric and morphology data, J. Appl. Crystallogr. 44 (2011) 1272–1276. https://doi.org/10.1107/S0021889811038970.

[15] S.M. Disseler, J.A. Borchers, C.M. Brooks, J.A. Mundy, J.A. Moyer, D.A. Hillsberry, E.L. Thies, D.A. Tenne, J. Heron, M.E. Holtz, J.D. Clarkson, G.M. Stiehl, P. Schiffer, D.A. Muller, D.G. Schlom, W.D. Ratcliff, Magnetic structure and ordering of multiferroic hexagonal LuFeO3, Phys. Rev. Lett. 114 (2015) 1–6. https://doi.org/10.1103/PhysRevLett.114.217602.

[16] S. Venugopalan, M.M. Becker, Raman scattering study of LuFeO3, J. Chem. Phys. 93 (1990) 3833–3836. https://doi.org/10.1063/1.458768.

[17] M.C. Weber, M. Guennou, H.J. Zhao, J. Íñiguez, R. Vilarinho, A. Almeida, J.A. Moreira, J. Kreisel, Raman spectroscopy of rare-earth orthoferrites RFeO3 (R =La, Sm, Eu, Gd, Tb, Dy), Phys. Rev. B. 94 (2016) 1–8. https://doi.org/10.1103/PhysRevB.94.214103.

[18] A.A. BOKOV, Z.-G. YE, Dielectric Relaxation in Relaxor Ferroelectrics, J. Adv. Dielectr. 02 (2012) 1241010. https://doi.org/10.1142/s2010135x1241010x.

[19] L. Eric Cross, Relaxor ferroelecirics, Ferroelectrics. 76 (1987) 241–267. https://doi.org/10.1080/00150198708016945.

[20] Y. Park, K.M. Knowles, K. Cho, Particle-size effect on the ferroelectric phase transition in PbSc1/2Ta1/2O3 ceramics, J. Appl. Phys. 83 (1998) 5702–5708. https://doi.org/10.1063/1.367424.

[21] C.A. Randall, A.S. Bhalla, Nanostructural-property relations in complex lead perovskites, Jpn. J. Appl. Phys. 29 (1990) 327–333. https://doi.org/10.1143/JJAP.29.327.

[22] L.D. Landau, E.M. Lifshitz, Electrodynamics of Continuous Media, 1960.

[23] U. Chowdhury, S. Goswami, D. Bhattacharya, S.S. Rajput, A.K. Mall, A. Garg, R. Gupta, S.D. Kaushik, V. Siruguri, S. Saravanakumar, S. Israel, R. Saravanan, T. Chatterji, Origin of Ferroelectricity in Orthorhombic LuFeO$_3$, (2017) 1–12. http://arxiv.org/abs/1710.02381.

[24] M. Nakhaei, D.S. Khoshnoud, Study of structural , optical and electrical properties of ReFeO3 (Re=La, Pr, Nd, Sm & Gd) orthoferrites, Phys. B Phys. Condens. Matter. 612 (2021) 412899. https://doi.org/10.1016/j.physb.2021.412899.

[25] S. Acharya, J. Mondal, S. Ghosh, S.K. Roy, P.K. Chakrabarti, Multiferroic behavior of lanthanum orthoferrite (LaFeO3), Mater. Lett. 64 (2010) 415–418. https://doi.org/10.1016/j.matlet.2009.11.037.

[26] S.M. Disseler, X. Luo, B. Gao, Y.S. Oh, R. Hu, Y. Wang, D. Quintana, A. Zhang, Q. Huang, J. Lau, R. Paul, J.W. Lynn, S.W. Cheong, W. Ratcliff, Multiferroicity in doped hexagonal LuFe O3, Phys. Rev. B - Condens. Matter Mater. Phys. 92 (2015) 1–9. https://doi.org/10.1103/PhysRevB.92.054435.

[27] I.I. Makoed, N.A. Liedienov, A. V. Pashchenko, G.G. Levchenko, D.D. Tatarchuk, Y. V. Didenko, A.A. Amirov, G.S. Rimski, K.I. Yanushkevich, Influence of rare-earth doping on the structural and dielectric properties of orthoferrite La0.50R0.50FeO3 ceramics synthesized under high pressure, J. Alloys Compd. 842 (2020). https://doi.org/10.1016/j.jallcom.2020.155859.

[28] S. Leelashree, S. Srinath, Investigation of Structural, Ferroelectric, and Magnetic Properties of La-Doped LuFeO 3 Nanoparticles, J. Supercond. Nov. Magn. (2019). https://doi.org/10.1007/s10948-019-5114-4.

[29] S. Chaturvedi, P. Shyam, M.M. Shirolkar, S. Krishna, B. Sinha, Tunable magnetization in nanoscale LuFeO 3 : Role of morphology , ortho-hexa phase ratio and local structure, (n.d.) 1–16.

[30] Y. Qin, X. Qiang Liu, X. Ming Chen, Dielectric, ferroelectric and magnetic properties of Mn-doped LuFeO 3 ceramics, J. Appl. Phys. 113 (2013) 3–8. https://doi.org/10.1063/1.4789605.

[31] B. Ahmmad, M.Z. Islam, A. Billah, M.A. Basith, Anomalous coercivity enhancement with temperature and tunable exchange bias in Gd and Ti co-doped BiFeO3 multiferroics, J. Phys. D. Appl. Phys. 49 (2016) 95001. https://doi.org/10.1088/0022-3727/49/9/095001.

[32] T.J. Park, G.C. Papaefthymiou, A.J. Viescas, Y. Lee, H. Zhou, S.S. Wong, Composition-dependent magnetic properties of BiFeO3 -BaTiO 3 solid solution nanostructures, Phys. Rev. B - Condens. Matter Mater. Phys. 82 (2010) 1–10. https://doi.org/10.1103/PhysRevB.82.024431.

CHAPTER 7

SUMMARY AND FUTURE-SCOPE OF THE PRESENT THESIS

The seventh describes the summary of the present study and also gives some future scope to work on these systems.

7.1. Summary

7.1.1. Structural, magnetic and dielectric properties of $Lu_{1-x}Ho_xFeO_3$ $(0 \leq x \leq 1)$

Nanocrystalline $Lu_{1-x}Ho_xFeO_3$ (x = 0.0, 0.05, 0.1, 0.2, 0.25, 0.3, 0.4, 0.5, 0.6, 0.8, 1.0) powders are synthesized by hydrothermal method and annealed at 750 ºC for 8h. The Rietveld refinement of the XRD spectra for x = 0.0 (0.05) yields the phase fractions as 91.5 % (6 %) hexagonal and 8.5 % (94 %) orthorhombic. For Ho concentrations beyond x = 0.05, a pure 100% orthorhombic phase is found in the samples with x ranging from 0.1 to 1.0. Following Vegard's law, the lattice parameters increase linearly with the Ho concentration. The lattice parameters are used to calculate the FeO_6 octahedral tilt angles $\theta_{[101]}$ and $\varphi_{[010]}$ of the FeO_6 octahedral cages around the pseudo-cubic (pc) $[101]_{pc}$ and $[010]_{pc}$ axes and the attendant structural (orthorhombic) distortion, both are caused by the size of the R^{3+} ions. From the linear Halder-Wagner plot, volume-weighted mean crystallite size is calculated for all the samples and found to be in the range between ~20 to 47 nm. The average particle size from FE-SEM varies from ~31 to 82 nm for all the samples.

Raman spectroscopy also confirms the presence of mixed orthorhombic and hexagonal phases for x = 0 and 0.05 and only orthorhombic phase for x > 0.05, in agreement with the XRD results. Two new Raman modes are observed at ≈ 53 cm^{-1} and ≈ 69 cm^{-1} in all the compositions ($0 \leq x \leq 1$). These additional RA modes are attributed to the asymmetric vibration of R^{3+} ions across the surfaces/interfaces/boundaries of nanoparticles. We demonstrate that the contribution to the Raman shifts due to the variations in the R-O/Fe-O bond lengths with x primarily governs the observed functional dependence of the Raman mode wavenumber on x in accordance with the simple harmonic oscillator approximation. The RA mode $A_g(3)$ [$A_g(5)$] wavenumber increases linearly with the FeO_6 octahedra tilt angle $\varphi_{[010]}$ [$\theta_{[101]}$] indicating that these independent modes are sensitive to orthorhombic distortion induced by the size of R^{3+} ions.

The T_{SR} and T_{comp} traced from the $M_{ZFC}(T)$ and $M_{FC}(T)$ curves shifts to higher temperatures with increasing x. This shift is a consequence of the enhancement in the Ho^{3+}- O^{2-}- Fe^{3+} interaction strength as the Ho concentration increases. As the temperature is lowered below ~ 30 K, the paramagnetic (PM) Ho^{3+} moments tend to progressively order in an antiferromagnetic (AF) configuration due to the Ho^{3+}- O^{2-}- Ho^{3+} superexchange interaction. The spontaneous ordering of the Ho^{3+} moments at low temperatures is made all the more obvious by the observation of the Curie-Weiss (CW) behavior of the FC susceptibility with $\theta_{Ho} = -4.5 \pm 0.5\ K$. The negative value of θ_{Ho} is indicative of the AF coupling between the Ho^{3+} moments. M_{FC} (T = 3 K, H = 100 Oe) is plotted as a function of x and the percolation picture is found to describe the observed variation of M with x quite well. Agreement between theory and experiment asserts that the percolation of the Ho^{3+} moments on the Ho^{3+} sub-lattices takes place above the threshold concentration of $x_c \approx 0.05$, which is the minimum Ho concentration at which the orthorhombic structure stabilizes in the presently synthesized $Lu_{1-x}Ho_xFeO_3$ nanoparticles. High T_N at ~620 K from M_{ZFC}(T) and M_{FC}(T) thermomagnetic curves were taken at H = 100 Oe in the temperature range 300 K - 900 K reflects a strong interaction between Fe^{3+} ions which increases with x. When octahedral tilt decreases due to Ho doping, the Fe^{3+}- O^{2-}- Fe^{3+} bond angle increases, resulting in a higher T_N as x increases following Goodenough-Kanamori rules. Another transition around 850 K is due to the presence of a tiny amount of impurity Fe_3O_4 phase which completely evaded detection in the x-ray diffraction and Raman scattering experiments.

When Ho is substituted for Lu, net magnetization of the system increases because of the additional Ho^{3+}- O^{2-}- Fe^{3+} and Ho^{3+}-O^{2-}- Ho^{3+} interactions, and the virgin curves of the M-H hysteresis loops highlight that, at 3 K, M has a tendency to saturate for $H > 20\ kOe$. The Brown-Néel model proposed for the approach-to-saturation of magnetization in ferromagnetic systems closely reproduces the virgin M-H isotherms taken at 3 K in the field range $20\ kOe \lesssim H \leq 90\ kOe$. A striking similarity between $b^*(x)$ (so obtained from the fits) and $H_C(x)$, measured at 3 K asserts that the root cause of H_C in the LHFO nanoparticles is magnetocrystalline anisotropy. $M_{90\ kOe}$, increases linearly with the Ho concentration, x, at any temperature in the range 3 K - 800 K. The straight line fits through the data points facilitates to extract M_{LFO} and M_{HFO} (*LFO* and *HFO* contributions to $M_{90\ kOe}$ at a given temperature). The calculated $M_{LFO}(T = 0)$ = 0.245 $\pm$ 0.001 μ_B per *f.u.* which is in perfect agreement with that (0.24 μ_B per *f.u.*) reported previously for bulk o-LFO. χ_{HFO} follows the Curie-Weiss and the effective magnetic moment calculated, $\mu_{eff} = 10.9 \pm 0.1\ \mu_B$, has nearly the Ho^{3+} free-ion value of $\mu_{eff} = 10.6\ \mu_B$. The negative value for θ_{HFO} $(-10 \pm 1\ K)$ reflects the antiferromagnetic ordering of the Ho^{3+} spins at low temperatures.

The intrinsic switchable polarization, P_{int}, versus the electric field, E, hysteresis loops, measured using an experimental protocol that gets rid of the non-remanent contributions arising from the electric leakage currents and non-switchable polarization, provide conclusive evidence for the existence of permanent electric dipole moments in, and ferroelectric nature of, the nanocrystalline $Lu_{1-x}Ho_xFeO_3$ ($0 \leq x \leq 1$) samples at room temperature. As x increases from $x = 0$ to $x = 1$, the saturation value of intrinsic polarization, P_{int}^{sat}, presents an overall decreasing trend with a dip at $x = 0.4$. While the decrease in P_{int}^{sat} with increasing x is a consequence of the increase in the unit cell volume and reduction in the electric dipole moment due to decline in orthorhombic distortion, the peak in the crystallite/particle size at $x = 0.4$ is shown to account for the dip in the $P_{int}^{sat}(x)$, ε' and in the static dielectric permittivity, $\varepsilon_0(x)$, at $x = 0.4$.

In order to determine unambiguously the ferroelectric-to-paraelectric phase transition temperature, T_C, the P– E and P_{int} – E hysteresis loops have been measured at fixed temperatures for $x = 0.6$. As expected, the intrinsic remnant polarization P_{int} drops sharply with increasing temperatures and falls to an extremely small value at a temperature T = 600 K which is very close to T_C. The real (ε') and imaginary (ε'') parts of the complex dielectric permittivity, measured as a function of temperature exhibits a peak at T_C. The T_C is always higher than T_N. This indicates that magnetic ordering drives the ferroelectric ordering. T_N tracking T_C is thus a signature of Type-II multiferroicity.

ε' and ε'' measured at room temperature over the ac electric-field frequency range, $20 \text{ Hz} \leq f \leq 2 \text{ MHz}$, unravel two different types of frequency variations of ε' and ε'' in nanocrystalline $Lu_{1-x}Ho_xFeO_3$. In type-I, ε'' goes through a peak as a function of f at f_{max} while ε' increases with decreasing f and approaches a constant but composition-dependent value (20 – 50) at low frequencies in the compositions $0.2 \leq x \leq 0.8$. By contrast, in type-II, both ε' and ε'' increase with decreasing f and exhibit a very steep rise when f falls below ≈ 1 kHz reaching values as high as $10^3 - 10^4$ as f approaches the lowest measurement frequency of 20 Hz, in Ho concentrations $0 \leq x \leq 0.1$ and 1.0. The type-I (type-II) frequency variation has been understood in terms of the (non-Debye) relaxation of elementary electric dipoles which interact with one another and have different relaxation times (relaxation associated with the hopping of charge carriers between various localized states in the presence of a time-varying external electric field). The frequency-induced crossover from Type-I to Type-II dielectric relaxation is observed above room temperature until ~530 K, above which only the Type-

II dielectric relaxation is observed. This indicates that with increase in temperature, more and more charge carriers hop between their localized states.

7.1.2. Structural, magnetic and dielectric properties of $Lu_{1-x}La_xFeO_3$ ($0 \leq x \leq 0.25$)

$Lu_{1-x}La_xFeO_3$ (x = 0, 0.05, 0.1, 0.15, 0.2, 0.25) nanoparticles were synthesized by the hydrothermal method and annealed at 820°C for 8h. For the undoped as well as for the La doping till 0.2, both the hexagonal (h-LFO) and orthorhombic (o-LFO) phases exist. Further increase in La to 0.25, the hexagonal phase is completely suppressed and only the orthorhombic phase is present. The observed percentage of phase fraction does not vary systematically with increase in *x*. Raman spectra measured on these samples also confirms the presence of the mixed phases.

The measured P-E loops do not saturate even at the highest applied field (which is not as strong as the field at which the breakdown occurs) and exhibit lossy behavior. In order to bring out the effect of phase fraction on dielectric and ferroelectric properties, ε', measured at 2 MHz (as a representative), and P_{max} are plotted against the h-LFO %. Clearly, both ε' and P_{max} increase with increasing h-LFO % due to the polar nature. Dielectric constant and tanδ were also measured as a function of temperature at various frequencies ranging from 1 kHz to 2 MHz and a peak is observed at ~ 650 K. The temperature at which the dielectric constant (ε'_{max}) peaks is taken as T_C, the ferroelectric-to-paraelectric transition temperature. The striking similarity between the variations of T_C and the crystallite size of orthorhombic phase is plotted against *x* along with the T_C determined from ε'(T) at 700 kHz, indicates relaxor behavior.

The non- saturating M-H hysteresis loops with the finite coercivity and pinching effect establish the presence of competing ferromagnetic and antiferromagnetic interactions in this system. The magnetization ($M_{90\ kOe}$) is observed to strongly depend on the h-LFO %. The negative strain, calculated for the hexagonal phase from Halder- Wagner plots, compresses the unit cell such that the characteristic bond lengths, Fe-O(1) and Fe-O(2) shorten. Consequently, the hexagonal phase has smaller bond lengths compared to its orthorhombic counterpart. Thus, the presence of h-LFO enhances the magnetization. In the present system, the observation of P-E and M-H loops at RT along with the observation of dielectric peak close to T_N indicates the presence of magneto-electric coupling. To find out the effect of La substitution on T_N, M-T measurements were carried out, in the FC and ZFC modes, at an external field of H = 500 Oe from 300 K to 900 K. For o-LFO, T_N has the value ~ 630 K. With increasing La concentration, T_N shifts from 634 K for $x = 0.0$ to 656 K for $x = 0.25$. This behavior is expected as the T_N = 750 K of $LaFeO_3$ is higher than T_N = 630 K of $LaFeO_3$.

7.2. Future Scope

- Some more analysis is required to understand the nature of the relaxation time (τ) calculated for $Lu_{1-x}Ho_xFeO_3$ ($x = 0$ to 1) at higher temperatures.
- To understand the Fe influence on the magnetic properties of the system, Mössbauer measurements can be carried out.
- The substituted La concentration should be extended beyond $x = 0.25$, to understand the effect of non-magnetic dopant on the dielectric and magnetic properties in the entire composition range.
- Direct measurement of magneto-electric effect can be carried out to estimate the strength of the magneto-electric coupling.

LIST OF PUBLICATIONS BASED ON THE RESEARCH WORK

1. Effect of progressive substitution of Lu by Ho on the structural and dielectric properties of nanocrystalline $LuFeO_3$ orthoferrite

   Leelashree S, S.N. Kaul and S. Srinath; Materials Research Bulletin 145, 111570 (2020).

2. Investigation of Structural, Ferroelectric, and Magnetic Properties of La-Doped $LuFeO_3$ Nanoparticles

   S Leelashree, S Srinath; Journal of Superconductivity and Novel Magnetism 33 (6), 1587-1591 (2020).

3. Structural and Magnetic properties of Room Temperature Multiferroic $Lu_{0.9}Ho_{0.1}FeO_3$

   Leelashree S, P.D. Babu, S.N. Kaul and S. Srinath; International Journal of Innovative Research in Physics 1 (2), 37-41 (2020).

4. Effect of La doping on dielectric and magnetic properties of room temperature multiferroic $LuFeO_3$

   S Leelashree, PD Babu, S Srinath; American Institute of Physics Conference Series 1953 (1), 120076 (2018).

Manuscripts under preparation

1. Effect of Ho substitution on the magnetic and dielectric properties of nanocrystalline $Lu_{1-x}Ho_xFeO_3$ orthoferrites

   Leelashree S, P.D. Babu, S.N. Kaul and S. Srinath

2. Role of hexagonal and orthorhombic phase fractions in magnetic, dielectric and ferroelectric properties of $Lu_{1-x}La_xFeO_3$

   Leelashree S, P.D. Babu, S.N. Kaul and S. Srinath

Other Publication

1. Terahertz radiation and second-harmonic generation from a single-component polar organic ferroelectric crystal

   Uppari Venkataramudu, Chakradhar Sahoo, **S Leelashree,** Mottamchetty Venkatesh, Damarla Ganesh, Sri Ram Gopal Naraharisetty, Anil Kumar Chaudhary, Sanyadanam Srinath, Rajadurai Chandrasekar; Journal of Materials Chemistry C 6 (35), 9330-9335 (2018)

Awards Received

1. Received **'Best Poster award'** for presenting the work with title 'Investigation of Structural, Ferroelectric, and Magnetic Properties of La-Doped $LuFeO_3$ Nanoparticles' at 'International Conference on Magnetic Materials and Applications' (ICMAGMA-2018) held at NISER, Bhubaneswar.
2. Receiver of **'K V RAO SCIENTIFIC SOCIETY RESEARCH AWARDS (Runner-up I)'** held virtually on July 3rd, 2021 for presenting my research work titled 'Structural and Magnetic Properties of Room Temperature Multiferroic Ho Doped o- $LuFeO_3$'.

Conferences Attended

1. 'International conference on magnetic materials and applications' organized by MSI, India during 1st-3rd February, 2017. (Presented Poster)
2. 'International conference on Condensed matter and applied physics at Bikaner during 24th-25th November, 2017. (Presented Poster)
3. 'International Symposium on Integrated Functionalities' organized during 10th-13th December, 2017 at New Delhi. (Presented Poster)
4. 'Frontiers in Nanoscience and Technology' during 6th-7th April, 2018 at University of Hyderabad. (Presented Poster)
5. 'National conference on Physics at small scales and Advanced materials' held during 8th-9th September, 2018 at University of Hyderabad. (Presented Poster)
6. International conference on magnetic materials and applications' organized by MSI, India during 9th-13th December, 2018 held at NISER Bhubaneswar (Presented poster).
7. 'Applied Physics and Materials Science' organized by Vasavi College of Engineering during 7th-8th September, 2018. (Oral presentation)
8. 'International conference on Condensed matter physics' at Institute of Engineering and Management, Kolkata during 14th-16th November, 2019. (Oral presentation)
9. '2020 Annual Conference on Magnetism and Magnetic Materials' held virtually during November 2nd-6th, 2020. (Oral presentation)

Workshops Attended

1. A one-day workshop on ‘Material characterization using Electron Back-Scatter Diffraction Technique’ on 14th March, 2016 held at BITS, Hyderabad campus.
2. ‘Summer school on Magnetism’ during 11th-15th July, 2016 held at Thapar University, Patiala, Punjab.
3. ‘Functional Magnetic Materials’ during 26th February to 3rd March, 2018 conducted by UGC-NRC, University of Hyderabad.
4. ‘Workshop on characterization & modelling of magnetic materials’ held at BITS, Hyderabad campus during 13th-14th July, 2018.
5. ‘Neutrons as probes of condensed matter’ organized by UGC-DAE, BARC, Mumbai during 28th October to 1st November, 2018.

"Structural, Dielectric and Magnetic Properties of Single-phase Room Temperature Multiferroic – (Ho, La)-LuFeO_3"

by Leelashree S

Submission date: 16-Dec-2021 02:07PM (UTC+0530)
Submission ID: 1731880706
File name: Leelashree_Thesis_Final_Plagiarism_check.pdf (27.19M)
Word count: 40890
Character count: 181519

"Structural, Dielectric and Magnetic Properties of Single-phase Room Temperature Multiferroic – (Ho, La)-LuFeO_3"

ORIGINALITY REPORT

33%	8%	30%	3%
SIMILARITY INDEX	INTERNET SOURCES	PUBLICATIONS	STUDENT PAPERS

PRIMARY SOURCES

1	S. Leelashree, S.N. Kaul, S. Srinath. "Effect of progressive substitution of Lu by Ho on the structural and dielectric properties of nanocrystalline LuFeO3 orthoferrite", Materials Research Bulletin, 2021 Publication	21%
2	S. Leelashree, S. Srinath. "Investigation of Structural, Ferroelectric, and Magnetic Properties of La-Doped LuFeO3 Nanoparticles", Journal of Superconductivity and Novel Magnetism, 2019 Publication	3%
3	S. Leelashree, S.N. Kaul, S. Srinath. "Effect of progressive substitution of Lu by Ho on the structural and dielectric properties of nanocrystalline LuFeO3 orthoferrite", Materials Research Bulletin, 2022 Publication	1%
4	etheses.saurashtrauniversity.edu Internet Source	<1%

5	mafiadoc.com Internet Source	<1%
6	Ujjal Chowdhury, Sudipta Goswami, Dipten Bhattacharya, Arindam Midya, P. Mandal. "Determination of intrinsic ferroelectric polarization in lossy improper ferroelectric systems", Applied Physics Letters, 2016 Publication	<1%
7	ir.amu.ac.in Internet Source	<1%
8	E Fazio. "Complete characterization of (2 1)D soliton formation in photorefractive crystals with strong optical activity", Journal of Optics A Pure and Applied Optics, 09/01/2003 Publication	<1%
9	renati.sunedu.gob.pe Internet Source	<1%
10	darwin.bth.rwth-aachen.de Internet Source	<1%
11	Submitted to Manipal University Student Paper	<1%
12	Submitted to Higher Education Commission Pakistan Student Paper	<1%
13	irgu.unigoa.ac.in Internet Source	<1%

14	baadalsg.inflibnet.ac.in Internet Source	<1 %
15	TONEY, MICHAEL F.. "XRD", Encyclopedia of Materials Characterization, 1992. Publication	<1 %
16	aip.scitation.org Internet Source	<1 %
17	hdl.handle.net Internet Source	<1 %
18	tudr.thapar.edu:8080 Internet Source	<1 %
19	Melvin M. Vopson. "Fundamentals of Multiferroic Materials and Their Possible Applications", Critical Reviews in Solid State and Materials Sciences, 2015 Publication	<1 %
20	ethesis.nitrkl.ac.in Internet Source	<1 %
21	S.N. Kaul, Umasankar Messala. "Chirality-driven intrinsic spin-glass ordering and field-induced ferromagnetism in Ni3Al nanoparticle aggregates", Journal of Magnetism and Magnetic Materials, 2016 Publication	<1 %
22	Johan Bielecki, Peter Svedlindh, Dessie T. Tibebu, Shengzhen Cai, Sten-G. Eriksson, Lars	<1 %

Börjesson, Christopher S. Knee. " Structural and magnetic properties of isovalently substituted multiferroic BiFeO : Insights from Raman spectroscopy ", Physical Review B, 2012

Publication

23	Submitted to University of Hyderabad, Hyderabad Student Paper	<1 %
24	Jin, Li, Fei Li, and Shujun Zhang. "Decoding the Fingerprint of Ferroelectric Loops: Comprehension of the Material Properties and Structures", Journal of the American Ceramic Society, 2014. Publication	<1 %
25	Submitted to Indian Institute of Technology, Madras Student Paper	<1 %
26	lib.dr.iastate.edu Internet Source	<1 %
27	exodus.poly.edu Internet Source	<1 %
28	Chanda, Sadhan, Sujoy Saha, Alo Dutta, Bushra Irfan, Ratnamala Chatterjee, and T.P. Sinha. "Magnetic and dielectric properties of orthoferrites La1−x PrxFeO3 (x = 0, 0.1, 0.2,	<1 %

	0.3, 0.4 and 0.5)", Journal of Alloys and Compounds, 2015. Publication	
29	www2.l-3com.com Internet Source	<1 %
30	www.ukas.org Internet Source	<1 %
31	Abja Keshar Kar, Bidisa Chattopadhyay, Ratnadwip Singha, Abhisikta Barman et al. " Effect of Co and Mg doping at Cu site on structural, magnetic and dielectric properties of α-Cu V O ", Journal of Physics: Condensed Matter, 2021 Publication	<1 %
32	P. M. Visakh. "Nanostructured Multiferroics", Wiley, 2021 Publication	<1 %
33	lbk.fe.uni-lj.si Internet Source	<1 %
34	dspace.ncl.res.in:8080 Internet Source	<1 %
35	archive.org Internet Source	<1 %
36	Submitted to University of Kent at Canterbury Student Paper	<1 %
	ntrs.nasa.gov	

37	Internet Source	<1 %
38	www.dovepress.com Internet Source	<1 %
39	Kummari V. Sreenivasulu, Naresh K. Rotte, Vadali V. S. S. Srikanth, Sharika Nandan Kaul. "Non-collinear ferromagnetic short range order in MgO decked multi-layered graphene", Physical Chemistry Chemical Physics, 2017 Publication	<1 %
40	nozdr.ru Internet Source	<1 %
41	Liu, X.J.. "Magnetic, electrical transport and electron spin resonance studies of Fe-doped manganite LaMn"0"."7Fe"0"."3O"3"+"@d", Journal of Magnetism and Magnetic Materials, 200706 Publication	<1 %
42	digital.lib.usf.edu Internet Source	<1 %
43	Hui Zhang, Dechang Zeng, Zhongwu Liu. "The law of approach to saturation in ferromagnets originating from the magnetocrystalline anisotropy", Journal of Magnetism and Magnetic Materials, 2010 Publication	<1 %

44	Tanushree Sarkar, Suja Elizabeth, P.S. Anil Kumar. "Enhanced magnetization and reduced leakage current by Zr substitution in multiferroic ScMnO 3", Journal of Magnetism and Magnetic Materials, 2017 Publication	<1 %
45	scholarbank.nus.edu.sg Internet Source	<1 %
46	hal.archives-ouvertes.fr Internet Source	<1 %
47	"Polar Oxides", Wiley, 2004 Publication	<1 %
48	Babusona Sarkar, Biswajit Dalal, S K De. " Correlation among disorder, electronic and magnetic phases of SrRuO ", Journal of Physics: Condensed Matter, 2015 Publication	<1 %
49	cyseni.com Internet Source	<1 %
50	Md. F. Abdullah, P. Pal, Surender Lal, S. R. Mohapatra, K. Chandrakanta, Som Datta Kaushik, C. S. Yadav, Anil Singh. "Dielectric anomalies and robust magnetodielectricity in Y-type $Ba_2Mg_2Fe_{12}O_{22}$ hexaferrite", Materials Research Express, 2018 Publication	<1 %

51	Submitted to University of Edinburgh Student Paper	<1 %
52	acikerisim.dicle.edu.tr Internet Source	<1 %
53	etheses.whiterose.ac.uk Internet Source	<1 %
54	Submitted to Landmark University Student Paper	<1 %
55	Monalisa Halder, Ajit Kumar Meikap. "Influence on loading terbium manganate on optical, thermal and electrical properties of polyvinyl alcohol nanocomposite films", Journal of Materials Science: Materials in Electronics, 2019 Publication	<1 %
56	raiith.iith.ac.in Internet Source	<1 %
57	core.ac.uk Internet Source	<1 %
58	www.act.edu.in Internet Source	<1 %
59	muroran-it.repo.nii.ac.jp Internet Source	<1 %
60	Fiza Mumtaz, Ghulam Hassnain Jaffari, S Ismat Shah. "Peculiar magnetism in Eu	<1 %

	substituted BiFeO_3 and its correlation with local structure.", Journal of Physics: Condensed Matter, 2018 Publication	
61	pubs.rsc.org Internet Source	<1 %
62	repositorio.uam.es Internet Source	<1 %
63	ses.library.usyd.edu.au Internet Source	<1 %
64	ujcontent.uj.ac.za Internet Source	<1 %
65	www.israc.gov.il Internet Source	<1 %
66	K.C. Verma, R. K. Kotnala, Navdeep Goyal. " Multiferroic Systems of BiFeO and BaTiO Nanostructures: New Ideas and Insights from Recent Magnetoelectric Advancements ", Wiley, 2021 Publication	<1 %
67	shura.shu.ac.uk Internet Source	<1 %
68	web.njit.edu Internet Source	<1 %
69	"Magnetic Nanoparticles", Wiley, 2009 Publication	<1 %

70	Submitted to Marquette University	Student Paper	<1%
71	authors.library.caltech.edu	Internet Source	<1%
72	dspace.kuet.ac.bd	Internet Source	<1%
73	iopscience.iop.org	Internet Source	<1%
74	wrap.warwick.ac.uk	Internet Source	<1%
75	www.geophysik.uni-muenchen.de	Internet Source	<1%
76	Chevalier, B.. "Superconductivity in fluorinated La"1"."8"5"-"xNd"xSr"0"."1"5CuO"4 solid solution with 0=	Publication	<1%
77	S P Mathew. "Magnetic irreversibility, spin-wave excitations and magnetocaloric effect in nanocrystalline Gadolinium", Journal of Physics Conference Series, 01/01/2010	Publication	<1%
78	epdf.pub	Internet Source	<1%
79	Submitted to iGroup	Student Paper	<1%

80	lib.buet.ac.bd:8080 Internet Source	<1%
81	piers.org Internet Source	<1%
82	rruff.info Internet Source	<1%
83	www.kfa-juelich.de Internet Source	<1%
84	"Handbook of Electroporation", Springer Science and Business Media LLC, 2017 Publication	<1%
85	Hirotoshi Terashita. "Possible role of phase segregation in the disagreement between the metal-insulator and ferromagnetic transition temperatures in some colossal magnetoresistance compounds", Physical Review B, 04/2001 Publication	<1%
86	Cai, L.. "Structure and dielectric properties of Ln"3NbO"7 (Ln=Nd, Gd, Dy, Er, Yb and Y)", Journal of the European Ceramic Society, 2007 Publication	<1%
87	L. F. Chen, C. K. Ong, C. P. Neo, V. V. Varadan, V. K. Varadan. "Microwave Electronics", Wiley, 2004 Publication	<1%

Exclude quotes	On	Exclude matches	< 14 words
Exclude bibliography	On		

This is to certify that the thesis entitled **'Structural, Dielectric and Magnetic Properties of Single-phase Room Temperature Multiferroic – (Ho, La)-$LuFeO_3$'**, submitted by my student Leelashree S (Regn. No. 15PHPH07), has been screened by the Turnitin software at the Indira Gandhi Memorial Library (IGML)- University of Hyderabad. This software shows 33% similarity index out of which, 25% came from the candidate's research articles (where she is the first author) directly related to this thesis. This leaves out a 8% similarity index with other sources which is well within the acceptable limits for the submission of the Thesis.

Prof. S. Srinath
Thesis supervisor
School of Physics
University of Hyderabad

Dr. S. Srinath
Professor
School of Physics
UNIVERSITY OF HYDERABAD
Central University P.O.
Hyderabad-500 046.